UNIVERSITY OF CALIFORNIA SAN DIEGO

Engineered scaffolds for targeted molecular imaging and drug delivery via biomolecular self-assembly

A Dissertation submitted in partial satisfaction of the requirements
for the degree Doctor of Philosophy

in

NanoEngineering

by

Raina M. Borum

Committee in charge:

Professor Jesse V. Jokerst, Chair
Professor Jinhye Bae
Professor Andrew C. Kummel
Professor Nicole F. Steinmetz
Professor Yingxiao Wang

2023

The Dissertation of Raina M. Borum is approved, and it is acceptable in quality and form for publication on microfilm and electronically.

University of California San Diego

2023

DEDICATION

For my parents and sister.

TABLE OF CONTENTS

LIST OF FIGURES

LIST OF TABLES

ACKNOWLEDGEMENTS

I want to thank my advisor, Professor Jesse Jokerst. His mentorship, patience, trust, and passion for science helped me grow beyond what I thought was possible. I prize every lesson I've learned from him. I would also like to thank my committee members: Professor Jinhye Bae, Professor Andy Kummel, Professor Nicole Steinmetz, and Professor Yingxiao Wang. Their guidance, research, and courses were a source of energy and inspiration throughout my journey, and they provided help and insight that were vital to my projects.

I am profoundly grateful for the support from the UCSD Cancer Researchers in Nanotechnology training program (NIH T32 CA153915). The program's financial support was critical to my progress, and the cross-training in cancer biology along with Professor Kummel's guidance supercharged my stamina and ideas.

Many people helped me along the way: I am very grateful for my lab mates. They were all extremely patient with me when I was learning new techniques and disciplines, and I enjoyed working with them on our projects. I am privileged to have learned from and studied alongside strong teammates and talented scientists, but moreover, I am privileged to have made lifelong friends.

Additionally, I would like to thank all my mentees and students. They've taught me some of the most valuable lessons during my career, and their grit, curiosity, and energy never failed to revitalize me.

I am also very grateful for Dr. Yi Chen. He was the first to take a chance on me and teach me important skills in research and at the bench. Without this, I wouldn't have been able to be as effective or productive throughout my PhD education. I carried much of my

training on nucleic acid engineering and chemistry from this chapter of my life with me over the following years.

Finally, to my dear parents, and my big sister Alana—I acknowledge with a gratitude that can't be articulated. For their wisdom, strength, unwavering faith in me, and love.

I am also grateful for my collaborators:

Chapter 1, in full, is a reprint of the material as it appears in Molecules 2022. Borum, Raina M.; Lin, Avery E.; Dong, Xiangyi; Kai, Mingxuan; Chen, Yi. The dissertation author was the primary investigator and author
of this paper.

Chapter 2, in full, is a reprint of the material as it appears in Biomaterials Science 2021. Borum, Raina M.; Jokerst, Jesse V. The dissertation author was the primary investigator and author of this paper.

Chapter 3, in full, is a reprint of the material as it appears in Bioconjugate Chemistry 2021. Borum, Raina M.; Moore, Colman; Kim, Soo Khim; Steinmetz, Nicole F.; Jokerst, Jesse V. The dissertation author was the primary investigator and author of this paper.

Chapter 4, in full, is a reprint of the material as it appears in Advanced Science 2023. Borum, Raina M.; Moore, Colman; Mantri, Yash; Xu, Ming; Jokerst, Jesse V. The dissertation author was the primary investigator and author of this paper.

Chapter 5, in part is currently being prepared for submission for publication of the material. Borum, Raina; Retout, Maurice; Creyer, Matt; Chang, Yu-Ci; Gregorio, Karlo; Jokerst, J.V. The dissertation author was the primary researcher and author of this material.

VITA

2017 Bachelor of Science in NanoEngineering, University of California San Diego

2020 Master of Science in NanoEngineering, University of California San Diego

2023 Doctor of Philosophy in NanoEngineering, University of California San Diego

PUBLICATIONS

1. R. M. Borum, C. Moore, Y. Mantri, M. Xu, and J.V. Jokerst, “Supramolecular Loading of DNA hydrogels with Dye Drug Conjugates for real time Photoacoustic Monitoring of Chemotherapy,” *Advanced Science*, 2204330 (2022)
2. R. M. Borum, A. E. Lin, X. Dong, M. Kai, and Y. Chen, “DNA Origami Disguises Herpes Simplex Virus 1 Particles and Controls their Virulence,” *Molecules*, 27, 7162 (2022)
3. R. M. Borum, C. Moore, SK. Chan, N. F. Steinmetz, and J.V. Jokerst, “A Photoacoustic Contrast Agent for miR-21 via NIR Fluorescent Hybridization Chain Reaction,” *Bioconjugate Chemistry*, 33, 1080-1092 (2021)
4. R. M. Borum, and J. V. Jokerst “Hybridizing clinical translatability with enzyme-free DNA signal amplifiers: recent advances in nucleic acid detection and imaging,” *Biomaterials Science*, 9, 347-366 (2020)
5. C. Moore, R. M. Borum, Y. Mantri, M. Xu, P. Fajtová, A. J. O’Donoghue, and J. V. Jokerst, "Activatable carbocyanine dimers for photoacoustic and fluorescent detection of protease activity," *ACS Sensors*. 6, 2356-2365 (2021).
6. Y. Cheng, R.M. Borum, A.E. Clark, Z. Jin, C. Moore, P. Fajtova, A. O’Donoghue, A. Carlin, J. V. Jokerst. A dual-color fluorescent probe allows simultaneous imaging of main and papain-like proteases of SARS-CoV-2-infected cells for accurate detection and rapid inhibitor screening. *Angewandte Chemie*. 61 (2021).
7. W. Yim, R. M. Borum, J. Zhou, Y. Mantri, Z. Wu, J. Zhou, Z. Jin, M. Creyer, and J. V. Jokerst, “Ultrasmall gold nanorod-polydopamine hybrids for enhanced photoacoustic imaging and photothermal therapy in second near-infrared window,” *Nanotheranostics*, 6, 79, (2022).
8. J. Zhou, M. Xu, Z. Jin, R. M. Borum, N. Avakyan, Y. Cheng, W. Yim, T. He, J. Zhou, Z. Wu, Y. Mantri, and J.V. Jokerst, “Versatile Polymer Nanocapsules via Redox Competition,” *Angewandte Chemie*, 60, 26357-26362.
9. Z. Wu, J. Zhou, C. Isalomboto Nkanga, Z. Jin, T. He, R. M. Borum, W. Yim, J. Zhou, Y. Cheng, M. Xu, N. F. Steinmetz, and J. V. Jokerst, “One-step Supramolecular

Multifunctional Coating on Plant Virus Nanoparticles for Bioimaging and Therapeutic Applications," *ACS Applied Materials & Interfaces*, 14, 13692-13702, (2022)

10. W. Yim, K . Takemura, J. Zhou, J. Zhou, Z. Jin, R. M. Borum, M. Xu, Y. Cheng, T. He, W. Penny, B. R. Miller III, J. V. Jokerst, "Enhanced Photoacoustic Detection of Heparin in Whole Blood via Melanin Nanocapsules Carrying Molecular Agents," *ACS Nano*, 16, 683-693 (2021)
11. M. Xu, W. Yim, J. Zhou, Z. Jin, C. Moore, R. Borum, A. Jorns, and J. V. Jokerst, "The application of organic nanomaterials for bioimaging, drug delivery, and therapy". *IEEE Nanotechnology Magazine*. 99, 2-22 (2021).
12. Z. Jin, Y. Mantri, M. Retout, Y. Cheng, J. Zhou, A. Jorns, P. Fajtova, W. Yim, C. Moore, M. Xu, M. Creyer, R. Borum, J. Zhou, Z. Wu, T. He, W. Penny, A. O'Donoghue, J. V. Jokerst. A charge-switchable zwitterionic peptide for rapid detection of SARS-CoV-2 main protease. *Angewandte Chemie*. 61, e202112995 (2021).
13. Y. Cheng, A. E. Clark, J. Zhou, T. He, Y. Li, R. M. Borum, M. N. Creyer, M. Xu, Z. Jin, J. Zhou, W. Yim, Z. Wu, P. Fajtova, A. O'Donoghue, A. F. Carlin, J.V.Jokerst, "Protease Responsive Peptide-Conjugated Mitochondrial-Targeting AIEgens for Selective Imaging and Inhibition of SARS-CoV-2-Infected Cells" *ACS Nano*, 16 12305-12317 (2022)
14. M. Retout, Z. Jin, J. Tsujimoto, Y. Mantri, R.M. Borum, M.N.Creyer, W. Yim, T. He, Y. Chang, J.V. Jokerst. "Di-arginine additives for dissociation of gold nanoparticle aggregates: A matrix-insensitive approach with applications in protease detection," accepted for publication, *ACS Applied Materials & Interfaces* (2022).

ABSTRACT OF THE DISSERTATION

Engineered scaffolds for targeted molecular imaging and drug delivery via biomolecular self-assembly

by

Raina M. Borum

Doctor of Philosophy in NanoEngineering

University of California San Diego, 2023

Professor Jesse V. Jokerst, Chair

Noncovalent assemblies constitute some of the most robust and keystone interactions in biology. Hydrogen bonding, for example, drives hybridization between single DNA strands into double helices for genetic informational storage, while the combination of electrostatic, Van der Waals, and hydrophobic amino acid sequences underpin binding specificity between antibodies and antigens as well as stability in proteins. Similarly, intermolecular forces can yield novel physical, chemical, and optical properties for new materials, such as tunable self-quenching between fluorophores and functionalized surfaces on nanoparticles. Engineered biomolecular self-assembly can thus be a tool to design nanomaterials with specificity to biological events or targets for (1) drug delivery to diseased tissue, (2) signaling for

biosensing, or (3) contrast for bioimaging. This dissertation presents strategies for engineered molecular contrast agents and drug delivery platforms using bottom-up bio- and inter-molecular self-assembly pathways. In chapter one, electrostatic interactions establish DNA origami's ability to cover and disguise the surfaces of herpes simplex virus 1 particles for infection against cancer cells, even when the mammalian strain of the virus is different from the mammalian strain of the host cell. Chapter two outlines the value of enzyme free and isothermal self-assembly between oligonucleotides via strand amplification for resultant signal amplification to detect nucleic acid biomarkers. Chapter three demonstrates this value by presenting strand amplification for triggered contact quenching between NIR fluorophores, leading to enhanced and ratiometric photoacoustic contrast when miR-21 is detected in live cells and within sub-centimeter penetration depths in tissue mimicking phantoms. Chapter four leverages aggregative photoacoustic enhancement when an NIR dye-tagged chemotherapeutic is densely intercalated into a DNA-clad hydrogel for real-time pharmacokinetic tracking. Chapter five examines the resultant geometries from two self-assembly pathways between an engineered tumor-homing peptide and an NIR molecular dye for targeted tumor photoacoustic imaging and targeted photodynamic therapy, underscoring the significance in nanoparticle architecture on resultant interactions with biology at the live cell and live tissue scales.

CHAPTER 1. DNA ORIGAMI DISGUISES HERPES SIMPLEX 1 PARTICLES AND CONTROLS THEIR VIRULENCE

ABSTRACT: DNA nanostructures are well-established vectors for packaging diversified payloads for targeted cellular delivery. Here, DNA origami rectangular sheets were combined with Herpes Simplex Virus 1 (HSV1) capsids to demonstrate surface coverage of the particle via electrostatic interactions. The optimized origami:HSV1 molar ratios led to characteristic packaging geometries ranging from dispersed “HSV1 pockets” to agglomerated “HSV1 sleeves.” “Pockets” were disguised from cells in HeLa and B16F10 cells and were 44.2% less infective than naked HSV1 particles. However, the pockets were 117% more infective than naked HSV1 particles when the origami sheets were coated with folic acid. We observed infectivity from naked origami, but they are 99.1% less infective with respect to HSV1 and 99.6% less infective with respect to the pocket complexes. This work suggests that DNA origami can selectively modulate virus infectivity.

1.1 Introduction

The precise presentation of biomolecules between the surfaces of cells and pathogens drives their interactions. Bacteria, viruses, and other foreign bodies present characteristic proteins to facilitate uptake and infection[1–7] Tailored mimicry of this molecular dialogue may offer several advances in synthetic biology. First, details of pathogenicity may be better clarified and emulated. More importantly, controllable pathogenicity may be achieved [8,9] for improved delivery of therapeutically engineered viruses[10] such as oncolytic viruses for cancer therapy[11,12], which are limited by neutralizing antibodies from the host, premature degradation, and liver clearance pathways[13–15].

The ability to mask native surface proteins on a virus while presenting a desired class of proteins can disguise the virus and modify its uptake. This approach requires a biocompatible material that can organize the desired proteins at a controllable density while maintaining coverage over the original surface. Cell membrane coating technologies are popular for the disguise and delivery of foreign entities into cells but suffer from coating inefficiencies during fabrication, low-yielding purification from uncoated entities[16], and inflammation with collateral immunogenicity[17]. Polymeric and silica coatings have been proposed, but both materials have minimal control over peptide or protein decoration for cell uptake; they are also toxic towards immune cells via oxidative stress and pro-inflammatory activation while lacking immunostimulatory stealth[18–20].

DNA nanotechnology uses programmed strands that complimentarily self-assemble into a coherent structure via base-pair specificity. DNA offers an unrivaled ability to organize molecules with single nanometer precision[21,22], fabricate structures with high yield[23,24], and maintain integrity in vivo while delivering therapeutic agents[25,26]. Some reported DNA structures have demonstrated low immunogenicity in vivo[27]. DNA nanostructures can be fabricated in

several ways including “DNA origami” where small “staple strands” use complimentary forces to fold one long “scaffold strand” into the programmed shape. An alternative is “ODN or oligonucleotide approach” where short oligonucleotides self-assemble into the structure[28].

There are many compelling reports on combining DNA nanostructures with viruses. DNA origami rectangles have been loaded with cowpea chlorotic mosaic virus (CCMV) capsid proteins for increased transfection into cells[29]. DNA “nano-stars” have demonstrated robust avidity to dengue virus (DENV) by precisely organizing aptamers in a pattern identical to the complimentary DENV glycoprotein distribution to mute their infectivity[30]. Elegant icosahedral DNA structures have demonstrated complete entrapment and neutralization of hepatitis B and adeno-associated viruses in human cells[31]. A next step in the field is selective viral infectivity.

Here, we report the ability to disguise herpes simplex virus 1 particles with DNA origami nanosheets. The origami sheet carries a net negative charge from the phosphate backbones of the DNA to cover the positively charged HSV1 capsid proteins via electrostatic interactions[32]. We explore and report this packaging mechanism with origami sheets containing overhanging strands that anchor the targeting ligand folic acid on the outer surface, as biomarker receptors are a promising avenue in targeted nanomedicine (Figure 1.1A) [33–36]. This folic acid decoration efficiently delivers the viral HSV1 particle cargo to folic acid receptor-positive cell surfaces via the DNA origami (Figure 1.1 B). Without this decoration, charge repulsion between the origami coating and the cell membranes prevents HSV1 entry. This work describes an applied nanomaterial that can modulate delivery of engineered oncolytic viruses; HSV1 is a fundamental backbone for talimogene laherparepvec (T-VEC)—the first FDA-approved oncolytic virus to combat Stage 3 and Stage 4 melanomas and lung cancers[12].

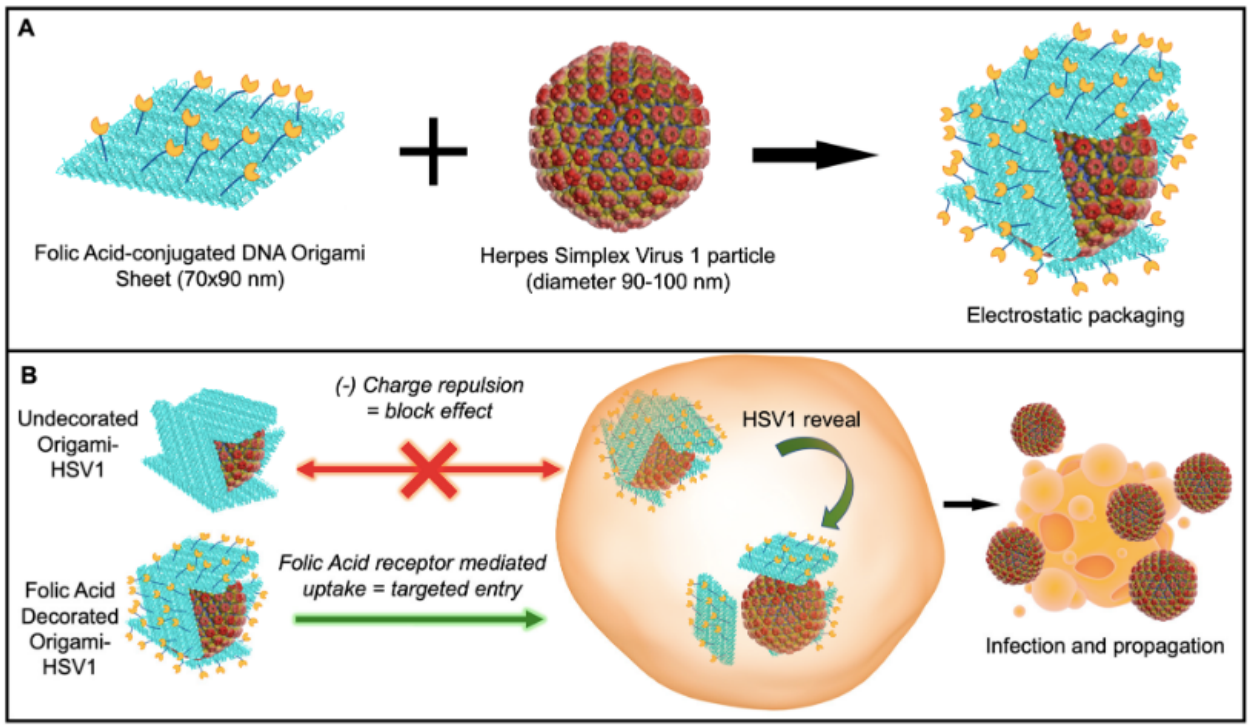

Figure 1. 1. Schematic of Disguised HSV1 through DNA Origami.

(A) Wrapping HSV1 in folic acid (yellow)-adorned DNA origami (blue). (B) In vitro delivery experiments on the (1) disguise of HSV1 (yellow)-adorned DNA origami (blue). (B) In vitro delivery experiments on the (1) disguise of HSV1 and (2) targeted initial uptake into folate-receptor positive cell surfaces.

1.2. Methods

1.2.1 Materials

The materials for this research include DNA Origami and ssDNA strands (Integrated DNA Technologies (IDT)), M13mp18 scaffold strand (Guild Biosciences) PEG-maleimide-folic acid (NanoCS) Monkey Vero-propagated Herpes Simplex Virus 1 particles (Bio-Rad, MPP010), HSV1/2 Major Capsid Protein ICP5 Primary Antibody (Santa Cruz Biotechnology), Goat anti-mouse IgG Horseradish Peroxidase (BioLegend), Azure Radiance Q Substrate (Azure). HeLa and B16F10 cells were generously gifted by Professor Liangfang Zhang's Nanomedicine Laboratory (UC San Diego).

1.2.2. DNA Origami

Plated DNA strands were first centrifuged, then aliquoted to 100 μM with MilliQ water. Strands were then collected to add with the M13mp18. Strands were then mixed at a 1:10 M13mp18 to staple strand molar concentration in 1× TAEMg (Tris-base Acetic acid, EDTA, Mg) buffer. If Folic Acid strands were included in the sample, the strands were also incubated with the folic-acid DNA strands at a 1:10:10 M13mp18:staple:folic acid strand molar ratio. The strand mixtures were first heated to 90 °C for one minute before 3 h cooling to 4 °C. If not immediately used, origamis were stored at 4C.

1.2.3. DNA-Folic Acid Conjugation

Thiolated ssDNA strands (SH-ssDNA) were also ordered from IDT. In summary, the ssDNA-SH was incubated with tris (2-carboxyethyl)phosphine (TCEP) at a 1:10 molar ratio in 50× TAE (Tris-base, Acetic acid, EDTA) for 6 h room temperature, in order to reduce disulfide bonds from the thiol-tagged ssDNA. Maleimide-PEG-Folic Acid was then added to the reaction and given overnight to link to the strands at room temperature. The conjugation reaction was halted and purified by letting the sample run through a spinning dialysis (3000MWCO) tube in a 2 L beaker with MilliQ Water overnight. Conjugation yield was verified through a 20% Urea Denature PAGE.

1.2.4. HSV1-DNA Origami Assembly

HSV1 Particles were obtained from Bio-Rad. For ratio experiments, the HSV1 particles were previously diluted in 1× Phosphate Buffer (1xPBS, pH 7.5). At the specified ratios, HSV1 particles and the pre-made DNA Origami were mixed together in 1.5 M NaCl concentration, diluted as necessary in 1× TAEMg Buffer. After pipetting to promote even mixture, the complexes were allowed 2 h to react at 4 °C. The complexes were either used in 1% Agarose Gel

Electrophoresis for mobility shift assaying, directly added to freshly cleaved mica substrates for Atomic Force Microscopy, or directly added with DMEM for cell related experiments.

1.2.5. Complex Characterization

For all complex characterization methods, every sample, (i.e., DNA Origami, naked HSV1 capsid particles, and the complexes at different ratios) were characterized under the same reaction solvent conditions, (1.5 M NaCl, 1xTAEMg buffer) throughout.

Agarose Gel Electrophoresis Mobility Shift Assay (AMSA) AMSA was implemented using a 1% Agarose/1xTAEMg gel. The gel was immersed in 1xTAEMg as the running buffer. The gel was stained with 0.5 μg/mL Ethidium Bromide. After 20 μL of each sample was loaded into each well in the gel, the gel was run at 90 V (constant voltage) for one hour. To prevent heat-denaturing of the DNA Origami higher order structure from electrophoresis adverse heating effects, the gel electrophoresis box was covered and surrounded by dry ice pellets. After the run, the gel was exposed to ultraviolet light for imaging.

Dynamic Light Scattering (DLS) 100 μL of each sample was loaded into a microvolume cuvette, and all DLS measurements were done on a Malvern Zetasizer Nano ZS.

Atomic Force Microscopy (AFM) AFM was performed under room temperature dry conditions. Then, 5 μL of the sample was drop casted onto a freshly cleaved mica surface and incubated at room temperature for several minutes. The substrate was washed with 2 mM Mg $(Ac)_2$ solution and dried by compressed air.

1.2.6. Cell Cultures

HeLa cervical cancer cells and B16F10 mouse melanoma cells were cultured in Dulbecco's Modified Eagle Medium (DMEM) with 10% Fetal Bovine Serum, 1% Penicillin-Streptomycin at 37 °C at 5% CO_2, and were permitted at least 3 passages before use in experiments.

1.2.7. Viral Plaque Assay

300,000-cell monolayers were first seeded into 6-well plates. After reaching 90–100% confluency, media was decanted and the cells were washed once in ice cold 1× Phosphate Buffer Saline (PBS) before infected with HSV1, DNA Origami, or HSV1-DNA Origami complexes for 2 h at 37 °C, 5% CO_2. The plates were gently rocked every 30 min to promote even distribution of inoculum. Inoculum was then aspirated and the cells were overlaid with 0.3% Agarose/DMEM and provided 4–6 days for incubation. ImageJ particle analysis was used for plaque counting. Images for processing were converted to 8-bit type before threshold adjustments were held constant for every sample. These plaque formation in the images were then counted through the ImageJ particle analysis tool (Figure 1.12). Our statistical analysis utilized Welch's *t*-test, which assumes unequal variance between samples.

Infectivity rate is generally quantified as Plaque Formation Units per volume (*PFU*/mL). This rate is found by relativizing (*P*) plaque number by (*D*) dilution factor of the pathogen and (*V*) total inoculum volume[37] as described below as Formula (1):

$$\frac{PFU}{mL} = \frac{P}{D * V} \quad (1)$$

For the complexes, the infectivity was calculated using Formula (2):

$$\frac{PFU}{mL} = \frac{P}{\phi * V} \quad (2)$$

$$\text{where } \phi = \frac{D_O * D_H}{D_O + D_H} \quad (3)$$

where this formula is described in the discussion section with derivation specified in the supporting information.

1.2.8. In vitro Structural Stability Experiments

All dilutions and packing ratios were replicated as identical to the viral plaque assay experiments. In summary, origami, origami-Folic acid, and HSV1-packed complexes of both origami cases were incubated in same FBS and antibiotic content in DMEM at 37 °C for 2 h, then further analyzed through 1% Agarose Gel Electrophoresis. As a control, these were compared to complexes identically prepared, yet incubated at 4 °C and in extra 1xTAEMg as opposed to the cell culture media.

1.2.9. Western Blotting

1,000,000 cells were seeded into individual T-25 flasks and were provided several days to reach 85–90% confluency. Flasks were then inoculated with HSV1 and Origami-HSV1 complexes and overlaid with sufficient media for one week (a total volume of 4 mL). The media was collected after the infection period and then spun down at 1000× g for 15 min. The top 75% of this supernatant was extracted and mixed with reducing SDS loading buffer (50 mM Tris-HCl pH 6.8, 2% SDS, 10% glycerol, 1% 2-mercaptoethanol, 12.5 mM EDTA, 0.02% bromophenol blue). Samples were run in an SDS Bis-Tris gel at 165 V for 45 min, then transferred to a nitrocellulose membrane at 15 V for 30 min. Membranes were blocked in 5% milk/0.1% PBST for one hour, incubated with HSV1 ICP5 Major Capsid Protein at a 1:1000 ratio in Milk/PBST overnight at 4 °C, then incubated for 2 h with goat anti-mouse IgG-Horseradish Peroxidase at a 1:1000 ratio for 2 h rocking at room temperature. Membrane was then rinsed with deionized water before reacted with Azure Radiance Q Chemiluminescent substrate for 5 min. Autoradiography films were exposed to the membrane for ten seconds before image processing.

1.3. Results and Discussion

DNA Origami Design. The DNA Origami sheet design was adopted from one of Rothemund's original DNA rectangle designs[23]. These sheets were first fabricated by mixing 235

staple strands that fold a scaffold strand into 70 × 90 nm rectangles by hybridizing with multiple regions on the scaffold and each other[23]. The scaffold strand is M13mp18 ssDNA, a bacteriophage genome strand that is conventionally used for most origami scaffolds due to its extensive length (7413 nucleotides)[23,28]. Rectangles were successfully formed after annealing all strands together from 90 °C to 4 °C in the span of three hours (Figure 1. 2A). We further installed 12 "overhanging" polyA strands that tether covalently conjugated folic-acid polyT strands for cell-targeting demonstrations (Figure 1.1, Figure 1.2B and Figure 1.6).

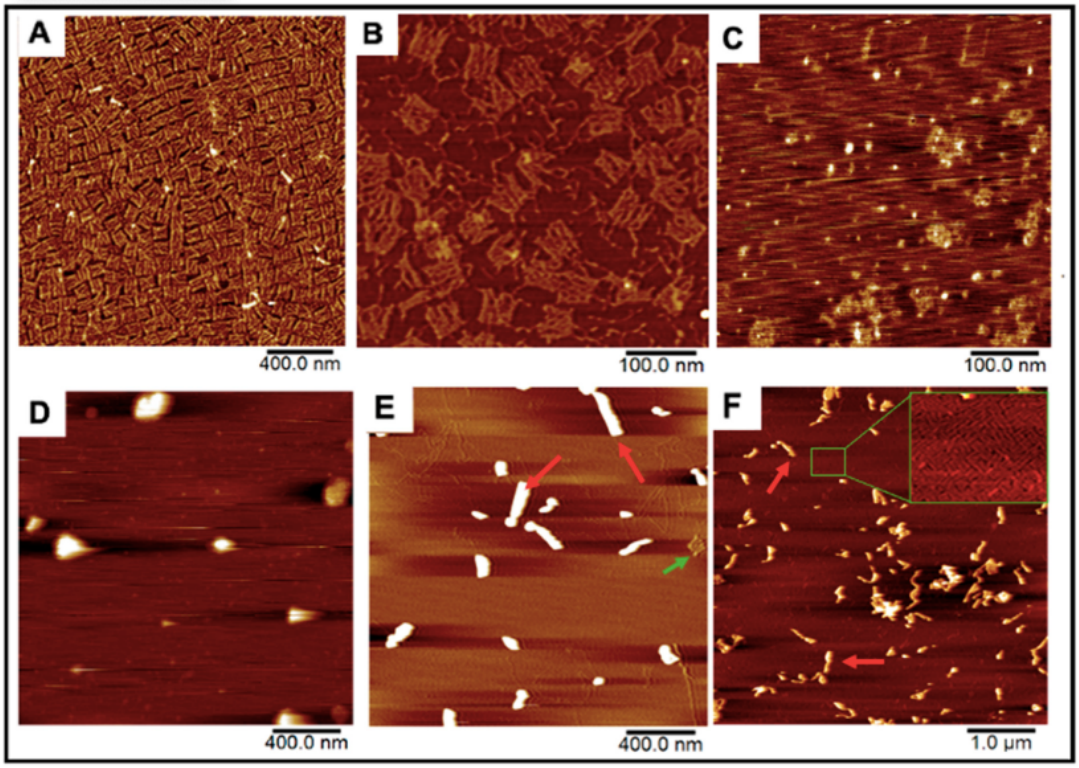

Figure 1. 2 AFM Images of our DNA Origami, HSV1 particles, and the resulting complexes after mixing.

(**A**,**B**) Origami and folate-decorated origami sheets. Salt bi-products from formed origami were observed as seen in (**B**). (**C**) HSV1 particles (**D**) Origami:HSV1 "pockets" established at a 2:1 Origami:HSV1 molar ratio (**E**) 20:1 ratio "sleeves" and (**F**) 50:1 ratio "sleeves" where many excess sheets are left unbound. Green arrows show unbound sheets in the packing reactions while red arrows show products of the HSV1-origami "sleeve" complexes.

DNA Origami-HSV1 Particle Packing. These origami rectangles were then mixed with commercially prepared HSV1 capsid particles from 2:1 to 50:1 molar ratios, where the HSV1 particles previously had their envelope and glycoproteins removed to expose the positive charged capsid by the manufacturer (Figure 1.2C). The charge-mediated union between the origami and HSV1 particles consistently resulted in specific packing morphologies. The comparable dimensions between the sheets (70 × 90 nm) and the HSV1 capsids (90–100 nm in diameter) allowed us to hypothesize that 2:1 and 3:1 origami:HSV1 molar ratios can sufficiently cover the virus. Under these proportions, the particles were wrapped in dispersed, rounded, "pocket-like" structures as seen via atomic force microscopy (AFM) (Figure 1.2D). However, as we decreased HSV1 content so that the ratio shifted towards 10:1, 20:1 and 30:1, the packaged complexes assembled into elongated or "sleeve-like" structures, where capsid aggregates were packaged into many origami sheets at once with minimal unbound sheets remaining in the reaction (Figure 1.2E). Yet, at higher 40:1 and 50:1 ratios, these sleeve structures were sustained while many unbound origamis were observed, suggesting that a critical packing ratio between the HSV1 particles and DNA sheets had been surpassed (Figure 1.2F).

These packing behaviors were further validated with 1% agarose gel electrophoresis mobility shift assays (AMSA). There was no visible band from the lane loaded with naked HSV1 particles because their positive charge prevented them from traveling along the same electrophoretic direction as origami-related samples. (Figure 1.3A,B). On the other hand, the origami band displayed lower mobilities as the HSV1 particles were packaged within the origami structures. As previously realized in the AFM micrographs, AMSA confirmed a critical ratio between 35:1 and 40:1 provided the sudden lighter mobility of the 40:1 and 45:1 packing ratios with respect to the other loaded ratios (Figure 1.3A and Figure 1.8).

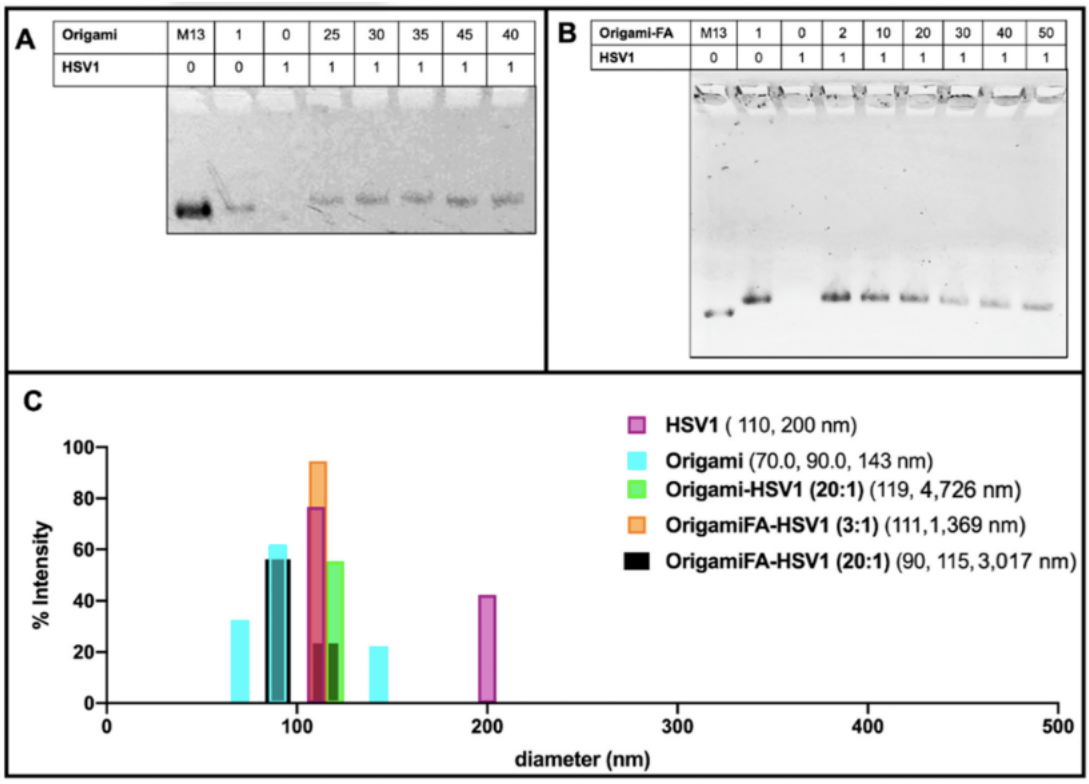

Figure 1. 3 Electrostatically HSV1 particle-loaded DNA Origami.

(**A**) 1% Agarose Mobility Shift Assay (AMSA) analysis of HSV1-loaded origami shows a sudden change in mobility between 35:1 and 40:1 origami:HSV1 ratios from otherwise decreased mobility, suggesting the critical packing ratio and (**B**) Folic-Acid adorned origami similarly loaded with HSV1 particles, where 20:1 is the demonstrated critical packing ratio. Both (**A**,**B**) also show a decreased mobility from the free M13mp18 scaffold strand to the fully annealed DNA Origami in the first two left lanes of both gels. (**C**) Dynamic Light Scattering validation of HSV1 particle and DNA Origami size dimensions where occasional dimerized configurations were observed. Data also confirms the complex package sizes at a 2:1 ratio origami-HSV1 and 3:1 ratio of origami Folic Acid to HSV1 complexes. No leftover origamis are observed, but agglomeration is noted.

Dynamic Light Scattering measurements further validated this capsid coating behavior. When complexed at a 2:1 origami:HSV1 ratio, 55.4% of size dimensions were 98.51 nm in diameter with 44.3% 308 nm in diameter. These measured sizes are comparable to the dimensions of single-particle and dimerized aggregates. However, we chose to use the DLS data of higher packing ratios as a supplement provided that micron range dimensions—as was seen in the sleeves—lead to less accurate scattering properties (Figure 1.3B,C and Figure 1.7A–D).

Dynamic light scattering also confirmed the behavior of the HSV1 capsids alone. If the capsid particles were otherwise not disperse in the solvent, as is seen with the detected 110 nm size measurement, which is both expected of the capsids and the majority of the detected size of the sample, there was occasional dimerization (as is seen with 200 nm detected sizes), but no agglomeration or submicron to micron clustering was observed. This implies that when the capsids are packed into larger sized aggregates by the origami, it is not due to their propensity to aggregate alone.

While Folic Acid-functionalized origamis displayed loading capabilities like the unfunctionalized origamis, AMSA experiments clarified that the critical packing ratio shifted from 35:1 to near 20:1 (Figure 1.3B). We believe the extra positive charge from the folic acid led to a diminished efficiency in electrostatic packaging between the negatively-charged DNA sheets and the positively-charged virus capsid[38]. Regardless of the sudden change in band mobility after the 20:1 ratio, the bands continued to decrease in intensity even as 30:1, 40:1 and 50:1 ratios were explored. This may be due to a wider distribution of packing morphologies such as a combination of pockets, longer sleeves, and shorter sleeves (Figure 1.3B and Figure 1.9). Moreover, the decreased band intensity is caused by the majority of the loaded sample remaining in the well rather than traveling down the gel matrix; there are thus complexes of larger sizes under these ratios. This distribution behavior was further validated through DLS and confirmed the increased polydispersity index (PDI) values of 0.81, 0.96 and 1.00 for 30:1, 40:1 and 50:1 ratios, respectively. The PDI values for lower ratios ranged between 0.55 to 0.71.

The AFM images at both low and high magnification, in combination with the DLS data presented in Figure 1.2 and Figure 1.3, indicate that higher ratios of origami to HSV1 particles promote linear, “sleeve-like” assemblies. This conformation is most likely due to patchy

aggregation before full outer coverage: The higher amount of available origami sheets allows some of them to bind in between particles as electrostatic patches first[39], bridging the particles together while residual sheets cover remaining exposed and positive charged regions on the capsid particles' surfaces[40,41]. The presence of sleeves is made possible due to more available free origami sheets, but it is not necessarily the preferred assembly, as is exemplified by the high PDI values from DLS and the persistent presence of pockets at these higher ratios.

Infectivity Analysis in vitro. After establishing these structural and packing properties, we studied the virulence of origami-HSV1 and Folic-Acid-Origami-HSV1 complexes using the 3:1 origami:HSV1 molar packing ratio. Plaque assays were implemented here because they are the gold standard for titering and characterizing infectivity rate of pathogens[37,42–44]. To summarize the process, cell monolayers are infected with the pathogen and then cleaned and further fixed in agarose-media to localize plaque formations. The epicenters of infections are within the monolayers and identified as plaque[37]. Here, HeLa cells were used as a model cell line due to their density in folic acid receptors[45]. When HeLa cultures were inoculated, there was a 46.8% heightened plaque formation from folate-decorated HSV1-origami pockets above naked HSV1 particles alone. Surprisingly, there was a 42.1% less plaque formation when the HSV1 particles were masked in undecorated origami (Figure 1.4A,B). We believe that this muted formation is due to negative charge repulsion between the cell membranes and the phosphate backbones of the bare origami surfaces[29,46].

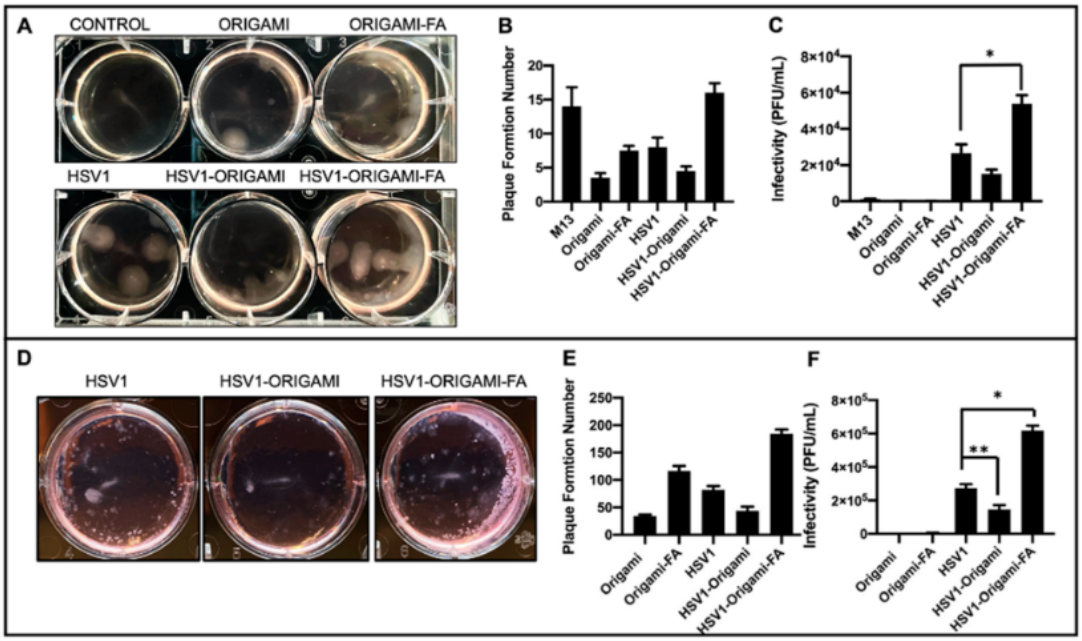

Figure 1. 4 In vitro analysis of Origami-HSV1 complexes.

(**A**) Plaque assay of HeLa cells showing HSV1 in origami-Folic Acid led to heightened plaque formation above HSV1, but also showed muted plaque formation for HSV1 wrapped in bare origami. (**B**) Quantified plaque formation numbers from those observed in panel A as is described in the methods section. (**C**) The infectivity rates (Plaque Formation Unit/mL) shows that DNA Origami plaque leads to negligible infectivity relative to HSV1 and complexes, and that HSV1 wrapped in origami-Folic Acid is the most infective above native HSV1 (* denotes Welch's unpaired *t*-test, $p = 0.0293$). (**D**) Plaque Assays of Mouse Melanoma B16F10 show heightened plaque formation from HSV1 in folic acid decorated origami complexes alongside decreased plaque formation from HSV1 in bare origami as compared to HSV1 alone. (**E**) Quantified plaque formation numbers of infected B16F10. (**F**) Resulting infectivity rate (Plaque Formation Unit/mL) of B16F10 outlining comparable behavior as those results from the HeLa plaque assays (* denotes Welch's unpaired *t*-test, $p = 0.0065$, ** denotes Welch's unpaired *t*-test $p = 0.0370$). Error bars are the standard deviation.

There was plaque formation in the HeLa cells when they were inoculated with the naked origami sheets—either bare or further decorated with the folic acid. (Figure 1.4A,B). Yet, both cases resulted in fewer plaque formations than HeLa cells inoculated with the naked "scaffold strand," M13mp18 (Figure 1.4B and Figure 1.11). Prior work has shown that foreign M13mp18 strands can become internalized and persist in eukaryotic cell lines[47–49]. Our data show that the M13mp18 strands generated 300% more plaque than the bare origami and 89.3% more than folate-decorated origami due to suppressed exposure of the strand from hierarchical folding with the

staple strands. While both origami designs produced plaque, the folate-functionalized origami generated an average of 121% more plaque than the bare origami suggesting a forced uptake of the origami through folic acid reception.

However, plaque formation numbers alone are an incomplete outline on the virulence of the origami, HSV1, and HSV1-Origami complexes. To elucidate this, the infectivity rate is generally quantified as Plaque Formation Units per volume (PFU/mL). This rate is found by relativizing (P) plaque number by (D) dilution factor of the pathogen and (V) total inoculum volume[37]. This applies directly to the HeLa inoculated with the origami sheets, Folate-decorated origami sheets, and naked HSV1 particles (Formula (1)).

However, because the origami and HSV1 particles are simultaneously administered at differing dilution factors when the packed complex is the inoculum, a parallel function is necessary to compensate for both entities. (Formula (2)) shows the justification and derivation of parallel function further detailed with the Supplementary Figures).

These results indicate that the plaque-forming origami sheets did not contribute to infectivity rates comparable to the native HSV1 particles and the complexes—either bare or further adorned with folic acid (Figure 1.4C). In fact, naked origami was at least 99.7% less infective than complexes and 99.3% less infective than naked HSV1. This claim is further supported in that the naked origamis were inoculated at the same dilution factors as the origamis involved in the complex inoculums.

The infectivity rates of these complexes against B16F10 mouse melanoma cells were also tested under identical conditions as those with the HeLa cells. Because the HSV1 particles are natively propagated in Vero cells and are therefore ape-derived, we hypothesized it would be increasingly difficult for them to establish initial infectivity in a mouse cell line[50] unless coerced

inside by folic-acid mediated uptake. While HeLa and B16F10 are from different species, both are folic acid receptor-positive[51]. Indeed, B16F10 infection experiments showed similar plaque formation behaviors as observed during the HeLa experiments, but the infectivity of the folic acid-decorated origami-HSV1 pockets led to a 127% increase over the native HSV1 (Figure 1.4D–F). The B16F10 line formed at least 30 more plaque formations than HeLa, but their sizes were significantly smaller than those in the HeLa line (Figure 1.4A,D). The smaller plaque sizes are in fact due to infection attenuation from the virus[52] likely because the HSV1 is infecting a species foreign to its own origin (Figure 1.4D).

Validation of HSV1-Origami Complex stabilities in vitro. We next tested if the increased plaque from the HSV1-Origami-Folic Acid complexes was due to their short stability in vitro, i.e., a mere accumulation of the origami and HSV1 plaque formations from full-dismantlement in cell culture conditions. There are three approaches to resolve this question. First, we implemented Western blotting to directly monitor changes in the concentration of produced HSV1 ICP5—the major capsid protein. This is an accurate method to measure HSV1 based on delivery methods because the origami would not contribute to the ICP5 band (wrapped in bare or decorated origami, or administered completely naked). The Western Blot confirmed that the folate-adorned origami wrapped HSV1 led to the most ICP5 protein even over naked HSV1 particles (Figure 1.5A).

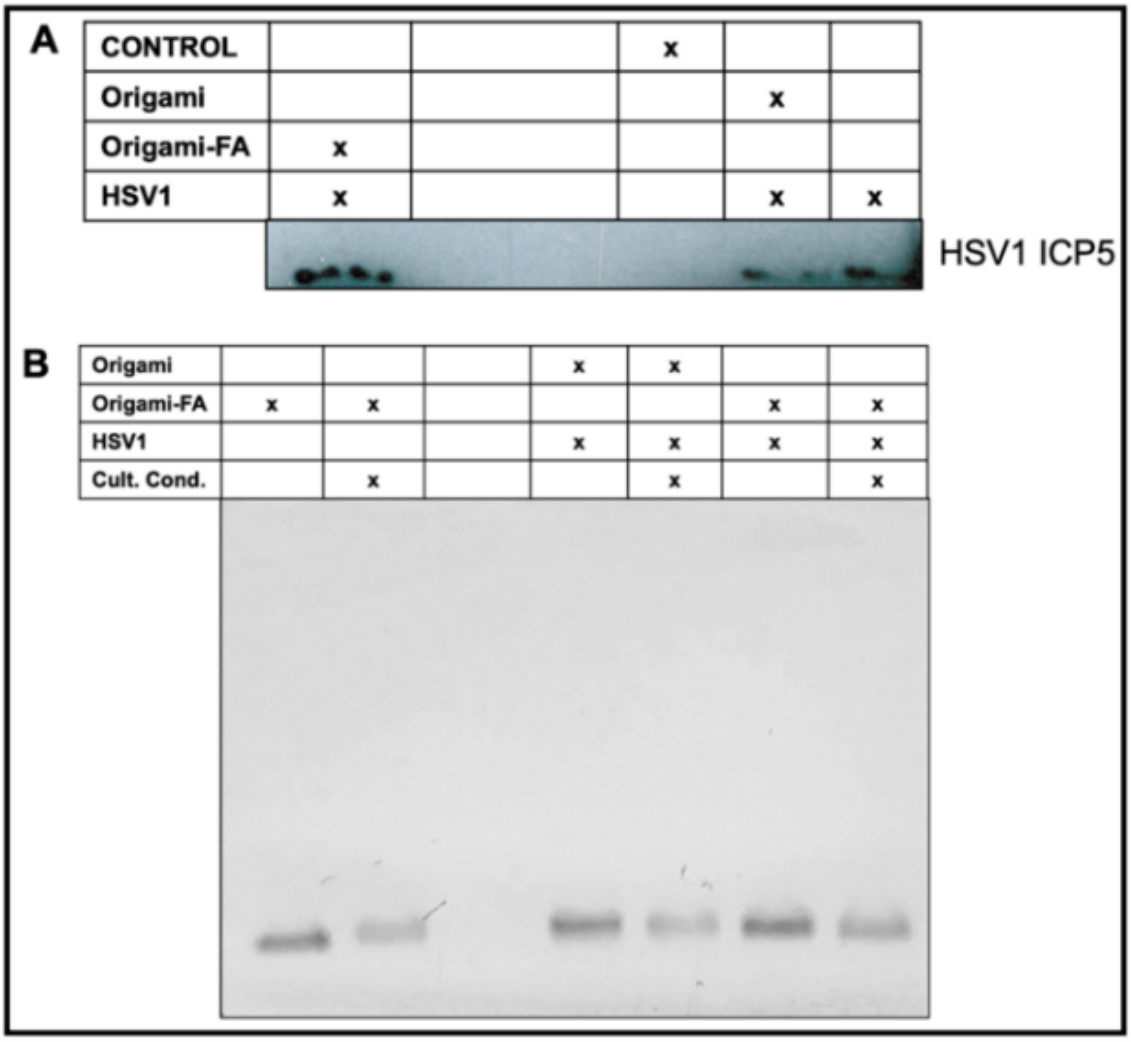

Figure 1. 5 Validated HSV1 delivery and packaging stability of the Origami-HSV1 complexes in vitro.

(**A**) Western Blot characterization on produced ICP5 HSV1 Major Capsid after HSV1 infection based on delivery or masking method. (**B**) Validated stability of the Folate-adorned Origami-HSV1 complexes in vitro under cell culture conditions identical to the conditions during the plaque assay inoculum stage. The corresponding table legends for (**A**,**B**) indicate the present entities and conditions for each sample in each lane.

Second, AMSA analysis was implemented on the complexes to examine their structural stability under cell culture conditions. Incubation of DNA origami in standard cell culture conditions (10% FBS, Dulbecco's Modified Eagle Medium, 1% Pen-Step under 37 °C at 5% CO_2) led to (1) denaturation of the structure and (2) digestion of the structural DNA due to nuclease activity and diminished cationic stability[53,54]. We therefore incubated origami and origami-HSV1

complexes under these conditions while strictly matching incubation time periods and dilutions as was performed in the plaque assays. We then compared these samples to those left at the bench under the same time. There was no mobility shift when the origami was loaded with HSV1 and then incubated under cell culture conditions (Figure 1.5B). While the band intensity slightly decreased suggesting some digestion activity, the remaining origami structures do maintain their binding to the HSV1 particles due to the unshifted band. If the band lowered to its original level when unloaded, then this would suggest that the free-floating origami is exposed and infective to the cells on their own.

Each inoculum led to consistent plaque numbers, and thus we implemented mathematical predictions on the resultant infectivity of these complexes including if the origami completely detached from the HSV1 particles or completely stuck with them during administration in vitro. If the complexes dissociated before they reached the cells for infection, then the plaque from the complexes would have resulted in numbers similar to the sum of the plaques from the origamis and HSV1 particles alone. However, if they remained completely intact prior to reaching the cell, then the resultant plaque from the complex might resemble plaque formed but with the plaque from the origamis alone subtracted (Figure 1.13). When we modeled both of these cases and compared them with the empirical results, neither of the complex infectivity rates compared with the predicted detachment cases. On the other hand, they resulted in heightened infectivity numbers than those in the fully attached case but it is crucial to note that we did not account for the continuous production of the HSV1 particles—leading to more infectivity—when the complexes are fully attached. The results suggest that the HSV1-Origami complexes maintained their packing integrity when employed for infections against the cell lines, and that enhanced infectivity form the folic acid-adorned Origami-HSV1 pockets is due to the increased efficiency of their uptake.

1.4. Conclusions

Here, for the first time, HSV1 particles were wrapped in DNA origami and evaluated for controllable viral delivery. Inspired by past demonstrations on DNA origami's electrostatic affinity towards positively charged viral plant capsid particles, we corroborated the translatability of this binding interaction with a larger mammalian viral capsid particle[29]. When the particles are wrapped in bare origami sheets, their recognition and uptake into cells are noticeably diminished by a 44.2% decreased infectivity rate. This muted infectivity further supports previous reports on DNA origami's potential to inhibit viral infections by structurally covering and thereby trapping virus cores[30,31]. On the other hand, when wrapped in origami that is outwardly functionalized with folic acid, folate-receptor mediated uptake allowed the viruses to have increased HSV1 protein production and 117% heightened infectivity. This therefore reveals unique and potentially therapeutic value in the context of engineered, antitumor viral infections. Plaque assays were used to monitor the infectivity of the Origami-HSV1 complexes and the origami sheets themselves. While origami sheets displayed plaque forming and infective behavior, we validated that (1) their infectivity is negligible relative to native HSV1 and (2) they maintained packing integrity in vitro. Thus, the origami sheets did not individually contribute to the enhanced infectivity of the HSV1-wrapped origami complex in folic acid. Future work may investigate the administration of these complexes during longer inoculation times both in vitro and in vivo to further elucidate their stability. Different packaging mechanisms besides electrostatic binding can be explored. Perhaps most importantly, these results encourage future research on DNA nanotechnology—specifically origami—in a system where pathogenicity is more rigorously examined. Although more recent reports continue to demonstrate the nontoxic and low immunogenicity of DNA origami when administered in vivo[27,55], more stringent characterizations on origami geometries and potential adverse effects should be investigated.

This will be a large stride in the global effort to introduce DNA Origami—and DNA Nanotechnology altogether—into serious consideration for therapeutic translatability.

1.5. Acknowledgements

Chapter 1, in full, is a reprint of the material as it appears in Molecules 2022. Borum, Raina M; Lin, Avery E.; Dong, Xiangyi; Kai, Mingxuan; Chen, Yi. The dissertation author was the primary investigator and author of this paper.

1.6. Supporting Figures

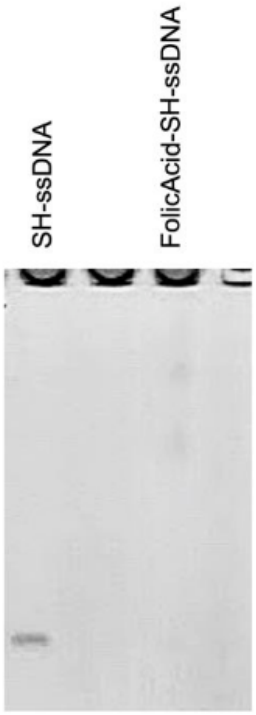

Figure 1. 6 20% Urea Denature PAGE on Folic Acid-DNA conjugation.

When the thiolated ssDNA is covalently linked to Maleimide-PEG-Folic Acid as facilitated by TCEP reduction, the band for the thiolssDNA completely disappears. Both strands were loaded at identical starting concentrations.

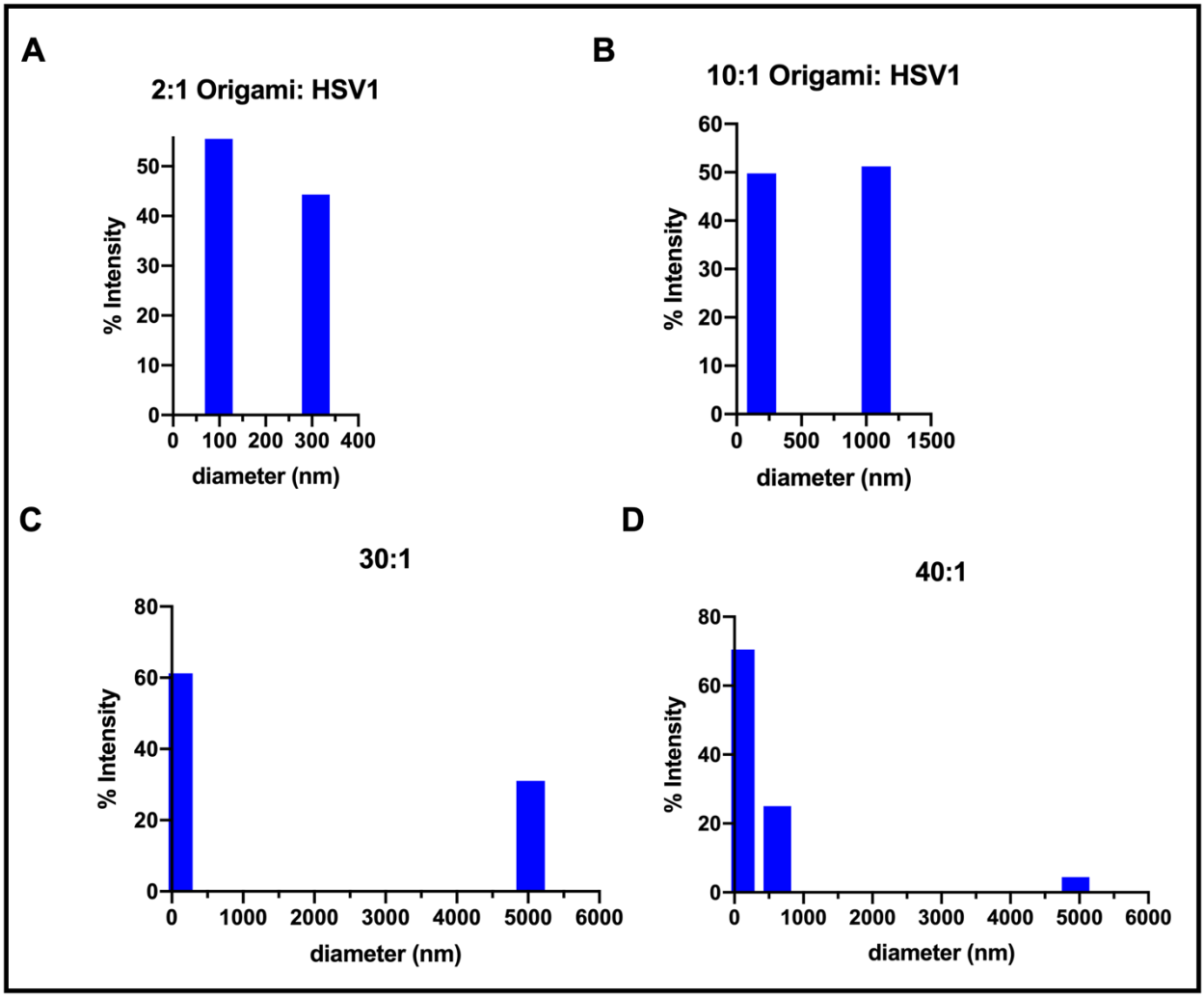

Figure 1. 7 Supplementary DLS measurements of our origami:HSV1 complexes based on molar packing ratio.

When origami:HSV1 molar ratios approached past 10:1 (191 nm, 1077 nm), and throughout 20:1 (119 nm, 4726 nm) and 30:1 (90 nm, 5036 nm), micron range agglomerates continued to grow in size, first developing from near 1000nm in size and approaching 5000nm in diameter at the maximum. As was otherwise characterized in our AGE and AFM experiments, we predicted a 40:1 ratio (90 nm, 622 nm, 4946 nm), being past the critical ratio, would indicate a sudden or noticeable change in these agglomerated sleeve behaviors.

Origami	(M13)	1	0	0.5	1	3	10	30	40
HSV1	0	0	1	1	1	1	1	1	1

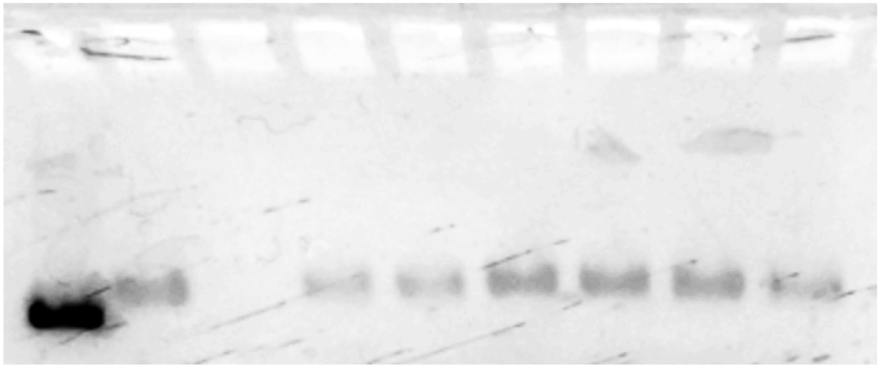

Figure 1. 8 Further 1% AGE validation of Origami-HSV1 loading depending on molar ratios.

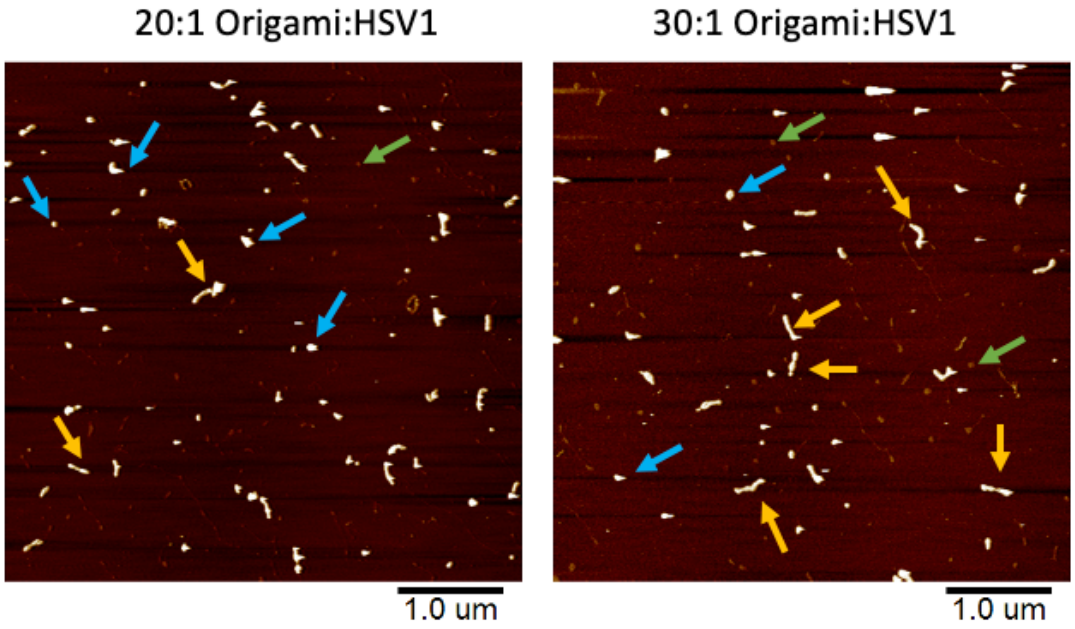

Figure 1. 9 Low Magnification Atomic Force Micrographs of DNA Origami-HSV1 Complexes

show a distribution of different complex geometries, ranging from pocket like structures (as indicated with blue arrows), sleeves (yellow arrows) and occasional unbound origami (green)

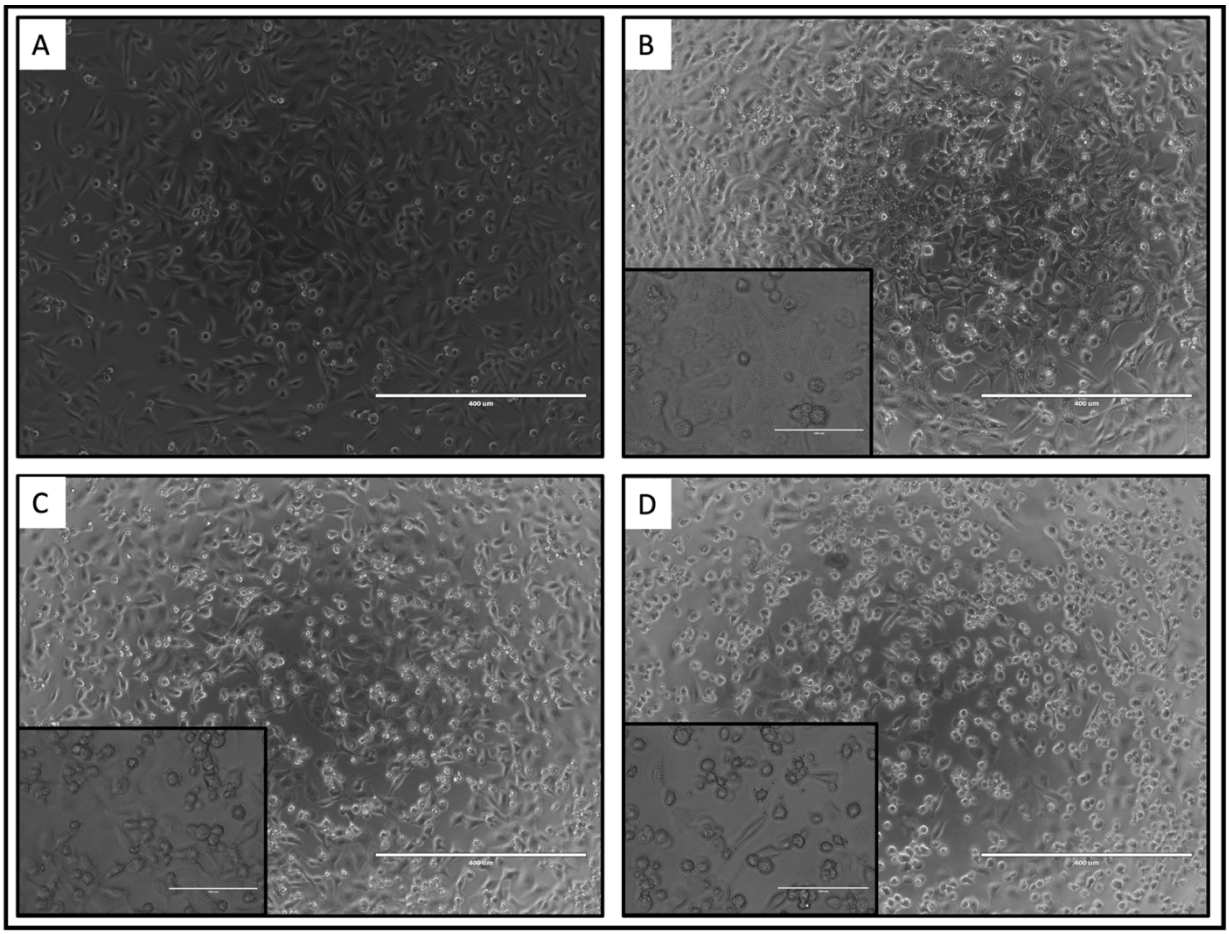

Figure 1. 10 HeLa cells 24 hours post infection.

(A) Mock-infected (control), **(B)** HSV1-infected, **(C)** HSV1-Origami infected, and **(D)** HSV1-Origami-Folate infected where most the cells were visibly detached**.**

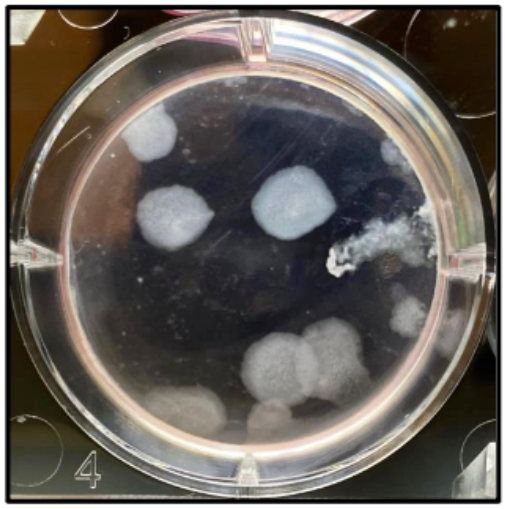

Figure 1. 11 Plaque Assay result of HeLa inoculated with naked M13 strands at the same concentration as inoculated origami.

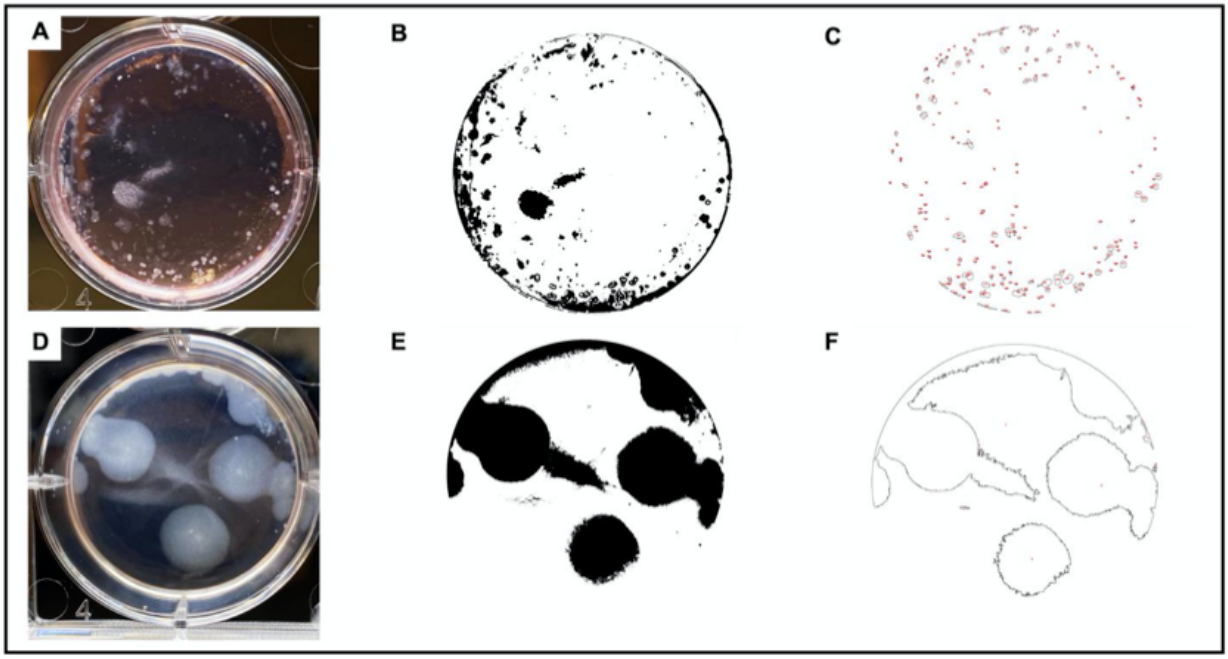

Figure 1. 12 Plaque Assay Plaque counting using ImageJ.

(**A,D**) original image of plaque in well. (**B,E**) Image after adjusted to 8-bit image type with threshold tuned to capture as many isolated plaques as possible. Threshold conditions were kept constant for all wells during plaque counting. (**C,F**) Resultant counted plaques when using Particle Analysis tool in ImageJ. **(A-C)** shows the B16F10 plaque assay post HSV1 infection, while **(D-F)** shows the same infection with HeLa. Both cell lines resulted in these characteristically different plaque morphologies.

$$\frac{PFU}{mL} = \frac{P}{D * V}$$

$$\frac{P}{D * V} = \frac{P}{D_O * V} + \frac{P}{D_H * V}$$

$$\frac{1}{D} = \frac{1}{D_O} + \frac{1}{D_H}$$

$$\frac{1}{D} = \frac{D_o + D_H}{D_O * D_H}$$

$$\therefore \boldsymbol{D} = \frac{\boldsymbol{D_O * D_H}}{\boldsymbol{D_O + D_H}}$$

Derivation of parallel function used for infectivity (PFU/mL) calculations for origami-HSV1 complex cases. Here, D_o is dilution factor for inoculated origami and D_H is dilution factor for inoculated HSV1. Plaque number (P) and total inoculum volume (V) are held constant as both origami and HSV1 are administered at the same time as a complex, resulting in one constant plaque number under the total volume of the inoculum. Therefore, it is appropriate to only analyze the adjusted infectivity calculation (PFU/mL) with respect to differing dilution factors for both entities.

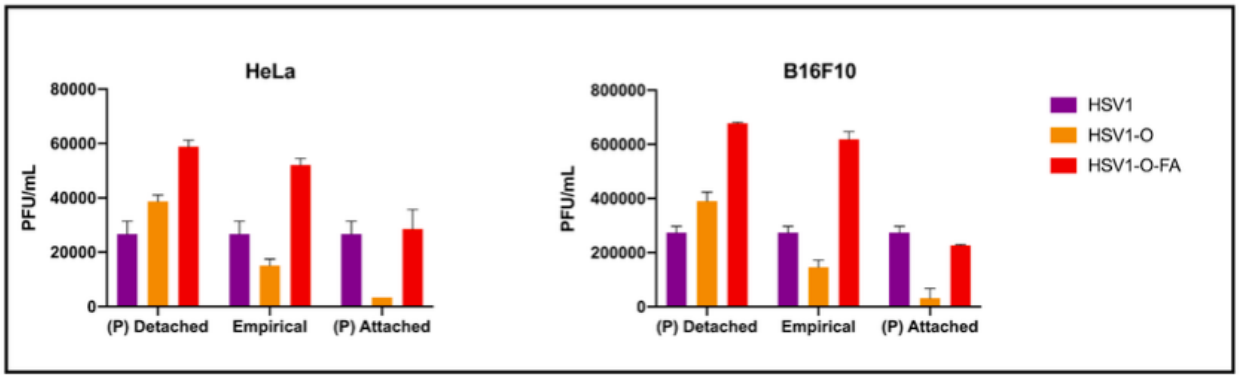

Figure 1. 13 Predicted infectivity rates based on complex stability or instability in vitro, as compared with empirical results.

We were primarily concerned that our plaque numbers resulted from full detachment of our complexes in vitro.

CHAPTER 2. HYBRIDIZING CLINICAL TRANSLATABILITY WITH ENZYME-FREE DNA SIGNAL AMPLIFIERS: RECENT ADVANCES IN NUCLEIC ACID DETECTION AND IMAGING

ABSTRACT: Nucleic acids have become viable prognostic and diagnostic biomarkers for a diverse class of diseases, particularly cancer. However, the low femtomolar to attomolar concentration of nucleic acids in human samples require sensors with excellent detection capabilities; many past and current platforms fall short or are economically difficult. Strand-mediated signal amplifiers such as hybridization chain reaction (HCR) and catalytic hairpin assembly (CHA) are superior methods for detecting trace amounts of biomolecules because one target molecule triggers the continuous production of synthetic double-helical DNA. This cascade event is highly discriminatory to the target *via* sequence specificity, and it can be coupled with fluorescence, electrochemistry, magnetic moment, and electrochemiluminescence for signal reporting. Here, we review recent advances in enhancing the sensing abilities in HCR and CHA for improved live-cell imaging efficiency, lowered limit of detection, and optimized multiplexity. We further outline the potential for clinical translatability of HCR and CHA by summarizing progress in employing these two tools for *in vivo* imaging, human sample testing, and sensing-treating dualities. We finally discuss their future prospects and suggest clinically-relevant experiments to supplement further related research.

2.1 Introduction

An extensive variety of RNA and DNA molecules are characteristically under or over-expressed in many diseases[56]. Although discovered in 1948,[57] extracellular nucleic acids were correlated to disease nearly 40 years later[58,59] when their overexpression was seen in the serum of cancer patients. Similarly, heightened intracellular abundance of signature nucleic acids in vesicles and exosomes has been observed in metastatic cell lines.[60] Now, the abnormal regulation of diversified functional nucleic acids—such as intracellular, noncoding, circulating, and even genomic species—is a hallmark for the presence and progression of cancers, diabetes, stroke, and cardiovascular diseases.[61] Nucleic acid biomarkers' particular relation to cancer involves their release from lysed tumor cells into plasma[56] as well as their exosomal transfer between cells[62]. Messenger RNA (mRNA), cell-free DNA (cfDNA), and microRNA (miRNA) are some the most notable disease footprints[63]. miRNA is a particularly popular marker because it is short (~22 nt) to sequence and is stable in serum[64,65]. miRNA concentrations can also predict survival time in cancer[66].

Opportunities from standardized nucleic acid profiling are as versatile as they are novel: examples include early stage diagnosis, accurate surveillance after cancer remission or ongoing therapy, nucleic acid species-specific mapping between disease variants, or refined prognosis and estimated survival. Furthermore, circulating nucleic acids are characteristically present in plasma,[67,68] serum,[59,66,67] saliva,[69,70] urine,[68,71] sputum/pleural effusions,[72,73] and tissue based on the location and nature of the disease. Nucleic acid species are therefore attractive targets for sensitive, economic, and time-efficient liquid biopsies.

Current gold standards for nucleic acid detection include northern blotting, microarrays, and quantitative reverse transcription PCR,[56,74,75] but these tools are expensive and time-consuming. qRT-PCR particularly suffers from dubious RNA sequencing accuracy because the

required primers generate multiple complimentary DNA strands from the original sequence either (1) in a nonspecific manner thus reducing quantification accuracy or (2) in a wasteful way such that separate reactions are required for each primer. This makes it unsuitable for samples with low abundant targets.[76] Nanotechnology strategies include DNA-grafted gold nanoparticles for fluorescent imaging of live cells[77]based on miRNA and mRNA recognition, but this falls short to a required dense input probe concentration and is therefore not as practical for clinical diagnosis applications. These related platforms also lack signal amplification, so their sensitivity remains inferior to other methods such as qtPCR.

Strand amplification—the continuous generation of nucleic acid strands upon an event such as hybridization with a target nucleic acid—is a provocative idea to detect trace amounts of nucleic acid. The ability to sense native nucleic acid with synthetic nucleic acid is biocompatible, safe, nanoscale, and noninvasive. The ability to functionalize synthetic nucleic acids with dyes, proteins, nanoparticles, and chemical reporters is standardized and well-defined[78,79] thus offering pragmatic translatability for clinical imaging and liquid biopsies. For example, rolling circle amplification (RCA) is a robust method to indefinitely produce single-stranded (ss)DNA by enzymatic cycling through a circular template ssDNA. RCA can therefore mass produce DNA upon endogenous nucleic acid detection,[80] but the required DNA polymerase and ligase limit the platform for *in vivo* applications. RCA also requires thermocycling to enable hybridization and amplification deactivation, further limiting its use beyond the benchtop. Though thoroughly practiced, this high-maintenance platform has limited candidacy in realistic diagnostic applications—particularly *in vivo* applications.

The advent of enzyme-free and isothermal strand amplification, as pioneered by Pierce in the early 2000s,[81,82] completely reshaped the landscape of DNA amplification. Here,

hybridization between nucleic acid strands could trigger continuous DNA production without external events or entities. These engineered amplification methods typically use hybridization chain reaction (HCR) or catalytic hairpin assembly (CHA); both have exceptional detection limits while yielding synthetic DNA for a characteristic readout. HCR and CHA both require a "fuel strand"—the target analyte—to hybridize with synthetic nucleic acid strands that catalyze the indefinite growth of artificial DNA duplexes. HCR and CHA fundamentally require only two strand species and one fuel strand to trigger the programmed cascades; they therefore have inherently low limits of detection and high specificity. This makes them ideal candidates for nucleic acid detection and disease profiling.

In this review, we examine recent milestones achieved by HCR and CHA that bring them closer to clinical applications, with an emphasis on diagnostic and prognostic devices as well as nucleic acid mapping *via in vivo* imaging. We outline advances in three key areas: (1) enhancements in live cell imaging, (2) designs with very low detection limits (attomolar range), and (3) multiplexed sensing abilities. We further report recent progress in utilizing these methods in pragmatic clinical use including demonstrations of *in vivo* imaging, nucleic acid sensing in human samples, and theranostics.

2.2. Principles of strand amplification

Strand amplification is an inviting approach to intensify signals for nucleic acid sensors that require low detection limits. In general, it yields either (1) a large output of synthetically duplexed DNA or (2) constant cycling of duplex formation or strand exchange upon recognition of one target strand. Toehold-mediated strand displacement (TMSD) is a DNA programming tool that has ultimately enabled enzyme-free signal amplification; in this approach, recognition of one target strand results in a product strand or duplex.[83] In TMSD, the toehold—or exposed target recognition region for hybridization—is concealed until the target is present. One way to

execute this is by kinetically trapping the target recognition sequence in DNA metastable hairpins.[84] TMSD has resulted in powerful logic gates, machines, motors, and programmed events on the molecular scale. Two such DNA programming tools that utilize TMSD for pragmatic nucleic acid sensing include hybridization chain reaction (HCR) and catalytic hairpin assembly (CHA).[85,86]

2.2.1. Hybridization chain reaction (HCR)

In hybridization chain reaction (Figure 2.1A), one target strand serves as fuel to activate the continuous growth of nicked concatemers.[81] Two uniquely-sequenced HCR strands initially store potential energy as metastable hairpin loops in the "OFF state". Upon contact with the fuel strand, strand type 1 will open from its hairpin state into a single stranded "ON state", partially hybridizing with the fuel strand while simultaneously hybridizing with strand type 2. The remaining region in strand type 2—which is identical to the fuel strand sequence—enforces the cascade by retriggering hybridization with the beginning of a new strand type 1 (Figure 2.1 A). This results in indefinite growth of a double helical superstructure until hairpin supply is depleted. The total molecular weight of the HCR product has an inverse relationship with the starter fuel strand concentration.[81] Since its first demonstration in 2004 by Dirks and Pierce,[81] HCR has become the foundation of strand amplification engineering. The earliest studies on HCR demonstrate impressive *in situ* RNA mapping in zebrafish embryo samples,[87] but serious drawbacks from required sample preparation and strand washing have restrained the platform from immediate clinical utility. Live cell imaging was at first impossible because the cells required further pre-treatment such as fixation and cycled washing of unhybridized probes. Still, their mapping demonstrations proved 200-fold sensitivity from HCR above unamplified hybridization fluorescence.

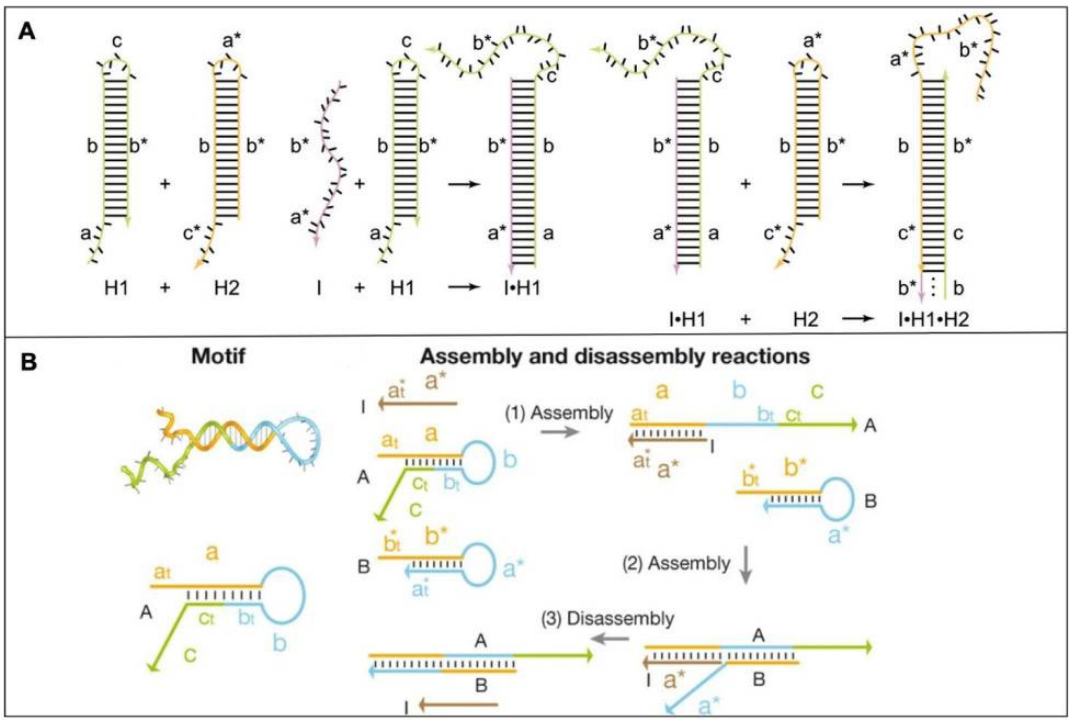

Figure 2. 1 Strand-hybridization induced signal amplification methods.

(A) Basic principles of HCR, where the target strand (purple) fuels duplex amplification by hybridizing with loop probe 1 (green), thus exposing the remaining unbound region of probe 1 to hybridize with probe 2 (orange). Copyright (2004) National Academy of Sciences, U.S.A.[81] (B) Principles of CHA. Copyright 2008, Nature Publishing Group[82].

2.2.2. Catalytic hairpin assembly (CHA)

A close relative to HCR is catalytic hairpin assembly (CHA), an entropy-driven[88] catalysis reaction which was also invented by Pierce's group in 2008.[82] The mechanism is comparable to HCR in the sense that two metastable hairpin loops are stimulated for duplex formation upon fuel strand recognition. However, as the fuel strand hybridizes with the first probe, it is released to allow further assembly between the first and second probes for accumulated production of discretized, short duplexes (Figure 2.1 B). This provides an advantage over HCR because the target strand can be continuously recycled, decreasing the cascade reaction time and generating "100-fold signal amplification in a few hours".[89]

2.3. Improvements in live cell imaging

Signal amplification from HCR and CHA often uses fluorescent dyes tethered to the strands. These fluorescent methods typically utilize (1) fluorescent *in situ* hybridization (FISH), where the hybridization between two strands leads to the excitation of a dye molecule upon incident light; or (2) Förster resonance energy transfer (FRET), where distance-dependent dye-quencher or dye–dye pairs are within sufficient proximity to transfer excitation energy between each other. With these techniques, HCR and CHA have consistently demonstrated unprecedented nucleic acid imaging in cells while precisely preserving spatial expression; this has exhibited striking patterns of different RNA species across the same tissue sample.[87,90,91] HCR first mapped mRNA patterns in zebrafish embryos in 2010,[87] but only imaged live cells in 2015 after grafting fluorescent HCR probes onto gold nanoparticle carriers.[92] Since then, major developments have strengthened imaging quality and efficiency in live cells.

One ultimate goal with live cell imaging is graduation to robust *in vivo* imaging. While *in vivo* visualization of nucleic acid has never been seriously explored, HCR and CHA can give clinicians the power to observe nucleic acid patterns within live tissue for a more localized understanding of disease markers. Spatial monitoring of tell-tale nucleic acids is also an appealing method to gather clues on a developing disease while elucidating survival. To advance HCR and CHA from *in vitro* to *in vivo* imaging, (1) visualization, (2) biostability and biocompatibility, as well as (3) target diversity must be optimized.[93]

2.3.1. Visualization improvements

Outstanding advances in HCR and CHA-mediated imaging include enhancing contrast, reducing background, and expediting required imaging time. A notable contribution to these efforts comes from Pierce's “third generation HCR” in 2018.[91] One problem with the original HCR was nonspecific binding between the HCR probes and random nucleic acids, which result

in heightened background fluorescence and signal leakage.[91,94] Third generation HCR overcomes this problem by replacing the first amplification probe with two "split-initiator probes"; these split initiators carry only half of the original amplification strand (Figure 2.2 A). In order to gather the correct signal, the target strand must hybridize with both split initiators before cascading. This method therefore coerces more rigorous sequence specificity to suppress nonspecific background (Figure 2.2 B).

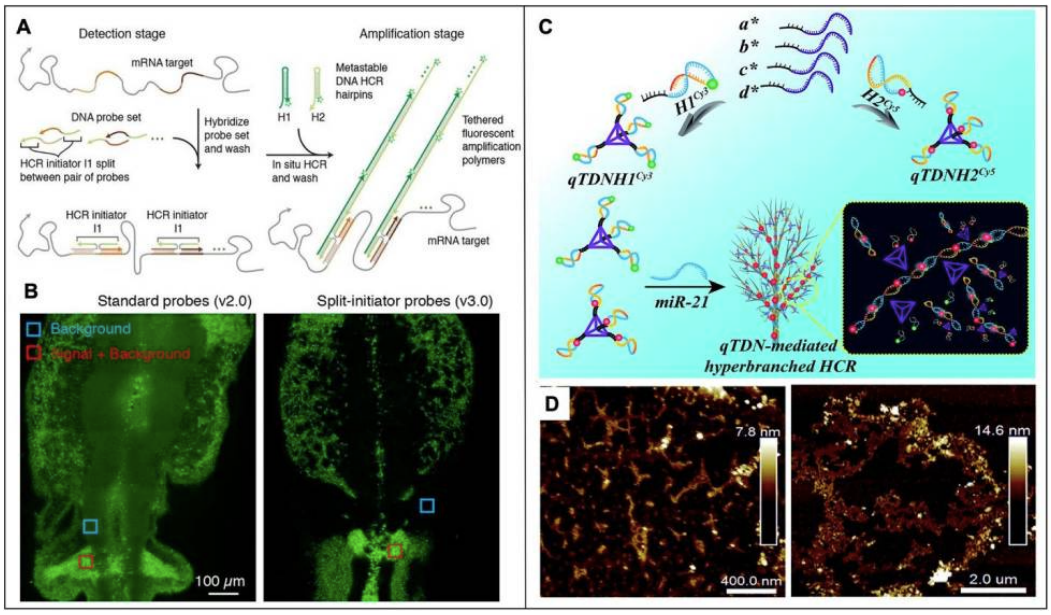

Figure 2. 2 Live cell imaging

(A) Schematic on third generation HCR where split initiator probes improve the specificity of the fuel strand binding for an amplified signal. (B) Comparison of second-generation HCR with third generation HCR where the background fluorescence in third generation HCR is noticeably minimized with the split initiator probe method. Copyright 2018 Company of Biologists.[91] (C) Schematic representation of tetrahedron mediated HCR (qTDNH), which leads to accelerated signal amplification time and larger superstructures based on fuel strand-initiated assembly. (D) Generated superstructures using (left) traditional HCR and (right) tetrahedron enabled HCR. Published by the Royal Society of Chemistry 2019.[95]

A critical goal in fluorescent-probed strand amplification is coherent and spatial imaging of the targets in live cells. In this regard, creating imaging contrast between areas of different nucleic acid distributions has been a hurdle. CHA particularly suffers from reduced contrast because target strand recycling produces discrete duplexes rather than expanding duplex

superstructures. Consequently, traditional CHA products have scattered and sparse fluorescence—regardless of how many duplexes are produced—which reduces contrast and CHA's inherent imaging viability. Huang *et al.* directly address this limitation by designing CHA probes that form crosslinking tetrads upon mRNA (survivin or TK1) recognition.[96] The produced superstructures generated meshes that consolidate fluorescent signals for significant contrast improvements over traditional CHA. In fact, traditional CHA resulted in structures on the order of tens of nanometers while the crosslinked CHA meshes were several hundred nanometers at identical starting concentrations.

Another key challenge in strand amplification imaging is the required time to yield distinguishable fluorescence. Most HCR and CHA techniques need several hours for sufficient signal output (Tables 2.1 and 2).[87,97] The first demonstration of *in situ* HCR imaging required about 36 hours to effectively map RNA in embryo samples,[87] but progress has since reduced the reaction time to one to two hours in live cells (Tables 2.1 and 2). While many works demonstrate such reduced times, the various approaches were designed to achieve different goals while collaterally addressing this issue; for example, helper-delivery nanoparticles and secondary DNA structures contributed to 1–2 h reaction times. Reports from the past year, however, show that 3D DNA probes dependably accelerate the reaction time. Wang *et al.*'s work with HCR demonstrated observable fluorescence in an impressive 20 minutes.[95] The amplification kinetics were hastened by 3D tetrahedral DNA structures. Key advantages to this architecture include (1) enabled quadrivalency in hybridization sites at the tetrahedron vertices and (2) increased local concentration of reaction sites for HCR to occur (Figure 2.2 C). Not only did this improve the reaction time 70-fold *versus* traditional HCR, but it generated micron-ranged superstructures that provide clearer, brighter, and more coherent fluorescence (Figure 2.2D). CHA was similarly re-

designed for heightened reaction speed. Qing *et al.* similarly utilized 3D tetrahedrons to improve CHA reaction kinetics; this same approach reduced the time for a sufficient signal-to-noise ratio from 48 minutes to only 3 minutes.[98]

Higher order DNA structures can therefore decrease reaction time and increase contrast, but the works above do not show any demonstrations in a whole animal; future work invites the incorporation of these design strategies in a mouse model. It would be imperative to corroborate the sustainability of heightened reaction time and enhanced contrast in a living system. One can also couple Third Generation HCR with higher order DNA structures to avoid background fluorescence during imaging.

2.3.2. Diversity in molecular target imaging

Besides nucleic acids, DNA and RNA have high affinity to proteins through characteristic binding interactions, and their standardized covalent labeling with reactive organic groups expands their avidity to a wider class of entities;[99] by chemically linking single strands with other molecules such as peptides and click-chemistry actors, nucleic acid possesses the unique potential to image diversified targets on the nanoscale.

Aptamers are structural nucleic acids with high specificity to a wide range of biomolecular species and possess binding strengths that are analogous to the antibody-protein model. These secondary structured nucleic acids install themselves along grooves and reactive sites with K_D values in the nanomolar to as low as picomolar range.[100,101] Aptamers are therefore coupled with strand amplification to minimize the required concentration of target protein analytes. Qin *et al.* utilized an aptamer-embedded hairpin and two additional hairpin probe species to form HCR-networked superstructures upon cytokine sensing.[102] Their target fuel-protein, IFN-γ, first hybridizes with the aptamer probe, elongating the remainder of the strand to hybridize with hairpin 2. Hairpin 2 is allowed to bind with the aptamer probe in two different

orientations, leading to two different aptamer-hairpin 2 products. Similarly, the multiple conformations of hairpin 3 re-exposes binding points for hairpin 2, accommodating two different aptamer-hairpin 2–hairpin 3 products. When hairpin 2 binds with these diverse products, the hierarchical network continuously grows (Figure 2.3 A). This simple mechanism competes with current standards in IFN-γ sensing—primarily immunological assays—which are costly and laborious. Besides triggered hierarchical assembly, aptamer-HCR has been implemented in other ways such as by Boolean-mediated HCR circuits for the "smart sensing" of two protein species.[103]

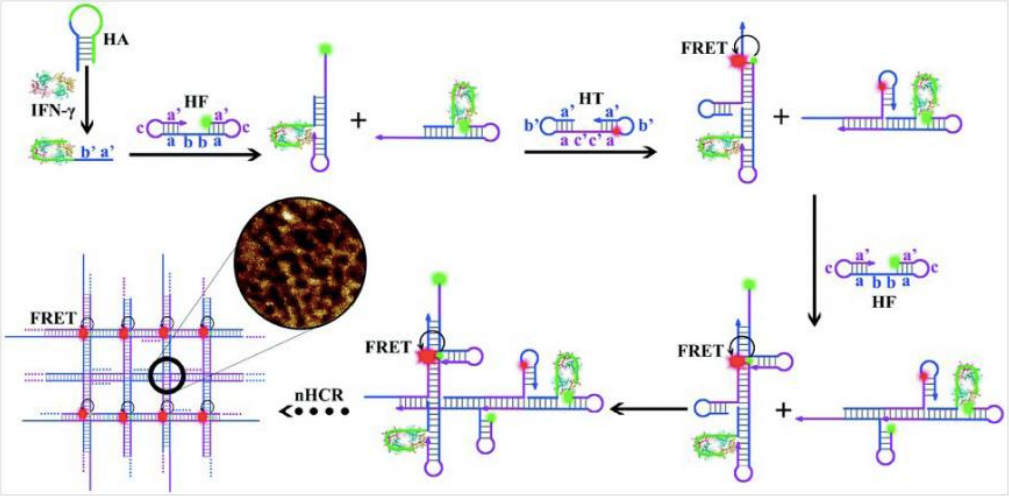

Figure 2. 3 Aptamer-activated HCR networks for the sensing of I FN-γ whereby the output signal is provided by FRET fluorescence.

The multiple conformations adopted after each cascaded hybridization upon incident I FN-γ recognition enables the crosslinked and mesh superstructures. I FN-γ initially binds with hairpin aptamer (HA), which consequently links with fluorescent FAM-dye-labeled and TAMRA-labeled hairpins (HF), (HT) for effective FRET. Copyright 2019 Nanoscale, Royal Society of Chemistry.[102]

The good compatibility of nucleic acids with other molecular species has enabled HCR and CHA to effectively detect other endogenous targets (Tables 2.1 and 2). Strand-induced

signal amplification has monitored cytokines, sialic acid species,[104] and specific glycosylation events across cell membranes.[99,105] In fact, the prevalence of cell free proteins and other biomolecules welcome molecular programming tools like strand amplification to enable highly sensitive bioimaging.

2.3.3. Stability to and within live cells

The stability and safety of strand amplification in live cells are equally crucial during experimental design. Synthetic nucleic acids are unstable against the rich abundance of RNAse, DNAse, and other nucleases within cytoplasmic and extracellular space. Consequently, most synthetic nucleic acids are digested within several minutes while higher-order DNA nanostructures inevitably undergo structural denaturation.[106] Furthermore, their negatively-charged phosphate backbone makes it difficult for them to surpass the cell membrane alone. Besides these weaknesses in nucleic acid, live-cell imaging methods require a light source that will not collaterally damage skin and other tissues. Thus, (1) near ultraviolet (UV) sources must be avoided, (2) nucleic acid chemical and structural modifications should be investigated for heightened stability, and (3) inert delivery of the probes to the designated target should be thoroughly explored. Because HCR requires at least one to a few hours for a signal, probes should be designed to withstand at least four to five hours for practical *in vivo* applications.

Chu *et al.* addressed all of these issues by grafting HCR hairpin probes onto lanthanide ion-doped upconverting nanoparticles (UCNPs) to guide delivery and deliberately activate HCR.[107] Not only do the UCNPs act as a vehicle to ensure hairpin delivery, but they also serve as a safe source to ignite the HCR reaction by presenting the hairpin toehold only when necessary (Figure 2.4 A). UCNPs are chemically engineered nanoparticles whose crystal asymmetry accelerates a near infrared (NIR) source wavelength to a UV output wavelength. Incident NIR translates into UV light when the HCR hairpins are grafted onto the UCNPs. This breaks a

photocleavable crosslinker embedded in the hairpins and exposes them to their target once inside the cell. This controllable activation led to c-MYC mRNA-based HCR with superb spatial and temporal resolution. The system only required a harmless 980 nm light source.

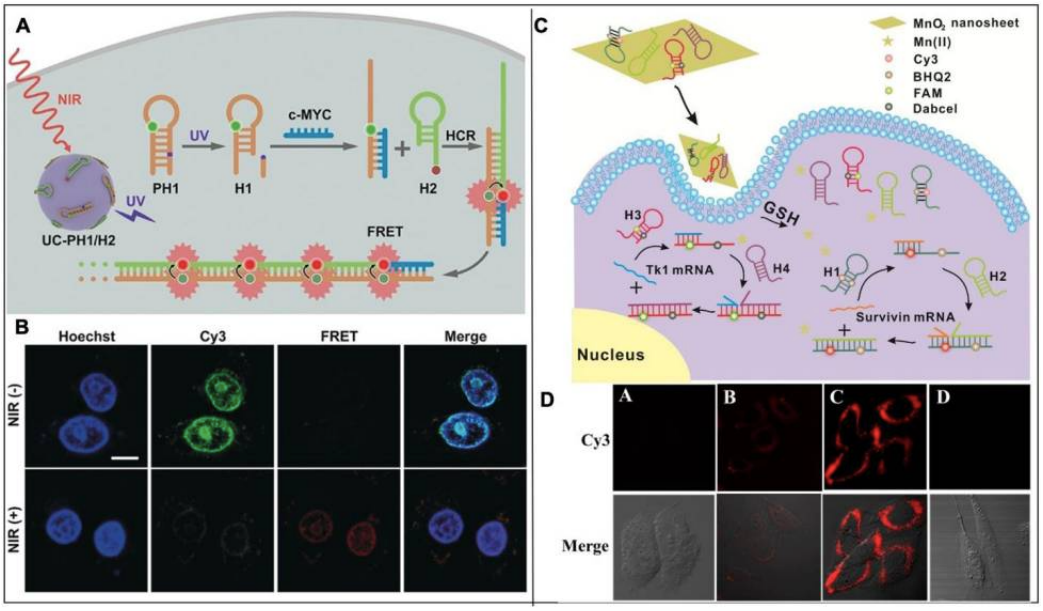

Figure 2. 4 Sustaining stability and safety when administering HCR and CHA probes to live cells.

(A) UCNP mediated HCR allows the HCR probes to remain stable en route to target cells while the NIR activation leads to UV cleaving of the hairpin probes thus preparing them for hybridization with the target and signal amplification. (B) Resulting images of the cells: without NIR activation (above), Cy3 signal dominates while FRET Copyright 2019 Angewandte Chemie International Edition[107]. (C) MnO_2.mediated delivery of CHA signal amplification. (D) Validation of MnO_2 delivery efficacy where Da depicts the hairpin probes without the sheets, Db Hairpin probe 1 with the nanosheet, Dc both hairpin probes delivered by the nanosheet, and Dd incubated with a cell line that is negative of the target miRNA. Copyright 2019 Microchemical Journal.[108]

Table 1.1 Recent strategies that advance live cell imaging through HCR.
Limit of detection (within the picomolar to femtomolar range), dynamic range, reaction time (ranging from a few minutes to several hours), and target are specified from the reports. Specificity strategies for sensing efficiency are also outlined. N/R= not reported.

Method	Advantage	LoD	Dynamic Range	Reaction Time	Target	Specificity	Ref
UCNP-conjugated HCR	Spatio-temporal imaging, use of NIR activation	0.6 pM	N/R	1 hr	c-MYC mRNA	Compared with other mRNA and miRNAs	107
Dumbbell structural motifs for HCR	Nuclease resistance, stable up to 16 hours	3.2 pM	25 pM-100 nM	1.5 hr	miR-27a	Single to multi-base mismatch	111
i-motif triggered HCR.	pH-activated imaging	N/R	N/R	5 hr	miR-21	Imaged target negative epithelial cell line	112
Quantum dot-HCR	Brighter fluorescence, spatial imaging	2.78 fM	10 fM-100 pM	N/R	miR-200c-3p	Compared mismatched sequences	109
Click-reaction triggered HCR	Cell glycosylation imaging	N/R	N/R	1.5 hr	Sialic acid, galactosamine, glycosylation events	N/R	99
Multiple-aptamer logic device mediated HCR	Boolean logic to accurately sense cell subtype	N/R	N/R	1.5 hr	Tyrosine protein kinase-like 7 (PTK7) and TCO1 proteins	Compared across different cell lines	103
3D DNA tetrahedron HCR	70-fold faster imaging	2.14 pM	2-40 pM	20 min	miR-21	One-base mismatch	95
Alkyne-modified HCR to detect azide labeled SiaGcs	Directly quantify SiaGC secretion	N/R	N/R	4 hr	Sialoglycoconjugate (SiaGCs)	N/R	141

Table 1.2 Recent strategies that advance live cell imaging through CHA.

Limit of detection (within the picomolar to femtomolar range), dynamic range, reaction time (ranging from a few minutes to several hours), and target are specified from the reports. Specificity strategies for sensing efficiency are also outlined. N/R= not reported.

Method	Advantage	LoD	Dynamic Range	Reaction Time	Target	Specificity	Ref
Streptavidin-DNA tetrads for CHA	High contrast in living cells	0.8 pM-0.9 pM	5 pM-1 nM	1.5 hr	Survivin mRNA, TK1 mRNA	Compared to single- and two-based mismatch	96
CHA-mediated nanobrush motif assembly	Image short and long nucleic acid strands	1.03 - 1.88 nM	5-25 nM	4 hr	miR-21, BRCA1 oncogene DNA	Single and three-base mismatch	297
3D tetrahedron CHA	15.6-fold reaction rate alongside CHA, increased stability	0.15 nM	N/R	48 min	MnSOD mRNA	Tested against different sequences	98
Tetrahedron mediated FRET amplification	9.6-fold faster than traditional CHA.	3.5 pM	0-10nM	1.5hr	MnSOD mRNA	Single, two and three-based mismatch	155
Genetically encoded fluorescent CHA	High sensitivity and Broccoli incorporation for fluorescence	2.5 nM	N/R	2 hr	N/R	Compared with different strand sequences	183
Gold nanoparticle-CHA coupled system	Reduction of false-positive signals, enhanced SNR	3.7 pM	10-1000pM	4hr	miR-21	Compared with miR-41	298

Manganese oxide (MnO_2) nanosheets can be oriented into planar networked sheets and are economical, biocompatible, and degradable *via* glutathione.[110] MnO_2 offers efficient fluorescence quenching to further encourage its union with biomolecular imaging probes. Li *et al.* showed that MnO_2 can sustain nucleic acid stability and signal amplification with either HCR or CHA as the amplifier.[108,111] In both cases, the nucleobases on the probe strands strongly bind to the sheets *via* physisorption. Without the sheets, there was weak fluorescent output *in vitro*. However, their same probes at identical concentrations generated bright and apparent fluorescence after nanosheet-mediated delivery (Figure 2.4 D).

Other strategies have reported heightened stability. These include the incorporation of secondary structures that promote endonuclease resistance[112] or pH-activatable structures[113] (Table 1). In general, these approaches utilize clever strategies in structural DNA nanotechnology such as unique architectures and pH sensitivity based on C-G base-pair density to avoid interactions with the surrounding microenvironment. However, many purely DNA-based probes—whether more stable against endonucleases[112] or more reactive for a decreased fluorescence time[95]—require lipofectamine—a cationic and highly toxic delivery agent[114,115]—to aid in their transfection into cells. While lipofectamine is canonically used as a transfection agent for gene therapy research, its union with HCR and CHA raises safety concerns for *in vivo* applications. Therefore, the design of probe structures that can be functionalized with a safe helper vehicle—such as targeting ligands or the MnO_2 sheets described above—should be considered seriously.

In general, many approaches have tackled live cell imaging-related challenges that afflict HCR and CHA (Tables 1 and 2). Of course, these methods needed to confirm that the probe maintains target specificity. Benchtop selectivity tests—where HCR and CHA probes are mixed

with strands besides the target—were commonly implemented to demonstrate the probes' power to discriminate targets from nonspecific binding. Other reports confirmed selectivity by imaging with probes in cancerous cell cultures in parallel with noncancerous, target-negative cultures.[108] Future *in vitro* specificity experiments can implicate HCR and CHA probes in co-cultured, multidimensional models[116,117] so that the probes can realistically (1) discriminate between healthy and diseased cell lines and (2) map dynamic nucleic acid expressions that both differ and agree between healthy and disease cell lines. These are reasonable precursor experiments to support possible *in vivo* specificity.

2.4. Lowering limit of detection

The prevalence and lifetime of many nucleic acids can be influenced by a combination of subjective factors such as sex, body weight, and age,[118] so a limit of detection (LoD) below femtomolar levels is a paramount goal for strand amplification's clinical translatability.[119] While HCR and CHA have shown novel nucleic acid imaging capabilities, the detection limit for most imaging probes is in the picomolar to femtomolar range (Tables 1 and 2, Figure 2.11). Therefore, other strategies on strand amplification employment have been developed for even lower LoD values. Only recently, attomolar to sub-attomolar ranged detection by HCR and CHA has been consistently achieved.

2.4.1. Electrochemical sensing

Perhaps one of the more successful approaches in lowered LoD is electrochemical sensing. Subtle hybridization events, strand conformational changes, or nucleic acid harnessing of other chemicals through intercalation or physisorption produce slight yet definite redox changes on the electrode surface for a quantifiable signal.[120,121] The simplicity and lower cost of electrochemical sensors have made them more attractive for DNA detection above PCR, surface-enhanced Raman scattering (SERS) and localized surface plasmon resonance (LSPR). Most

electrodes for DNA detection utilize gold because they can easily hybridize with thiolated DNA. Indeed, DNA electrochemical sensors are not new in the biosensor world and already offer attomolar detection,[122] but these assay designs require a denser number of input strands for the subsequent readout and can therefore be more costly and time-consuming to prepare. Therefore, strand amplification offers a more efficient and economical way to produce electrochemical nucleic acid sensors.

An increasingly popular strategy in HCR electrochemical sensing involves capturing chemical labels upon hybridization. In particular, derivatives of cationic RuHex $[Ru(NH_3)_6]^{3+}$ have strong affinity to DNA duplexes by electrostatic anchorage on the phosphate backbones. Their accumulation on the strands can generate an oxidation current[123] as the electrochemical reporter of DNA hybridization. Guo *et al.* utilized this mechanism to sense exosomal miRNA (miR-122) by HCR.[124] Hairpin probes complimentary to the target miRNA were first grafted to a gold electrode surface. Upon hybridization with the target, the rest of the probe hybridizes with the remaining hairpins to catalyze HCR and capture RuHex molecules in an increasingly dense manner (Figure 2.5 A). This method achieved a low LoD of 53 aM and further reduced the chances of false positive signals by introducing exonucleases to the system prior to the start of HCR; probes not conformed into hairpins were digested by the exonucleases and were eliminated from the total output signal. The conformational sensitivity of unhybridized probe strands is important because any slight microenvironmental charge change can result in undesired self-folding and strand collapse, thus accidentally capturing RuHex. Therefore, the endonucleases act as a novel quality control by destroying unbound strands altogether. Lv *et al.* also studied RuHex captivation by sandwiching the target DNA (*H. pylori* DNA) and HCR event between a gold electrode and gold nanoparticles functionalized with the HCR

initiator.[125] The growing HCR concatemers on the nanoparticle surface facilitated an accumulation of dendritic RuHex species on the surface and electrode, thereby resulting in heightened signal. This work achieved an impressive LoD of 0.63 aM.

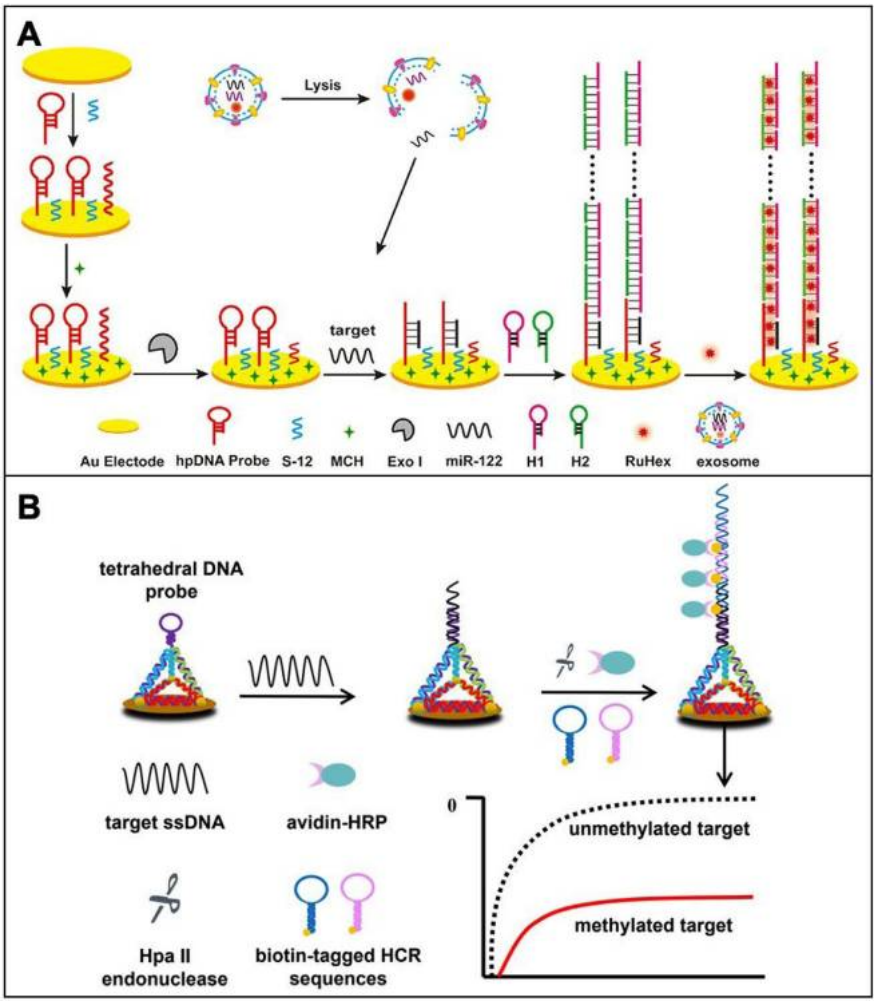

Figure 2. 5 Electrochemical approaches in lowering the detection of target analytes.

(A) Schematic on RuHex-mediated capture using HCR, where S-2 strands evenly space the HCR hairpin probes and MCH (6-mercapto-1-hexanol) effectively covers bare surface binding sites. Copyright 2020, American Chemical Society.[124] **(B)** Schematic on DNA tetrahedron-mediated electrochemical sensing of methylated DNA. HCR probes are decorated at the point of DNA tetrahedron motifs, which are immobilized on the gold electrode for an even separation of the reduction of both background and nonspecific binding. In this case, HCR probes were decorated with biotin so they could capture avidin-functionalized horseradish peroxidase as a chemical reporter Copyright 2019, American Chemical Society.[126]

Immobilization of higher order DNA structures on electrodes can also gather distinguished signals after strand amplification. For example, DNA tetrahedrons were grafted onto gold electrodes with an exposed hairpin probe for the target to catalyze HCR[126] (Figure 2.5B). The primary role of the tetrahedral motif is to maintain probe stability on the electrode by evading inter-probe entanglement and nonspecific adsorption of other molecules and random strands. This approach resulted in a LoD of 0.93 aM. Another strategy utilized nonlinear, Y-shaped DNA motifs that continuously branch into HCR dendrimers while remaining grafted to the gold electrode.[127] The Y shaped motif was chosen for its stability and heightened selectivity to miR-25 over normal ssDNA and duplex motifs. The purely-DNA based approach led to a higher LoD of 334 aM because no chemical reporters were involved.

2.4.2. Electrochemiluminescence (ECL)

Electrochemiluminescence (ECL) is another signaling approach with low-attomolar LoD. Similar to electrochemical sensors, ECL relies on the change of electron transfer near an electrode surface, but it uniquely generates an excitation state that permits light emission for observable signal.[128] Due to its low background and high sensitivity, ECL has become increasingly attractive in biomolecular sensing applications and is already commonly employed in standard bioanalysis methods such as western blotting and immunoassays. Thus, ECL-based HCR and CHA could bring them closer to more practical biosensor technologies.

For example, Zhang *et al.* exploited ECL for a 18.6 aM LoD by hybridizing hairpins on ZnO-coated gold nanoparticles such that HCR dendrimers allowed branched electroactive ferrocene.[129] The growing ferrocene density would ultimately consume O_2 co-reactants from the ZnO shell, quenching ambient ECL in the sensor. Despite the low LoD, this working mechanism depends on a switched “ON to OFF-state” where the ECL signal is omnipresent only until the target is detected. Ge *et al.* similarly used HCR-ECL but with desirable “OFF to ON-state” for a

4.97 aM LoD.[130] In their approach, HCR probes are grafted onto mesoporous silica nanoparticles where $AgNO_3$ was loaded inside. $AgNO_3$ was released upon hybridization between the DNA and target RNA strands allowing Ag ions to be captured within cytosine-rich DNA strands that cluster and quench the surrounding quantum dots for heightened ECL.

2.4.3. Magnetic detection strategies

Magnetic signal methods have also achieved impressive attomolar to sub-attomolar LoD (Tables 2.3 and 4). For example, bio-bar-coding—first established by Chad Mirkin's lab[131]—was recently coupled with CHA by Xueji Zhang's group for a 97.9 zeptomolar LoD of miR-21.[132] This is the lowest established LoD reported using strand signal amplification and enhances traditional bio-bar-coding's initially reported LoD of 500 zM.[131] Bio-bar-coding operates by sandwiching the target strand between (1) probe gold nanoparticles and (2) magnetic microparticles. Both particle species are functionalized with oligonucleotides such that the target partially hybridizes each of them simultaneously. When the target strand enables dimerization between the gold and magnetic nanoparticles, the gold nanoparticles are magnetically isolated for analysis. Conventionally, the barcode strands would be interpreted alone as amplifiers but Zhang's group strengthens this process by coupling the barcode strands with CHA after magnetic separation (Figure 2.6). Additionally, Tang *et al*. demonstrated 13 aM LoD *via* colorimetric-based detection. They engineered HCR to enable triggered aggregation of magnetic networks, therefore providing an observable colorimetric change in solution.[96]

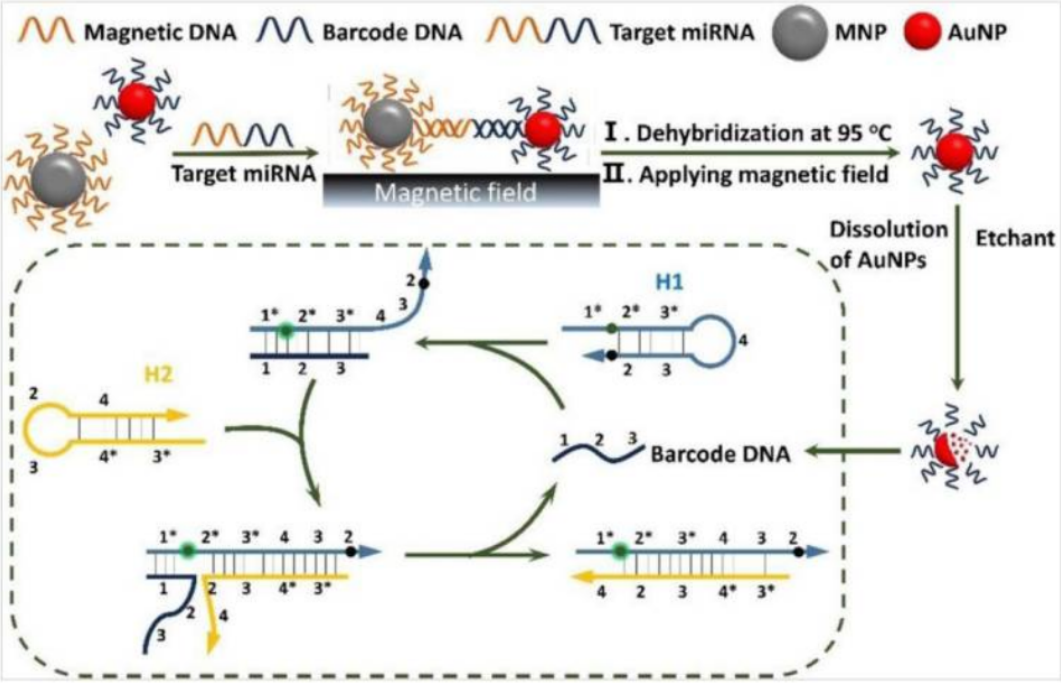

Figure 2. 6 Schematic on CHA-mediated Bio-Barcoding.

CHA is introduced into the Bio-Bar-Coding system after barcoded DNA is isolated from the magnetically-separated gold nanoparticle probes. This achieved 97.9 zM LoD, being the lowest value yet reported. Adapted with permission[132], Elsevier, 2018

Table 1.3 Recent strategies that advance lowered LoD of nucleic acids using HCR.

Limit of detection, dynamic range, reaction time, and target are specified from the reports. Specificity strategies for sensing efficiency are also outlined. N/R= not reported.

Method	Signal	LoD	Dynamic Range	SNR	Target	Specificity	Reference
Magnetic networks by HCR	Colorimetric	13 aM	0.05 fM-12 nM	3	let-7a (miRNA)	Compared with let-7b, let-7c and miR-21	299
Nonlinear HCR on bare gold electrodes	Electrochemical	334 aM	1 fM-10 pM	N/R	miRNA-25	Single-base mismatch and other miRNA species	126
Au-immobilized HCR to intercalate RuHex, exonuclease editing	Electrochemical	53 aM	100 aM-100 nM	4.13	miR-122	Single-base mismatch	123
Au-electrode-AuNP HCR sandwich to capture RuHex	Electrochemical	0.68 aM	1 fM-100 fM	3	Helicobacter pylori DNA	Compared with mtDNA, ncDNA, DNA from human serum	111
Ag-nanocluster quenched-ECL via HCR	ECL	4.97 aM	100 aM-1000 pM	3	miRNA-21, thrombin	Thrombin versus AFP, CEA and PSA	129
Gold immobilized DNA tetrahedron base, HCR	Electrochemical	0.93 aM	1 aM-1 pM	N/R	Methylated DNA	Compared single and multi-base mismatched sequences	125
AuNP@ZnO NCLs	ECL	18.6 aM	100 aM-100 pM	N/R	miRNA-21	Compared with miRNA-122, miRNA-141 and miRNA-155	128
4-arm junction with Fe	Electrochemical	3 aM	10 aM-10 fM	3	miR-21	One-base to multi-base mismatch	300

Table 1.4 Recent strategies that advance lowered LoD of nucleic acids using CHA.

Limit of detection, dynamic range, reaction time, and target are specified from the reports. Specificity strategies for sensing efficiency are also outlined. N/R= not reported.

Method	Signal	LoD	Dynamic Range	SNR	Target	Specificity	Reference
Bio-bar-coding with CHA	Fluorescence	97.9 zM	10 aM-10 pM	4	miRNA-21	Single and three-base mismatch and complimentary target strand	131
Mesoporous Silica NPs with combined CHA and HCR	Electrochemical	37 aM	N/R	N/R	miR-21	Compared with miRNA 27a, miRNA 375, let-7d, miRNA R-200b	301
NiO@N coupled with CHA	Electrochemical	45 aM	100 aM-100 pM	46.1	Not specified	Tested against single and three-base mismatch sequences	147

2.5. Multiplexed Sensing

Nucleic acid molecules have promise as disease biomarkers but can also be non-specific.[133] The simultaneous detection of multiple disease-correlated targets can further validate the extent and presence of diseases. Recent endeavors in strand amplification have therefore explored optimized techniques that enable multiplexity. An earlier work in HCR demonstrated 5-species multiplexity *via* five different HCR probe species.[87,91] Progress has since improved multiplexity by maximizing the bandwidth of HCR and CHA probes to recognize multiple targets at once or with minimal probe diversity. Advancements in multiplexed strand amplification have been translated to both imaging and chemical sensing modalities.

2.5.1. Branched and nonlinear DNA nanostructures

One such approach could involve secondary DNA structures that enable probing of multiple targets (Table 5). Xu *et al.* designed DNA structures such that traditional HCR hairpin probes are instead designed as branched DNA structures upon hybridization;[134] the probe ultimately cascades into networked DNA superstructures when both target sequences are recognized. However, if only one of the two targets is detected by the probe, then linear and characteristic structures are formed. This is primarily due to the extension of one *versus* two unique branch sequences for superstructure formation. This method therefore makes it easy to differentiate a product where both targets are present from a product where only one or no targets are present. This approach only needs two probe strands for two targets while traditional HCR would require 4 probe strands (Figure 2.7 A and B). This work demonstrated multi-sensing of two targets but suggests there is room to engineer the probe for three or even more targets. Lv *et al.* similarly explored higher order structures using 3D tetrahedron HCR probes.[135] The tetrahedron vertices were functionalized with Y-shaped DNA motifs which possess the necessary HCR hairpins. The Y-shaped motifs were comprised of two different species, allowing the tetrahedron to sense two different target strands within two sites on the total structure (Figure 2.8 A). This work displayed simultaneous imaging of miR-21 and miRNA-203 within the same cells on the same probe by functionalizing them with two different dye-quencher pairs (Cy3-BHQ2 and FAM-BHQ1) for FRET. The different dye-quencher pairs led to resultant red and green fluorescence, making it easy to visually distinguish between the different target species. The resulting micrographs corroborated the different densities of both targets within HeLa and MCF-10A cells (Figure 2.8 B).

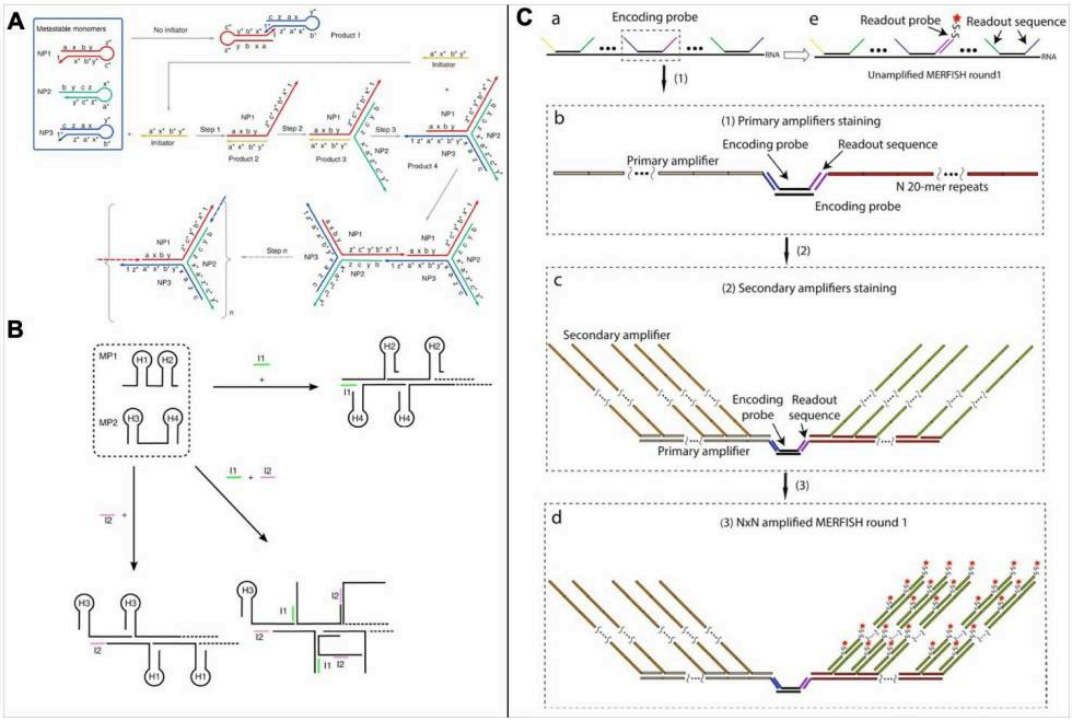

Figure 2. 7 Strategies in nonlinear and branched HCR for improved multiplexity.

(A) Schematic of branched HCR amplification method, where the detection of one target leads to serial strand displacement and hyperbranched products. **(B)** Multiplex feature of the branch strategy, where target 1 and 2 (I1 and I2) trigger with hairpins H1-2 and H3-4, respectively. The presence of both targets results in the hierarchical organization of the HCR loop strands. On the other hand, the presence of only one target produces linear, "chain-like" HCR structures, regardless of which target is chosen. Adapted from Microsystems and Nanoengineering, Nature Publishing 2018[134]. **(C)** MERFISH approach. **Ca-b,** the encoding probes which bind to multiple points of the target strand, which simultaneously link to the readout strand. **Cc-d** secondary and then HCR-mediated amplification of the MERFISH sensing. Adapted from Scientific Reports, Nature Publishing 2019.[136]

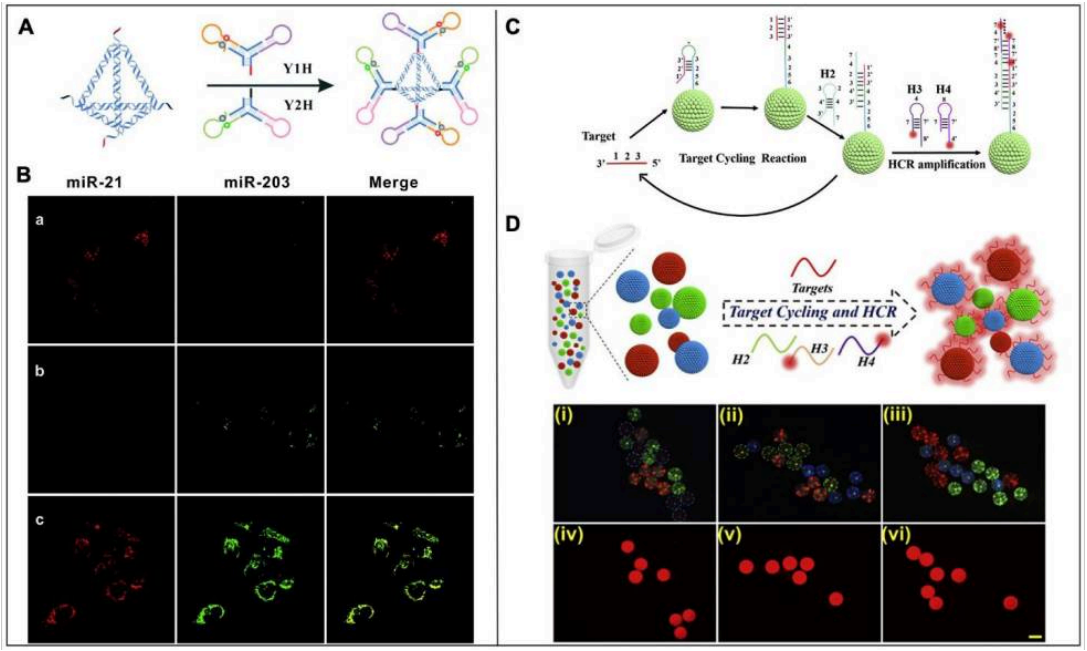

Figure 2. 8 Strategies in visualized multiplexed strand signal amplification using live cell imaging for biosensors.

(A) Schematic representation of tetrahedron multiplexed HCR. **(B)** Resultant multiplexed imaging of miR-21 and miR-203 in **Ba** HeLa cells, **Bb** MCF-10A and **Be** HeLa pretreated with miR203. Reproduced from ref [137] with permission from Royal Society of Chemistry. **(C)** Dopamine surface functionalization of photonic crystals (PhCs) to enable attachment of HCR probes on their surface. Probes that recognize three different targets are grafted onto PhCs that are optically tuned to reflect either blue, green, or red reflection peaks as seen in **(D). (D)** (i)-(iii) optical microscopy of the PhCs after recognition of different target nucleic acids, where the intensity of reflected color is diminished with the corresponding PhCs whose HCR reactions are catalyzed. Copyright 2019 Biosensors and Bioelectronics[138]

Table 1.5 Recent approaches in optimizing multiplexity within HCR methods.

Method	Signal	LoD	Targets	Max diversity	Specificity	Reference
Branched HCR	Surface acoustic wave sensor (SAW)	25 nM	Not specified	2	N/R	133
CHA on fluorescent microbeads "Luminex xMAP »	fluorescence	2 pM	miRNA-21, mi-RNA-122, miRNA-222	3 demonstrated ("as many as 500" proposed)	Single-base mismatch and other miRNA species	126
HCR on Photonic Crystals PhCs	Optical (fluorescence)	8 fM	miR-21, miR-155, miR210	3	Single- and three-base mismatch	123
Time-gate FRET (TG-FRET)	Photoluminescence	1.7 pM (miRNA), 0.88 pM (NA)	miR-20a, miR-21	2	Compared with miRNA-20b	111
MERFISH-HCR	fluorescence	N/R	Not specified	130	N/R	129
Magnetic beads with biotin-HCR to capture streptavidin-peroxidase	Electrochemical	0.66 pM	miR-21, let-7a, miR-31	3	Single and double base mismatch, other strands	149
DNA tetrahedron-Y-motif	Fluorescence imaging	7pM (miR-21) 3pM (miRNA-203)	miR-21, miRNA-203	2	Compared with random sequences and nonhomologous RNA	136

Table 1.6 Recent approaches in optimizing multiplexity within CHA methods.

Method	Signal	LoD	Targets	Max diversity	Specificity	Reference
CHA on fluorescent microbeads "Luminex xMAP »	fluorescence	2 pM	miRNA-21, mi-RNA-122, miRNA-222	3 demonstrated ("as many as 500" proposed)	Single-base mismatch and other miRNA species	126
CHA-based gel electrophoresis assay	Gel electrophoresis	10fM	miRNA-21, miRNA-373, miRNA-10b	3	Single and double base mismatch	88

Another nonlinear DNA-based method utilized "multiplexed error robust fluorescence *in situ* hybridization" (MERFISH) with branched HCR for multiplexed RNA imaging (Figure 2.7 C).[136] MERFISH was invented by the same team, Xiaowei Zhuang's group in 2015,[139] but has since been coupled with HCR in 2019. In principle, MERFISH requires the use of both (1) "error-robust" barcode DNA probes and (2) FISH fluorescent DNA probes for signal upon hybridization. MERFISH has alone measured 140 species of RNA.[139] Above traditional FISH-mediated HCR, MERFISH-HCR achieves impressive brightness because fluorescence from a single target RNA is produced by binding several labeled probes. A weakness to this demonstration, however, is the need for 16 probes per RNA species, which is not practical for *in vivo* applications and may be taxing for biosensor designs. Nonetheless, the significant advancement from 92 required probes to only 16 encourage further work to utilize MERFISH while continuing to minimize diverse barcode probes per target.

2.5.2. Optically-responsive multiplexity

A simple yet efficient demonstration of optically-mediated multiplexity utilized traditional HCR probes with unique time-gated FRET (TG-FRET).[140] Guo *et al.* executed this

concept by engineering two HCR probe species (based on the two different targets) resulting in two characteristic photoluminescence decay times by installing different TG-FRET molecules within the HCR products. This work demonstrated multiplexing of two miRNAs, but this platform may accommodate higher order multiplexing based on a higher number of allowed relaxation times.

Other optical multiplexing approaches rely on grafting different hairpin probes on nanomaterials with tuned optical responses (Tables 2.5 and 6). For example, Zhao's group immobilized three HCR species and CY3-labeled HCR amplifiers on different 200 nm silica photonic crystals (PhCs) (Figure 2.8 C and D).[138] The PhCs are tuned to reflect characteristic wavelengths of red, green, and blue light. This method is advantageous over naked fluorophore signaling due to PhCs' narrower spectral width, biostability, and reduced background.[141] Meanwhile, the CY3-tagged HCR strands on the PhC surface will accurately correlate fluorescence with target concentration. Upon recognition of the target and consequential HCR cascading, (1) PhC fluorescence will emit and remain relative to target strand concentration, and (2) the surface of the related PhC will reduce scattering and thus change the reflective intensity of the tuned color. The fluorescence and reflectivity of the green, blue, and red particles were compared between each other based on presence of miR-21, miR-155, and miR-210 respectively. As the wavelength difference is maximized between red, green, and blue peaks, this mechanism can only accommodate third-order multiplexity while maintaining distinguishable signals. While this generates a beautiful method to visualize the presence of different miRNAs, it cannot be used for imaging but is rather a photonic biosensor. A similar strategy involved the union between CHA and fluorescent and color-coded microspheres.[142] While the work demonstrated

the ability to efficiently sense miR-21, miR-222, and miR-122 at once, the authors claim their platform theoretically allows “as many as 500 targets” to be detected simultaneously (Table 6).

2.6. Clinical Translatability

As explored above, a variety of technical advances have bolstered the strand amplification's viability for clinical analysis. Therefore, more recent reports have deployed HCR and CHA for *in vivo* imaging and proof-of-concept liquid biopsies (either from tissue, blood, or urine samples) (Table 7).

2.6.1. In vivo imaging

HCR-mediated imaging in living organisms has only been demonstrated twice in the last year, yet the platform shows promise for future *in vivo* mapping. The advantages include exploitation of higher order DNA structures for the HCR scaffold and the use of MnO_2 carriers for effective delivery and contrast with the HCR probes.

Wu *et al.*[143] successfully achieved targeted delivery to cancerous cells so that the HCR probes could correctly and spatially signal the presence of cancerous miR-21. The HCR probe was only one component of their Y-shaped structural design; two ends of the Y-motif enabled linear HCR while the third end of the Y was covalently conjugated to folic acid, a popular cancer targeting ligand in nanomedical drug delivery systems[144,145] (Figure 2.9 A and B). This work successfully sensed miR-21 in both HeLa and MCF-7 xenografted mice within a span of two hours (Figure 2.9 C), and no lipofectamine reagents were required to aid in the cellular uptake of the probes. Reported LoD was found to be 800 fM.

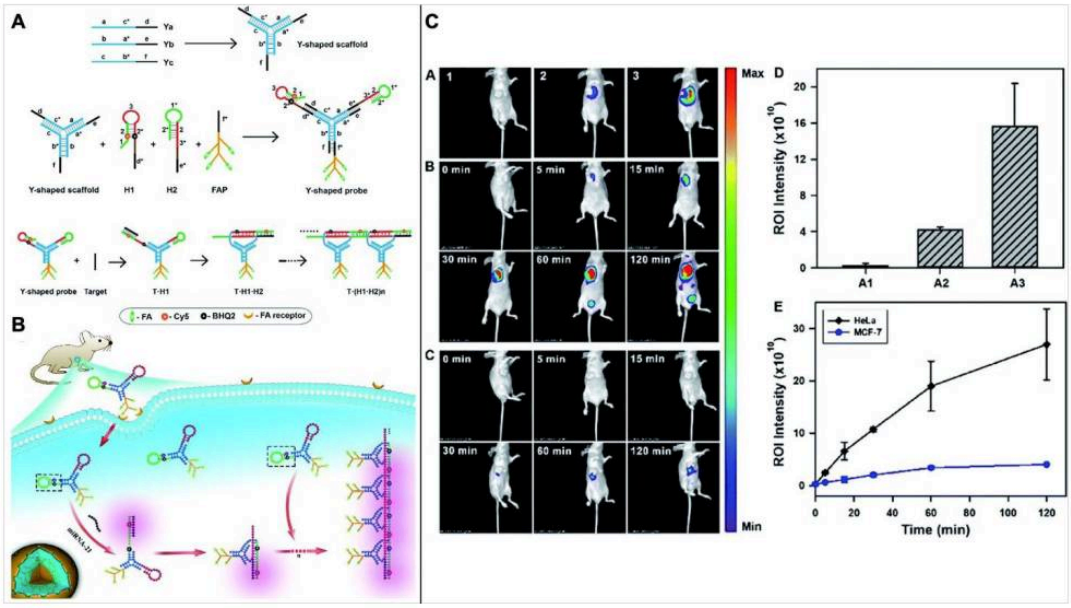

Figure 2. 9 In vivo imaging in live mice using Y-motif HCR Probes.

(A) Design of a Y-shaped motif where the two top ends are utilized for HCR while the third bottom end is linked with folic acid protein for cancer-cell targeting. **(B)** Schematic of the delivery of Y-HCR probes for cancer cell fluorescent imaging in live mice. **(C)** Fluorescent imaging data of live mice where **Ca** represents mice injected with either saline, MCF-7, or HeLa (from left to right. **Cb** represents HCR fluorescence of the HeLa in the span of 2 hours while **Cc** represents HCR fluorescence of the MCF-7 in the span of 2 hours. **Cd** Consequential fluorescence intensity in region of interest (ROI) and **Ce** Reaction time versus ROI intensity). Copyright 2019, Published by The Royal Society of Chemistry.[146]

Only several months later, Wei *et al.* demonstrated HCR-mediated miRNA imaging *in vivo* by combining HCR with magnetic resonance imaging (MRI).[147] "Honeycomb MnO_2 nanosponges" (hMN) carried the necessary DNA probes to cells and then dissolved into Mn^{2+} ions by glutathione. The HCR probes were coupled with DNAzymes that harness the dissolved Mn^{2+} ions for a magnetic resonance. The growing HCR strands produced an increased collection of Mn^{2+}, resultantly providing a stronger MRI signal. While MRI has notoriously suffered with weak sensitivity and poor contrast as a current live imaging medium, the Mn ions used here enhance the contrast on the localized tumor site, serving as an effective signal amplifier.

2.6.2. Human sample testing

Such recent advances in HCR and CHA-mediated detection have galvanized their ability to sense cfDNA in urine, serum, whole blood, lung fluid, and harvested tissue. These approaches do not use imaging methods but instead advantage from electrochemistry, ECL, optical signaling and even other techniques not previously described. These amplification methods have detected miRNA, ctDNA, tDNA, and enzymatic activity. Other works have reported the detection of these targets when they were artificially spiked in human samples,[127,148] *i.e.*, samples from a healthy donor, but these reports will not be detailed here. Here we highlight reports that used clinical samples from patients diagnosed with the disease of interest.

In one example, Zhao used the multiplexed photonic crystals[80,86] (Figures 2.8C and D) to detect miR133a, miR-143a, and miR-200b within the serum samples of bladder cancer patients.[149] Jirakova *et al.* (Table 5) used a multiplexed HCR electrochemical sensor[150] to screen miR-21, let-7a and miR-31 from cervical samples of HSIL alongside samples from healthy women; all healthy samples resulted in near negligible signal while let-7a, miR-21 led to significant signal difference ($p < 0.05$). Huang *et al.* (Table 7) developed an HCR-based electrochemical sensor where two dumbbell-shaped HCR probes self-assemble into nest-like superstructures that only attach to a gold electrode upon hybridization with target circulating tumor DNA (ctDNA).[151] While the LoD was only 3 pM, this work successfully detected ctDNA in serum and pleural effusion samples from breast cancer and hepatocellular carcinoma patients, respectively. This was also tested against samples from healthy patients, emphasizing the platform's powerful specificity. Their device maintained minimal to low signal in all 24 healthy samples while having heightened electrochemical signal in six of the 23 breast cancer serum samples and two of the 25 pleural effusion hepatocellular carcinoma patients. Urine samples were also screened for telomeric DNA by characterizing HCR-induced gold nanoparticle

aggregation networks *via* dynamic light scattering[152] for the diagnosis of bladder cancer. Their work showed a near 2-fold size increase of aggregates in bladder cancer urine, while the urine samples from healthy individuals, or individuals with liver, gastric, lung, or prostatic cancer maintained dimensions similar to the non-aggregated control sample.

While this compelling progress invites more exploration on HCR and CHA-based methods for clinical screening, we note that only three recent reports validate selectivity by testing samples from patients *versus* healthy controls (Table 7). Many other demonstrations validate selectivity only by replacing target strands with mismatched or scrambled sequences against the sensors in buffer. The most powerful assertion of specificity and therefore sensor efficacy would involve the analysis of other human samples where the target is predicted to be absent or significantly less abundant.

2.6.3. Theranostic demonstrations

HCR and CHA also have value for sensing-therapeutic dualities. Besides detection and imaging, some work in strand amplification has established the co-delivery of a drug or therapeutic biomolecule once the target is detected. The ability to intercalate drug molecules within DNA strands or decorate DNA structures with therapeutic strands such as siRNA for gene knockdown suggests that HCR and CHA have theranostic capacity.

For example, Ma *et al.* described pH-activated HCR[113] and included a delivery modality of antisense oligonucleotides. In their design, the antisense strand was complimentary to miR-21 and was installed at the end of an HCR hairpin (Figure 2.10). Exposure of this strand to the target miR-21 resulted in a gene silencing efficiency of up to 40%. Wang *et al.*'s worked on the tetrahedrally-scaffolded HCR for increased reaction rate with a drug release feature for photodynamic therapy. By intercalating methylene blue within the scaffold duplexes, the tetrahedrons could destroy over 70% of the cultured cancer cells upon 650 nm light irradiation

within three minutes. This work validated a viable “sense and treat” mechanism by demonstrating sustained FRET signaling of the mi-21 with maximum loading of methylene blue.

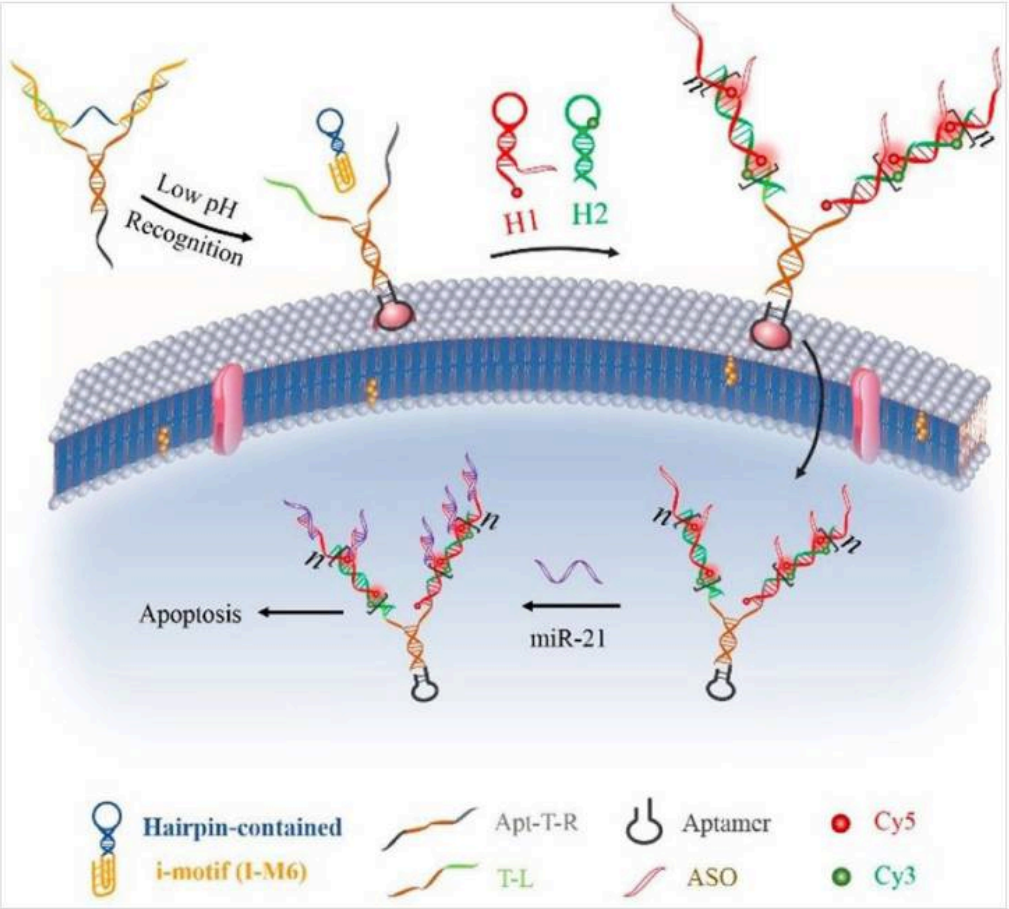

Figure 2. 10 pH activatable HCR and siRNA delivery dual-system.

The motif first approaches MCF-7 cell membranes with a cell-specific protein aptamer (black). The low pH from the cancerous microenvironment triggers the release of the disguise i-motif is released (yellow-blue), exposing the HCR hairpins on the system. HCR is activated by the T-L strand. An antisense oligonucleotide (pink ASO) is functionalized at the end of one of the HCR hairpins, thus capturing and silencing miR-21 activity. Reprinted (adapted) with permission from No. Copyright 2019 American Chemical Society[113]

While these reports demonstrate a novel new feature to strand-induced signal amplification, their work stopped at *in vitro* demonstrations. The above-mentioned *in*

vivo imaging strategies required multivalent HCR probes for cell targeting or stable delivery endeavors, and thus future theranostic work should investigate if the therapeutic feature might overload the system and dampen either the delivery, sensing, or drug release efficiency compared to those results found *in vitro*. Additionally, the continued monitoring of HCR sensing in tandem with drug release may more explicitly demonstrate the "sense and treat" duality because both reports depended on viability assays to verify therapeutic efficacy.

Table 1.7 Demonstrations on employing strand signal amplification with screening in clinical patient samples.

The more popular sample for screening is serum, but urine, tissue, and other samples are useful for HCR and CHA-based sensors.

Sample type	Number of specimens	Signal	Targets and condition	Specificity	Reference
Serum	10	PL intensity	miR-133a, miR-143, miR-200b (bladder cancer)	Tested against sequences with base mutations	148
Serum	10	potentiometric	Matrix-metalloproteinase-7 (MPP7) renal cancer, acute kidney injury	Single-base mismatch and other miRNA species	302
Pleural effusion, serum	25 (P.E), 23 (serum)	Electrochemical	ctDNA (circulating tumor DNA) (hepatocellular carcinoma, breast cancer)	Compared to mismatched DNA sequences, tested with 24 serum samples from healthy individuals	72
Urine	N/R	Dynamic light scattering	Telomerase substrate (TS) (bladder cancer)	Compared with miRNA-20b and urine samples from healthy individuals	151
Tissue (High grade squamous intraepithelial lesion HSIL)	3	Electrical current	miR-21, let-7a, miR-31 (cervical cancer)	Tested alongside 3 samples from healthy individuals	149
Whole blood	N/R	SAW resonant frequency	N/R	N/R	133

2.7 Future outlook

The past two years have demonstrated impressive progress in strand-mediated signal amplification: the field is currently tapping into *in vivo* imaging for the first time, and more work on analyte detection within clinical samples is being reported.

Nucleic acids have been consistently proposed as prognostic biomarkers just as much as diagnostic biomarkers, so future work invites HCR and CHA-related projects to include accurate

oversight of target abundance in (1) early or pre-disease states, (2) later disease progression such as during metastasis, and (3) disease abatement alongside ongoing treatment such as chemotherapy, radiation, or immunotherapy. This can validate HCR and CHA's ability to spatially correlate the presence of nucleic acid markers with disease progression.

3D DNA nanostructure probes have consistently improved imaging contrast, reaction time, delivery, complexity in multiplexity, stability in electrochemical sensing as well as intercalation of therapeutic agents for therapeutic duality. This pattern welcomes future research to investigate the use of these 3D DNA nanostructures under *in vivo* imaging applications; this is a particularly motivating avenue to explore as DNA nanotetrahedrons have characteristically increased cellular uptake due to their stable geometry.[27] To date, no 3D motifs have been implemented for *in vivo* HCR or CHA imaging, but this added dimensionality may complement the past report on targeting and sensing *in vivo* with controlled drug release.

Figure 2.11 shows that electrochemical sensing and ECL have demonstrated the lowest LoD along with the newly emerging bio-bar-coding method. Because these approaches are gaining promise as viable sensors of low-abundant analytes, future research may consider their design and manufacturing from a commercial and economic perspective. Inexpensive materials, coatings, and synthesis processes should be explored more seriously in future research involving these sensor technologies. Future work should also continue to develop the simplest detection approaches that require minimal auxiliary steps, such as washing away of unbound probes, further extraction or isolation of nucleic acids from clinical samples before screening.

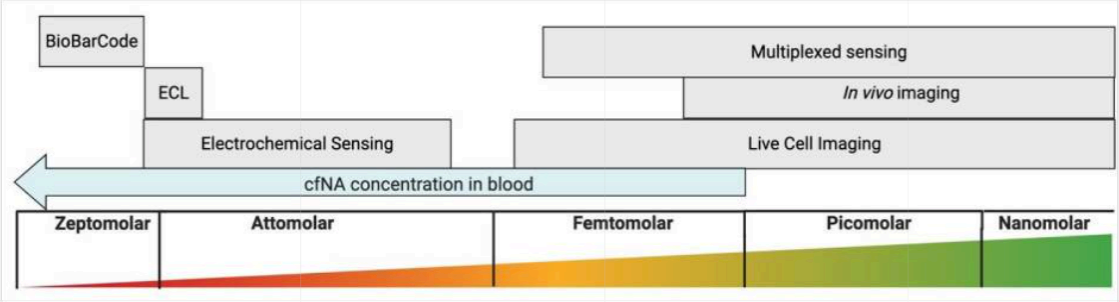

Figure 2. 11 Current status on nucleic acid detection limits and modalities using strand mediated signal amplification.

Electrochemical sensing and ECL remain the most sensitive modes in detection. Multiplexed sensing, though often also reported electrochemically, sacrifices LoD to higher order sensing of diversified targets. Works in imaging are still in the femto- to picomolar level, but they are pushing closer to the estimated abundance of circulation nucleic acid.

The microenvironment within different human samples should also be respected during the probe design process. Provided nucleic acid's susceptibility to unintended conformational changes from pH or electrolytic gradients or its binding abilities with a wide range of proteins,[153,154] Guanine-rich probes should be avoided, but nonetheless carefully investigated. For example, potassium-rich environments or other surrounding proteins may cause the spontaneous formation of G-quadruplex motifs, which can collapse amplification probes and obstruct hybridization growth.[155] Strategies to avoid inadvertent secondary structures should be carefully outlined in the context of clinical sample composition. For example, the salt content in urine may give a higher rise to these structural changes while heightened enzymatic activity and diversity in saliva may create a punishing environment for nucleic acid probes.

HCR has made significant contributions towards live cell imaging with a low LoD, good multiplexity, as well as theranostic and clinical translatability. Regardless, DNA signal amplifiers are generally comprised of a wide class of TMSD techniques that have also made novel contributions in this light. Enzyme-free DNA walkers, for example, have been engineered to have activated “walking” modalities upon target miRNA recognition; this resulted in

impressive and amplified FRET-based signaling.[156] While hairpin-free entropy driven catalysis (EDC) has also shown interesting sensor capabilities,[157] its reaction speed is slower than CHA and HCR,[158] requires more rigorous gel-based purification for stoichiometric accuracy,[159] has an LoD in the picomolar range for sensors,[160–162] and requires whole-blood spiking to achieve effective readouts of target miRNA.[163] While these sub amplification techniques are less robust than HCR and CHA, future research still encourages design optimization strategies that strengthen their translatability and versatility to imaging and detection modalities; diversifying approaches and capabilities within TMSD will widen the trajectory of strand amplification's impact on nucleic acid and molecular-scale diagnostic tools.

While discussed in detail in the live-cell imaging advances, it is noticeable that strand amplification can also detect other target molecules besides nucleic acid in other sensing platforms. For example, CHA was applied to exclusively sense exonuclease 1 for the start of the signal amplification within an electrochemical-based sensor.[164] CHA has also been utilized for the detection of biomarker proteins such as Mucin 1 *via* electrochemical signaling.[165] While further work is needed to integrate strand amplification electrochemical sensor methods with different target molecules and species, future research will likely involve a more specific comparison of strand amplification's ability to compete with other electrochemical sensors that are engineered to sense proteins, enzymes, and peptides.

Furthermore, imaging modalities beyond fluorescence should be considered in conjunction with HCR and CHA. While fluorescence imaging has provided unrivaled ability to image hybridization events with excellent resolution, it is not a practical imaging modality for *in vivo* applications. Ultrasound, PET, and CT-mediated imaging have already become highly standardized as clinical imaging approaches; coupling HCR and CHA methods with these

methods may make them even more applicable for clinical imaging of nucleic acids. While the clinically relevant modalities fall short of fluorescence in terms of resolution and tissue differentiation, they may nonetheless provide sufficient spatial information on the density and distribution of disease-correlated nucleic acid across different regions in the body.

2.8. Conclusions

The elegant self-assembly of amplified duplexed DNA without enzymatic or thermal intervention has revolutionized nucleic acid sensors. Recent milestones in the sub-disciplines of HCR and CHA for improved nucleic acid detection have advanced their candidacy for clinical translation. Over the last ten to fifteen years, both sub-techniques have made remarkable progress in improving imaging within live cells—ultimately leading to *in vivo* imaging—as well as in lowering LoD with accurate and even multiplexed sensitivity—now charting legitimate demonstrations in clinical sample screening. Though still young, these recent reports *in vivo* and with clinical samples demonstrate robust sensing abilities. Thus, there is a bright outlook for the integration of strand amplification with the current clinical echelon of nucleic acid detection. These advances underline the fundamental power behind molecular programming for trace detection of biological analytes.

2.9. Acknowledgements

Chapter 2, in full, is a reprint of the material as it appears in Biomaterials Science 2021. Borum, Raina M.; Jokerst, Jesse V., The dissertation author was the primary investigator and author of this paper.

CHAPTER 3. A PHOTOACOUSTIC CONTRAST AGENT FOR MIR-21 VIA NIR FLUORESCENT HYBRIDIZATION CHAIN REACTION

ABSTRACT: Nucleic acids are well-established biomarkers of cancer with immense value in diagnostics and basic research. However, strategies to monitor these species in tissue can be challenging due to the need for amplification of imaging signal from low analyte concentrations with high specificity. Photoacoustic (PA) imaging is gaining traction for molecular imaging of proteins, small biomolecules, and nucleic acids by coupling pulsed near-infrared (NIR) excitation with broadband acoustic detection. This work introduces a PA nucleic acid contrast agent that harnesses NIR fluorophore and quencher-tagged hybridization chain reaction (HCR) for signal amplification. This HCR probe was designed to enable contact quenching between NIR dye-quencher pairs by coercing their direct alignment when miR-21, a microRNA cancer biomarker, is detected. The probe demonstrated a ratiometric PA limit of detection of 148 pM miR-21, sequence specificity against one- and two-base mutations, and selectivity over other microRNAs. It was further tested in live human ovarian cancer (SKOV3) and noncancerous (HEK 293T) cells to exemplify *in situ* PA activation based on differences in endogenous miR-21 regulation ($p = 0.0002$). The probe was lastly tested in tissue mimicking phantoms to exemplify sustained contrast in centimeter-range depths and 85.3% photostability after 15 min of laser irradiation. The probe's miR-21-specific activation and its ability to maintain contrast in biologically relevant absorbing and scattering media support its consideration for live-cell PA microscopy and potential cancer diagnostics. Results from this probe also underscore the combined detection power between ratiometric PA signaling and strand amplification for more sensitive DNA-based PA sensors.

3.1 Introduction

Biomarkers are a large class of biomolecules that serve as crucial footprints from early to more developed stages of diseases. They therefore present a compelling opportunity to serve as analytes for early-stage screening to prevent advanced-stage cancer. While many protein biomarkers have been correlated to different stages in cancers, they often lack sufficient specificity, suffer from poor sensitivity to asymptomatic cases, or were reported with irreproducible results.[166,167] Nucleic acids, such as circulating DNA, micro RNA (miRNA), and mRNAs (mRNA), have eclipsed the efficacy of protein biomarkers because of their high specificity to a wide range of cancer species and consistent observations in many stages.[56,168] Signature nucleic acids responsible for core cellular events such as proliferation, differentiation, signaling, and apoptosis are shed during cancer cell death in even the earliest stages of tumor development.[56,169] Such indicative nucleic acids are thereafter found in serum and within many tissues. For this reason, nucleic acids can serve as both diagnostic and prognostic cancer biomarkers.[170]

MicroRNA species are among the most accessible and heavily investigated nucleic acid cancer biomarkers. miRNAs are characteristically short (~19–23 nucleotides)[171] and are therefore easy to sequence for corresponding detection probes. Moreover, miRNAs are stable in serum and other tissues despite their size,[172] so they can be detected *in vivo.* Some miRNAs show similar aberrant regulations across a vast range of cancers,[171,173,174] while other miRNAs are linked to specific cancers like leukemia,[175] lung cancers,[176] or gliomas.[177] Some miRNA species are identified as biomarkers, but some also serve as oncogenes and tumor suppressors.[173] miRNA species therefore hold critical value as indicators of cancer presence, progression, or even abatement from concurrent therapy.

A set of techniques have been established to detect miRNAs with impressive sensitivities. Current gold standards in nucleic acid detection, however, are reliant on *in vitro* sample testing. The most conventionally used platforms in this space are Northern blotting and quantitative reverse transcription polymerase chain reaction (qRT-PCR).[171] qRT-PCR is a reliable and increasingly available workhorse in nucleic acid detection, especially since the coronavirus (COVID-19) pandemic outbreak in late 2019.[178,179] While PCR can sense nucleic acid targets from human samples with excellent detection limits in a timely manner, it fundamentally lacks the ability to provide comprehensive information on the target's upregulation across different tissues from one reading. Northern blotting, like PCR, has this same limitation, and it is a time-consuming, labor-intensive, and costly process despite its ability to quantitatively detect the target. PCR and Northern blotting can be coupled with tumor biopsies, but tumor biopsies are often invasive to the patient and still lack complete surveillance on hidden malignancies.[180] Imaging modalities can offer a more diligent and streamlined profile on the distribution of miRNA markers because they can detect local upregulations in unexpected regions without the need to repeatedly probe the subject.[181,182] PCR and Northern blotting cannot be translated or re-engineered into contrast agents because they require a slew of multistep reactions, precursor primer strands, helper enzymes, and rigorous thermocycling for a single readout. In order to match the detection power of these techniques while further offering utility for contrast agents, novel miRNA detection probes should possess low nanomolar to attomolar limit of detections[171] (LoD) and operate without the need of amplifying enzymes, primer strands, or thermocycling.

Enzyme-free and isothermal nucleic acid-based sensing approaches have been designed to address this vision. These techniques primarily produce signal amplification so that a low

amount of the target leads to obvious signal.[183] These strand amplification approaches—which intensify reporter signals via cascaded hybridization between nucleic acid probe strands—are attractive because they are characteristically fast reactions (several minutes[95] to a couple hours [184]) that do not require precursor or helper entities (such as enzymes and primers) or thermocycling. Several robust nucleic acid hybridization strand amplification strategies have been invented such as catalytic hairpin assembly (CHA [82]) and hybridization chain reaction (HCR [81]). HCR is a heavily investigated amplification strategy because it allows one target nucleic acid to activate self-assembled growing DNA duplexes,[81] thereby creating a superstructure for measurable signal accumulation upon detection.

HCR-based probes achieved competitive detection limits and demonstrated ability to image localized nucleic acid targets in live mice.[146] Nonetheless, many of these reported imaging strategies lack translatability to live cells, *in vivo* imaging, and therefore clinical utility. For example, many fluorescence-based strand amplifying probes have been elegantly designed,[87,146] but they often require excitation wavelengths that are too low to penetrate tissue or cellular fixation for proper spatial imaging of expressed genes.

Photoacoustic imaging (PAI) is a rapidly expanding biomedical imaging modality that can demonstrably enable molecular contrast agents for ultrasound. [185] Incident pulsed NIR light irradiates the contrast agent, which in turn absorbs and translates the light to thermoelastic expansion that is detected through its acoustic footprint, thereby providing contrast in ultrasound imaging.[186] PAI's utilization of NIR light in the tissue transparency window with age-old ultrasound imaging present it as a nontoxic, revolutionary, yet clinically relevant technique.[187] Nevertheless, photoacoustic contrast agents for nucleic acid targets largely remain in their infancy. PAI has been reported with DNA-gold hybrids for miR-155 detection from

HCR-triggered nanoparticle aggregation,[188] but biofunctionalized gold can become unstable in many different biological environments, which can oftentimes result in false positives and even collaterally toxic aggregation. [189,190]

NIR fluorescent dyes are a fair nexus between small biomolecules and photoacoustic contrast agents. Their facile bioconjugation [191] allows them to be tethered to biomolecules such that fluorophores and fluorophore-quencher pairs can interact with each other (and thus modulate local thermal dissipation) via biomolecular events like pH change, binding affinities, and enzymatic cleavage.[187,192] DNA-NIR fluorophore and quencher strands have been designed to introduce nucleic acid as a dye-constituted PA contrast agent via nucleotide-based FRET and distance displacement.[193] Although a powerful discovery, this particular strategy remains largely unexplored and has not been paired with HCR.

There is strong work on strand amplification and NIR fluorophore based PAI for nucleic acid detection.[194] However, progress can still be made to expedite reaction time and maximize signal to background ratios at lower target concentrations. We hypothesized that a HCR-NIR fluorophore photoacoustic contrast agent can contribute to this progress because of its fast amplification nature that can occur within minutes[183,195] and bolstered ability to distinguish signal from background from the resultant superstructures.

This work introduces a nucleic acid "turn on" photoacoustic contrast agent that utilizes (1) heat dissipation from activated NIR fluorophore-quencher pairs between DNA strands,[193] and (2) HCR. The cascaded self-assembly of the synthetic DNA from HCR will allow NIR fluorophore and quencher molecules to align, enabling fluorescent quenching and heat dissipation upon NIR exposure, and thus "turn-on" PA signal (Figure 3.1). This mechanism provides accumulated photoacoustic signal upon recognition of miR-21—a well-known

microRNA species that has significant upregulation in over 80% of tumor samples. [171,196] This PA-HCR system established a ratiometric photoacoustic LoD of 148 pM miR-21 (8.80 × 10^9RNA copy number). This HCR-PA probe also demonstrated specificity to miR-21 down to 1 base pair mutation. Moreover, the contrast agent was incubated in SKOV3 and HEK 293T cell cultures and demonstrated *in situ* "turn-on" specificity to live cells that endogenously upregulate miR-21 within 1 h. The recognition of upregulated miR-21 in SKOV3 which was independently validated through qRT-PCR. The probe was finally tested in simulated tissue phantoms to evaluate imaging capability and quality at centimeter penetration depths.

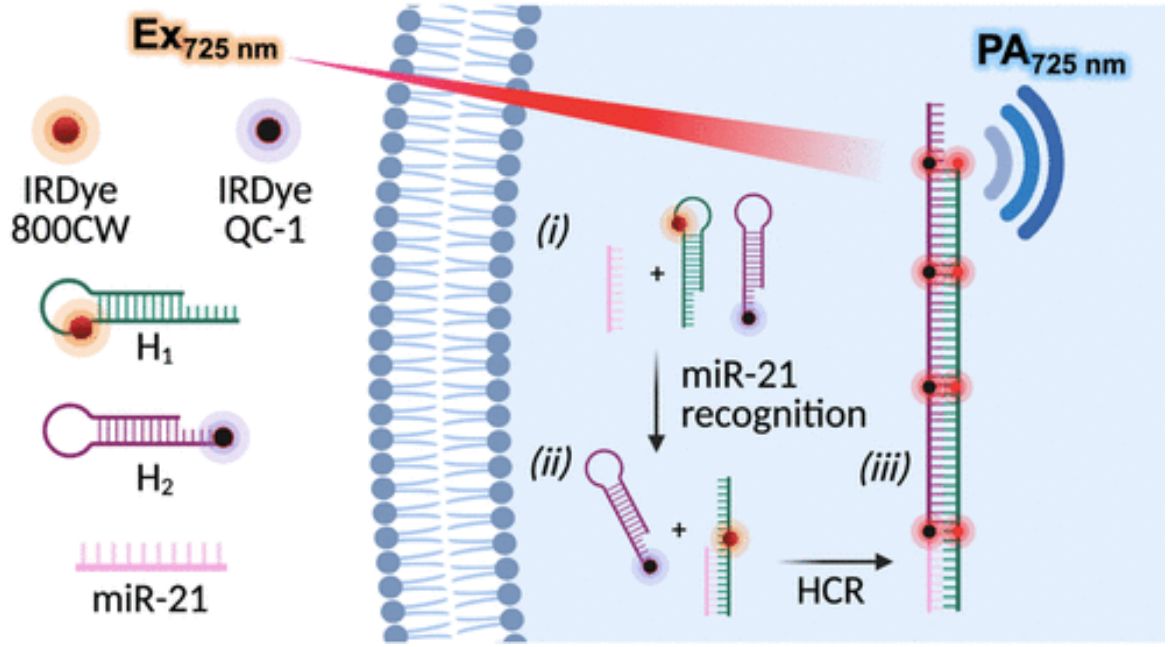

Figure 3. 1 Design for photoacoustic HCR.

Schematic on the hairpin design and resultant HCR by miR-21 target recognition, where hybridization between the hairpins coerces direct alignment between IR800CW and IRQC1 fluorescent dye-quencher pairs for contact quenching and photoacoustic signal.

3.2. Methods

3.2.1 Materials

All strands (hairpin contrast agent strands, miR-21, mutated strands, PCR primers) were designed and ordered from Integrated DNA Technologies (IDT). Tris Acetate EDTA (TAE) buffer was purchased from Alfa Aesar (J63677) and Ethidium Bromide (10 mg/mL) was from

Invitrogen (15585011). For qRT-PCR experiments, PrimeScipt RT Reagent Kit with gDNA Eraser (RR047A), and TB Green Premix Ex Taq (RR420A) were purchased from Takara Bio, and Zymo Quick-RNA miniprep kit (R1054). TransIT-LT is from Mirus Bio. HEK 293T cells were a gift from Prof. Liangfang Zhang's nanomedicine lab (UCSD NanoEngineering). Anatase TiO_2 (232033, Sigma-Aldrich) and India Ink (J61007, Alfa Aesar) were used for phantom experiments.

3.2.2. Preparation of HCR Hairpins

Stock hairpins were immediately resuspended in sterile, nuclease-free water in a 100 μM concentration. Concentration was validated via Nanodrop 2000. When not used, the stock was stored at −20 °C and carefully protected from light exposure. Hairpin samples were freshly prepared for every HCR experiment. In summary, 10 μM of each hairpin strand was heated to 95 °C for 5 min in 100 mM NaCl and allowed 2 h for a gradual cool-down to room temperature in the dark.

3.2.3. HCR Reaction

After the 2 h cooling period, the hairpins were mixed at equal concentrations. The miR-21 fuel strand and 1 and 2 base mismatch strands were subsequently added at different concentrations depending on the experiment. The reaction took place at 150 mM NaCl concentration in Milli-Q water at 37 °C in the dark, with samples completely sealed to avoid evaporation.

For miR-21 concentration and LoD experiments, copy number of RNA was found by multiplying the moles of the miR-21 with Avogrado's number.

3.2.4. Gel Electrophoresis

An agarose mobility shift assay was implemented by preparing 2% agarose gel in 1× TAE buffer in 4 μg/mL of ethidium bromide. Twenty microliter samples containing 30%

glycerol were loaded into each well. The gel was run at 130 V for 1 h and scanned using a BioRad ChemiDoc MP gel scanner and Image Lab 6.0 software. Both gels were run after hairpins were allowed 4 h to incubate with miR-21.

3.2.5. Absorbance and Fluorescence Measurements

HCR and hairpin mixtures were measured in a total volume of 100 μL in 96-well plates and read with a BioTek Synergy H1 plate reader. Absorbance spectra measurements were scanned between 500 and 900 nm with a step size of 2 nm. Fluorescence measurements for IR800CW used excitation at 730 nm with emission at 794 nm, with a step size of 2 nm.

3.2.6. PA Experiments

Photoacoustic images were acquired with a Vevo 2100 LAZR (VisualSonics, FujiFilm) using a 21-MHz transducer (LZ-250). Twenty μL of each sample was loaded into individual 0.86 mm polyethylene tubes. One tube was filled with reaction solvent (water in 150 mM NaCl or cell culture media) to serve as a blank. Samples were fixed in parallel within a 3D-printed holder described previously and placed 1 cm below the transducer in a vessel filled with water. Single-wavelength scans were operated at 725 nm at a frame rate of 5 Hz. To generate 3D images, the transducer was scanned with a stepper motor (step size = 0.054 mm) along the axial dimension of the tubes, and B-mode frames were registered via maximum intensity projection. Photoacoustic spectra were measured from 680 to 900 nm (2 nm step size).

For ratiometric characterization, the same samples were imaged both at 725 and 778 nm, and analysis was similarly performed in ImageJ as described above.

3.2.7. Cell Culture and Preparation

SKOV3 and HEK 293T cells were cultured in complete McCoy's 5A Modified Medium and Dulbecco's Modified Eagle Medium (both supplemented with 10% Fetal Bovine Serum, 1% Penicillin-Streptomycin), respectively, at 37 °C and 5% CO_2. Newly prepared cultures were

allowed at least three passages before experiments. Cells were passaged from 75 to 80% confluency using 0.25% Trypsin-EDTA.

3.2.8. Cell Experiments

SKOV3 and HEK 293T cells were seeded in 96-well plates (20 000 cells/well) overnight before experiments. The following day, old media was removed, and cells were rinsed in ice cold 1× PBS before fresh and warm medium was added to the cells. For transfection experiments, miR-21 was incubated with 8 μL of TransIT-LT in Opti-MEM for 30 min, before being added to the cell cultures for a total concentration of 100 nM transfected miR-21. The cells were given 4 h of incubation time, while some cell samples were not transfected as controls. After this incubation time, hairpins were mixed together at equimolar parts before being mixed with 8 μL of TransIT-LT in Opti-MEM for 30 min. This preparation was then added to all cell samples for a total hairpin concentration of 500 nM per cell sample. The samples were given 1 h incubation time before measured. Empty media served as a blank for plate reader measurements.

For photoacoustic cell experiments, media for HEK 293T was changed so that the cells were in DMEM without phenol red to reduce the photoacoustic background. After all cell samples were incubated with the TransIT-LT-transported hairpins for 1 h, cells were gently scraped, and both the cells and media were collected for PA measurements as described above.

3.2.9. qRT-PCR Experiments

First, 300 000 cells (SKOV3 and HEK 293T) were seeded into 6-well plates in triplicate overnight in complete medium. Thereafter, cells were detached and collected using cold 5 mM EDTA/PBS. Cell suspensions were then pelleted at 700*g* for 5 min at room temperature. After the supernatants were removed, the pellets were rinsed in cold sterile PBS to remove any excess salt. Total RNAs were extracted from cells using Zymo Quick-RNA miniprep kit according to manufacturer's protocol. RNA purity was validated with Thermo Scientific Nanodrop

2000/2000c at 260/280 and 260/230 ratios. GAPDH was regarded as the internal reference. The cDNA reverse transcription was performed using Takara PrimeScript RT reagent kit with gDNA Eraser, followed by qPCR using Takara TB Green Premix Ex Taq according to manufacturer's protocol. The qRT-PCR reactions were performed on BioRad CFX96 touch real-time PCR detection system. Relative miR-21 expression of cells was determined by the $2^{-\Delta\Delta C}{}_q$ method.

3.2.10. PA Phantom Experiments

1% agarose solution was doped with 0.8 mg/mL TiO2 and 0.005% India ink in a covered erlenmeyer flask. When the solution was brought to a slight boil, the media was allowed to mix with a magnetic stir bar for 15 min and slowly cooled to maintain a uniform distribution of the scattering and absorbing media throughout the gel. Next, the gel was casted on the phantom depth sample holder so that the gel completely covered the holder. Plastic tubing for sample loading was installed into the depth openings while the gel was casted.

After samples were loaded into the different depth leveled tubes, the phantom was immersed in water for subsequent PA experiments. PA imaging was thereafter executed similarly as described above. The gain was held constant for every scan. Fresh tubing was replaced inside the phantom after every sample was scanned.

For phantom image SBR analysis, images of the 2D cross sections were converted into 8-bit image types on ImageJ. Intensities between the ROI of the tube-loaded HCR sample from three ROI's of areas in the phantom immediately surrounding the sample were calculated as ratios.

3.2.11. Data and Statistical Analysis

Significance was calculated using the student's *t* test. For Lod experiments, PA and optical characterization were gathered from three independent experiments ($n = 3$). Ratiometric experiments were characterized from 4 replicates. For live cell optical characterization,

experiments were performed in 5 replicates (n = 5). For qrtPCR and all other PA experiments (specificity, PA characterization, PA in live cells, phantom experiments), experiments were done in triplicate (n = 3). Error bars represent standard deviation.

3.3. Results and Discussion

3.3.1. HCR Design

Two hairpin strands (H_1 and H_2) were designed so that their respective fluorophore and quencher molecules would become adjacent to each other once the hairpins form the catalyzed duplex. When H_1 encounters miR-21, the miR-21 strand will bind to the toehold region of H_1 and open H_1 from a metastable hairpin to a ssDNA conformation. The elongated H_1 will then expose a binding region for H_2 producing a duplex between them. The remaining, unbound region of H_2 contains a sequence identical to miR-21, and therefore, a new H_1 strand will bind to this region thus forming the ever-growing duplex (Figure 3.1). The placement of the fluorophore in H_1 and the quencher in H_2 had to be designed for direct alignment because H_1 and H_2 only partially bind to each other.[197] A triggered minimized distance between the fluorophore and quencher may maximize distinction between any background signal from local fluorophore-quencher concentrations and true positive signal from activated HCR. To accomplish this, fluorescent IRDye 800CW was embedded in the middle of H_1 (between 22 and 22 nucleotides) while quencher IRDye QC-1 is tagged at the 5′ end of H_2 (Figure 3.1.)

There are many NIR fluorophores commercially available such as cyanine-based dyes like Cy5.5 and Cy7.5; however, these cyanine-based dyes are often very hydrophobic. IRDye 800CW was chosen here because its sulfonated groups accommodate a more hydrophilic profile; it would thus have less nonspecific contact quenching with the hydrophobic interior of the DNA hairpin strands or the membranes of live cells (Figure 3.9). This dye was also chosen because its optical absorption is suitable for the blood optical window, and thus has more competitive

clinical candidacy. We additionally calculated the low relative fluorescence quantum yield of IRDye 800CW to be 6.4% and thus believed it would be an efficient PA contrast dye (Figure 3.10).

Agarose gel electrophoresis confirmed that miR-21 addition produced HCR structures from the hairpins at 37 °C in 150 mM salt (Figure 3.12). The gel also validated the stability of the hairpins when mixed together but without any miR-21 present (see the distinct single band (Figure 3.2a). When the target miR-21 strand is present, HCR catalyzes a broad distribution of larger DNA superstructures, thereby, i.e., a smear band.

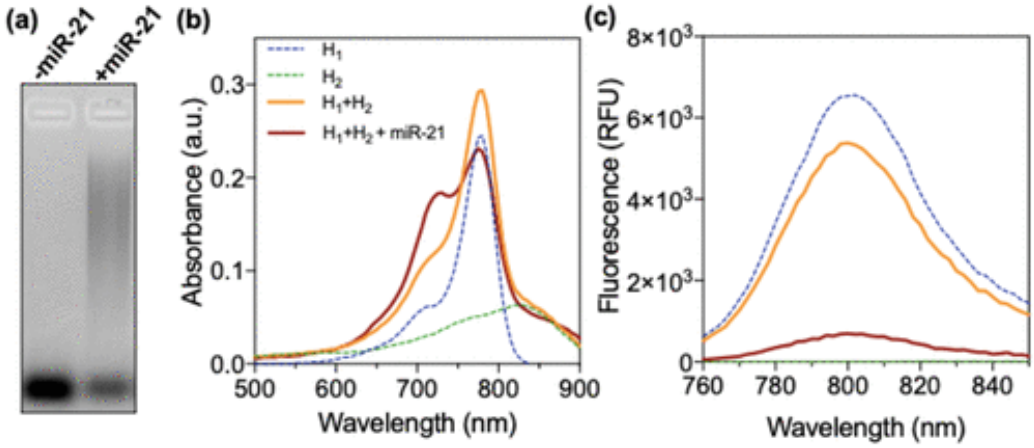

Figure 3. 2 Initial characterization on HCR.

(a) Agarose gel electrophoresis indicates that the hairpin mixture without miR-21 stably exists due to one distinct band and the hairpin mixture with present miR-21 results in the formation of a large distribution of DNA superstructures via the apparent smear. (b) Absorbance spectra of hairpins and hairpin mixtures with and without the target miR-21 present demonstrate a blue-shifted shoulder formation at 725 nm (c) Fluorescence spectra corresponding to the same reactions presented in panel (b) confirm that the HCR reaction from detected miR-21 results in fluorescent quenching.

Absorbance and fluorescence from the HCR product and hairpins were also observed. The negative control hairpin mixture had two characteristics: (1) it had an absorbance that was representative of additive absorbance spectra from the individual hairpins and (2) it maintained one distinct absorbance peak at 778 nm (Figure 3.2b). When miR-21 was mixed with the

hairpins, the resulting HCR formed the same spectral curve but with an additional blue-shifted shoulder peak at 725 nm: This is a unique feature in "contact quenching". [193,195] Contact quenching was further confirmed from 5-fold fluorescence quenching from the HCR product from the negative control hairpin mixture was observed (Figure 3.2c).

3.3.2. HCR Photoacoustic Initial Characterization

The photoacoustic (PA) signal was examined next. We compared the intensity from the 3 μM hairpin mixture with and without miR-21 with 725 nm excitation. We consider any PA signal from the hairpin mixture without present miR-21 as background. The addition of 100 nM miR-21 increased ($p < 0.0001$) the PA signal of the hairpins nearly 3-fold over PA background. PA intensity was also measured from individual hairpin types. H_1 had minimal signal, and H_2 had a PA signal that was comparable to the background PA ($p = 0.0653$). H_2 is therefore the primary contributor to background PA from the hairpin mixture since the hairpins (and thus dye and quencher molecules) are mixed at a 1:1 ratio (Figure 3.3a,b).

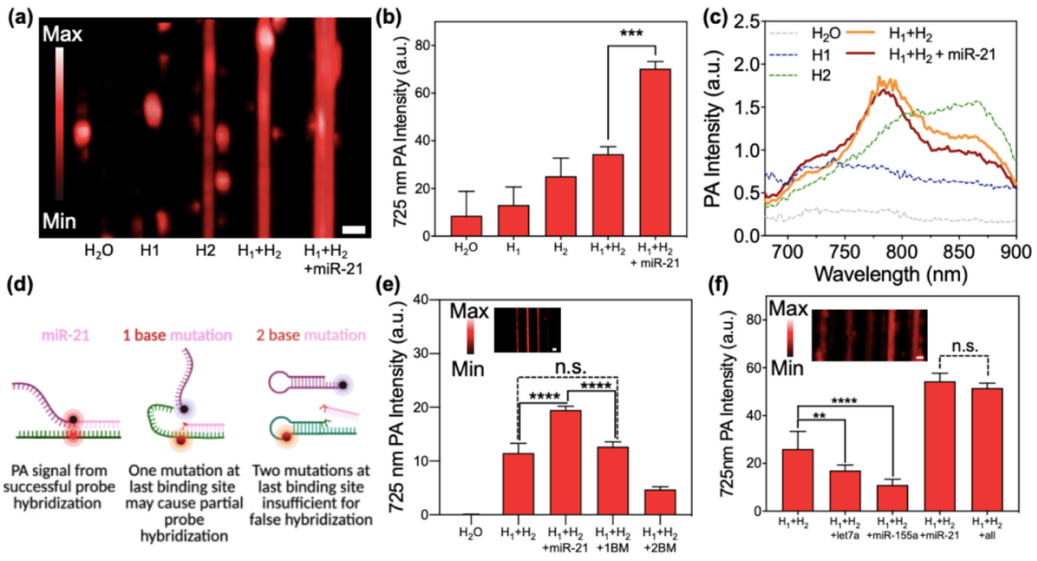

Figure 3. 3 Photoacoustically active HCR.

(a) Photoacoustic image of samples containing water, hairpin 1 (H_1), hairpin 2 (H_2), a mixture of the hairpins without miR-21, and a mixture with 100 nM miR-21 present (left to right) demonstrate the enhanced PA signal given off by the miR-21 triggered HCR. Random flecks of PA artifact signals are consequential from bubbles in the water bath that is containing the samples (see Materials and Methods for more details). (b) Quantitative analysis of PA intensity from the samples in panel a confirm significant PA enhancement (***$p < 0.0001$, $n = 3$) between HCR product and background hairpin mixture. (c) Corresponding photoacoustic spectra of samples in (a) and (b) confirm the unique 725 nm shoulder formation when the hairpins are incubated with miR-21. (d) Schematic of testing the hairpin recognition of miR-21 versus mutated strands at the far-most 3′ ends challenges sequence specificity of the probe. (e) Resultant specificity PA experiment demonstrates strongest PA signal from miR-21 HCR product, while 1 base and 2 base mutations (1BM and 2BM, respectively, as designed in panel d) are either less or comparable to PA provided from background hairpin mixture. Quantitative measurements of PA intensity confirms no significant PA enhancement ($p = 0.2338$) between background and one-base-mutated strand, while miR-21 triggered HCR sustained significant PA enhancement (****$p < 0.0001$, $n = 3$). (f) Specificity and selectivity of our miR-21 PA probe against other microRNAs, let-7a and miR-155, confirm that PA signal generation is specific to miR-21, and the hairpins can differentiate and detect miR-21 when other microRNAs of similar size are present, and that selectivity power is comparable to the true signal when hairpins are only incubated with miR-21 (n.s., $p = 0.0621$, $n = 3$), while the PA signal from hairpins incubated with other miRNAs showed a decrease in signal relative to hairpin mixture (**$p = 0.0051$, ***$p < 0.0001$, $n = 3$). All miRNAs were incubated with the hairpins at 100 nM (scale bar = 2 mm). Error bars represent standard deviations from 3 replicates, and PA scans were taken 4 h after strand incubation.

We next measured the photoacoustic spectra from 680 to 900 nm (Figure 3.3c). Spectral curves identified an increased PA signal from the HCR product at 725 nm over the background

hairpin mixture at the same wavelength. This increased PA at 725 nm could be a consequence of the heightened optical absorbance shoulder formation as was demonstrated in Figure 3.2b, as IR800CW-based photoacoustic spectra and optical absorbance behaviors are relatively similar to each other.[198] To completely corroborate that the activated PA is a product of contact quenching, we scanned the samples at 725 and 778 nm. These wavelengths were chosen because of the unique 725 nm shoulder formation from HCR products when their optical absorbance was examined. Indeed, maximized signal to background contrast was established when the samples were scanned at 725 nm (Figure 3.11a,b).

3.3.3. HCR Photoacoustic Specificity, Selectivity, and Sensitivity

The hairpins were incubated with one- and two-base-mutated strands to evaluate sequence-specificity. Our hairpins were designed such that the miR-21 target begins hybridization with H_1 from the 5′ to 3′ direction, so mismatch strands were designed such that the point mutations were located at the upmost 3′ ends to truly challenge miR-21 specificity: This location implies that much of the correctly sequenced regions of the strands could still initially bind with the toehold of H_1, causing it to partially open and potentially begin hybridization events with H_2 for a false positive (Figure 3.3d). Nonetheless, these mismatched strands were either comparable or less than the background PA signal. HCR catalyzed by the correctly sequenced miR-21 target (10 nM) produced a nearly 2-fold PA intensity enhancement from background. Meanwhile, one base mutation resulted in PA comparable to background (p = 0.2388) Surprisingly, however, the two base mutation strand had nearly 1/2 -fold PA signal as compared to background (Figure 3.3e).

The probe hairpins were incubated with other cancer-related miRNA markers, let-7a and miR-155. Similarly, these produced low PA signals either comparable to or lower than background when they were incubated with the hairpins. The hairpins were also incubated with a

mixture of let-7a, miR-155, and miR-21 together, and the PA enhancement from this case was comparable to the PA enhancement when the hairpins were incubated with miR-21 alone (p = 0.0621, n = 3) (Figure 3.3f). The decreased PA signal from background when the hairpins were incubated with 2-base mutation, miR-155, and let-7a ($p < 0.0001$, $p = 0.0051$, $p < 0.0001$, respectively) was unanticipated, but this is likely due to decreased self-affinity between the hairpins, thus decreasing any background PA from local concentrations between nonspecific IR800CW and IRCQ1 pairs.

The hairpins were then incubated with 1 pM to 100 nM miR-21. To examine the optical characteristics of HCR products based on target abundance, the absorbance behavior was observed for each miR-21 concentration. A 725/778 nm optical density ratio was evaluated to quantify the extent of the shoulder formation from HCR products. In particular, the 725/778 ratio from miR-21 (R_{HCR}) incubated reactions were compared to the 725/778 ratio from the hairpin mixture (R_{H1+H2}) (background) to clarify legitimate optical change between miR-21 absent and present samples. The 1 nM miR-21 incubated HCR repeatedly (n = 3) established a R_{HCR}/R_{H1+H2} ratio at around 1.25. Lower concentrations of miR-21 from 500 pM led to a ratio of 1.1 at most. However, higher concentrations of 50 and 100 nM miR-21 led to R_{HCR}/R_{H1+H2} ratios between 1.6 and over 2 (Figure 3.4b). Saturation at around a ratio of 2 occurs at higher concentrations (between 500 and 1000 nM) of miR-21.

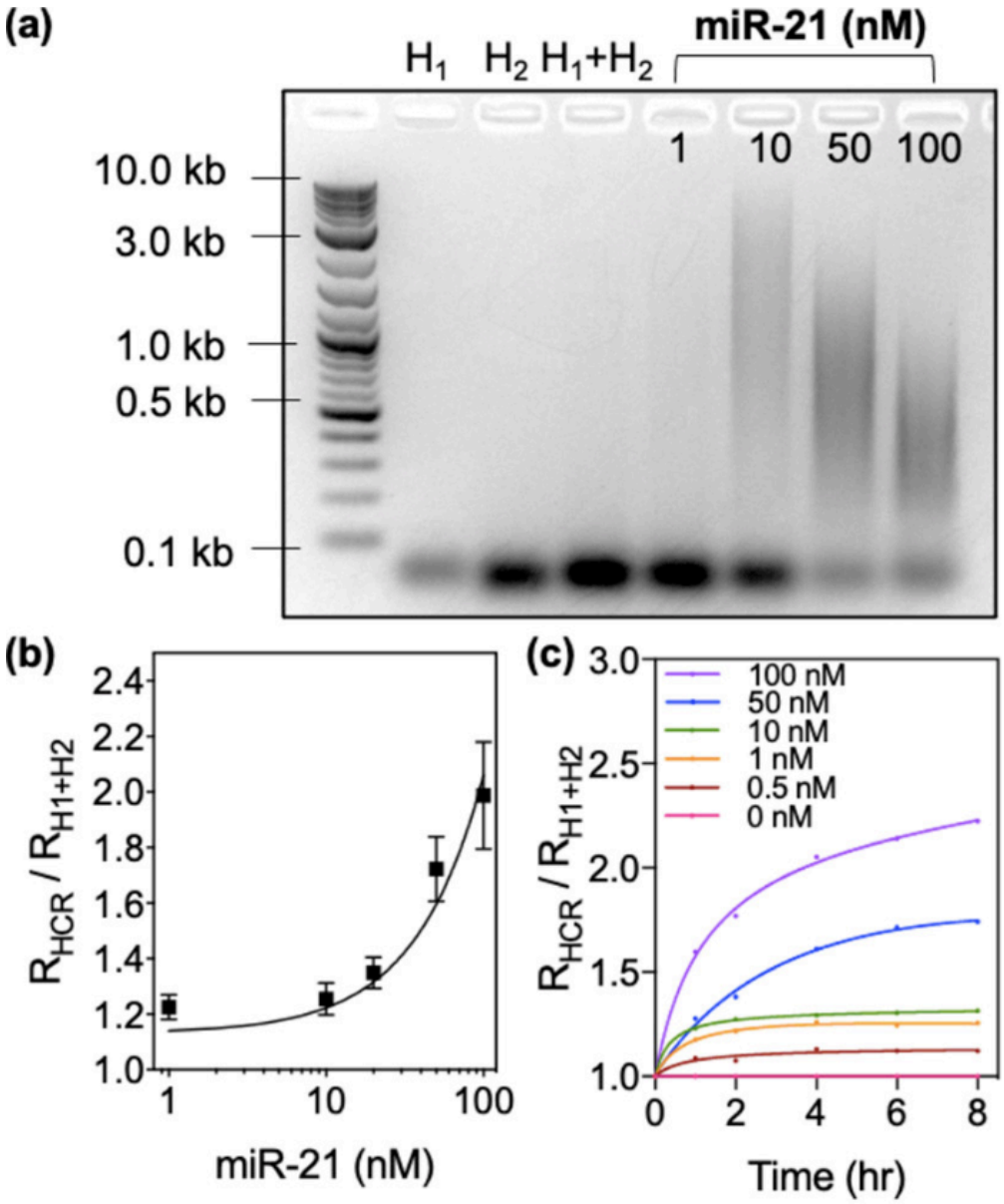

Figure 3. 4 HCR sensitivity.

(a) Agarose gel electrophoresis of different HCR products from miR-21 concentrations 4 h after incubation reveal that smaller concentrations of miR-21 lead to distributions of larger HCR duplex structures but with more leftover or unused hairpins. HCR products from the 1 nM miR-21 case most likely remained in the well during the gel run due to their larger sizes. (b) miR-21 concentration dependent 725/778 absorbance ratio taken between both miR-21 present and absent hairpin mixture samples (R_{HCR}/R_{H1+H2}) show 1 nM establishes a ratio near 1.25 that only increases with increasing miR-21 concentration. (n = 3); error bars represent standard deviation. (c) Kinetic absorbance measurements of the same ratio over time (0, 1, 2, 4, 6, 8 h) on varying miR-21 concentrations show saturation within the span of 4 h for lower miR-21 concentrations between 1 and 10 nM.

HCR is a powerful tool for nucleic acid detection because of its rapid kinetics that can occur within minutes.[95,195] Therefore, we measured the kinetics of signal activation as a function of miR-21 concentration. Kinetic measurements on change of 725/778 and the subsequent R_{HCR}/R_{H1+H2} ratio for each miR-21 concentration were collected over the span of 8 h. Interestingly, while all cases led to a change in absorbance ratios in as soon as 1 h, 1–10 nM miR-21 ranged samples achieved saturation within 4 h, while higher concentrations (50–100 nM miR-21) resulted in ratios that continued to grow (Figure 3.4c). We believe these kinetics remain in agreement with the observations we gathered via gel electrophoresis (Figure 3.4a): Lower concentrations of the fuel strand result in few but larger growing HCR products, while higher concentrations of the fuel strand will form many smaller, yet still growing HCR structures; thus, there is a slower time to achieve saturation from the larger miR-21 concentrations. All concentrations yielded noticeable 725 nm absorbance shoulders in as soon as 1 h, confirming that the rapid reaction of HCR maintains itself optically.

miR-21 in the picomolar regime did not produce distinguishable PA signal from background when scanned only with 725 nm (Figure 3.13c). However, 1 nM of miR-21 resulted in around 2-fold PA enhancement (Figure 3.5a, 3.13c,d). To elucidate the PA signal from HCR products based on target concentration, we evaluated the PA signal to background ratio (SBR) between varying concentrations of the miR-21 target by comparing their intensities. Consistently (n = 3), single nanomolar concentrations of the miR-21 led to an average PA SBR of 2, while higher concentrations produced SBR closer to 3, suggesting a point of PA signal saturation from the HCR products (Figure 3.5b). While sensitivity experiments were primarily implemented with 3 μM hairpin concentrations, the PA SBR held true when the hairpin concentrations were halved to 1.5 μM (Figure 3.13c,d). HCR products have a molecular weight with an inverse relationship

with target concentration.[81] The PA signal, however, maintains a direct relationship with target concentration. We believe this occurs from increased miR-21 concentration leading to increased probability of joining hairpins; thus, there is increased contact quenching and therefore enhanced PA signal.

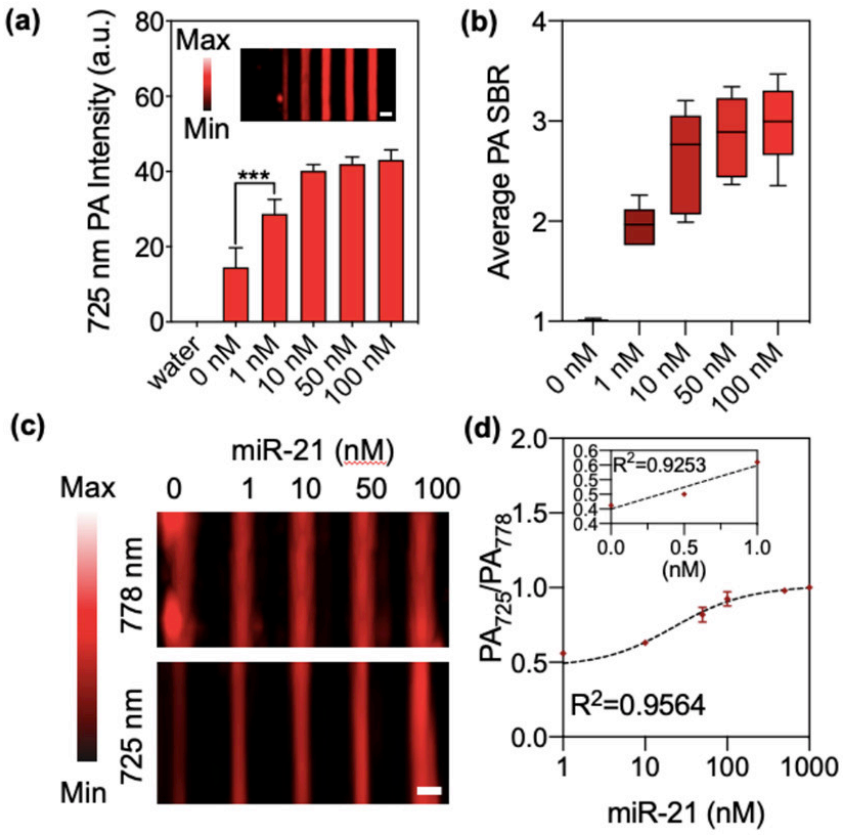

Figure 3. 5 PA sensitivity from single versus multiwavelength scanning.

(a) PA image and quantitative intensity analysis show at least 2-fold PA enhancement when 1 nM miR-21 is present under single 725 nm scanning (p = 0.0003, n = 3). (b) PA signal to background ratio (SBR) for different concentrations of miR-21 validate that a PA signal saturation occurs with higher concentrations of miR-21. (c) Image of multiwavelength scanning exemplifies constant 778 nm PA signal while 725 nm PA signal increases with increasing target miR-21, thus illustrating a form of ratiometric PA. (d) Quantitative characterization on the 725 nm/778 nm PA intensity ratio (n = 4) establishes picomolar ranged LoD. Error bars represent standard deviation. Panels a-b had 3 replicates, and panels c-d had 4 replicates; scale bar = 2 mm. All PA scans were taken 4 h after miR-21 incubation.

Photoacoustic imaging is notoriously plagued by high background from unactivated contrast agents, noisy artifacts, and signal distortion,[199] while PA probe sensitivity is limited by transducer efficiency, thermal noise (from medium, amplifier, or transducer), and incident laser fluence;[200] therefore, it is imperative to design contrast agents that maximize signal-to-background ratio. This HCR-PA probe establishes single nanomolar miR-21 visibility while maintaining a high PA SBR of 2 when scanned with a single wavelength of 725 nm; it consequently establishes a clinically relevant concentration while substantially satisfying Rayleigh criterion for human readability and crude scanning.[201]

Samples were further scanned under the hypothesis that PA spectra would reliably correlate to concentrations of present miR-21 in the reaction. Yet for this HCR system, we continuously observed that PA spectral measurements lack the same quantitative power on miR-21 concentration that optical absorbance spectral measurements possess (Figure 3.14). There are likely several reasons for the differences between optical and PA spectra. The first is related to the instruments themselves: Spectrophotometers are closed systems designed to count all transmitted photons using highly sensitive photodiodes (assuming no photons are backscattered). In contrast, our linear array PA scanner is designed for in vivo imaging—it is triggered by a tunable laser, and the transducers operate in ambient conditions. To collect PA spectra, we immobilize samples in capillary tubes under a transducer and collect B-mode images for that position as the laser scans from 680–970 nm. For any sample, we observe noisier PA spectra than optical spectra because (1) less volume is sampled from the cross section of a capillary tube than a full plate well and (2) the PA wave propagates in all directions and the linear array only collects a fraction of the total signal. Further, in this case, HCR products exist as a continuum of DNA superstructures across a wide range of sizes (Figure 3.4a). Therefore, it is likely that the

DNA superstructures are not distributed evenly by size within the capillary tubes. This would serve to further limit the precision of the measurement as different cross sections may contain different ratios of large DNA polymers, small aggregates, and unreacted hairpins. Thus, these differences can manifest as variations in the PA spectrum as they correspond to varying degrees of dye/quencher interaction. Indeed, while the PA spectra shows a trend similar to optical absorbance spectra (i.e., miR-21-detected hairpins yield an increased 725/778 nm as compared to miR-21 negative hairpins), the nature of the scan cannot cover all HCR products from the sample in one measurement (Figure 3.14). Regardless, PA spectra on this HCR-based contrast agent contains qualitative information that is able to differentiate which samples generate higher PA intensities than others. Therefore, while the intensities of the PA spectra are not ideally suited for quantitation, they can be used to observe spectral shifts that are expected based on absorbance spectra.

Nonetheless, PA 3D image scans produce averaged PA intensities on the entire sample at once, so it stood to reason that there would still be noticeable PA intensity differences when hairpins and HCR products were irradiated with a 725 nm- versus a 778 nm-pulsed laser. We noticed that while there was definite increase in 725 nm PA intensity as miR-21 concentration increased, there was no real correlation or change in 778 nm PA intensity under the same conditions (Figure 3.5c). However, any fluctuations in 778 nm PA intensity maintained consistent (n = 4) 725/778 nm PA intensity ratios upon miR-21 concentration: The intensity ratio increased from 0.4 to 1.0 with increasing miR-21 concentrations from 0 to 1 μM (Figure 3.5d). This behavior suggests that the HCR reaction possesses a form of ratiometric PA information that can quantify miR-21 concentration. Ratiometric features to activatable PA contrast agents have high value because of their enhanced sensitivity and lower detection limits.[192] When this

ratiometric component was explored with the HCR probe, the LoD was confirmed to be 148 pM using the method by Armbruster et al. [202] We therefore conclude that while 1 nM miR-21 detection is the lowest single-wavelength concentration where a change in PA signal has a sufficiently high SBR[201] for quick measurements, the ratiometric method accommodates quantitative sensitivity with picomolar LoD for more sensitive measurements. Additionally, microRNA markers in blood and plasma have reported concentrations in the picomolar range,[203] so this probe satisfies clinically relevant sensitivity.

Some established LoDs in other pure DNA-dye based photoacoustic probes are within the range of hundreds of nanomolar to micromolar,[204,205] but they do not utilize strand amplification techniques. Moreover, a report on a DNA HCR-based photoacoustic probe that did not possess ratiometric scanning reported a higher picomolar LoD than this work, validating the advantage of photoacoustic DNA probes that have combined ratiometric and strand-amplifying PA signaling. Another report on strand amplification-based ratiometric PAI reported an LoD in the tens of picomolar range, but their reaction required 6 h for a complete readout. [194] A possible reason for their approach's heightened sensitivity over the HCR approach is the fact that their ratiometric mechanism enables PA intensities at both wavelengths to change instead of just one for a wider dynamic range. Another reason is that there is simply more efficient signal generation based on the amplifying mechanism. However, the HCR-based mechanism introduced here possesses faster signal acquisition time, requiring a maximum of 4 h for a complete readout but only one for detection. A commonality that differentiates the detection capacity of these probes from other DNA-based probes is that they possess both (1) strand-based signal amplification and (2) ratiometric, multiwavelength PAI. Of course, while the majority DNA based PA probes rely on molecular dye-quencher interactions between IRDye 800CW and IRDye QC1,[194,204] others

utilize gold nanospheres[188] or newly formulated molecular dyes instead;[205] the difference in absorbing species can also therefore have a influence on PA signal efficiency. Moreover, the choice in instrumentation, laser, and other imaging parameters (gain, frame rate) also plays a fundamental role in the imaging quality.

3.3.4. HCR Optical Activation in Live Cells

We next used live SKOV3 (human ovarian adenocarcinoma) and HEK 293T (human embryonic kidney) cell lines to assess the activity of these PA-hairpins with endogenously produced miR-21. SKOV3 is known to upregulate miR-21 (as independently validated by qRT-PCR in Figure 3.17a,b);[206] therefore, we hypothesized it would be a suitable model cell line to activate our hairpins to HCR. We selected HEK 293T as a model cell line for two reasons: (1) the cell line does not natively upregulate miR-21[207] and could therefore serve as a negative control, and (2) the cell line is a popular host cell for genetic engineering via transfection. We therefore hypothesized that while HEK 293T alone cannot turn on HCR, it has the capacity to do so if artificially transfected with miR-21 RNA strands.

We added the hairpins to cell cultures via a commercially available transfection polymeric carrier (TransIT-LT) and monitored the subsequent optical behavior. We first observed that our hairpins were not toxic to the cells at the concentration they were administered (Figure 3.16). To measure changes in absorbance and contact quenching, we again compared the 725 nm/778 nm ratio between all our samples against hairpin mixtures in media and additionally monitored fluorescence. When we added our hairpins to SKOV3, we noticed fluorescence quenching, blue-shifted shoulder formation, and an increased 725/778 ratio within 1 h (Figures 3.6a,b and 3.15a,c). When we compared the hairpins in SKOV3 to the hairpin mixture in cell media, we observed a significant increase ($p < 0.0002$) in the 725/778 ratio and a decrease in fluorescence (Figure 3.6a,b). We wondered if further transfecting the SKOV3 cell line with miR-

21 would intensify contact quenching. However, there was no significant difference (p = 0.2074, n = 5) in 725/778 ratio between native and transfected SKOV3 when incubated with the hairpins, suggesting possible probe saturation with miR-21 in the SKOV3 cell line (Figure 3.6a).

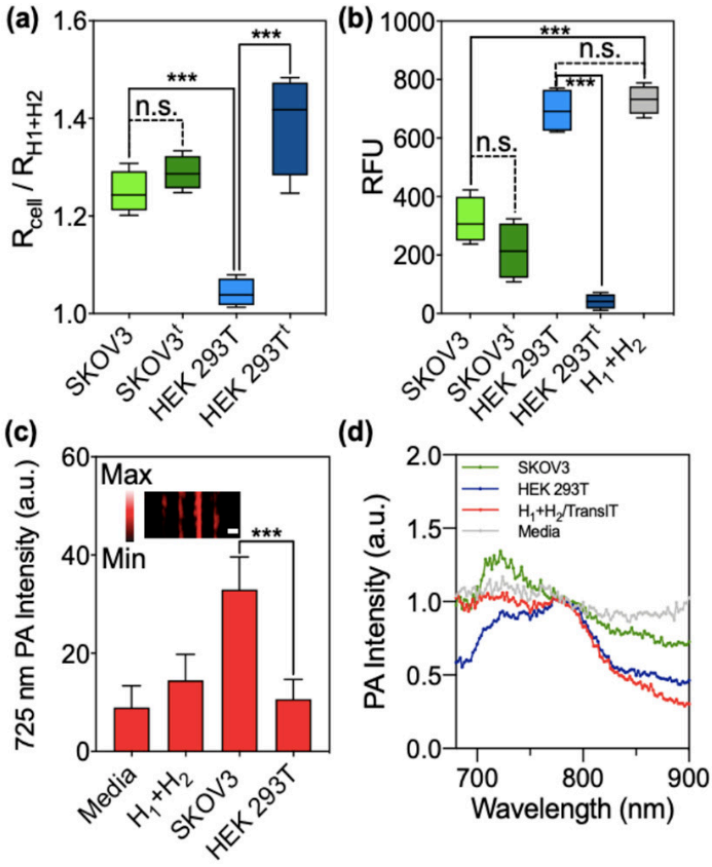

Figure 3. 6 Live cell activated HCR.

(a) The 725 nm shoulder formation emerges significantly with SKOV3 cells as compared with hairpin mixture in media, given the 725/778 ratio taken between both cases (R_{cell}/R_{H1+H2}), and further transfection of miR-21 into SKOV3 did not significantly influence shoulder formation (p = 0.2074). On the other hand, the ratio for HEK 293T does not increase from the hairpin mixture until miR-21 transfection. (p = 0.0006). (b) Fluorescence intensity from each sample further confirmed native SKOV3, transfected SKOV3, and transfected HEK293T results in quenching between the hairpins while the hairpin mixture in media and in native HEK 293T remains at around 800 RFU. Error bars for panels a-b represent standard deviation from 5 replicates. (c) Quantitative PA measurements from the hairpin-incubated cell samples shows significant enhancement from SKOV3 cells as compared with background in media and HEK 293T (p = 0.0002) with corresponding PA image taken after 1 h. (d) Corresponding normalized PA spectra of samples demonstrates an intensified signal at 725 nm for hairpins incubated in SKOV3 cells versus HEK 293T cells. Error bars represent standard deviation from 3 replicates. Scale bar = 2 mm

We implemented similar experiments with HEK293T. When we compared optical results from our hairpins added to HEK293T to hairpins mixed in complete HEK293T media, we noticed no significant enhanced 725/778 ratio between HEK293T and the hairpin mixture (Figures 3.6a, 3.15c). However, when we transfected HEK 293T with miR-21 before adding our hairpins, a heightened increase in 725/778 absorbance ratio and near complete fluorescent quenching occurred (Figure 3.6a,b). These results support that these hairpins are activated *in situ* only when the miR-21 target is present, and otherwise, they remain in a closed hairpin state with minimal background contact quenching.

The PA response of SKOV3 and HEK 293T cells incubated with hairpins was then examined. The cells (20 000/sample) were incubated with equal concentrations of the hairpins, then scraped and collected for PAI. This was chosen as the most reliable method of PA characterization of the cells because the PA could otherwise reflect off the plastic from a flask, plate, or dish should the cells have remained adherent. The PA characterization validated that (1) the hairpins in the TransIT transfection carrier had negligible background (Figure 3.6c) and (2) that hairpins incubated in HEK 293T exhibited PA signals comparable to background ($p = 0.2395$); however, those incubated in SKOV3 cells produced 2-fold PA enhancement ($p = 0.0002$) and a striking 725 nm PA intensity peak in normalized spectral characterization, PA from HEK 293T was lower than the hairpin mixture, and spectra from the hairpin mixture in media was comparable to empty media (Figure 3.6c,d). These results demonstrate the HCR-PA probe's ability to selectively activate in miR-21 upregulated live cell lines, where both contact quenching and PA signal were validated. Unlike many nucleic acid imaging probes, cellular fixation was not required and the excitation wavelengths (>700 nm) are highly suitable for tissue penetration.

These results suggest the potential for live cell imaging via photoacoustic microscopy (PAM). [208] Optical resolution photoacoustic microscopy (OR-PAM), for example, has achieved single-micron optical resolution, enabling it to be a novel candidate for single cell photoacoustic imaging. If such HCR-PA probes were utilized for live-cell OR-PAM, OR-PAM could provide spatial information on the upregulated miR-21 within and throughout the cancer cell based on localized PA signals in the cell from HCR products.

3.3.5. PA Imaging in Tissue Phantoms

We finally assessed the contrast quality of our probes by testing them in tissue mimicking phantoms. We therefore designed a phantom that simulates biologically relevant light and sound transport over a wide wavelength gamut: India ink (0.005%) and anhydrous TiO2 particles (0.8 mg/mL) were doped into 1% agarose gel to replicate absorption and scattering conditions, respectively.[209,210] The respective optical absorption and optical reduced scattering coefficients under these conditions are 0.2 and 11 cm^{-1}. The general coefficient values for many soft tissues are around 0.1 and 10 cm^{-1} at 800 nm, [209] so the composition of our phantoms possessed sufficient biological relevance. The gel phantom was cast over a 3D-printed polylactic sample holder with sample-loading openings at increasing depth. The sample loading inserts were equally distanced at 2.0 mm depth spacing and 0.8 mm lateral spacing[211] (Figure 3.18). This setup therefore simulates realistic biological absorption and scattering behaviors while allowing us to controllably explore penetration depth limitations associated with the PA probe (Figure 3.7k).

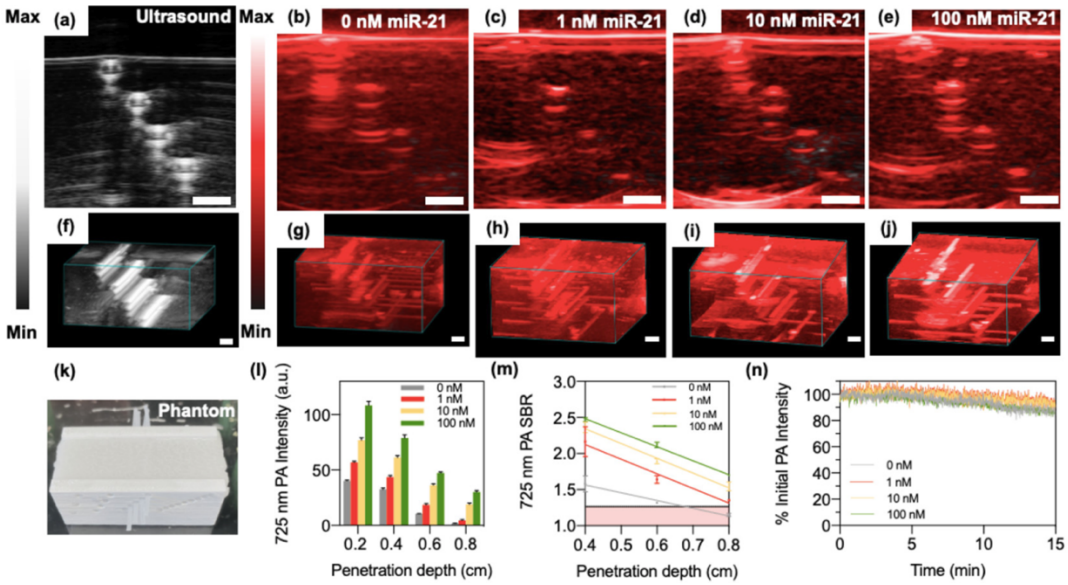

Figure 3. 7 Single wavelength scanning of PA-HCR probe in Tissue Simulating Phantoms.

(a) B-Mode 2D ultrasound image of the sample tube vessels fixed in the tissue simulating phantom, separated by 0.2 cm lateral depths from the surface. (b–e) Respective combined photoacoustic and ultrasound 2D images of the hairpins incubated with 0 1, 10, and 100 nM miR-21 show increasing 725 nm PA intensity with increasing miR-21 concentration that can be distinguishable above background PA signal from the phantom. (f) 3D ultrasound image of the same experimental setup for phantom imaging (g–j) Respective 3D PA images similarly illustrate increased 725 nm PA enhancement with increasing miR-21 throughout the sample holding tubes. (k) Photograph of the tissue simulating phantom where tubes are casted in gel composed of scattering and absorbing media. (l) Quantitative 725 nm PA intensity analysis with respect to miR-21 concentration and penetration depth verifies miR-21 specific PA enhancement throughout all depth levels. (m) SBR at different penetration depths for each concentration of miR-21 analyzed using simple linear regression. The resultant slopes were used to approximate the farthest penetration depth achievable for each miR-21 concentrations for sufficient imaging quality using a single wavelength 725 nm scan. The cutoff SBR value is 1.246, as depicted in the red shaded region. R^2 values for 0, 1, 10, and 100 nM miR21 activated PA are 0.92, 0.91, 0.98, and 0.97 respectively (n) photostability of the hairpins after irradiation to 725 nm pulsed laser for 15 min show that at the shallowest depth (0.2 cm), the hairpins lost less than 15% of initial PA intensity. Images and PA scanning were taken 4 h after incubation with miR-21.

We first noticed that the hairpin mixture (with 0 nM miR-21) emitted nonspecific PA signal as seen previously, but the PA signal from the hairpins encounters significant interference from the background PA throughout the phantom at around 0.8 cm depth (Figure 3.7b). However, an increased presence of miR-21 in as low as 1 nM led to at least 2.2-fold increased PA intensity and a minimum of 1.3-fold heightened PA SBR (Figures 7b–e, g–j, l, m). The

average SBR for each miR-21 containing sample decreased from over 2 to 1.5 with increasing depths. The shallowest depth (**0.2 cm**) had a lower SBR in the phantom versus in buffer because of the high reflection of PA signal between the transducer and the surface of the phantom (Figure 3.7b–e, 3.19).

The Rayleigh criterion suggests SBR > 1.264 for contrast agent imaging quality.[201] This is satisfied at miR-21 concentrations of 1 nM, 10 nM, and 100 nM at depths of 0.82, 0.93, and 1.3 cm, respectively, using 5 μM hairpins (Figure 3.7m, 3.19). This suggests that single-wavelength PA probe scanning at the 725 nm contact quenching event can image miR-21 through up to one centimeter of tissue with sufficient readability, overgoing the usual single-millimeter penetration depth limits associated with purely fluorescent bioimaging probes. [212,213] The photostability of the miR-21 HCR probe was examined next. Hairpins mixed with 0, 1, 10, and 100 nM were exposed to a pulsed 725 nm laser for 15 min at each penetration depth (0.2, 0.4, 0.6, and 0.8 cm). As expected, hairpins and activated HCR products were most photosensitive at the shallowest depth (0.2 cm) because they received the most fluence. Deeper samples (0.8 cm) maintained 100% of the original signal intensity for the entire 15 min (data not shown)). At 0.2 cm, the hairpin PA signal intensity reduced by 14.75% (Figure 3.7n), which is much less than many other dye-based PA contrast agents such as cyanine dyes. [214,215] There was also no real correlation between increased or weakened photostability versus miR-21 concentration. This suggests the HCR probe has robust photostability and can be scanned multiple times.

Multiwavelength PA scans can compensate for tissue homogeneity, and we hypothesized that better sensitivity or imaging depths could be achieved with ratiometric imaging. To test this hypothesis, samples were loaded and subsequently imaged at 0.6, 0.8, and 1.0 cm depths from

the phantom surface (Figure 3.8a). The PA intensity difference between 725 and 778 nm (contact quenching vs IRDye 800CW peak wavelengths) scans decreased with increasing miR-21 (Figure 3.8b–k).

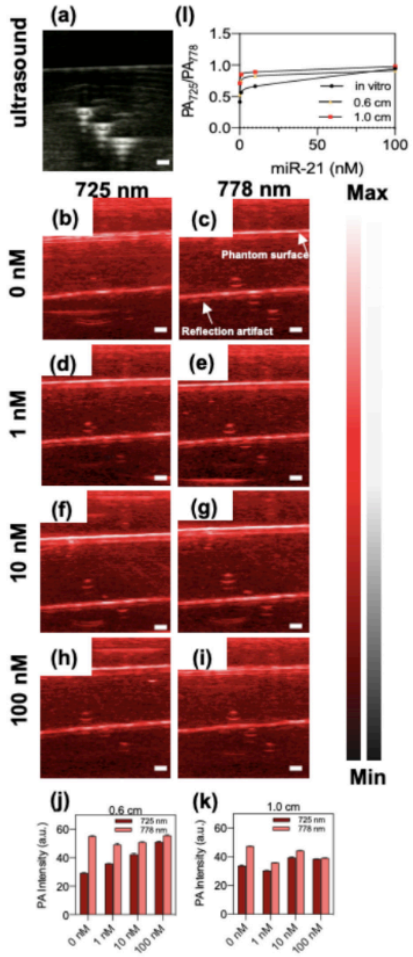

Figure 3. 8 Ratiometric characterization in tissue phantom experiments.

(a) B-Mode Ultrasound image of the sample tubes relative to the surface are 0.6, 0.8, and 1.0 cm deep. Panels b,d,f,h show increasing 725 nm PA intensity with increasing miR-21 concentration, while panels c,e,g,i show relatively constant 778 nm PA signal regardless of miR-21 concentration, therefore demonstrating sustained PA ratiometric potential despite background PA from the phantom. (j, k) Quantified PA intensities show increasing 725/778 ratios with higher miR-21 concentrations in a phantom depth of 0.6 and 1.0 cm, respectively. (l) Comparison of ratiometric characterization from in vitro experiments with respect to samples scanned at 0.6 and 1.0 cm depths. Error bars are from standard deviations from three replicates. PA scanning took place 4 h after miR-21 incubation. Scale bar = 2 mm.

We then compared the ratiometric analysis from this phantom experiment to our original ratiometric results reported in Figure 3.5c,d: Background PA does not sufficiently interfere with a trend between increasing 725 nm/778 nm ratios with increasing miR-21 (Figure 3.8l). The 0.6 and 1.0 cm depths were characterized because reflection artifacts─most likely from the transducer surface from the surface of the phantom and the water it was immersed in─interfered with the PA signal at 0.8 cm. While we previously showed that the 725 nm signal starts to meld with the background PA from the phantom with larger penetration depths (Figure 3.7), The 778 nm signal maintains a pronounced PA signal with a SBR of at least 2 as deep as 1.0 cm (Figure 3.8), thus accommodating deeper penetration depths over the single 725 nm wavelength scanning.

While biomolecularly self-assembled imaging probes have shown novel and promising *in vivo* viability,[216] a major challenge to this work is to couple the HCR probes with a biocompatible and stealthy *in vivo* carrier that does not increase any background PA signal. Carriers for the hairpins with biologically inert or even cancer-targeting capabilities hold significant value because their efficient delivery may allow more careful analysis of any "turn-on" versus background PA and potentially faster detection readout times *in vivo.* Plant virus nanoparticles,[217] for example, are protein-based carriers with excellent drug delivery capacity *in vivo*. Furthermore, plant virus nanoparticles are not constituted by any lipid bilayer that could potentially cause contact quenching and therefore background PA. Other commonly used carriers such as PLGA particles should also be considered.

3.4. Conclusions

Hybridization chain reaction was harmonized with activatable photoacoustic imaging for the amplified PA detection of miR-21 in live cells. This contrast agent established a miR-21 limit of detection at 148 pM using ratiometric PA scanning at 725 and 778 nm laser wavelengths. The

findings in this proof-of-concept present groundwork for engineering robust PA-nucleic acid probes for sensing native nucleic acids as a clinically relevant imaging modality. Future studies along this line should address other features that can bolster the viability of HCR- PA contrast agents, such as but not limited to (1) carriers with cell-targeting capabilities that minimize background PA, (2) exploratory hairpin fluorophore designs and mechanisms that continue to minimize PA background, (3) heightened nuclease resistance, (4) increased economic availability in NIR fluorophore-strand conjugates, and (5) multiplexed nucleic acid probes that operate at different PA wavelengths. Besides these considerations, *in vivo* studies can also advance the candidacy of these nucleic acid constituted contrast agents. Finally, a novel avenue in this work would be to harmonize PA-HCR with loaded anticancer drugs that are released upon miRNA recognition. Provided HCR's structural capacity to coload drugs for therapy,[218] PA-HCR with a therapeutic payload may offer an innovative anticancer theranostic platform. However, the photoacoustic modality of this probe welcomes coupling PA detection of localized miR-21 targets with subsequent ultrasound-based therapeutics, such as anticancer sonomechanical therapy.[219] This paper is one of many that continues to demonstrate the biomedical value behind hybridization chain reaction.

3.5. Acknowledgements

Chapter 3, in full, is a reprint of the material as it appears in Bioconjugate Chemistry 2022. Borum, Raina M.; Moore, Colman; Chan, Soo Khim; Steinmetz, Nicole F.; Jokerst, Jesse V., The dissertation author was the primary investigator and author of this paper.

3.6. Supporting figures

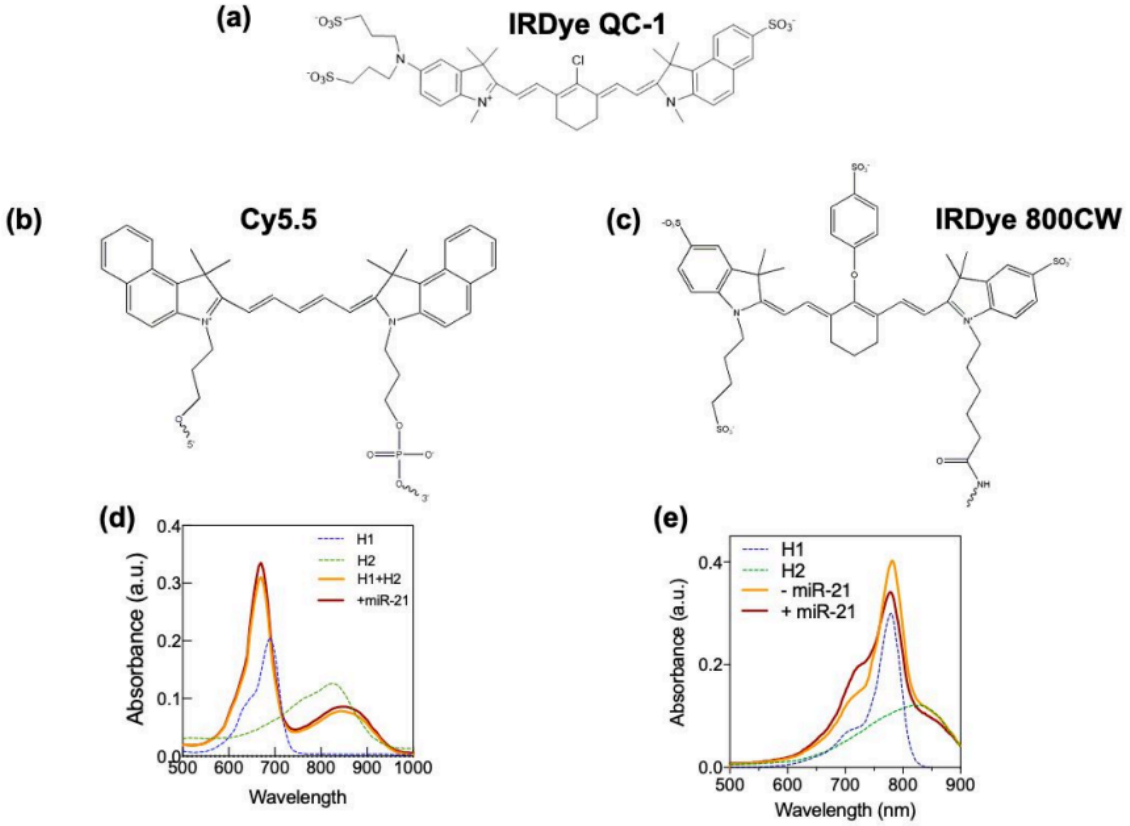

Figure 3. 9 Selecting an NIR fluorophore dye for a viable PA nucleic acid HCR contrast agent.

(a) structure of IRDye QC-1 quencher, **(b)** structure of Cy5.5 dye, and **(c)** structure of IRDye 800CW. **(d)** When tagging the H_1 strand with Cy5.5 and H_2 with IR Dye QC1, the hairpin mixture and HCR reaction show identical contact quenching behavior; thus Cy5.5 was too hydrophobic to produce signal from HCR above the background hairpin mixture. **(e)** There is true contact quenching from miR-21-activated HCR when H_1 is instead labeled with IR Dye 800CW; there is no contact quenching for the negative control hairpin mixture demonstrating IRDye 800CW's potential to serve as an activatable PA contrast agent for miR-21. IRDye800CW-NHS ester is conjugated to a primary amine group within the DNA strand.The IRDye QC-1 is similarly conjugated to the 5' end of the other hairpin from NHS-ester mediated conjugation to the primary amine group of the DNA strand.

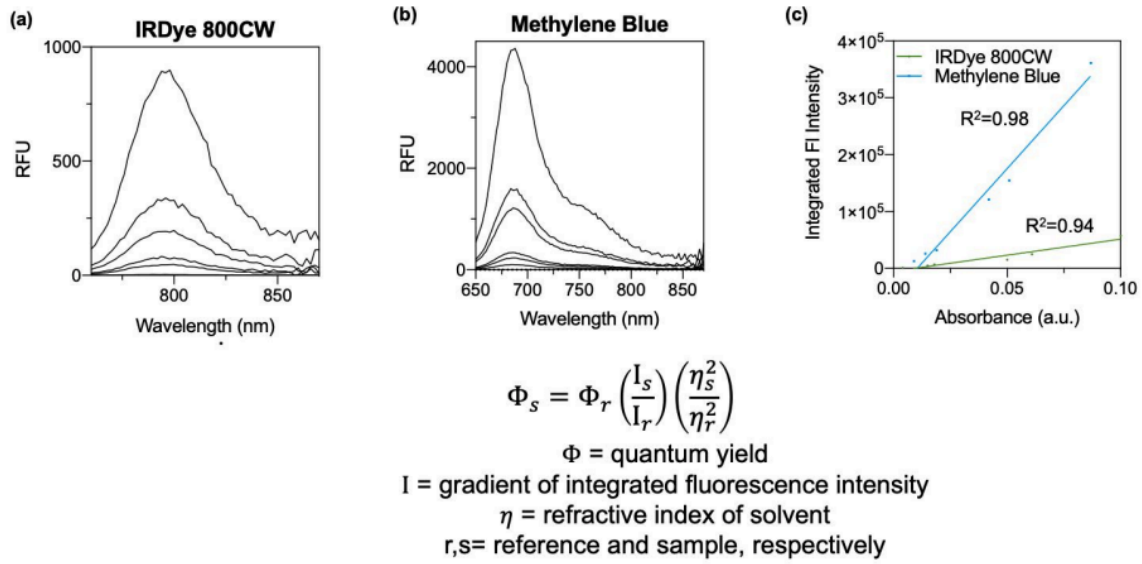

$$\Phi_s = \Phi_r \left(\frac{I_s}{I_r}\right)\left(\frac{\eta_s^2}{\eta_r^2}\right)$$

Φ = quantum yield
I = gradient of integrated fluorescence intensity
η = refractive index of solvent
r,s= reference and sample, respectively

Figure 3. 10 Relative Quantum yield of IRDye 800CW in water

(a) Fluorescence curves of IRDye 800CW show clearly diminished fluorescence intensity when compared to the curves of **(b)** methylene blue when both dye samples were scanned under the same absorbance optical densities **(c)** The differences in (a) and (b) are evident in a plot of the dyes' integrated fluorescence intensities relative to shared optical densities. The formula below outlines the calculation for relative fluorescent quantum yield, where methylene blue is the reference dye, and both were characterized in pure water. The known quantum yield for methylene blue in water is 52%, and the calculated relative quantum yield of IRDye 800CW is 6.8%. Previous reports on IRDye 800CW quantum yield span between 3.4-9.0[1-2]%

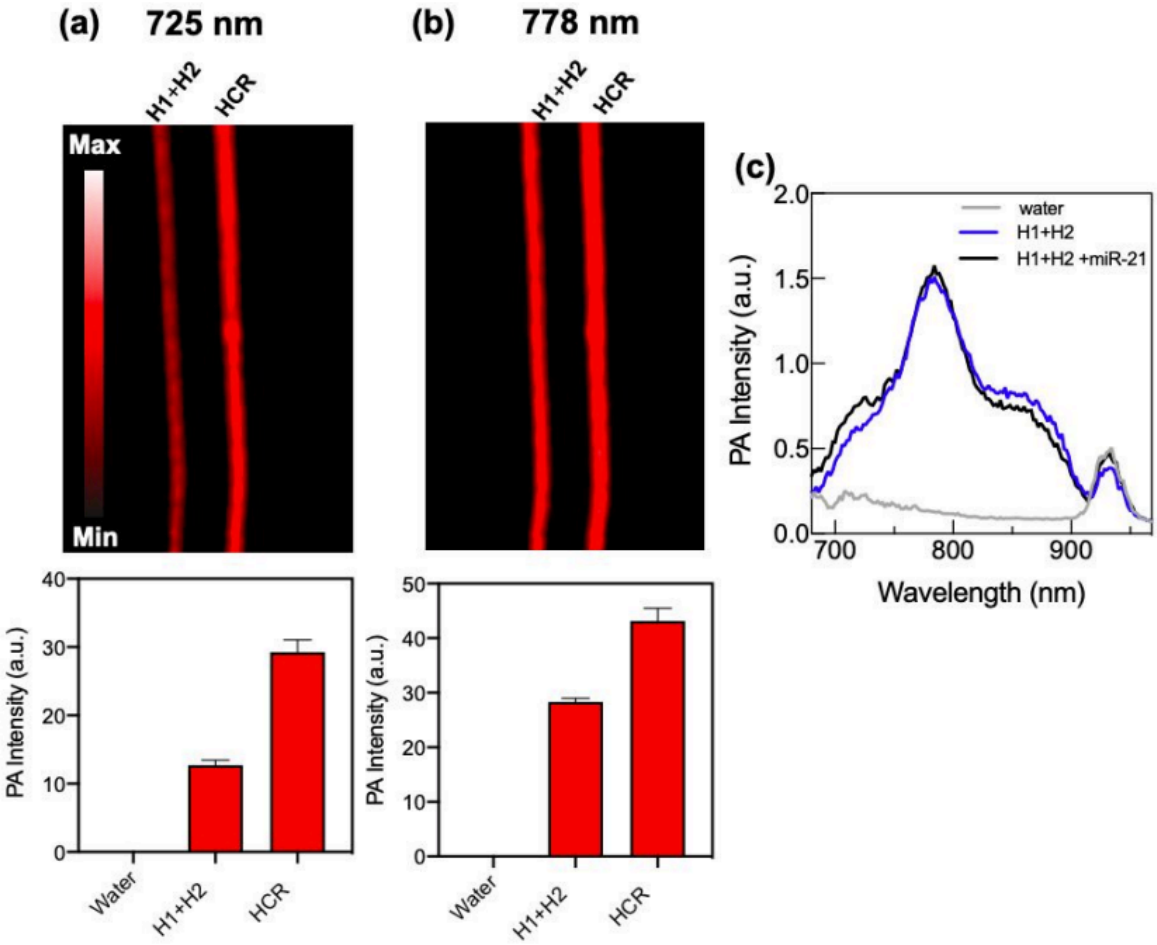

Figure 3. 11 PA contrast versus laser wavelength.

(a) 725 nm laser showed 2-fold PA contrast between background and 10 nM miR-21 activated HCR. **(b)** 778 nm laser showed minimal contrast between the same samples indicating that the contact quenching from emergent 725 peak in absorbance measurements shown in Figure 1b in the main text primarily leads to activated photoacoustic "turn on" signal. **(c)** PA spectral data validates heightened PA signal at 725 nm from miR-21-activated HCR. We note however, that while both 725 and 778 nm wavelengths led to a significant PA enhancement over the hairpin mixture ($p<0.0001$ and $p=0003$ respectively) we also clarify that in these images, the 725nm/778nm ratio of PA intensities for 10 nM miR-21 is 0.68 while the ratio between the hairpin mixture is 0.39, which remain in agreement with the established ratio when 0 and 10 nM of miR-21 are present (See **Figure 5C** in the main manuscript text). Therefore, while the 778nm PA signal can sometimes be higher than the PA from the mixture, it still preserves the ratiometric quantification ability when additionally scanned at 725 nm.

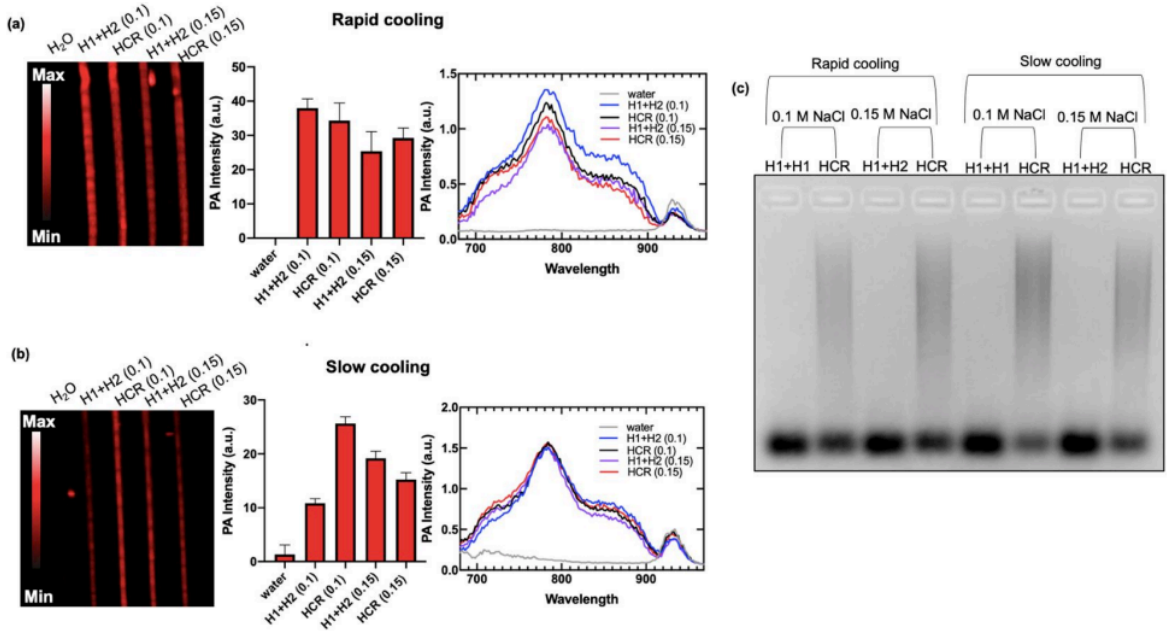

Figure 3. 12 Closed-state hairpin preparation on photoacoustic signal.

Nucleic acid hairpins are often either prepared by heating the strands to 95ºC, followed by either a rapid cooling (quenched in ice to 4ºC) or a gradual cooling to room temperature so that the hairpins will not bind together and form HCR without the target fuel miR-21. The presence of salt can also affect proper closed hairpin formation due to DNA inter-strand hybridization. **(a)** Photoacoustic comparisons of hairpin mixtures versus miR-21 activated HCR (labeled 'HCR' in figure) when hairpins are cooled rapidly in the presence of either 0.1 or 0.15 M NaCl show no PA contrast from HCR products thus showing the failure of the formed hairpins in closed state. **(b)** Photoacoustic comparisons of hairpin mixtures versus miR-21 activated HCR when hairpins are cooled gradually in the presence of either 0.1 or 0.15 M NaCl show PA contrast and distinct 725 nm formation from HCR products when the hairpins were initially cooled to RT in 0.1 M NaCl. These results confirm that the formed hairpins were in a closed state. **(c)** Agarose gel electrophoresis corroborates that the HCR is run most efficiently when the hairpins are slowly cooled in 0.1 M NaCl as can be seen by the more intense smear band and more faded leftover hairpin band relative to the other cases.

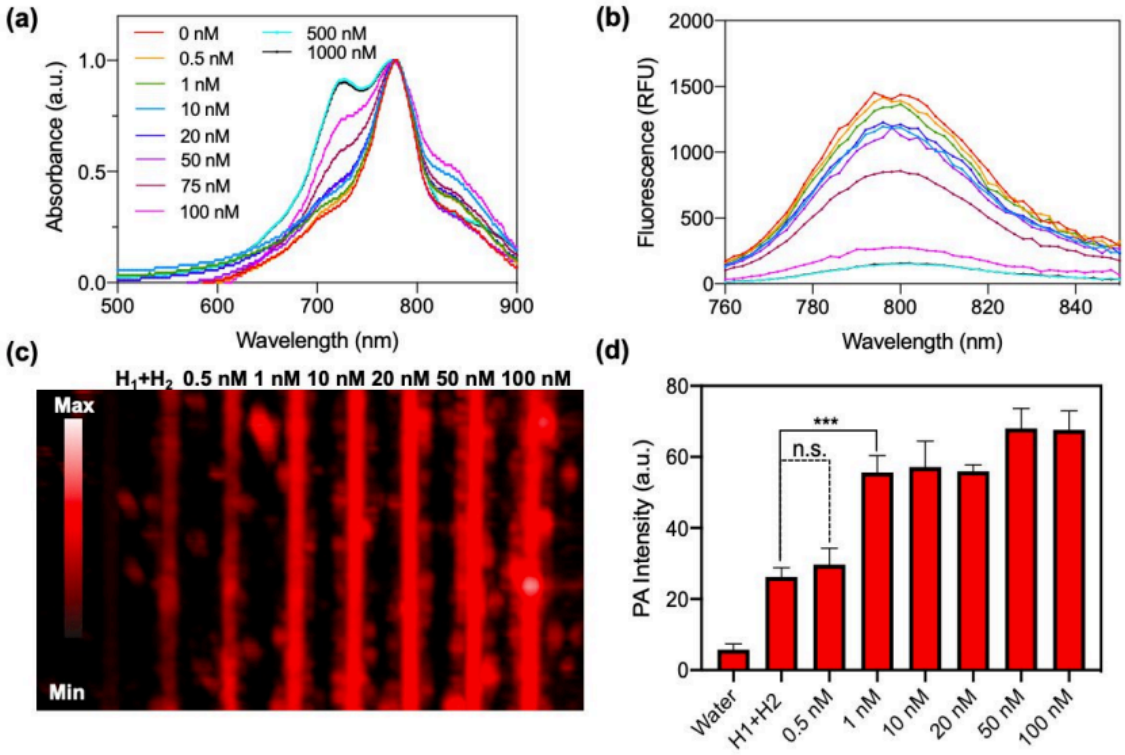

Figure 3. 13 Single wavelength 725 nm PA experiments on varying miR-21 concentrations with 1.5 μM hairpins.

(a) Normalized absorbance spectra of hairpins incubated with miR-21 from 0.5-1000 nM miR-21 shows a continuous and gradual emergence of the shoulder formation at 725 nm. **(b)** Fluorescence measurements exemplify the consequential gradual quenching with increasing miR-21 concentration. **(c)** PA images of samples incubated with different miR-21 concentrations with respect to background hairpin mixture at 1.5 μM and **(d)** quantified relative PA intensities from the samples confirm consistent with PA enhancement versus miR-21 concentrations such as the two-fold PA enhancement from 1 nM miR-21.

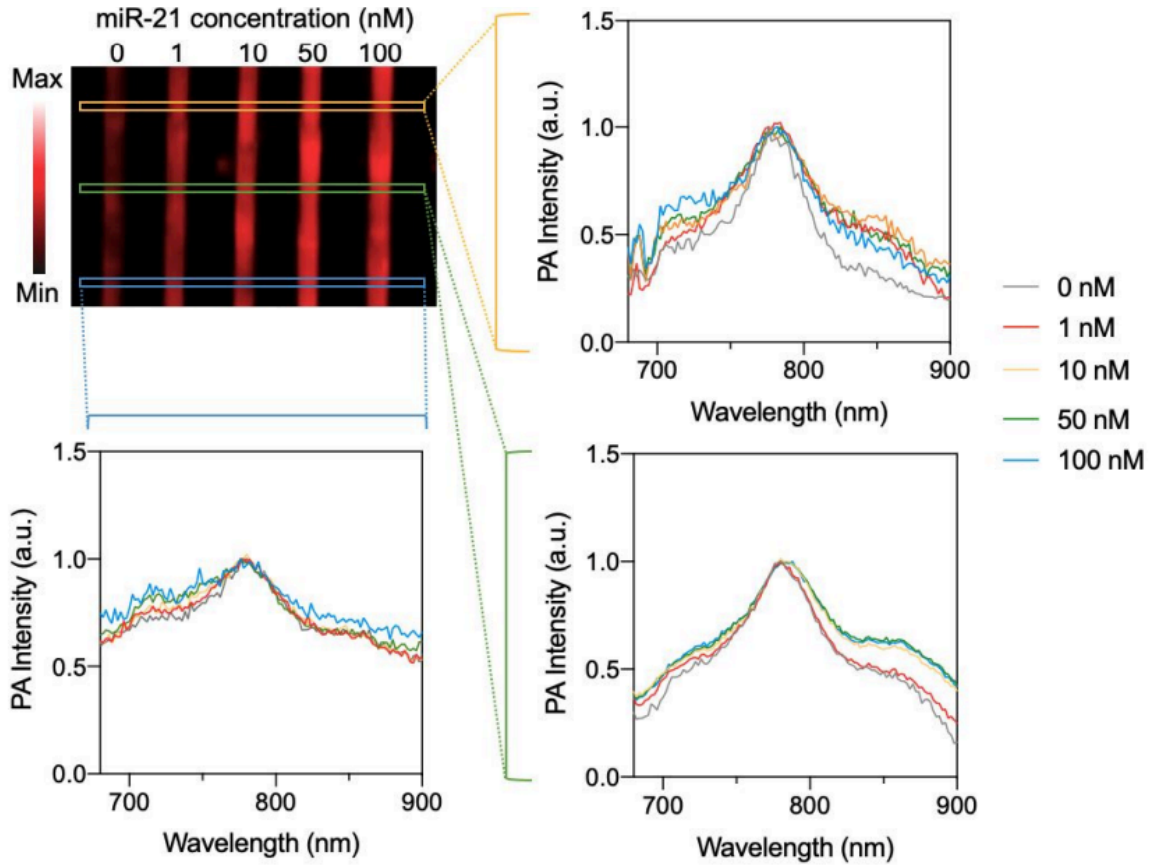

Figure 3. 14 PA spectral scans of the same samples

(a)PA spectra of hairpins with or without miR-21 incubation at controlled concentrations show inconsistent differences in spectral PA intensities when the same samples are scanned multiple times and in different areas of the loaded tubes. The spectral curves were normalized to carefully monitor changes in shape between samples. Clearly, there is remarkable spectral differences between and within different scans; this can be most visible when comparing the differences between hairpins mixed with 0nM miR-21 versus those with 100 nM (gray vs blue curves, respectively).

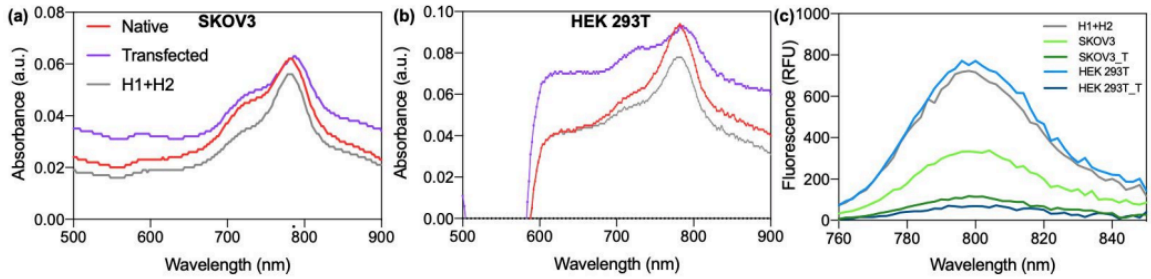

Figure 3. 15 Raw absorbance and fluorescence data from hairpins after incubation with SKOV3 and HEK 293T cells.

(a)A 725 nm shoulder formation is apparent when the hairpins are incubated with either wild type or miR-21-transfected SKOV3 cells with no significant difference between the two. This was compared to the hairpin mixture in SKOV3 media where such 725 nm absorbance is absent. **(b)** Similar measurements from HEK 293T show no significant difference between hairpins in media and hairpins incubated with natural HEK 293T cells, but there was a significant 725 nm shoulder formation when the cells were further transfected with miR-21. The steep dip before 600 nm for these curves are most likely due to the blank sample, which was empty DMEM media with phenol red that has a characteristic absorbance peak at 600 nm. **(c)** Fluorescence measurements show hairpins incubated in SKOV3 yield a more than 2-fold fluorescent quenching versus hairpins incubated in media; no quenching occurs in HEK293T. However, dramatic fluorescent quenching is seen when both cells were transfected with miR-21 before hairpin addition. These spectra display the selectivity of the hairpins to activate contact quenching in different cell lines based on miR-21 regulation.

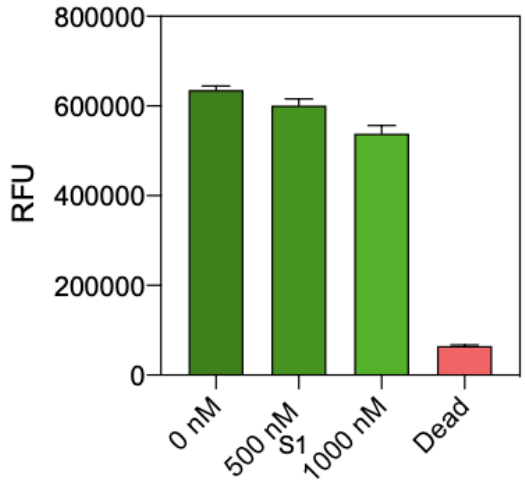

Figure 3. 16 Toxicology results from hairpins after overnight incubation with HEK 293T cells.

(a) 20,000 cells incubated with 500 nM of hairpins demonstrated 95% viability when compared to healthy and dead cells. The hairpins were administered into the cells following protocol from the cell experiments. While 1000 nM hairpin concentration was not used for these experiments, it was similarly evaluated and was found to decrease viability by 17%. However, the 1000 nM concentration may have less of an effect on cell viability if the cell population size is consequently larger. Hairpins were incubated overnight with the cells in triplicate before a Resazurin Toxicology kit was used. Percentage values were calculated such that the fluorescence values from live, untouched cells and dead, bleached cells were treated as the upper and lower bounds.

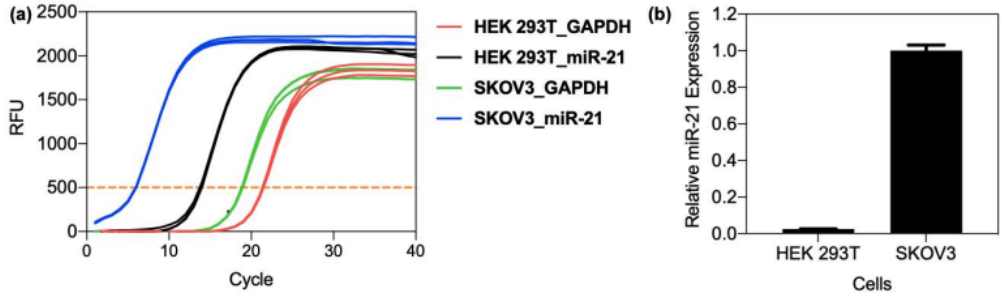

Figure 3. 17 qRT-PCR data on miR-21 expression levels of miR-21 and GAPDH extracted from SKOV3 vs HEK 293T cell lines

(a)qRT-PCR expression curves versus PCR cycle. **(b)** Relative miR-21 expression analysis revealed a 42-fold increase in miR-21 expression from SKOV3 versus HEK 293T thus showing that the cell lines are useful for miR-21 studies. Error bars represent standard deviation of triplicate experiments.

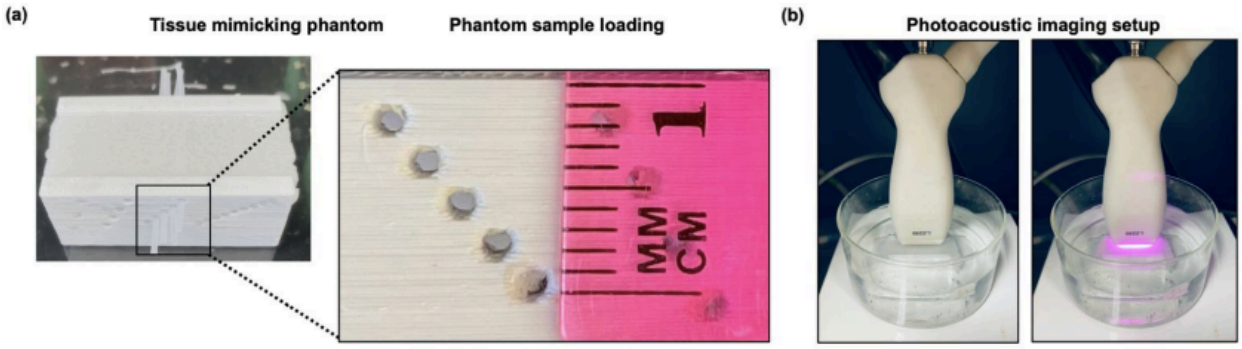

Figure 3. 18 Experimental setup for tissue mimicking phantom imaging experiments.

(a) Photograph of 3d printed sample holder with programmed depth lengths casted in 1% agarose with 0.8 mg/mL TiO_2 and 0.005% India ink give a solid, completely opaque gel material with biologically relevant scattering and absorbing media conditions. Closeup image of the sample loading station shows tubes can be inserted into the phantom at controlled 0.2 cm depth distance. **(b)** Photoacoustic imaging setup where the phantom is immersed in water and the transducer is placed directly above the surface of the phantom.

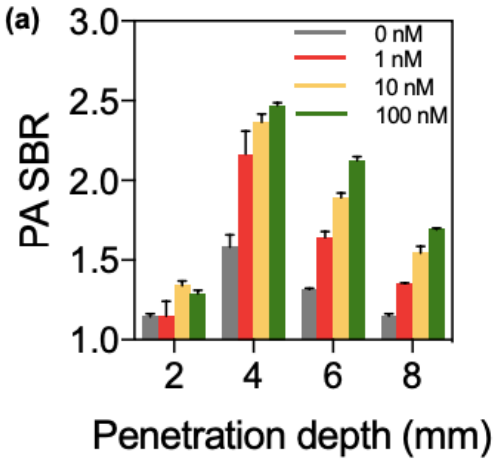

0 nM: Y= -1.077X + 1.995 R^2=0.92

1 nM: Y= -2.027X + 2.935 R^2=0.91

10 nM: Y= -2.047X + 3.162 R^2=0.98

100 nM: Y= -1.994X + 3.260 R^2=0.97

Figure 3. 19 SBR analysis of different penetration depths

(a) SBR at different penetration depths for each concentration of miR-21. The resultant slopes from linear aggression analysis (see figure 7m in main text) were used to approximate the farthest penetration depth achievable for each miR-21 concentrations for sufficient imaging quality using a single wavelength 725 nm scan. The cutoff SBR value is 1.264, the defined SBR metric for Rayleigh Criterion's definition on resolution. The limiting depths (where SBR=1.264) were 0.82, 0.93, and 1.3 cm for 1, 10, and 100 nM miR-21 respectively. 2mm penetration depth suffered from overall poor SBR primarily due to the reflection artifact at the surface of the phantom.

CHAPTER 4: SUPRAMOLECULAR LOADING OF DNA HYDROGELS WITH DYE-DRUG CONJUGATES FOR REAL-TIME PHOTOACOUSTIC MONITORING OF CHEMOTHERAPY

ABSTRACT: A longstanding problem with conventional cancer therapy is the nonspecific distribution of chemotherapeutics. Monitoring drug release in vivo via noninvasive bioimaging can thus have value, but it is difficult to distinguish loaded from released drug in live tissue. Here, this work describes an injectable supramolecular hydrogel that allows slow and trackable release of doxorubicin (Dox) via photoacoustic (PA) tomography. Dox is covalently linked with photoacoustic methylene blue (MB) to monitor Dox before, during, and after release from the hydrogel carrier. The conjugate (MB-Dox) possesses an IC50 of 161.4×10^{-9} M against human ovarian carcinoma (SKOV3) cells and loads into a DNA-clad hydrogel with 91.3% loading efficiency due to MB-Dox's inherent intramolecular affinity to DNA. The hydrogel is biodegradable by nuclease digestion, which causes gradual release of MB-Dox. This release rate is tunable based on the wt% of the hydrogel. This hydrogel maintains distinct PA contrast on the order of days when injected in vivo and demonstrates activatable PA spectral shifts during hydrogel degradation. The released and loaded payload can be imaged relative to live tissue via PA and ultrasound signal being overlaid in real-time. The hydrogel slowed the rate of the murine intraperitoneal tumor growth 72.2% more than free Dox.

4.1. Introduction

Drug tracking in vivo offers value on understanding the therapeutic efficacy and pharmacokinetics of chemotherapeutics. For example, traditional cancer drugs can have nonspecific cytotoxicity. Emerging small molecule therapeutics may have different protein-binding interactions, novel biodistribution pathways, downstream asynthetic phase I and II reactions (e.g., oxidation, reduction, methylation), unforeseen conjugation reactions during metabolism, or differences in excretion or clearance pathways.[220] If molecular drugs can be monitored in detail and in real-time, then their side effects and potencies—or lack thereof—can be better understood for improved strategies or personalized treatments against chronic diseases.

Biomedical imaging is a robust and multifunctional modality that can track drugs; unlike analyte detection in biological sampling, biomedical imaging allows both real-time and spatial information on drug location.[221,222] A popular strategy to accomplish this is by combining the drug with a contrast agent when administered in vivo. However, several accessory capabilities from this pairing are essential for an image-based drug tracking system to be considered viable: (1) quantitative drug monitoring[223] or the ability to characterize the amount of drug present, loaded, or released in vivo; (2) activatable contrast change[185] to report if the drug is released from a carrier, metabolized, or bound to other macromolecules; (3) sustained contrast from the drug for longitudinal monitoring; and (4) real-time imaging in live tissue. There are many imaging modalities to use, but photoacoustic imaging (PAI) has gained particular traction in this context.[224,225] PAI is an ideal modality to monitor drugs in vivo because the incident near infrared (NIR) light can safely penetrate tissue to activate nano- and molecular-scale contrast agents for acoustic broadband signal while simultaneously imaging live tissue with conventional ultrasound[226,227]. Unlike other modalities such as magnetic resonance imaging (MRI), computed tomography (CT), or radiography, PAI does not require full body scans or ionizing radiation.

Many strategies have demonstrated novel drug monitoring systems via PAI, but none satisfy all four abovementioned metrics. For example, Duan et. al. combined doxorubicin and NIR squaraine reporting dye into pH-sensitive polymeric micelles for controlled release in the tumor microenvironment.[228] Sun et al. later introduced a multifunctional nanoparticle that carries both chemotherapeutic Pt(II) metallacycle molecules and an NIR-II molecular dye into melanin nanoparticles for combined imaging, chemotherapy, and photothermal therapy.[229] However, the co-loaded nature of the drug and the dye only provides image contrast with respect to the carrier alone or signal loss when the payload is released from the carrier. These systems do not enable contrast to follow the drug upon its release. This leads to crucial information on the overall pharmacokinetics of the drug itself.[224] Jeevaranthiam and Lemaster et al. covalently linked a chemotherapy drug (paclitaxel) to the contrast agent (methylene blue, MB) for more precise drug localization during PAI. This new molecule remained invisible to PAI until its release from polymeric PLGA nanoparticles due to the changed oxidation of MB via the "blue bottle effect."[230] One limitation of this approach was that paclitaxel could only be imaged when released.

Here, we describe a system where Dox is photoacoustically visible both when encapsulated and when released in vivo. Dox was first conjugated to MB for photoacoustic signal. This conjugate is then loaded into an injectable and biodegradable DNA cross-linked hydrogel due to the molecule's strong intermolecular affinity to bind into double helical DNA with its planar and aromatic structure, and the facile ability to make DNA hydrogels with tunable mechanical strength and biodegradability.[231] The tight packaging and heightened local concentration of the conjugate in the DNA hydrogel causes a redshift in the MB PA signal relative to conjugate free in solution phase. As a result, when the hydrogel gradually degrades

from nuclease activity, local concentration gradients cause the released conjugate to produce a PA signal at a different wavelength. Thus, imaging can determine if the drug is loaded or released (Figure 4.1). Furthermore, the gradual degradation of the hydrogel enables slow and controllable release of the payload, which in turn offers good antitumor efficacy relative to conventional chemotherapy.

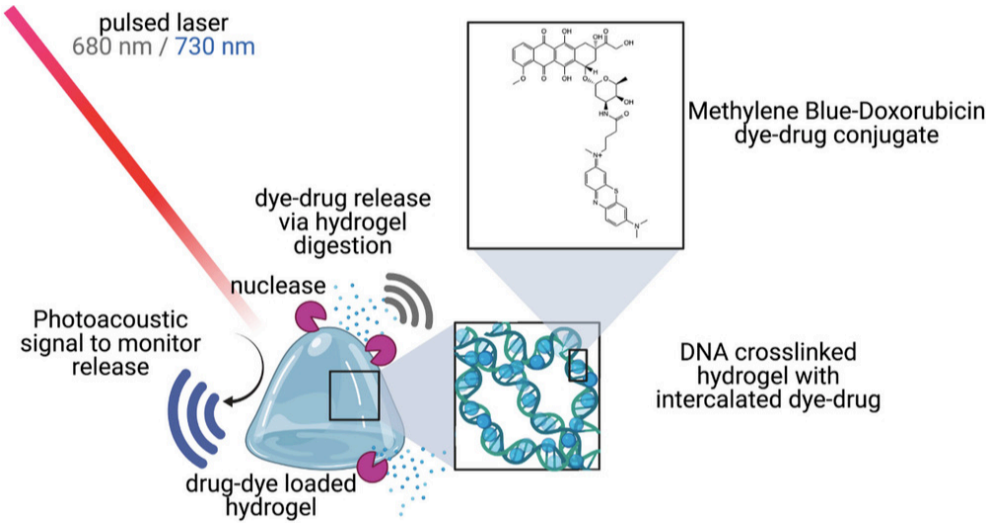

Figure 4. 1 A biodegradable hydrogel photoacoustically monitors chemotherapeutic drug release.

Here, a pure DNA cross-linked hydrogel is loaded with methylene blue (MB) doxorubicin "MB-Dox" dye–drug conjugate via hydrophobic binding. The MB-Dox compound has activatable wavelength-specific photoacoustic (PA) signal when loaded in the hydrogel and during drug release from photoacoustic signal from MB. The hydrogel degrades from in vivo nuclease activity.

4.2. Methods

4.2.1. Synthesis and Purification of MB-Dox

"MB-Dox" was synthesized using amine linkage of succinimidyl ester (NHS) activated MB with the sugar moiety of doxorubicin. MB-NHS ester and doxorubicin powders were mixed together with TEA at 1:1:1.5 molar ratios in DMSO, and allowed to react overnight at 300 RPM and 30 °C in the dark. This reaction was then dried under vacuum centrifugation using Vacufuge Plus (Eppendorf, Hamburg) at 60 °C for 2 h.

Crude dry pellets were resuspended in MeCN/H_2O (30:70 v/v) and purified via isocratic RP-HPLC with a Shimadzu LC-40 on a Shim-pack C18 column (5 μm) over 70 min. During purification, fractions were collected and diluted to 90% (v/v) MeOH before analysis with ESI-MS in positive mode, centroid scan on Micromass Quattro Ultima Triple Quadrupole mass spectrometer. Pure products were then lyophilized and stored in the dark for later use.

4.2.2. Optical Characterization of MB-Dox

Absorbance spectra were measured with a BioTek Synergy H1 plate reader. Samples were measured in 100 μL volumes in 96-well plates, and absorbance measurements were taken from 400 to 800 nm.

4.2.3. Nuclear Magnetic Resonance Spectroscopy

Dry MB-Dox was dissolved in DMSO-d_6 with a 300 mHz Bruker Avance III HD NMR spectrometer at room temperature. The chemical shifts were calibrated using the nondeuterated DMSO residue (2.50 ppm) in the deuterated solvent as an internal reference from the literature[232]

4.2.4. DNA Hydrogel Preparation

DNA strands as described in Table 8 were ordered from Integrated DNA Technologies (IDT). Briefly, amplifying strands were heated at 95 °C for 5 min and were then quenched on ice and cooled down to 4 °C. These were then mixed at equal ratios and then 50× higher with the initiating strand at 1XTAEMg Buffer (40×10^{-3} m Tris-base, 20×10^{-3} m acetic acid, 2×10^{-3} m EDTA, 12×10^{-3} m Mg acetate) and left overnight at room temperature.

4.2.5. Hydrogel Loading

Dry MB-Dox was first resuspended in pure Milli-Q water and was pipetted into the DNA hydrogel and the mixture was left to react overnight. The hydrogel was gently lifted from the supernatant of the reactant and was rinsed by resuspending, removing, and resuspending in fresh Milli-Q water twice. The supernatant was analyzed via absorbance spectroscopy to estimate

DLE. Drug loading content was calculated by taking the mass ratio between the loaded MB-Dox and total loaded hydrogel.

4.2.6. PA Imaging

PA images of in vitro samples were acquired with a Vevo 2100 LAZR (VisualSonics) using a 21 MHz transducer (LZ-250). Samples were loaded into 0.86 mm polyethylene tubes and fixed in parallel with a 3D printed sample holder. One tube was filled with reaction solvent (water) to serve as a reference. The fixed samples were placed 1 cm below the transducer in a vessel filled with water. Single wavelength scans were operated at 680 and 730 nm at a frame rate of 20 Hz. For 3D PA images, the transducer was scanned with a stepper motor along the axial dimension of the tubes. PA spectra were taken from 680 to 900 nm with a step size of 2 nm.

4.2.7. Cell Culture

SKOV3 cells were cultured using McCoy's 5A medium supplemented with 10% fetal bovine serum and 1% penicillin-streptomycin. Cells were incubated at 37 °C and media was replaced every 1–2 days. Cells were passaged at 75–85% confluence with 0.25% Trypsin EDTA.

4.2.8. Cytotoxicity assays

Cells were seeded into 96-well plates (1100 cells per well) overnight. The media was then replaced with media containing either MB-Dox, Dox, MB, or the loaded hydrogel at different concentrations for 48 h. For PDT studies, the cells were incubated with MB-Dox for 2 h before half of the samples were exposed to 100 mW of 660 nm light for 10 min. These cells were left to incubate for 48 h and were compared to those left in the dark. A resazurin assay was used to evaluate the cell viability for all cytotoxicity experiments.

4.2.9. Animal Studies

All mice studies described below were performed in accordance with National Institutes of Health (NIH) Guidelines approved by the Institutional Animal Care and Use Committee

(IACUC) under protocol S15050 at University of California, San Diego. Female J:NU mice of 5 weeks of age were used for all in vivo experiments. For imaging experiments, mice were anesthetized with isoflurane. For both imaging and therapeutic assessment, hydrogels were administered at a 9 mg kg^{-1} dosage of the MB-Dox compound, which falls under the maximum tolerated dosage (MTD) or MB and doxorubicin (>20 mg kg^{-1} and 10 mg kg^{-1}, respectively) in rodents.[50, 51]

4.2.10. In vivo PA imaging of Hydrogel

The hydrogel was injected with a 21-gauge syringe subcutaneously into the dorsal site of a mouse after resuspension in PBS. The injected region was subsequently imaged on the mouse on days 0, 1, 3, 5, 7, and 8 under the same PA and B-mode gain. PA spectra were also taken during this time. Photoacoustic images were analyzed on ImageJ to evaluate intensity.

4.2.11. In vivo therapeutic study

Mice were divided into five groups. 800 000 SKOV3-luc cells were injected (with 50% Matrigel/PBS v/v) intraperitoneally on the right side of the mice. On day 3, the mice were intraperitoneally injected with MB-Dox loaded hydrogel (9 mg kg^{-1}), Dox (9 mg kg^{-1}), MB-Dox (9 mg kg^{-1}), Dox for periodic dosing (4.5 mg kg^{-1}), and PBS. On day 7, the mice with periodic dosing were injected with Dox once more (4.5 mg kg^{-1}). To measure tumor burden, mice were imaged with D-luciferin on days 3, 5, 7, 9, 11, 14 with 100 mg kg^{-1} dosage in PBS. The bioluminescence was measured and imaged via IVIS Perkin-Elmer Illumination and LivingImage software. For laser-activated toxicity, the mice were exposed to a 100 mW 660 nm laser for 10 min every 2 days.

For ex vivo analysis, tissues from the injection site of the mice were extracted, fixed, and submitted to Pacific Rim Pathology (San Diego) for sectioning and H&E staining.

4.2.12. Data and Statistical Analysis

All presented data in this manuscript was not preprocessed or normalized. Values and error bars represent mean and standard deviations of measurements between replicates, respectively. Sample sizes are specified in the captions of the figures for each quantitated result. One sided *t*-tests were used to evaluate differences between groups. For the in vivo therapeutic study, the hydrogel was compared to both the single and double-dosed doxorubicin cases using ANOVA analysis.

4.3. Results and discussion

4.3.1. Methylene Blue and Doxorubicin Conjugate

4.3.1.1. Chemical synthesis and characterization of "MB-Dox"

MB was chosen as the contrast agent due to its widespread use in medicine, long half-life on the order of 5–6 h,[233,234] NIR excitation for photoacoustic (PA) signal, potential to link with Dox, and propensity to intercalate into DNA and thus a DNA-constituted hydrogel.[235] MB and Dox are Food and Drug Administration (FDA) approved drugs and have been used in the clinic for decades, but their co-administration poses a unique advantage: Past reports have demonstrated that the redox potential of MB can overcome the cardiotoxic reactive oxygen generation from Dox without compromising antitumor efficacy.[236,237] MB was covalently linked to Dox (MB-Dox) through a simple NHS-ester-amine reaction as outlined in (Figure 4.2a and Figure 4.8). The amine group on the sugar moiety of Dox allows it to react with an NHS-ester attached to MB. This process was assisted by triethylamine (TEA) in DMSO solvent. After incubation, DMSO was removed from the reaction, and the sample was then purified via isocratic reverse phase high performance liquid chromatography (RP-HPLC) in 30% acetonitrile solvent (Figure 4.2b and Figure 4.9). The structure of this compound was confirmed via electrospray ionization mass spectrometry (ESI-MS). The positive mode of ESI-MS validated the

characteristic 881.3 *m/z* ratio peak, which corresponded to the total molecular weight of the compound (Figure 4.2c). The compound was further characterized using ^{1}H NMR (Figure 4.10). The synthesis yield of this reaction was 14.8%.

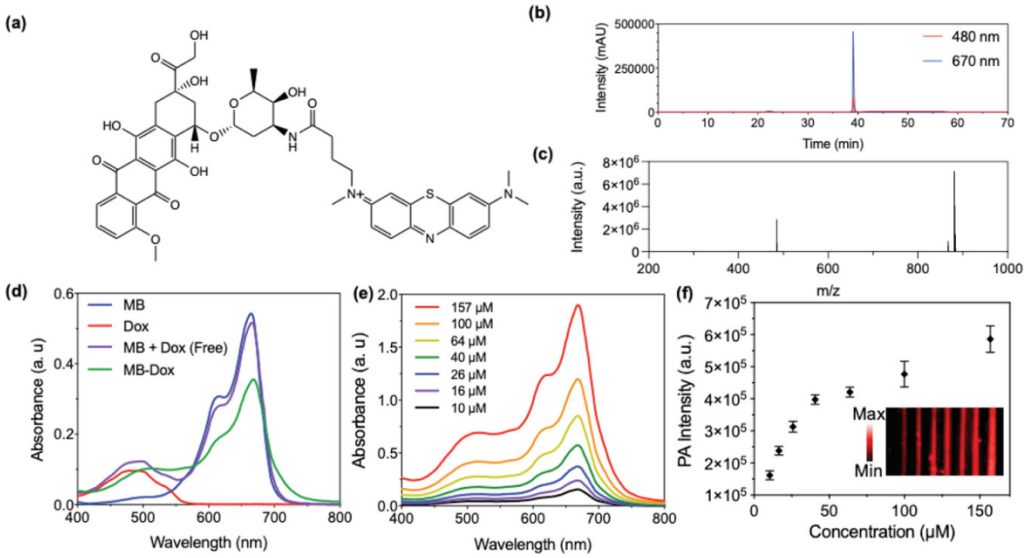

Figure 4. 2 Chemical, optical, and photoacoustic characterization of MB-Dox.

a) Chemical structure of the conjugate—the reaction involves the amine group on the sugar moiety of doxorubicin and the NHS-ester of NHS-activated methylene blue (MB). b) Liquid chromatograms of purified MB-Dox via HPLC where 480 nm absorbance and 670 nm absorbance are for Dox and MB, respectively, were monitored. c) Electrospray ionization (ESI) *m/z* for MB-Dox $C_{46}H_{49}N_4O_{12}S^+$, expected: 881.31; found: 881.3064. d) Optical absorbance spectra of MB, Dox, MB mixed with Dox unconjugated, and the MB-Dox conjugate show the conjugate maintains curves from MB and Dox with a peak absorbance near 670 nm in water. e) Absorbance spectra of MB-Dox with increasing micromolar concentrations in water show increasing absorbance at 670 nm with no MB mediated dimerization. f) PA image of tubes and quantified PA intensity show increasing concentration of MB-Dox leads to increasing PA signal at 690 nm. The inset is a longitudinal image of the tubes loaded with respective increasing concentrations of MB-Dox from left to right.

4.3.1.2. Optical MB-Dox Characterization

The solubility of the compound was also observed from optical absorbance curves of the compound both in DMSO and in pure water (Figure 4.2d and Figure 4.11a,b). The absorbance curve of the compound was representative of the additive curves found in MB and Dox on their own with a slight 3 nm red-shifted peak from MB (Figure 4.2d and Figure 4.11a, Supporting

Information). This confirmed that the molecule should still be viable for PAI due to this NIR optical peak absorption. Interestingly, increasing micromolar concentrations of the compound did not lead to increased or emergent secondary blue-shifted peak formations commonly observed[238] and as we demonstrated with MB alone, (Figure 4.2e and Figure 4.12a–c,), thus implying that the Dox appendage in the compound has a structural protective effect against typical MB dimerization in water. There is a need for molecular drugs to avoid uncontrollable aggregation in vivo,[239] and thus this feature is advantageous for MB-Dox's therapeutic viability.

4.3.1.3. MB-Dox Photoacoustic Characterization

The conjugate was then characterized for PA signal generation; 680 nm incident light was chosen for PA activation because it was the closest wavelength to MB-Dox's peak optical absorbance curve. The PA signal increased with respect to increasing MB-Dox concentration (Figure 4.2f), and the limit of detection (LoD) for this compound was found to be at 11.6×10^{-6} M. When the compound was irradiated with pulsed NIR light ranging from 680 to 900 nm, the photoacoustic intensity reached its maximum at 680 nm, which is characteristically seen in MB photoacoustic studies (Figure 4.3e).[230] Therefore, the free compound maintains a photoacoustic profile that is relatable to MB, and Dox does not affect this peak or compromise PA signaling.

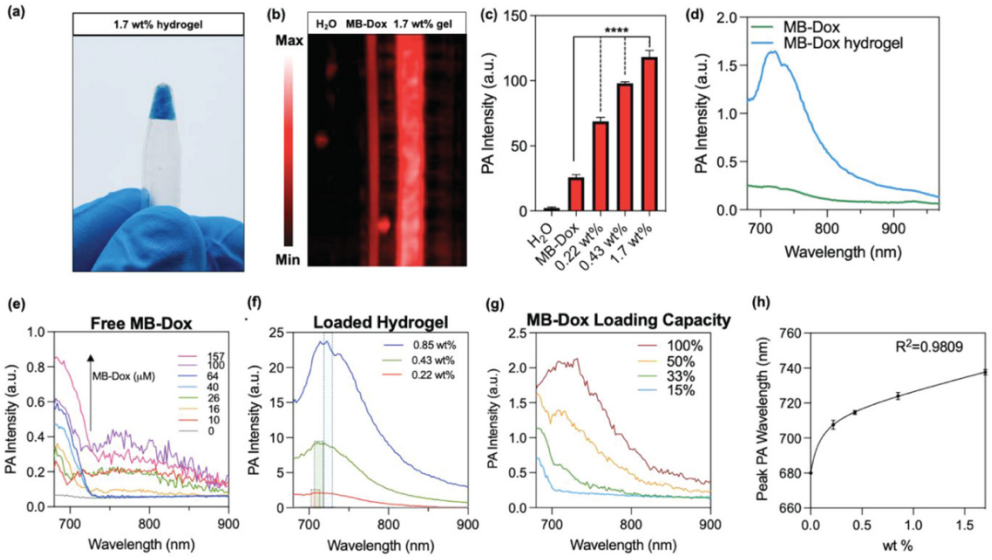

Figure 4. 3 DNA hydrogel loaded with MB-Dox.

a) Photograph of cross-linked 1.7 wt% DNA loaded with blue MB-Dox in an upside-down sample tube shows a highly loaded hydrogel. b) PA image of tubes comparing the PA signal enhancement from the loaded hydrogel in comparison to the PA signal of the same concentration of MB-Dox free in water shows heightened contrast by the hydrogel. c) PA signal quantification demonstrates that increased wt% of hydrogel leads to increased PA signal when loaded with equal amounts of MB-Dox. d) PA spectra of MB-Dox hydrogel shows a peak near 730 nm while free MB-Dox has peak PA intensity closer to 680 nm. e) It can be observed that with increasing concentrations of MB-Dox in water, there is no wavelength shift in PA maximum absorbance (i.e., MB-Dox maintains a PA peak at 680 nm). f) Increasing wt% of the MB-Dox loaded hydrogel, on the other hand, not only shows an overall increase in PA intensity, but also an increasing red-shifted PA peak from between 710 to 730 nm from 0.22 to 0.85 wt%, respectively. g) Spectral measurements on the hydrogel with changed amount of loaded MB-Dox in terms of achieved loading capacity corroborates that the spectral shifts in panel (f) are in fact true to changing gel wt% as opposed to changing amount of added payload. h) PA spectral shifts are indicative of gel wt%.

4.3.1.4. MB-Dox Cytotoxicity

The compound's cytotoxicity was then tested and compared to that of MB and Dox at matching concentrations. The IC50 value of each molecule was evaluated with SKOV3. Dox alone maintained the lowest IC50 value (68.56×10^{-9} m), while MB-Dox yielded an IC50 of 161.4×10^{-9} m, and MB of 1460×10^{-9} m (Figure 4.13a). The IC50 for Dox reported here is

similar to the 68 × 10^{-9} m IC50 of paclitaxel in Jeevaranthiam and Lemaster et al.'s work, however, their conjugate had an IC50 value that increased to 447 × 10^{-9} m.[230]

MB has also demonstrated photodynamic therapeutic effects upon NIR light irradiation.[240] Therefore, we further exposed the cells incubated with the compound to a 100 mW 660 nm laser for 10 min, which was suitable for MB activation, and compared the cytotoxicity results to those left in the dark. The cytotoxicity increased by 37% when administered at the IC50 concentration and irradiated with light, but the overall photodynamic therapy (PDT) effects from the compound did not lead to significant cytotoxicity enhancement (p = 0.114) (Figure 4.13b).

4.3.2. MB-Dox Loaded Hydrogels

4.3.2.1. Hydrogel Formulation and MB-Dox Loading

Engineered nanoparticle systems have faced several challenges as carriers for small molecule drugs and chemotherapy.[241] For example, some nanoparticle carriers experience premature burst effects, leaking, or degradation from lymphatic channels, the liver, urinary tract, or bile. On the other hand, other nanoparticle carriers are too stable for effective drug release while in the tumor microenvironment.[242]

A hydrogel was chosen as the MB-Dox carrier for structural and functional reasons. First, hydrogels can load higher amounts of payload relative to nanoparticles, but their tunable mechanical strength can also lead to a tunable release rate of the payload.[243] We thus hypothesized the payload may release slower than it were to be loaded into nanoparticles, which is ideal for systematic chemotherapeutic dosage against drug resistance.[244,245] Second, we hypothesized that a higher loading of cargo would increase local concentrations of the contrast

agent and thus increase the signal-to-background ratio (SBR) in vivo. Higher PA contrast becomes increasingly essential as NIR background signal is ever-present in tissue, blood, hemoglobin, melanin, and other endogenous absorbers.[246]

The macroscopic hydrogel in this work is composed of highly concentrated DNA strands cross-linked by canonical base pairing rules. The rationale for DNA as the hydrogel skeleton is twofold. First, nucleic acids are a biocompatible and biodegradable material, and thus the hydrogel is inert to tissue while its degradation is inevitable due to ubiquitous nuclease activity. Second, small and planar aromatic molecules have strong affinity to the interior of DNA due to hydrophobic stacking interactions.[247] MB is a common stain for nucleic acid while Dox's cytotoxic nature is due to its damage in cellular nucleic acid through intercalation.[235,248] In fact, DNA hydrogels and structures have widely demonstrated promise in harboring Dox molecules for drug delivery.[248–250] Moreover, DNA nanostructures have been reported as viable scaffolds for photoacoustic contrast agents with the ability to even modulate their activatable wavelengths by controlling distances between discrete dye molecules.[193,251,252] Besides the specific case of DNA hydrogels, other similarly aromatic driven stacking interactions have led to drug delivery systems with efficient loading capacity.[253] Therefore, the MB-Dox conjugate was expected to load strongly into a DNA-based hydrogel.

The hydrogel in this work directly used Wang et. al.'s gelation design, which is cross-linked by two amplifying single strand species and one gel-forming initiator strand via the hybridization chain reaction (HCR).[254] In brief, when the initiator strand binds to one amplifying strand through base-pair specificity, that strand will bind with the other amplifying strand to form a cascaded self-assembly of a hierarchical double-stranded DNA superstructure. The highly

concentrated DNA strands are linked by base pairing to form a superstructural gel after hybridization, and gel wt% tunability is possible by modulating the total DNA concentration in solution.

After the gel was synthesized, it was mixed gently with MB-Dox. The drug loading efficiency (DLE) of MB-Dox into the gel averaged 91.3% while the hydrogel loading content (DLC, i.e., loading content) was 52.4%; while most nanoparticle drug carrier systems are only starting to accomplish drug loading content over 10%, fabrication of these carriers is more labor intensive and loading efficiency can also suffer.[255] These results therefore demonstrate the DNA hydrogel's competitive and robust drug loading potential. The hydrogel could load the compound on the order of hundreds of micromolar; it adopted MB-Dox's blue color (Figure 4.3a and Figure 4.15).

4.3.2.2. Hydrogel PA Characterization

When irradiated with 680-nm pulsed NIR laser, the photoacoustic signal from the loaded 1.7 wt% hydrogel was fivefold higher than the signal of same concentration of free MB-Dox in water (Figure 4.3b–d), which can be explained by the forced aggregation between the molecules and a net decrease in efficient heat transfer between them.[256] When the PA spectrum of the hydrogel was compared to the spectrum of the free MB-Dox, however, the hydrogel showed a red-shifted photoacoustic peak that ranged between 710 and 730 nm depending on the wt% of the hydrogel (Figure 4.3f). This characteristic energy shift is most likely due to the increased local concentration between the MB-Dox molecules. The tight assembly of intercalated organic molecules into DNA resulted in increased J-aggregation (“head to tail” molecular assembly), which characteristically red-shifts peak absorption.[257–259] The red-shifted peak in the loaded

hydrogel—both by increased weight % and increased loading capacity—confirm that the MB-Dox molecule orients itself within double helical DNA via head-to-tail assembly rather than stacking. This change in peak wavelength is a valuable feature[260] that can photoacoustically differentiate loaded MB-Dox from free MB-Dox in solution.

Patterns in PA spectral shifts can be exploited for quantitative characterization. Changes in gel wt% (i.e., fixing the added MB-Dox amount in the gels while tuning their wt% in the solvent) resulted in signature PA wavelength shifts; thus, it was essential to investigate any characteristic shifts based on the extent of drug content. Therefore, PA spectra were plotted with respect to drug loading capacity in the hydrogels. When the hydrogels were loaded at up to 100% loading capacity (i.e., full drug loading content is achieved when loading the hydrogel), the PA peak remained at around 730 nm. The PA peak was at 680 nm below this amount, even at as much as 50% loading capacity, similar to free MB-Dox in solution (Figure 4.3g). Drug loading capacity does not possess the same spectral shift behavior as is seen with the gel wt%. This can be explained by the fact that the MB-Dox molecule is not intercalated within the hydrogel at full capacity: J-aggregation is less prevalent with less red-shifted PA wavelengths as observed at higher loading capacities. This behavior provides an advantage because spectral shifts from the hydrogel can be directly tied to change in wt% of the hydrogel itself, with no ambiguity as to whether the changed amount of loaded drug contributed to the shift. Therefore, spectral shifts of the hydrogel after in vivo administration can indicate the change in the gel wt% that can amount to quantitative capabilities when monitoring the hydrogel in live tissue (Figure 4.3h).

The photostability of the hydrogel was also evaluated. In brief, the hydrogels were exposed to the pulsed NIR laser for 15 min, and the change in PA intensity was monitored and

analyzed. When hydrogels with different loaded amounts of MB-Dox were tested, the PA intensity decreased below 90% at 33% loading capacity (Figure 4.16a,bOn the other hand, when gels at 100% loading capacity but with different wt% ranging from 0.22 to 0.88 wt% were tested, the lowest photostability (for the 0.22 wt% hydrogel) still maintained 93% PA intensity (Figure 4.16d,e). When free MB-Dox was tested for photostability, the lowest concentration (17.53×10^{-6} m) had decreased photoacoustic intensity to 94% (Figure 4.16c,f). These results underline the robust photostability of the compound and the loaded hydrogel.

4.3.2.3 Hydrogel Degradation and Cytotoxicity

The transient nature of the hydrogel is due to its digestion from rich nuclease activity in biological fluids. When the hydrogel was administered to SKOV3 cell cultures, its initial visibility to the naked eye disappeared over the span of 24–48 h depending on the wt% of the gel. Yet because MB is also a fluorescent molecule, fragments of the hydrogel and the payload with respect to the cells could be monitored using fluorescent cell microscopy: A fluorescent channel with an excitation wavelength of 635 nm was sufficient to localize MB signal. After 24-h hydrogel incubation, cell death was apparent while micron-ranged gel fragments were present in the media. Red fluorescent signal was seen both from unreleased MB-Dox inside the fragments, and inside of the dying cells (Figure 4.4b–d). It was therefore corroborated that the cytotoxic effects of the hydrogel against the cells (Figure 4.4a) was due to MB-Dox release and internalization. MB-Dox was also incubated in cell culture media for 24 h at 37 °C and characterized via ESI-MS; it was confirmed that the compound maintained molecular integrity and was not cleaved by biological media (Figure 4.14).

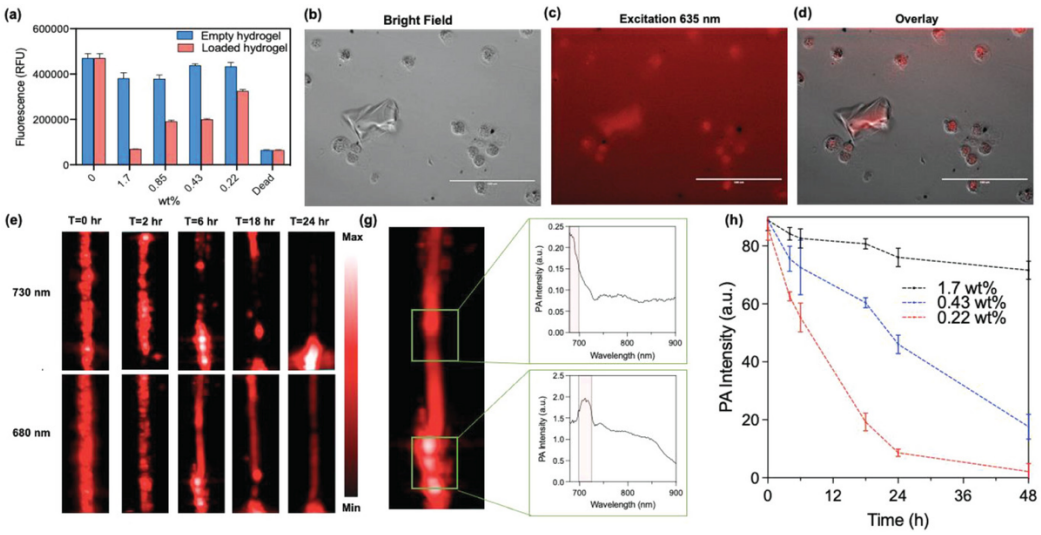

Figure 4. 4 Hydrogel degradation and MB-Dox release in vitro.

a) Cytotoxicity measurements of SKOV3 cells with empty versus loaded hydrogels at differing wt% show that increasing wt% of loaded hydrogel is increasingly toxic to the cells while empty DNA hydrogels had no toxicity. b) Bright field image of dying SKOV3 cells and hydrogel fragments. c) Fluorescent image with excitation of 635 nm of the same image and d) overlay show fluorescence from the MB is present in both the hydrogel fragment and dying cells and that the MB-Dox in fact enters inside the cells for its cytotoxic effects. e) PA images of degrading MB-Dox loaded hydrogel sample at different wavelengths show a decrease in PA signal at 730 nm while PA signal at 680 nm becomes more uniform, thus outlining the decay of the hydrogel and release of free MB-Dox. g) Spectral scanning at different areas of the reaction tube elucidate where the degrading hydrogel fragments are versus released free MB-Dox by their characteristic 730 and 680 nm PA peaks, respectively. h) Decreased PA intensity of the hydrogels at 730 nm with different wt% DNA hydrogels indicate that decreasing wt% leads to faster degradation and faster decrease in hydrogel PA signal when scanned at time points over 48 h (n = 3).

The release kinetics of the transient hydrogel was monitored with respect to PAI. The hydrogel was incubated in 100% mouse serum at 37 °C, and the same sample was imaged over the span of 48 h. Samples of different wt% were evaluated. The hydrogel-serum samples were confined in plastic tubing and were not removed or agitated during the entire experiment. The tubes initially showed strong PA signal throughout the tube, but the signal became less uniformly distributed by 6 h of incubation time, and fragmentation of the gel with free floating or released MB Dox became increasingly apparent (Figure 4.4g). Release kinetics was quantified using

optical absorbance measurements alongside PA signal with independent samples: The increased absorbance of MB-Dox was monitored by measuring the supernatant surrounding the degrading hydrogel, while the decreased absorbance of DNA was monitored at the sediment at the bottom of the reaction tube (Figure 4.17).

However, during the PA monitoring of hydrogel degradation, the same sample was imaged both at 730 and 680 nm wavelengths, which are the peak PA wavelengths for the hydrogel and free MB-Dox, respectively. Over time, the PA signal across the tube at 730 nm scanning decreased and became less uniform while the PA signal at 680 nm became increasingly uniform throughout the entirety of the tube (Figure 4.4e). Spectral measurements were then taken at locations in the tube were there was more concentrated PA signal observed in the images, and the peak at these regions corresponded to the hydrogel spectra. These measurements illustrated that multiwavelength scanning could clarify both the structural decay of the hydrogel and the release of the MB-Dox that spread throughout the tube.

4.3.3. Hydrogel In Vivo Performance

4.3.3.1. Hydrogel Photoacoustic Evaluation in Live Tissue

The photoacoustic contrast of the hydrogel was next evaluated in vivo. First, the hydrogel was injected subcutaneously with a 21-gauge needle into the dorsal site of the mouse. The hydrogel was immediately localizable using PAI, and signal was maintained in the exact same location over the span of a week (Figure 4.5a–f). The PA spectra was taken at the region of interest (ROI) that surrounded the signal, and the absorbance peak was found to be at 750 nm. The spectrum of this ROI, however, had a gradual blue shift from 750 to 710 nm over that time (Figure 4.5g). This directly illustrates the gel's degradation and decreased weight percentage.

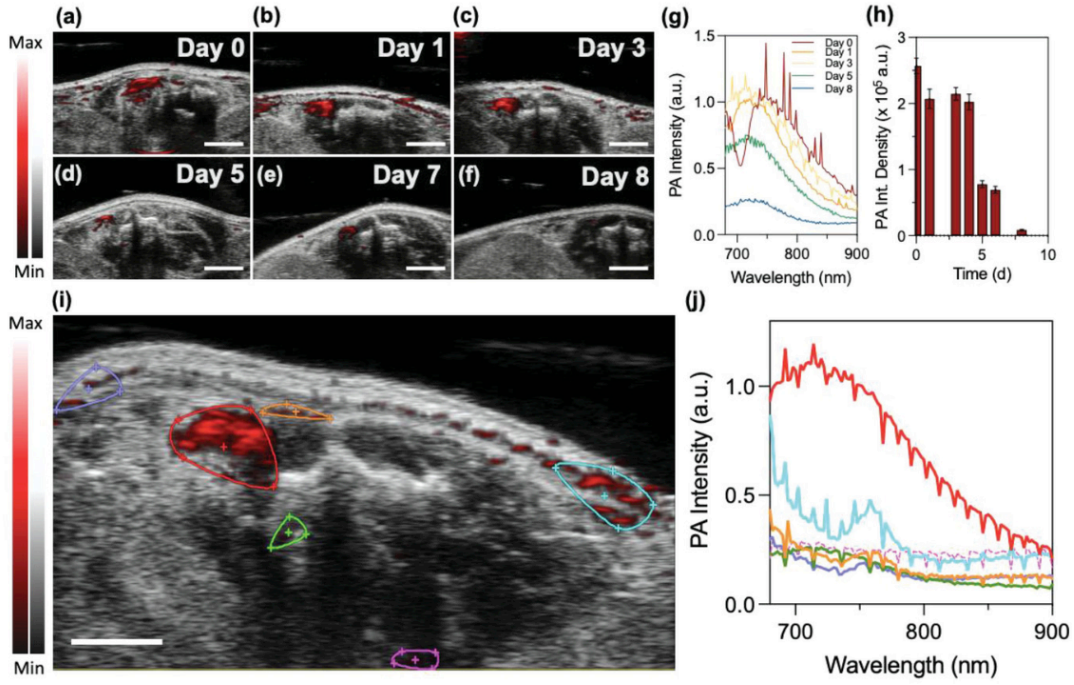

Figure 4. 5 Hydrogel in vivo photoacoustic imaging (PAI)

a–f) In vivo B-mode and PA overlay images show that the hydrogel maintains strong contrast under the same PA gain and remains in the same location after it was injected into a mouse over the span of 8 days. g) Corresponding PA spectra of the hydrogel over 8 days shows a gradual blue-shifted PA peak from 750 to 710 nm due to decreased wt% of the hydrogel from nuclease digestion in vivo. h) A decrease in in vivo PA signal of the hydrogel over the time span. i) PA-B mode overlay image with color coded ROIs and their corresponding spectra in (j) show that ROIs with 730 nm versus 680 nm peak PA signal can localize hydrogel fragments from released MB-Dox in live tissue. Scale bars: 2 mm. Spikes in PA spectra caused by pulse in live mouse while scanning.

It was important to assess the MB-Dox's ability to maintain PA visibility even after its release from the degraded hydrogel. There were several other regions in surrounding tissue that also emitted PA signal, but spectral scanning helped corroborate if those signals were from MB-Dox or background from endogenous molecules. Spectral scanning successfully localized sites of free MB-Dox because the spectra for these sites indicated a PA peak at 680 nm, which was identical to the spectral behavior from free MB-Dox in water (blue, purple, and orange ROIs with corresponding color-coded spectra in Figure 4.5i,j). The spectra taken from these regions

were compared to control background PA sites, which gave off broad, peak-free spectra that most likely originated from blood and hemoglobin, such as seen from the pink spectrum in Figure 4.5j corresponding to the pink outlined ROI in Figure 4.5i. Other regions of PA intensity maintained a spectral peak at 730 nm that was separate from the originating hydrogel location, which indicated fragments of the hydrogel travelled to other sites in tissue (green ROI and spectra in Figure 4.5i,j). This study confirms that when the wavelength of the free and loaded drug is established, it can be monitored in real-time and in live tissue.

The initial 740 nm PA intensity wavelength from the hydrogel becomes increasingly important in vivo as the SBR decreases especially as incident PA wavelengths approach 532 nm.[186] The peritoneal cavity, for example, is a common site for a wide class of reproductive and stomach cancers that have developed into advanced stages.[261,262] However, its highly dense networks of blood vessels make the region particularly difficult for many PA contrast agents to maintain adequate SBR.[263] When the hydrogel was intraperitoneally injected into the mouse (Figure 4.6c,d and Figure 4.18), it was localizable as much of the background was minimized when the mouse was scanned at a 740 nm laser (Figure 4.18).

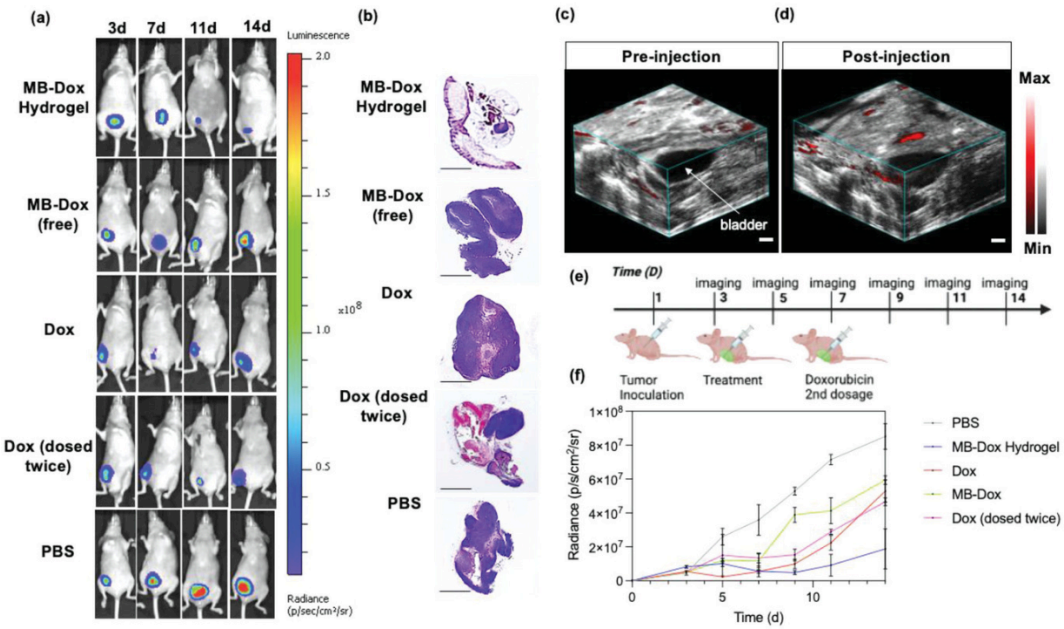

Figure 4. 6 Hydrogel performance for intraperitoneal antitumor efficacy.

a) Representative bioluminescent and photograph overlays of mice tumor burden when treated with different formulations over time demonstrate the hydrogel's efficient release and thus administration of doxorubicin. b) H and E images of the harvested peritoneal tissue after the treatment period: Dark purple indicates dense growth of tumor cells (scale bar = 2 mm. c,d) Pre- and postinjection of the photoacoustic hydrogel intraperitoneally, next to the bladder of the mouse on its right side Scale bar = 2 mm. e) Timeline of tumor burden study. f) Quantified tumor radiance against time shows mice treated with the MB-Dox hydrogel showed the most effective anti-SKOV3 activity (n = 5).

4.3.3.2. Hydrogel Therapeutic Efficacy In Vivo

The antitumor efficacy of the hydrogel was finally examined. The hydrogel was studied with an SKOV3-luciferase intraperitoneal murine model, and the tumor burden was monitored by observing changes in bioluminescent signal over 14 days (Figure 4.6e). The loaded hydrogel's efficacy was compared to the following controls: (1) Free MB-Dox intraperitoneally injected at the same concentration of loaded MB-Dox in the hydrogel (9 mg kg^{-1}), (2) Dox intraperitoneally injected at the same concentration of the MB-Dox (9 mg kg^{-1}), (3) Dox administered at half of

the concentration, but twice throughout the period (4.5 mg kg^{-1}), and (4) PBS as the negative control. These controls provide direct comparison between the hydrogel and its counterpart drugs as well as single versus periodic dosing. These different cases were intraperitoneally injected into the mice 3 days after they were inoculated with the SKOV3-luc cells. Before drug injections, luminescent imaging confirmed that each mouse had the same relative bioluminescence (Figure 4.6a and Figure 4.19b

Three days after drug injections, the mice injected with single dosage of dox had a direct response as the bioluminescence decreased by 54.2%. Meanwhile, the burden of the hydrogel remained relatively constant, as the bioluminescence did not significantly increase or decrease since it was initially injected. However, 7 days after the dosage, the mice with the hydrogel showed significant decrease in tumor bioluminescence, the lowest signal compared to the other cases. By the end of the study, the hydrogel treatment resulted in 77.91% (+/− 8.79%) decreased radiance, while free MB-Dox, single and double dosed dox resulted in 30.24% (+/− 5.78%), 38.92% (+/− 10.28%), and 55.67% (+/− 9.17%) decreased radiance, respectively (Figure 4.6f and Figure 4.19b). This trend remained in agreement with histology analysis of the mice subjects ex vivo, which revealed that there was less proliferation of the xenografted cancer cells in the live tissue, and that there was notably increased red fluorescence in the tumor tissue from the hydrogel-delivered MB-Dox, as opposed to when the MB-Dox was administered freely (Figure 4.6b and Figure 4.20). These results demonstrate that when compared to conventional chemotherapy, the hydrogel displays more efficient antitumor efficacy ($p = 0.0015$). This improved antitumor efficacy supports past reports on a hydrogel's advantageous use as a drug delivery vehicle: The slow matrix erosion enables a more gradual release of the drug. This in

turn reduces toxic levels of free doxorubicin, avoids a rapid decrease in drug concentration from fast metabolism, and prolongs therapeutic effects over a wider treatment timeline.[264–266]

Supplementary therapeutic effects from NIR laser activated MB-Dox remained in question. Therefore, a group of mice injected with the loaded hydrogel were further irradiated with an NIR laser (660 nm, 100 mW) for photoactivation (Figure 4.7a). Like the in vitro experiments (Figure 4.13), the endpoint tumor burden did not lead to a significant decrease in bioluminescence when compared to the loaded hydrogel that was not exposed to the light, as the NIR-irradiated group led to an average of 80.2% decreased radiance (+/− 5.34%) (p = 0.545). Yet interestingly, decreased radiance occurred earlier when compared to the loaded hydrogel alone, indicating the further light-activated hydrogel led to localized cytotoxicity that in turn amounted to a more expedited tumor toxicity (Figure 4.7b,c). Because the payload and the hydrogel have demonstrably robust photostability, and because drug release surveillance is more reliant on spectral shifts for quantitative evaluation, both imaging-assisted monitoring and light-assisted therapy can occur without significant risk of signal loss.

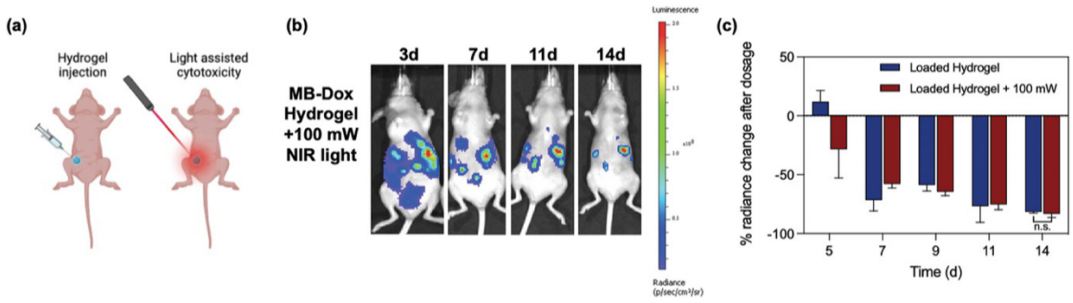

Figure 4. 7 NIR light activated cytotoxicity from the hydrogel.

a) Schematic shows setup of exposing the injected hydrogel to a 660 nm laser for NIR-activated cytotoxicity. b) Bioluminescent images of a mouse subject shows decreased radiance relative to the hydrogel treated mice in Figure 4.6a. c) Analysis of radiance shows that while light activation allowed an earlier decrease in radiance from the loaded hydrogel, the endpoint therapeutic efficacy was not significantly different ($p = 0.545$, $n = 5$).

The DNA hydrogel had three roles: (1) The hydrogel could load a high amount of the MB-Dox compound due to strong intramolecular affinity between the compound and the DNA framework. (2) The dense intercalation of the highly concentrated compound in the DNA framework promoted J-aggregation that led to distinct PA spectral shifts for quantitation of drug release. (3) Gradual erosion of the hydrogel due to nuclease activity led to the slow and local release of the MB-Dox drug so that the antitumor efficacy from the formulation outperformed doxorubicin, despite doxorubicin's lower IC50 value relative to MB-Dox. This report exemplifies that the formulation of therapeutics alone can offer unique advantages that may enhance the efficacy of the drug itself.

4.4. Conclusions

This work introduced a hydrogel that possesses chemotherapeutic efficacy while offering comprehensive monitoring of drug release and biodistribution via real-time bioimaging. While this study sought to specifically investigate a DNA hydrogel's ability to load photoacoustic anticancer drugs and control their release through gradual nuclease activity while monitoring the

state of the drug, several other accessory features can be considered with this system due to DNA technology's vast multifunctionality. For example, immunotherapeutic CpG sequences and cancer cell targeting aptamer motifs can be embedded in the DNA hydrogel itself. This work illustrates hydrogels as effective means of drug delivery, where the release of a drug is preferably gradual. In the future, hydrogel materials and formulations can be further evaluated for a wide range of treatment applications, such as embedded within bolus for stomach cancers, topically applied for melanoma and other skin-local cancers, transmucosal administration, or direct injection into neck cancers.

4.5. Acknowledgements.

Chapter 4, in full, is a reprint of the material as it appears in Advanced Science 2023. Borum, Raina; Moore, Colman; Mantri, Yash; Xu, Ming; Jokerst, Jesse V. The dissertation author was the primary investigator and author of this paper.

4.6. Supporting Figures

Table 4. 1 Sequences used for the DNA hydrogel, which was directly from Wang et al's design.[252]

'HG1' and 'HG2' are the amplifying strands that crosslink together after they recognize the initiating 'HGIn' strand that catalyzes the gelation.

Strand name	Sequence (5'→ 3')
HG1	GATCGCGATCCTGGCTCCTGTGATTGTGCTCTAGACATCGCTAGAGCACAATCACAGG
HG2	CTAGAGCACAATCACAGGAGCCAGTTTTCCTGTGATTGTGCTCTAGCGATGT
HGIn	CTA GAG CAC AAT CAC AGG AGC CAG

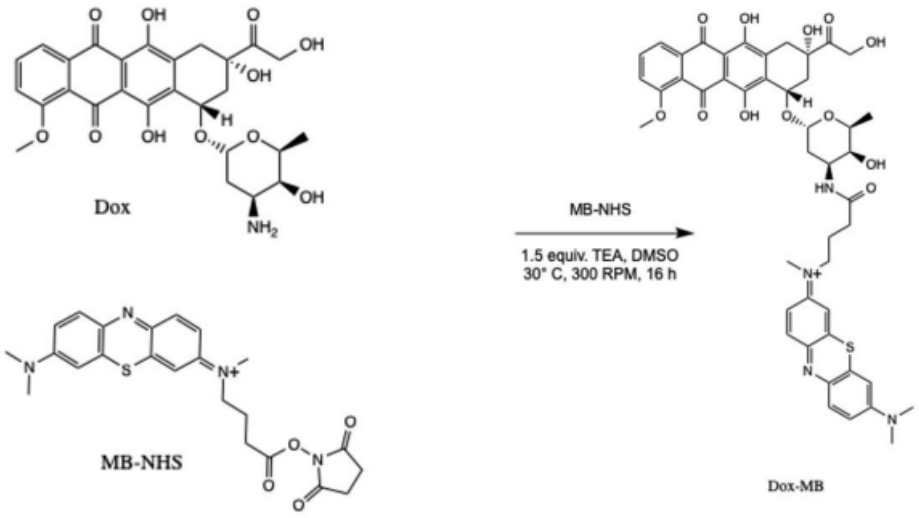

Figure 4. 8 Reaction scheme on the synthesis of MB-Dox.

NHS activated Methylene Blue is linked with Doxorubicin through a simple amine reaction between the sugar moiety and NHS tag on doxorubicin and methylene blue, respectively. The process was assisted by triethylamine (TEA) in DMSO over 16 hours.

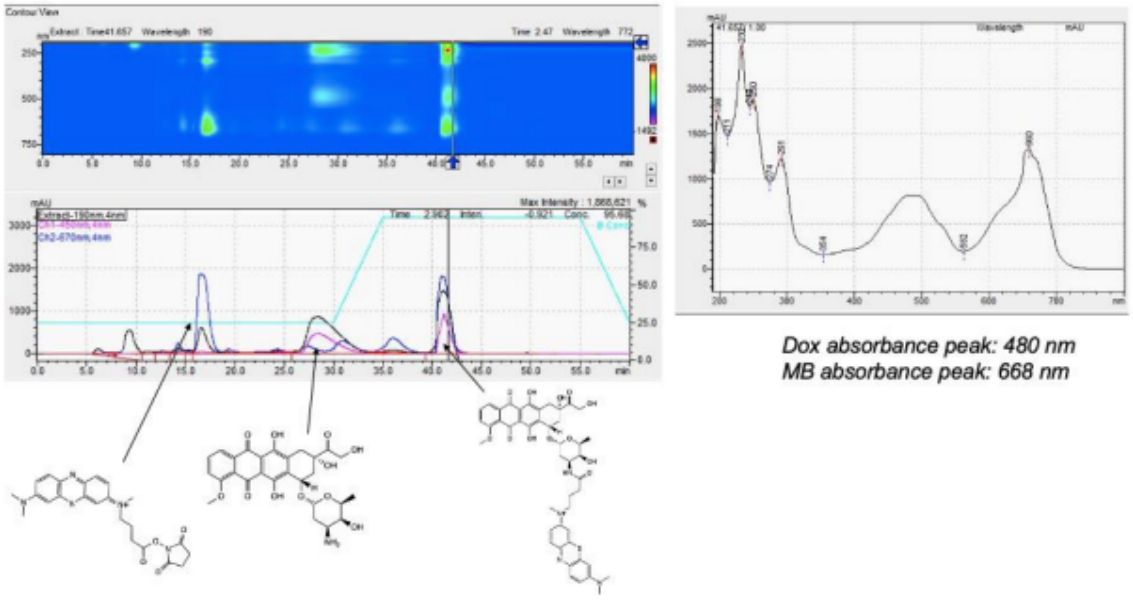

Figure 4. 9 RPP-HPLC liquid chromatogram of the purification process of MB-Dox.

Unconjugated MB and Dox fractions were eluted in isocratic 30% MeCN/H2O (v/v) between 15 and 30 minutes, respectively, while the product was released at 90% MeCN (B) concentration. The same protocol was run to validate pure MB-Dox products as in Figure 4.2B in the main text.

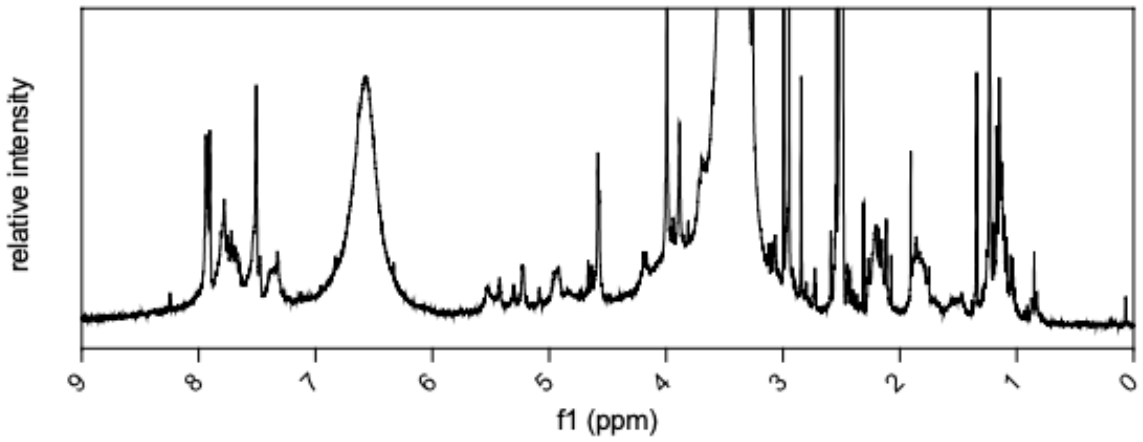

Figure 4. 10 1H NMR (300 MHz, DMSO-d6, δ)

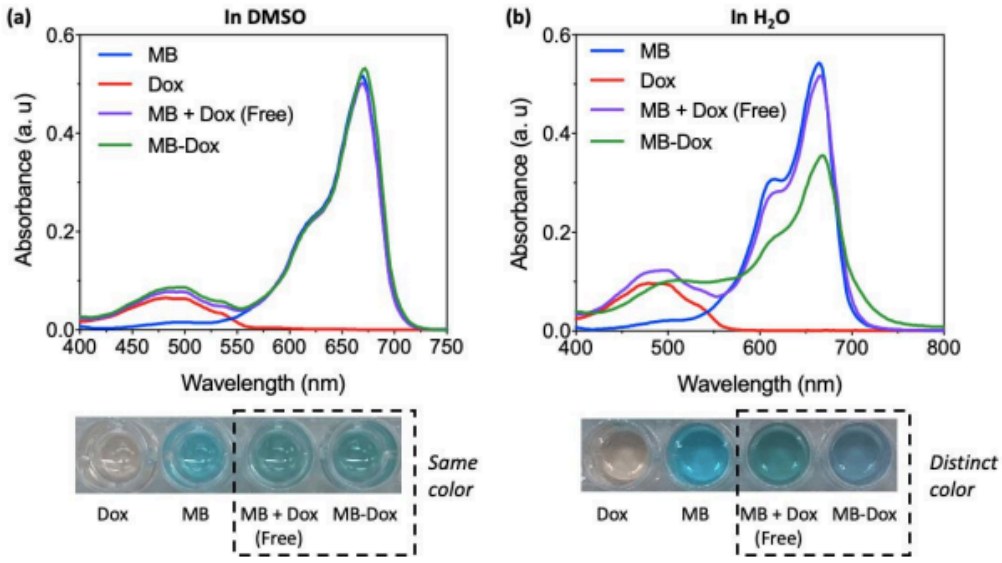

Figure 4. 11 Difference in optical absorbance spectra in MB-Dox when in DMSO versus water. (a) in DMSO, the absorbance peak of MB-Dox is nearly identical to additive curves MB and Dox when mixed together. However, when observed in water (b) the MB-Dox compound exhibited a slight 3 nm red shift.

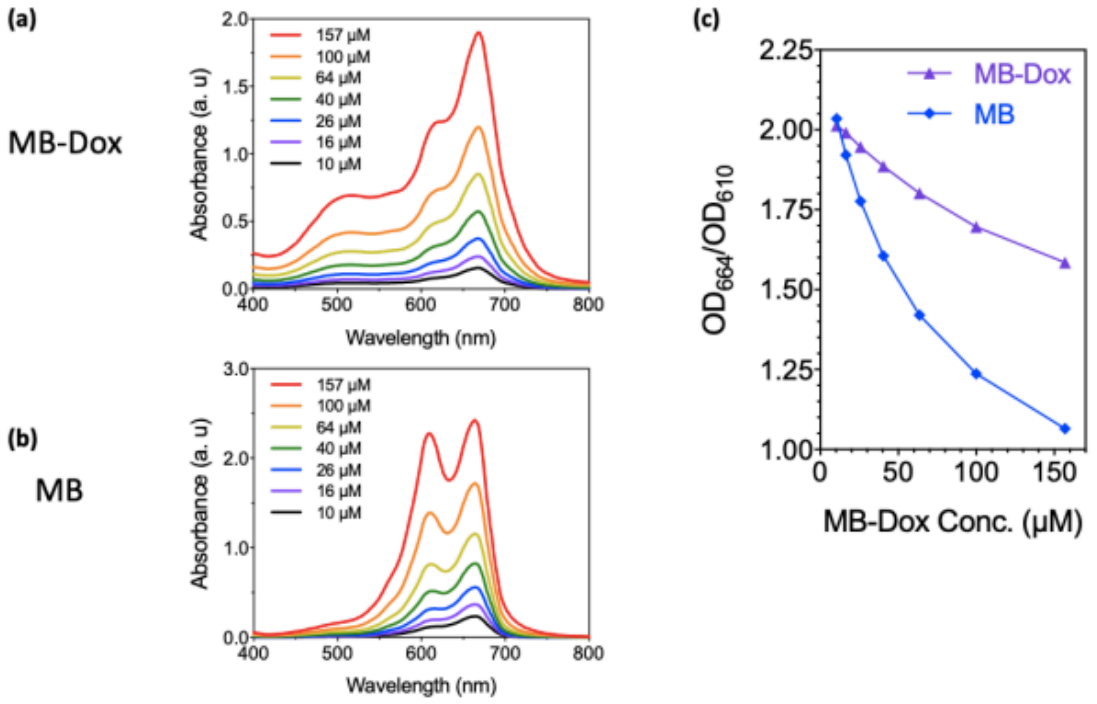

Figure 4. 12 Optical comparison between MB-Dox and MB.

(a)When MB-Dox has increasing micromolar concentrations in water, there is no increase in a secondary 610 nm peak that is usually seen in MB dye alone, which is typically caused by dimerization between the dye molecules. (c) Ratiometric absorbance measurements between MB-Dox and MB at increasing concentrations further demonstrate MB-Dox's structural protection over self-dimerization in water.

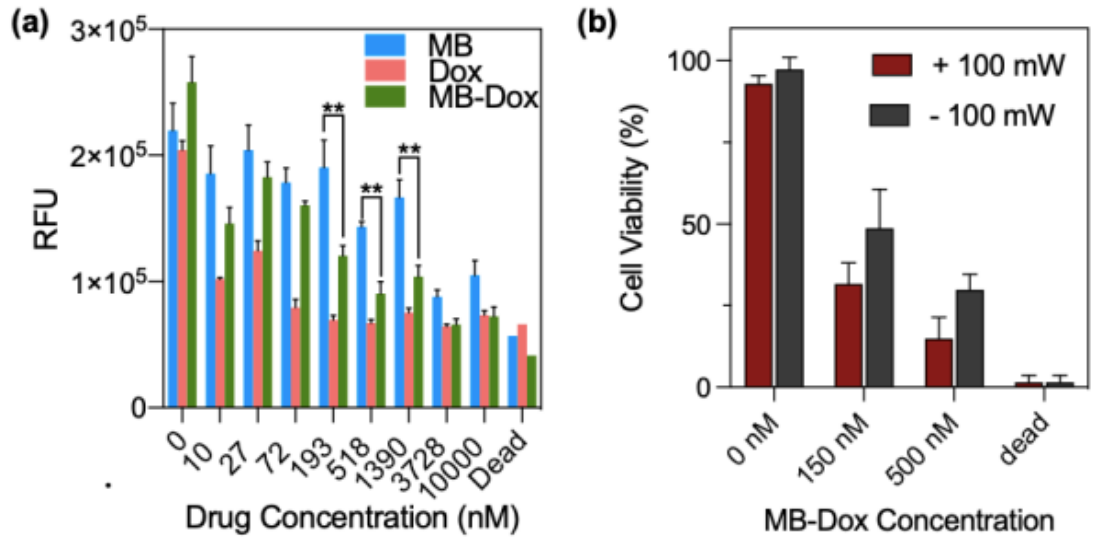

Figure 4. 13 MB-Dox cytotoxicity profile via resazurin assay, where increased fluorescence indicates less toxicity against the growing SKOV-3 cells.

(a)Cytotoxicity of MB-Dox, MB, and Dox against SKOV-3 cells (**P<0.001, student's t-test). (b) Photodynamic therapy demonstration shows higher cytotoxicity when cells incubated with MB-Dox are further exposed to 100 mW red light.

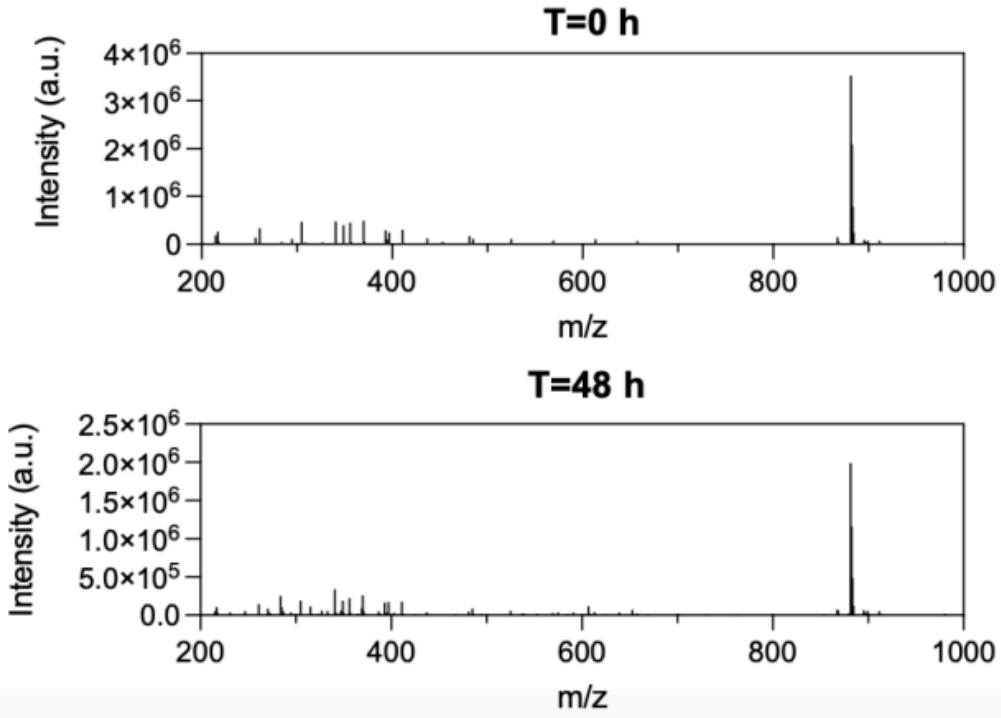

Figure 4. 14 Molecular stability of MB-Dox in cell culture media at 37°C over 48 hours as confirmed via ESI-MS.

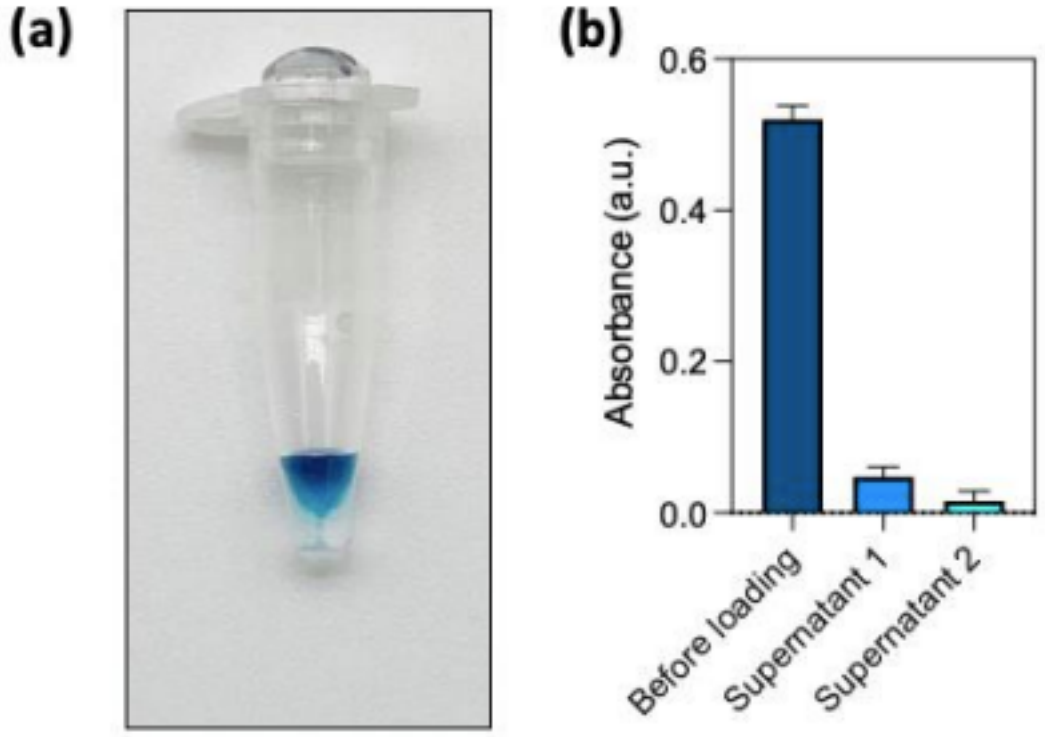

Figure 4. 15 Hydrogel loading efficiency with MB-Dox

(a)photograph of hydrogel floating in nuclease-free water of centrifuge tube shows that the MB-Dox does not leak out of the hydrogel and into the supernatant. (b) Quantified optical density of supernatants after rinsing loaded hydrogel demonstrate a 91.29% loading efficacy (n=3).

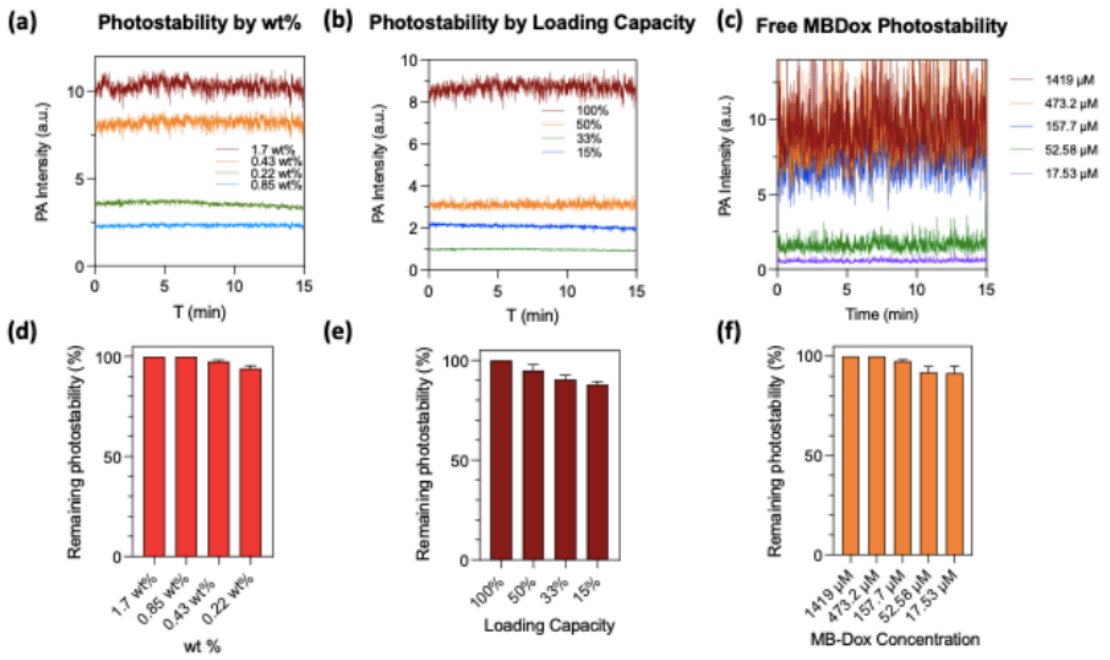

Figure 4. 16 Photostability of loaded hydrogels and MB-Dox.

(a)-(c) show raw data of photoacoustic intensity during 15-minute constant excitation for hydrogels based on wt%, loading capacity, and free MB-Dox in water, respectively. Panels (d)-(f) of corresponding decrease in PA intensity from panels (a)-(c) show that photostability does drop below 87%. The concentrations for free MB-Dox were chosen for photostability testing because these fit within the typical concentration of MB-Dox loaded in the hydrogel. (n=3)

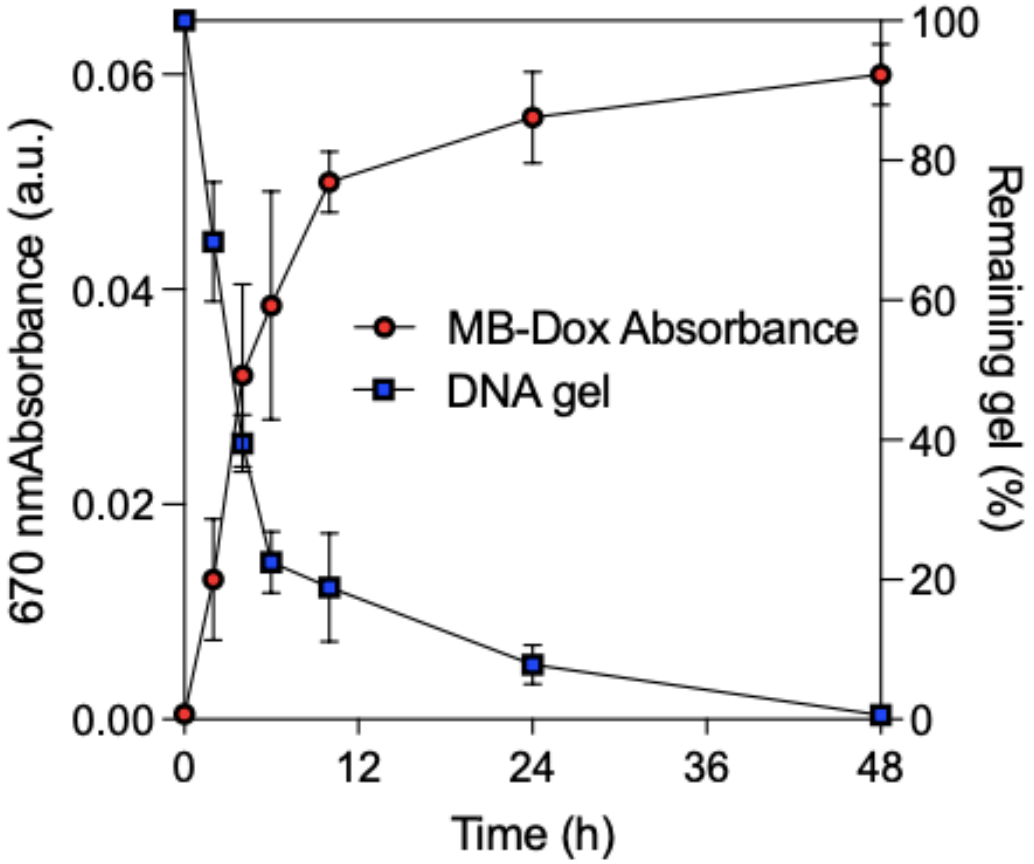

Figure 4. 17 Hydrogel degradation and MB-Dox release profile via optical absorbance measurements of a 0.22 wt% loaded hydrogel (n=3).

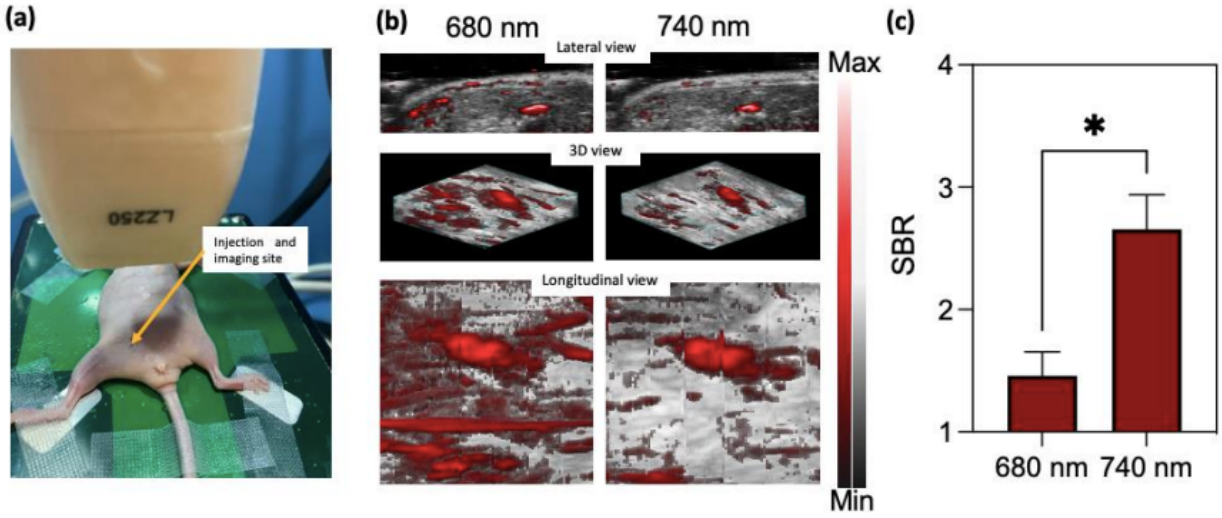

Figure 4. 18 Intraperitoneal PA imaging in vivo

(a) setup for in vivo intraperitoneal imaging, where the transducer is above the injection site of the mouse while it is fixed on a heating pad and anesthetized. (b) lateral, 3D, and longitudinal views of the photoacoustic hydrogel after intraperitoneal injection shows significantly improved contrast from the gel relative to endogenous PA by changing the NIR wavelength from 680 nm to 740 nm. (c) Although the same gel was imaged under both wavelengths, the 740 nm wavelength scanning showed a significantly ($p=0.0129$, student's t-test) enhanced signal to background ratio (SBR) over 680 nm scanning.

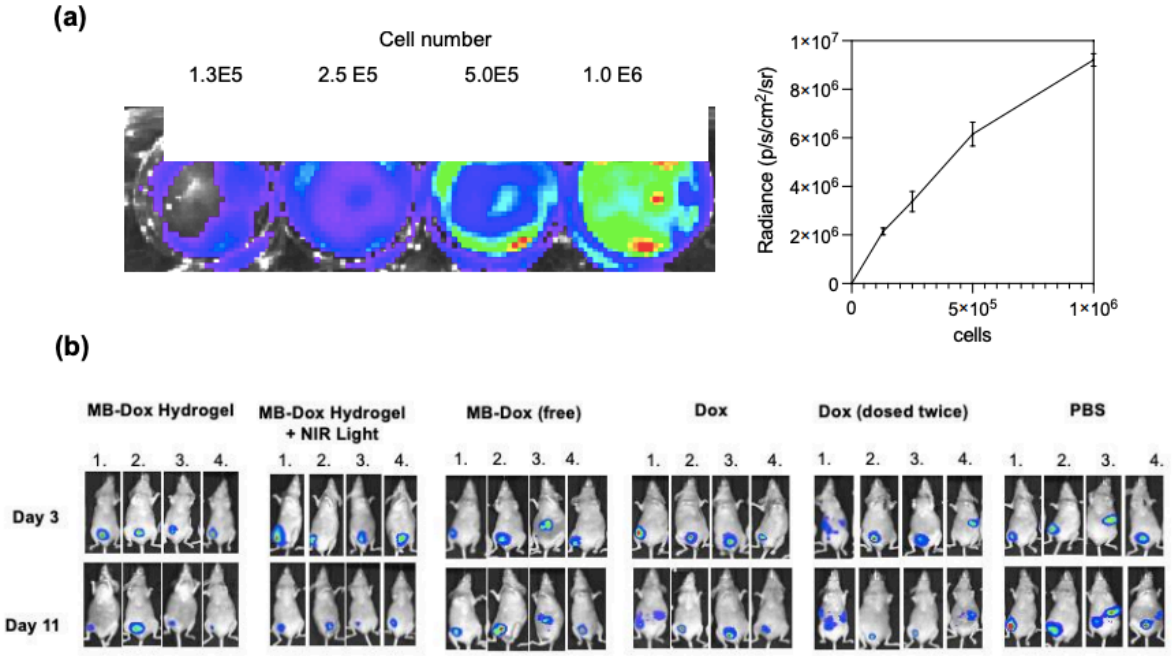

Figure 4. 19 Monitoring bioluminescence of luciferase expressing SKOV-3

(a) in vitro image and quantified bioluminescence of luciferase expressive SKOV-3 cells. (n=3) **(b)** Anti-tumor efficacy via in vivo bioluminescence monitoring: Bioluminescent images of the remaining four of five mice per group show similar relative bioluminescence three days after tumor inoculation, while the mice treated with the loaded hydrogel showed the most decreased bioluminescence from the gradual release of the MB-Dox payload.

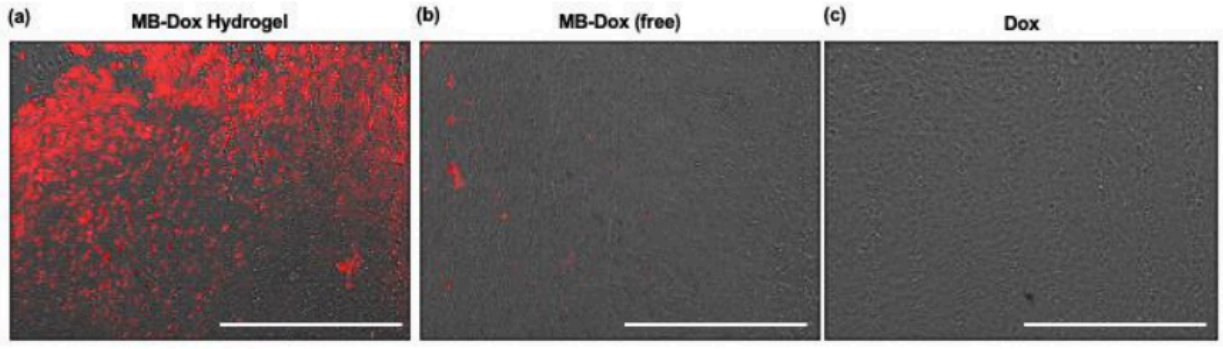

Figure 4. 20 Ex vivo fluorescent histology analysis of the harvested peritoneal tissue

(a) heightened fluorescence inside the cells from accumulated Methylene Blue signal from when the mouse was treated with the loaded MB-Dox hydrogel; the local delivery of the compound from the hydrogel erosion after installation outperforms the delivery of the MB-Dox when it was freely injected while in PBS, as is seen with significantly decreased fluorescence in panel (b). As a control, the mouse treated with free dox did not show any fluorescence as seen in (c). Scale bar=100

CHAPTER 5: AN INVESTIGATION OF SELF-ASSEMBLED PEPTIDE-DYE NANOSTRUCTURES FOR IN VIVO TUMOR IMAGING AND PHOTODYNAMIC TOXICITY

ABSTRACT: Designer peptides leading to self-assembled nanoparticles have value in activatable molecular imaging and targeted drug delivery. However, the adverse effects and behaviors of these particles with biological systems are poorly defined especially as a function of morphology and intramolecular assembly pathways. Here, we investigate noncovalent assemblies between peptides and molecular dyes via electrostatic and hydrophobic stacking into nanoparticle formulations. We then assess their optical properties, physical properties, and performance in live cell targeting, *in vivo* imaging, and *in vivo* photodynamic toxicity in parallel. iRGD and methylene blue were the model peptide and dye, respectively. We tuned the performance of iRGD by annealing aspartic acid (DD) or tryptophan doublets (WW) to promote electrostatic or hydrophobic stacking affinities with methylene blue, respectively. The iRGD-DD led to 150-nm sickle-like nanofibers, but iRGD-WW produced 200-nm nanospheres. The nanofibers yielded a redshifted 720-nm photoacoustic signal while the nanospheres had a peak at 680 nm more similar to monomeric methylene blue. The spheres and fibers produced 116.62% and 94.82% ROS-based increased reporter DCF fluorescence in SKOV-3 cells versus free methylene blue from targeted phytodynamic toxicity; targeted uptake was validated via competitive inhibition. Both nanospheres and nanofibers showed heightened and sustained contrast and specificity to solid tumors in murine intraperitoneal SKOV-3 models. Further, the nanofibers slowed tumor burden by 75.91% ($p=0.043$), while spheres decreased SKOV-3 tumor burden bioluminescence by an average of 58.89% ($p=0.089$) when activated for photodynamic therapy.

5.1. Introduction

Peptides have become a critical tool in drug discovery, therapeutics, and chemical biology. For example, peptides can be engineered to interact with T-Cell epitopes for triggered immunogenicity[267], upregulated membrane receptors in solid tumors[268], and enzyme biomarkers for targeted inhibition. Peptides have also been used to identify novel targets and new inhibitors[269]. Peptide engineering is also increasingly available and accessible to industry and small labs alike, where solid phase synthesis can be implemented in-house with many automated resources on the market, and analytical methods that have been standardized for decades[270]. Therefore, the use of peptides as biomolecular probes, small molecule carriers, and theranostics could offer indispensable value in biomarker targeting, molecular imaging, drug delivery, and live tissue imaging. Covalent ligation between peptides and the agent, however, can sometimes be costly or only promise modest conjugation yields, thus bottlenecking scale-up methods and availability, regardless of their promising initial results[271-272].

Nanoparticles and nanoscale assemblies, on the other hand, have demonstrated potential for novel therapeutics and drug delivery vectorizations. Self-assembling peptide nanoparticles (SAPNs) have thus gained increasing attention: Here, peptide sequences are engineered so that one component is biologically triggered while the other component tunes the peptide's physical properties via zwitterionic, charged, or hydrophobic regimes. Examples include tissue regeneration, targeted cytotoxicity, nucleic acid delivery, and molecular imaging.[273-274] However, this strategy yields nanoparticles with different architectures and shapes, which can affect their interactions with biology. While many reports discuss the ideal application for different resultant geometries of SAPNs[275], few reports explore this discussion by empirically comparing the performance between the different resultant geometries in parallel.

Here we investigate the non-covalent assemblies between a tumor homing peptide (iRGD) and molecular dye (Methylene blue). The interactions lead to different nanoparticle morphologies based on the addition of two extra amino acids. That is, we added amino acid residues on the tail of iRGD that promote either electrostatic or hydrophobic stacking affinities with methylene blue by using aspartic acid (DD) or tryptophan doublets (WW) respectively. iRGD was chosen as the model peptide because it is a well-established and robust bimodal targeting peptide against solid tumors: iRGD first internalizes into cancer cells via $\alpha V\beta 3$ and $\alpha V\beta 5$ integrin recognition. Upon cleavage into CRGDK/R, the exposed C-endR motif (R/KXXR/K) allows the fragmented peptide to enable the tumor microenvironment (TME) vasculature permeability through neuropilin-1 (NRP-1) interactions.[276-278] This peptide has demonstrably made it possible to introduce active targeted drug delivery by mere co-loading between the peptide and the drug rather than by covalent tethering. Methylene blue, an FDA-approved dye and longstanding workhorse in the clinical landscape, was selected as the molecular dye in this work for several reasons: As a molecule, it is both hydrophobic and cationic, making it possible to explore two possible self-assembled formulations. As a dye, it absorbs light in the NIR (~670 nm) window, making it visible under centimeter-scaled penetration and thus a candidate for live tissue imaging and photoacoustic contrast[279]. As a chemical, its redox potential enables activatable reactive oxygen species (ROS) generation, making it cytotoxic[280]. (Figure 5.1)

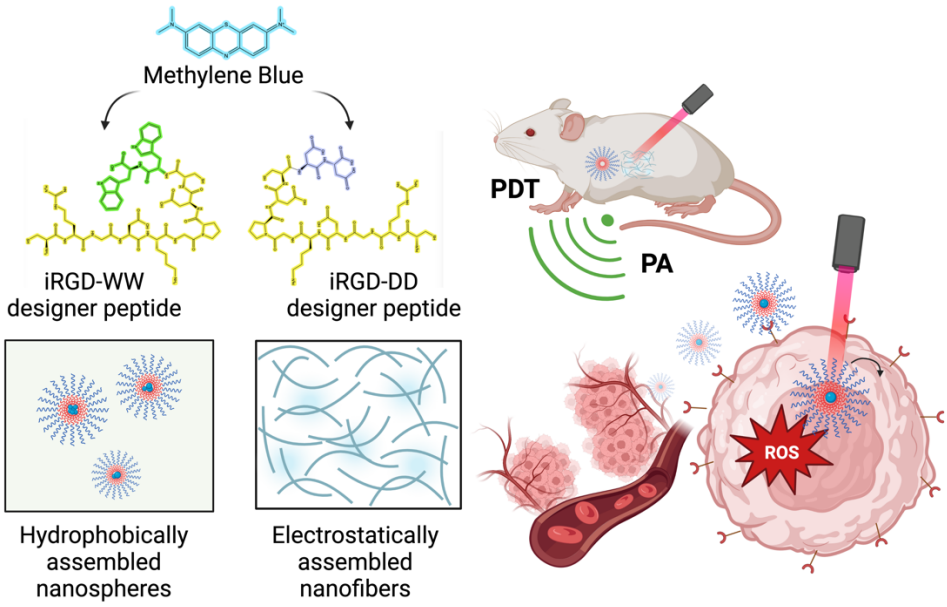

Figure 5. 1 iRGD-Methylene blue self-assemblies

(a) assembly of iRGD-methylene blue nanofiber and nanosphere formulations based on electrostatic and hydrophobic stacking affinities, respectively. (b) Designer iRGD-methylene blue

5.2. Methods

5.2.1. Peptide synthesis and preparation

Peptides were synthesized using standard solid-phase synthesis (AAPTec Eclipse) on Wang resin solid support. Peptides were cleaved with TFA:Phenol:Water:Thioanisole:EDOT (82.5:2.5:5:5:5) and washed thrice with cold diethyl ether. After lyophilization, peptides were resuspended in water and acetonitrile (30%), and then purified via reverse phase high performance liquid chromatography (RP-HPLC). Pure fractions were characterized via ESI-Mass Spectrometry, and further lyophilized before use.

5.2.2 Peptide Dye assemblies

Peptides were mixed with Methylene Blue in pure milliQ water at a 10:1 peptide-dye molar ratio unless specified. They were allowed to rest at 250 rpm in the dark for two hours.

5.2.3. Multispectral Nanoparticle Tracking Analysis

MANTA ® Multispectral Nanoparticle Tracking Analysis (Horiba Scientific, Irvine, CA) was used for size and concentration measurements of nanoparticles and particle formation kinetics. (MANTA) is a technique that builds images from particle light scattering via three lasers of blue, green, and red wavelengths. The wavelength of scattering depends on nanoparticle size. MANTA was performed with the ViewSizer 3000 (Horiba Scientific) instrument, and temperature was set to 25 °C during all measurements. 8-bit composite videos were generated, and 20 videos were used per analysis (300 frames for seconds). A quartz cuvette with a minimum volume of 1 mL was used for the measurement. Before each sample was measured, a blank measurement of the reaction solvent was measured to reduce background.

5.2.4. Cell Culture

Human Ovarian Adenocarinoma (SKOV-3), Epithelial Human Breast Cancer (MCF-7), and Human Embryonic Kidney Cells (HEK293-T) were used for the cell experiments. SKOV-3 was cultured in McCoy's 5A Medium, and MCF-7 and HEK 293T cells were cultured in DMEM. Medium was supplemented with 10% Fetal Bovine Serum (FBS) and 1% Penicillin Streptomycin. Cells were given 3 passages before use.

5.2.5. In Vitro Photodynamic Cytotoxicity

Cells were seeded overnight in 96 well plates, 10,000 cells per well. Methylene blue and peptide-methylene blue assemblies were then incubated with the cells for two hours before rinsing with PBS. For irradiation, a 100 mW NIR Laser (660 nm) was fixed on a ring stand and pointed to the well for 10 minutes before characterization. Dark control samples were seeded on an entirely different plate and were kept in the dark.

For ROS, 10 μM DCFDCA dye was incubated with the cells for one hour before peptide-dye and dye samples were incubated for two hours. The cells were rinsed in fresh PBS twice and then were exposed to irradiation.

5.2.6. Integrin validation

300,000 cells were detached with trypsin, and then washed in 1mL ice cold buffer (PBS, 5% BSA) at 700xG. The cells were resuspended in ice cold buffer further supplemented with 0.1% sodium azide. The cells were then incubated with the primary $\alpha V\beta 3$ (LM609) and $\alpha V\beta 5$ (P1F6) mAB antibodies ($20\mu g/\mu L$) (abcam) on ice for 30 minutes. After they were washed twice, the cells were incubated with goat anti-mouse IgG Alexa Fluor 488 for 30 minutes on ice in the dark. The cells were then washed twice and resuspended in 1 mL of ice cold buffer before flow cytometry was performed. The FITC channel was used.

5.2.7. Competitive Inhibition

300,000 cells were seeded overnight. For the competitive inhibition samples, cell cultures were incubated with $\alpha V\beta 5$ mABs for 90 minutes. After this time, all cells were incubated with the iRGD-NFs, iRGD-NSs, or methylene blue. The cells were trypsinized for detachment, collected at 700xG, and the media was decanted while the cells were resuspended in ice cold buffer for flow cytometry. The APC channel was used.

5.2.8. Endosomal escape

300,000 cells per culture were seeded overnight. The following day, the cells were incubated with the iRGD-NFs, iRGD-NSs, methylene blue, and the iRGD methylene blue mixture for 90 minutes before incubation with calcein for one hour. The cells were then rinsed, detached with trypsin, then resuspended in ice cold buffer for flow cytometry. The FITC and APC channels were used.

5.2.9. Photoacoustic imaging

PA images of in vitro samples were acquired with a Vevo 2100 LAZR (VisualSonics) using a 21 MHz transducer (LZ-250). Samples were loaded into 0.86 mm polyethylene tubes and fixed in parallel with a 3D printed sample holder. One tube was filled with reaction solvent to serve as a reference. The samples were placed 1 cm below the transducer in a vessel filled with water. Single wavelength scans were operated at 680 and 720 nm at a frame rate of 20 Hz. For 3D PA images, the transducer was scanned with a stepper motor along the axial dimension of the tubes. PA spectra were taken from 680 to 900 nm with a step size of 2 nm.

5.2.10. Animal studies

All mice studies described below were performed in accordance with National Institutes of Health (NIH) Guidelines approved by the Institutional Animal Care and Use Committee (IACUC) under protocol S15050 at University of California, San Diego. Female J:NU mice of 5 weeks of age were used for all in vivo experiments. For imaging experiments, mice were anesthetized with isoflurane.

5.2.11. In vivo photoacoustic imaging

Mice were inoculated with 800,000 SKOV3 (with 50% Matrigel/PBS v/v) intraperitoneally on the right side at the second nipple from the bottom. 10 days after inoculation, the mice were intraperitoneally injected with MB, iRGD+MB, iRGD-NF, iRGD-Ns, (9 mg/kg Methylene blue). As a negative control, a subject was not inoculated with SKOV3 cells but was injected with the iRGD-NS at the same concentration. During imaging, the mouse was anesthetized with isoflurane and laid on its back on the heating pad while the transducer was directly placed above the injection site. Subjects injected with MB, iRGD-NS, and iRGD+MB were imaged using 680 nm wavelength while the subject injected with iRGD-NF was imaged using 720 nm wavelength. All mice were imaged under the same PA and ultrasound gain.

5.2.12. In vivo bioluminescence

Mice were divided into five groups. 800,000 SKOV3-luc cells were injected (with 50% Matrigel/PBS v/v) intraperitoneally on the right side at the second nipple from the bottom. On days 3 and 6 the mice were intraperitoneally injected with MB, iRGD+MB, iRGD-NF, iRGD-Ns, (9 mg/kg), and PBS. To measure tumor burden, mice were imaged with D-luciferin on days 3, 6, and 9, with 100 mg/kg dosage in PBS. The bioluminescence was measured and imaged via IVIS Perkin-Elmer Illumination and LivingImage software.

5.2.13. Ex vivo analysis

After the subject was euthanized, the heart, lungs, liver, spleen, kidneys, and tumor were harvested and rinsed in PBS. The organs were then imaged for fluorescence signal via IVIS Perkin-Elmer Illumination and LivingImage software.

5.3. Results

5.3.1. Peptide design and assembly with Methylene Blue

Designer iRGD peptides and native iRGD were synthesized using solid phase synthesis. iRGD (CRGDKGPDC) was designed so that it was either tagged with aspartic acid doublets (iRGD-DD) or tryptophan doublets (iRGD-WW) to coerce electrostatic or hydrophobic assemblies with methylene blue. The products were purified via reverse phase high performance liquid chromatography (RP-HPLC) and characterized via ESI-Mass Spectrometry (Figure 5.7). Although native iRGD adopts a cyclic structure from disulfide bridging between cysteines, computational simulations demonstrated that the designer peptides do not adopt a secondary structure (Figure 5.6).

Multispectral Advanced Nanoparticle Tracking Analysis (MANTA) was used to monitor size changes and nanoparticle formations during assembly. As a control, native iRGD peptides were mixed with methylene blue at a 10:1 molar ratio in water. However, MANTA demonstrated

that these mixtures did not yield any nanoparticles, showing a maximum average size of 9 nm, which is representative of the size measurements observed from the native iRGD peptide in water alone. (Figure 5.2 b)

When iRGD-DD peptides were mixed with methylene blue at the same molar ratio in water, the size increased and stabilized to about 178 nm particles within 90 minutes. (Figure 5.2a, c) We predicted this assembly was caused by electrostatic attraction between the aspartic acid doublets and the methylene blue. To demonstrate this, we repeated the same assembly conditions, but under pH conditions that surpassed the isoelectric points of either iRGD-DD or methylene blue. When the pH was set to 12, methylene blue adopted a neutral charge, which did not result in stable nanoparticulate formations. The same results were observed when the pH was set below 2, allowing iRGD-DD to adopt a neutral charge. In both cases, the most abundantly observed sizes from MANTA were below 10 nm (Figure 5.8a-d).

When iRGD-WW peptides were mixed with methylene blue at a similar 10:1 molar ratio in water, 150 nm nanoparticles were formed under the same 90-minute time frame (Figure 5.2a,d). We wanted to again elucidate that this assembly was due to the hydrophobic stacking between the tryptophan doublets and the methylene blue molecules; to accomplish this, we altered the solubility of the peptide by replicating assembly but in organic DMSO and chloroform. Again, the nanoparticle formulations were not observed. (Figure 5.8e-f).

To visualize the resultant nanoparticle formulations from these assemblies, we imaged them via transmission electron microscopy (TEM) and used uranyl acetate staining for the peptides. The individual methylene blue molecules and peptides did not show any noticeable particles (Figure 5.2e-f). Similarly, a mixture between native iRGD and methylene blue did not reveal any visible assemblies besides some nonspecific aggregates (Figure 5.2 g). In contrast, the

iRGD-DD-Methylene blue assemblies were seen as “sickle-like” nanofiber matrices (“iRGD-NFs”) (Figure 5.2h), while iRGD-WW-Methylene Blue assemblies were seen as “bubble-like” nanospheres (“iRGD-NSs”) (Figure 5.2i), Figure (5.9). The sizes of these particulates both remained in agreement with the sizes that were charted via the MANTA measurements.

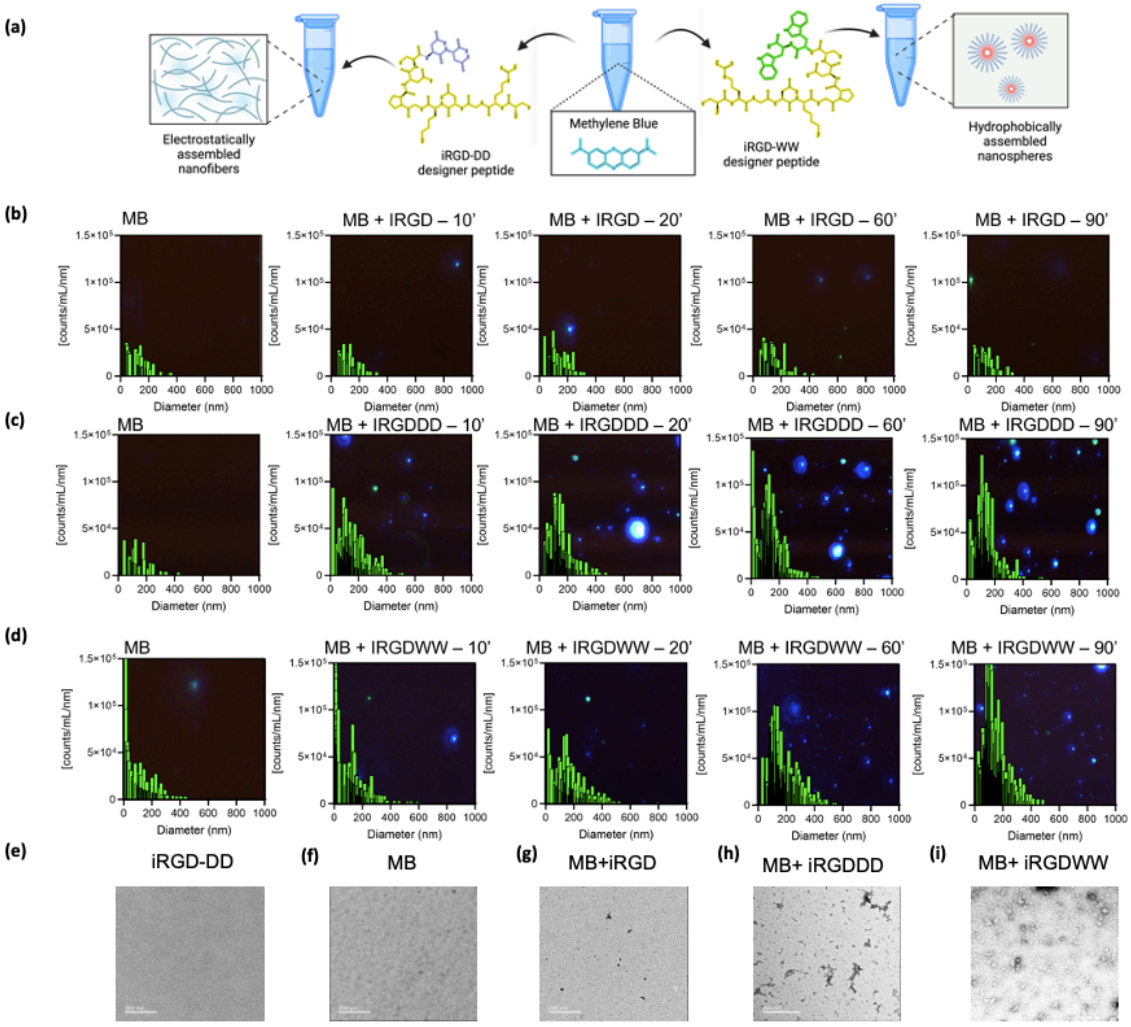

Figure 5. 2 Physical characterization of iRGD-methylene blue assemblies.

(a) schematic of reaction of assemblies: iRGD-DD or iRGD-WW is added to a solution of methylene blue to enable electrostatic or hydrophobic affinities into higher order structures. (b) MANTA measurements of the native iRGD peptide with methylene blue shows no particles with particular size are formed, while (c) shows 180 nm nanoparticle formation between iRGD-DD and methylene blue over 90 minutes, while (d) shows 150 nm nanoparticle formation between iRGD-WW and methylene blue over 90 minutes. The panels in figures (b) through (d) are overlaid with scattering light detected by the MANTA, corroborating the formation of growing nanoparticles. (e-i) TEM micrographs show that the iRGD-DD + methylene blue and iRGD-WW + methylene blue samples formed into sickle like iRGD nanofibers (iRGD-NFs) and iRGD nanospheres (iRGD-NSs) respectively, while the molecular dye, peptides, and combination between the dye and the native iRGD did not form assemblies with characteristic shapes.

5.3.2. Live cell interactions between the peptide-dye assemblies

Both iRGD-NF and iRGD-NS formulations were then tested in live cells to evaluate targeting capabilities. Flow cytometry was used to evaluate any increased uptake of methylene blue into the cells due to iRGD-mediated internalization; this experiment revealed that the iRGD-NF and iRGD-NS showed increased internal fluorescence in the cells above the free methylene blue and iRGD methylene blue mixtures (Figure 5.3b).

Targeted photodynamic toxicity was evaluated next. After incubation with either with methylene blue, a mixture of methylene blue with unmodified iRGD peptides, iRGD-NFs or iRGD-NSs, SKOV-3 cells were irradiated with 660 nm light to activate ROS production from the methylene blue, which was monitored with a fluorescent DCFDA assay. This experiment showed the spheres and fibers produced 116.6% and 94.82% ROS-based increased fluorescence over the case when the cells were incubated with methylene blue alone (Figure 5.10c). We also observed increased DCF fluorescence (153.7% and 134.2% increased fluorescence above free methylene blue for the nanospheres and fibers respectively) for MCF-7 human breast cancer cells. Live cell imaging further revealed that while ROS-fluorescence was lower when cells were not irradiated with light, the methylene blue fluorescence remained unchanged, thus indicating cellular uptake into MCF-7 (Figure 5.3a).

To further corroborate that ROS production was true to light activation and photodynamic toxicity, we designed an area-specific light experiment: A certain portion of the cell culture flask was irradiated with the NIR laser after it was incubated with the fibers and spheres, and then the ROS-based fluorescence was observed through live cell fluorescence microscopy. We noticed there was more green fluorescence in the laser-treated area (Figure 5.10b). These data confirmed that the light irradiation was the primary cause of ROS generation from the cells when the MB had increased uptake. Hoechst staining also showed that ROS

generation resulted in increased apoptosis (Figure 5.10a). On the other hand, the spheres, fibers, and methylene blue were incubated with noncancerous HEK 293T cells as a negative control. Interestingly, not only were there no elevated levels of ROS fluorescence when the HEK 293T cells were incubated with the assemblies, but the free methylene blue demonstrated more ROS fluorescence than the nanofibers (Figure 5.3c-d). SKOV-3, MCF-7, and HEK 293T integrin expression levels were validated with flow cytometry experiments (Figure 5.11).

The peptide formulations were challenged via competitive inhibition studies to demonstrate their interactions with the integrin receptors. Here, the cells were either first incubated with free methylene blue, with iRGD-NFs, iRGD-NSs or with $\alpha V\beta 5$ primary antibodies before iRGD-NFs or iRGD-NSs. Here, it was found that the fluorescence from the cells treated with $\alpha V\beta 5$ antibodies prior to iRGD-NFs or iRGD-NSs was less than the fluorescence detected when they were treated with free methylene blue alone. On the other hand, there was increased fluorescence when the cells were treated with iRGD-NFs or iRGD-NSs alone. However, when the same experiment was implemented with HEK 293T cells, there was no distinct difference in fluorescence between any of the cases tested. This helped corroborate that the designed iRGD peptide retained its $\alpha V\beta 5$-mediated uptake into cells (Figure 5.3e-f).

Endosomal escape has remained as a longstanding issue for nanoparticle drug delivery, and past reports have also validated that the iRGD peptide inherently increases endocytosis-mediated uptake[281]. Therefore, we tested the iRGD-NF and iRGD-NS abilities to escape the endosome after internalization into MCF-7 cells. We characterized calcein leakage fluorescence by flow cytometry after co-incubating the membrane-impermeable calcein dye either with iRGD-NFs, iRGD-NSs, methylene blue, or mixtures of iRGD and methylene blue.[282-283] The cells incubated with the iRGD-NF's showed 76.2% of the population was double positive in

methylene blue and calcein fluorescence and 14.9% of the population was predominantly positive in methylene blue fluorescence, while the iRGD-NS's showed 61.6% of the population

was double positive in methylene blue and calcein fluorescence while 32.2% of the population was predominantly positive in methylene blue fluorescence (Figure 5.3g).

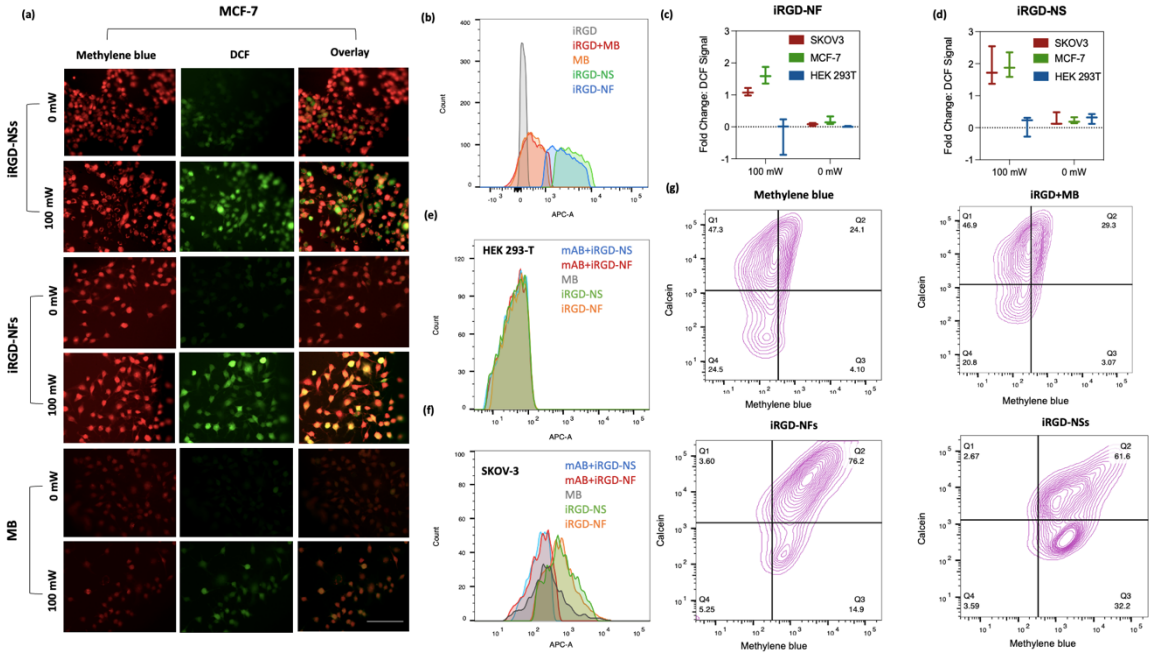

Figure 5. 3 iRGD-NF and iRGD-NS interactions with live cells for targeted internalization and ROS generation.

(a) live cell fluorescent microscopy shows that when the cells are exposed to 100 mW NIR light after incubation with the nanofibers and nanospheres, there is an increased fluorescence from DCFDA translation to DCF from ROS generation. However, this level of fluorescence is not generated when the cells are not exposed to 100 mW NIR light. (scale bar=100 micron) (b) flow cytometry shows increased methylene blue fluorescence detected in cells incubated with iRGD-NF , iRGD-NS compared to cells incubated with methylene blue alone and methylene blue mixed with iRGD , with a negative control of cells with iRGD peptide. (c) and (d) show quantitative fold change in DCF based ROS fluorescence between iRGD-NF and iRGD-NS respectively, over the DCF fluorescence from when the cells were incubated with methylene blue alone in SKOV3, MCF-7, and HEK 293T cells. (e) competitive inhibition with HEK 293T cells shows that whether the cells are incubated with $\alpha V\beta 5$ primary antibodies before incubation, there is no change in fluorescence increase when they are treated with iRGD-NF, iRGD-NS, and methylene blue alone. (f) competitive inhibition with SKOV-3 cells shows that when the cells are first treated with $\alpha V\beta 5$ primary antibodies before incubation with iRGD-NF and iRGD-NS (red and blue respectively), there is less fluorescence compared to when the cells are treated with methylene blue alone (grey), or with the iRGD-NFs and iRGD-NSs without prior antibody blocking (green and orange respectively). The same colors are correlated to the same cases in panel (e). (g) multicolor flow cytometry to monitor changes in calcein and methylene blue fluorescence show that while the cells treated with iRGD-NSs had increased methylene blue fluorescence, the decreased population of double positive fluorescence indicated less susceptibility to escape the endosome.

5.3.3. Optical characterization and Photoacoustic imaging with the peptide dye assemblies

The optical and photoacoustic properties of the assemblies were also studied. When the nanospheres and nanofibers were scanned from 400 to 700 nm for optical absorbance, both adopted a similar peak absorbance to methylene blue at 662 nm. When the peaks were normalized, there was no 614 nm shoulder growth when dimerizations typically form[236]. While the nanofiber samples maintained methylene blue's distinct blue color, the nanosphere samples shifted to a slightly greener color. The quantum yield for the nanofibers and the nanospheres relative to methylene blue (52%) were found to be at 43% and 31% respectively, as there was increased fluorescence self-quenching between the assemblies relative to the methylene blue reference at the same optical density (Figure 5.12).

The photoacoustic contrast of the formulations was evaluated in vitro and in vivo. First, the samples were loaded into tubes and irradiated under a pulsed NIR laser and imaged with an ultrasound transducer. Both the nanospheres and nanofibers had photoacoustic contrast at 680 nm, which is the native peak photoacoustic intensity of methylene blue. However, the nanofibers maintained distinct photoacoustic contrast at 720 nm while the nanospheres, mixture between methylene blue and iRGD, and methylene blue lost visibility (Figure 5.4a-b). Even when the iRGD-DD to methylene blue molar ratio was increased, these assemblies maintained a 720 nm photoacoustic contrast (Figure 5.13).

For the in vivo experiments, mice were xenografted with SKOV-3 cells intraperitoneally and were imaged throughout the progression of the inoculation. Six cases were explored: (1) SKOV-3 positive and imaged with free methylene blue, (2) SKOV-3 positive and imaged with a mixture of iRGD and methylene blue (3) SKOV-3 positive and imaged with the iRGD-NFs, (4) SKOV-3 positive and imaged with the iRGD-NSs, (5) SKOV-3 negative and imaged with the iRGD-NFs, and (6) SKOV-3 negative and imaged with the iRGD-NSs. The subjects were

imaged 10 days after inoculation. When the nanospheres and nanofibers were locally injected, PA contrast and intensity increased at a faster rate over the span of 15 minutes, while the PA contrast rate was slower when iRGD was co-injected with methylene blue. Methylene blue showed no specific increase in PA contrast over the same time frame, and there was no PA contrast for a SKOV-3 negative mouse (i.e., mice not bearing SKOV-3 tumors) injected with the iRGD nanospheres. (Figure 3c-d) When the mixture of the iRGD+MB was locally injected, local contrast was also observed, but after about 15 minutes, the PA intensity decreased by 38% (+/- 2.3%) and by a total of 72% (+/- 5.6%) after 30 minutes (Figure S8). On the other hand, when the nanospheres were injected, PA intensity decreased by only 4.9% (+/- 2.03%) after 15 minutes and by a total of 6.8% (+/- 1.31% after 30 minutes. When the nanofibers were injected, PA intensity decreased by 6.1% (+/- 1.02%) after 15 minutes and by a total of 7.4% (+/- 2.56%) after 30 minutes (Figure 5.14).

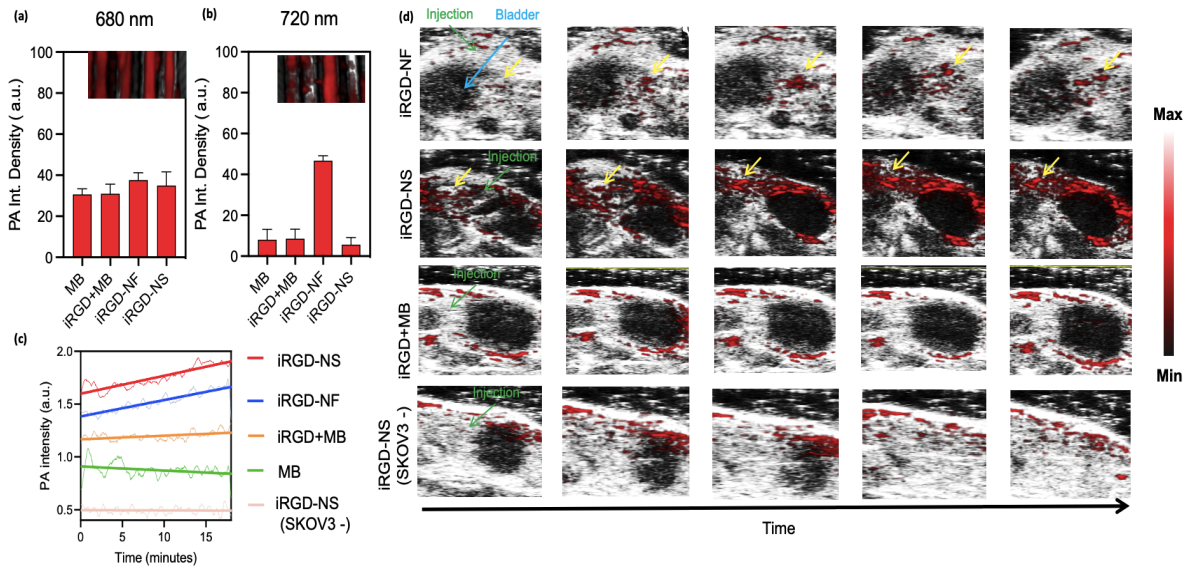

Figure 5. 4 Photoacoustic characterization in vitro and in vivo.

(a) Single wavelength in vitro PA scanning shows PA contrast at 680 nm wavelength for all formulations tested, which is true to the typical 680 nm photoacoustic contrast of methylene blue. (b) Single wavelength in vitro PA scanning shows sustained PA contrast from the iRGD nanofibers at 720 nm while the other formulations lost PA contrast. (c) quantitative analysis of overlaid PA and B-mode images in (d) show faster rate of PA contrast in SKOV-3 IP murine models when injected with the nanospherical and nanofiber formulations.

5.3.4. Photodynamic therapy against tumor bearing mice

Targeted photodynamic therapy against tumor bearing mice was also evaluated. Similarly, mice were inoculated with SKOV-3 intraperitoneally, but these cells expressed the luciferase gene for bioluminescence monitoring over time. After the subjects were given three days of inoculation, they were treated either with (1) PBS (2) Methylene Blue (3) iRGD+Methylene Blue, (4) iRGD-NSs, and (5) iRGD-NFs over the nine-day period. After overnight incubation, the subjects were exposed to a 660nm 100 mW light source locally pointed at the abdomen for 10 minutes each (Figure 5.5b).

Interestingly, the iRGD+methylene blue mixture and the iRGD-NFs treatments yielded the slowest tumor growth rate, while the iRGD-NS treatment was only slower. In particular, the fibers decreased tumor burden bioluminescence by an average 75.91% (+/- 11.48%) (p=0.043),

while spheres decreased tumor burden bioluminescence by an average of 58.89% (+/- 18.23%) ($p=0.089$). There was no significant difference in the decreased bioluminescence between the nanofibers and the co-loaded iRGD and methylene blue treatment ($p=0.7941$) (Figure 5.5a,c).

The vital organs of the subjects were harvested after euthanasia and analyzed for fluorescence from the methylene blue for biodistribution studies. Here, the subjects treated with only methylene blue showed nonspecific and low fluorescence in all of the vital organs. On the other hand, while the iRGD-NS, iRGD-NF, and iRGD+MB treated subjects showed heightened fluorescence in the extracted tumor, the iRGD-NS showed the most increased fluorescence in the liver above the other two cases (Figure 5.5d).

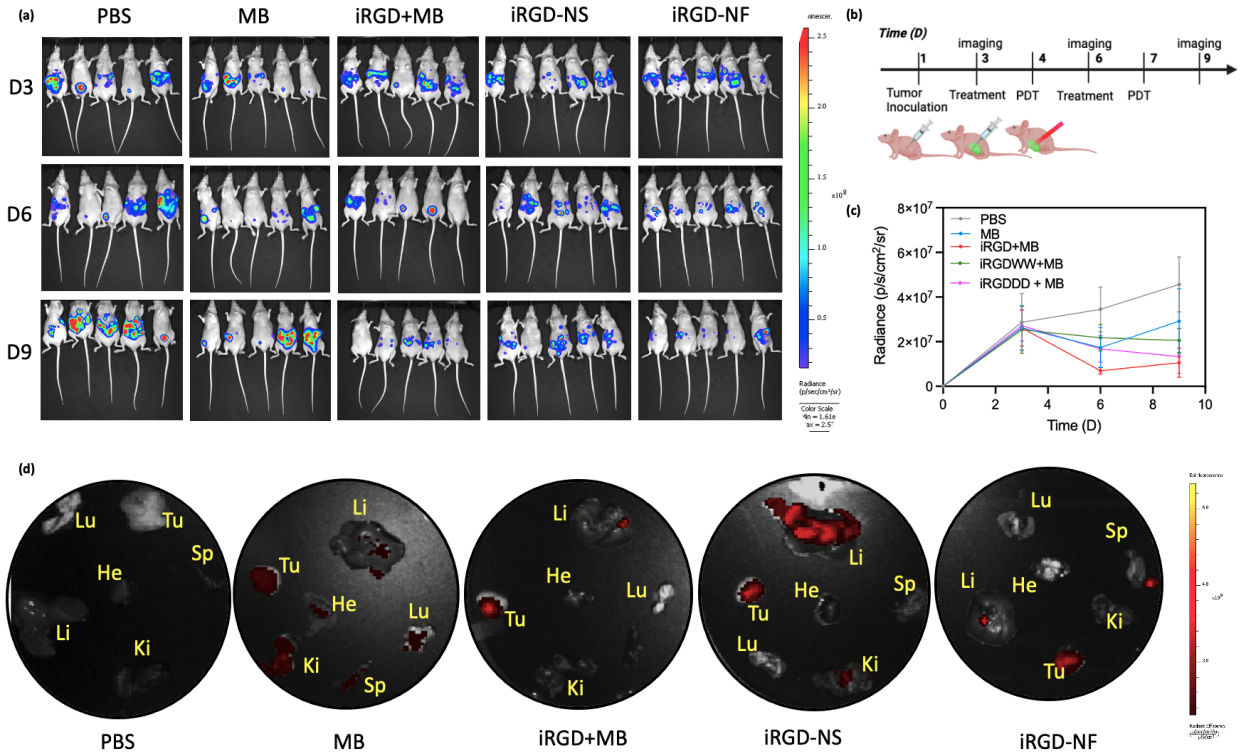

Figure 5. 5 in vivo photodynamic toxicity evaluation.

(a) and (c) show bioluminescent images and quantitative signal from SKOV-3 expressing luciferase in mice, showing that over 9 days, the subjects treated with iRGD+MB and the iRGD nanofibers decreased tumor burden the most. On the other hand, the subjects treated with iRGD nanospheres did not demonstrate comparable performance. (b) shows timeline schematic of inoculation, injection, and PDT of the subjects. (d) shows fluorescent evaluation of biodistribution, where the subjects treated with the iRGD-NS showed most methylene blue fluorescence in the liver, despite signal from the harvested tumor as well.

5.4. Discussion

Nanostructures have gained significant attention and an increasing clinical presence in medicine and analytical biology over the last couple of decades. Nanoparticles, such as lipid and polymeric nanoparticles, for example, have been used as carriers for genetic transfection, therapeutic RNA delivery, as well as targeted and disguised small molecule drug delivery for cancer therapeutics and vaccinations.

Simulations showed that although the native iRGD peptide typically adopts a cyclic structure due to disulfide bridging from the cysteines at either end, the designer peptides did not

adopt this confirmation (Figure 5.6). We found that the characteristic assemblies between our iRGD nanofibers and iRGD nanospheres concurred with similar assemblies previously reported in literature; electrostatically-mediated peptide-small molecule assemblies preferentially adopt "checkerboard-like" patterning between complimentary ionic forces that assemble into nanofiber networks[284-285]. On the other hand, the use of hydrophobic affinities between peptides and small molecules has become a well-established strategy to engineer designer vesicles, micelles, and nanoparticles[286]. While these previous reports have used the prescribed geometries for differing applications, such as for tissue generation or for drug delivery, there is a gap in evaluating their properties for similar applications in parallel.

The modulated ROS generation and competitive inhibition studies agree with past reports that SAPNs can retain their targeting modality after assembling into unnatural higher order formulations. However, the geometries of these formulations can still lead to adverse effects with live cells. Multicolor flow cytometry results show that while much of the methylene blue is internalized into the cells from the nanospherical formulation, more of the calcein dye remains trapped in the endosome with the fluorescence quenched, indicating that the fluorescence of the methylene blue in the cell can be from the dye internalized in the endosome. There are several reasons that may explain the nanosphere's entrapment: (1) nanospherical shapes have a high propensity to stay within the endosome, and (2), while hydrophobic R groups in amino acids normally aid in endosomal escape for viruses[287], the hydrophobic stacking between the tryptophan residues and the methylene blue molecules in the nanospheres most likely suppresses their availability to promote escape.

While subcutaneous tumor models are more popularly used to demonstrate targeted live tissue PA imaging, intraperitoneal models further challenge targeting tumors that are at

potentially lower depth penetrations. Additionally, intraperitoneal injections are ideal for targeted delivery and tumor toxicity as the peritoneal tumors are exposed to higher local concentrations of the contrast agent or drug[288]. We expected targeted contrast in subjects co-injected with iRGD and methylene blue, as the NRP-1 interactions with the peptide would guide increased methylene blue uptake in the tumor microvasculature, but the sustained contrast from the nanofibers and nanospheres demonstrated more efficient delivery of increased local concentrations of methylene blue.

The translation between live cell to live tissue efficacy, especially with targeted delivery, can also be compromised in a variety of ways. Although previous studies have shown that co-loaded iRGD and small molecule drug formulations have led to robust therapeutic results with simple administration, we did not expect the nanospheres to have a dampened tumor photodynamic toxicity in vivo. Nonetheless, nanoparticle formulations have shown significant impact on the pharmacokinetics and biodistribution[289]. The increased fluorescence in the liver indicates preferential liver clearance of spherical nanoparticles above the fiber nanoparticles. Liver clearance has remained as an important barrier for different kinds of nanospherical formulations, such as oncolytic viruses, lipid nanoparticles, and inorganic nanoparticles.[290,291] Strategies to overcome these barriers may include surface charge tunability and switchable self-assembly for better circulation and activated targeted delivery.[292]

However, the different assemblies cannot only constitute different behaviors with biology, but also different optical properties. Methylene blue has demonstrated photoacoustic contrast for widespread applications, but moreover, it has demonstrated switchable and activatable photoacoustic peak wavelength changes under certain formulations, such as with micelles or by electrostatic interactions with biologics[236,293]. The hydrophobic and the

electrostatic-driven encapsulations resulted in native and red-shifted photoacoustic wavelength intensities, respectively, which may indicate that these non-covalent assemblies can be utilized either to maintain native optical properties or instead promote aggregation-induced shifts such as J aggregation and self-quenching. Other protein-molecular dye formulations have been designed to prevent intramolecular assemblies to optimize fluorescent signal and quantum yield, but in the context of photoacoustic imaging, intramolecular self-assembly pathways are demonstrably more favorable.[294]

5.5. Conclusions

In summary, we report two nanoparticle formulations of the same precursor peptide and dye molecules and their differing optical properties, interactions with biology, and resultantly different capacities for in vivo tumor photoacoustic imaging and targeted photodynamic toxicity. The evaluation of only one of these formulations may mistakenly imply the formulation is an optimized vector for "multifunctionality." However, investigation of both formulations shed light on key differences between the two, including unshared advantages and disadvantages for translational applications. For example, the increased liver-uptake from the nanospheres can inspire an additional passive targeting modality for applications in targeted drug delivery for liver disease, as RGD motifs have also been investigated in the context of liver fibrosis[295]. Besides emphasizing the multiscaled effects SAPNs' architecture and shape may have on its interactions with biology, this work supports the prioritized need for tailored applications of nanoparticles over multifunctionality.[296]

5.6. Acknowledgements

Chapter 5, in part is currently being prepared for submission for publication of the material. Borum, Raina; Retout, Maurice; Creyer, Matt; Chang, Yu-Ci; Gregorio, Karlo; Jokerst, J.V. The dissertation author was the primary researcher and author of this material.

5.7. Supporting Figures

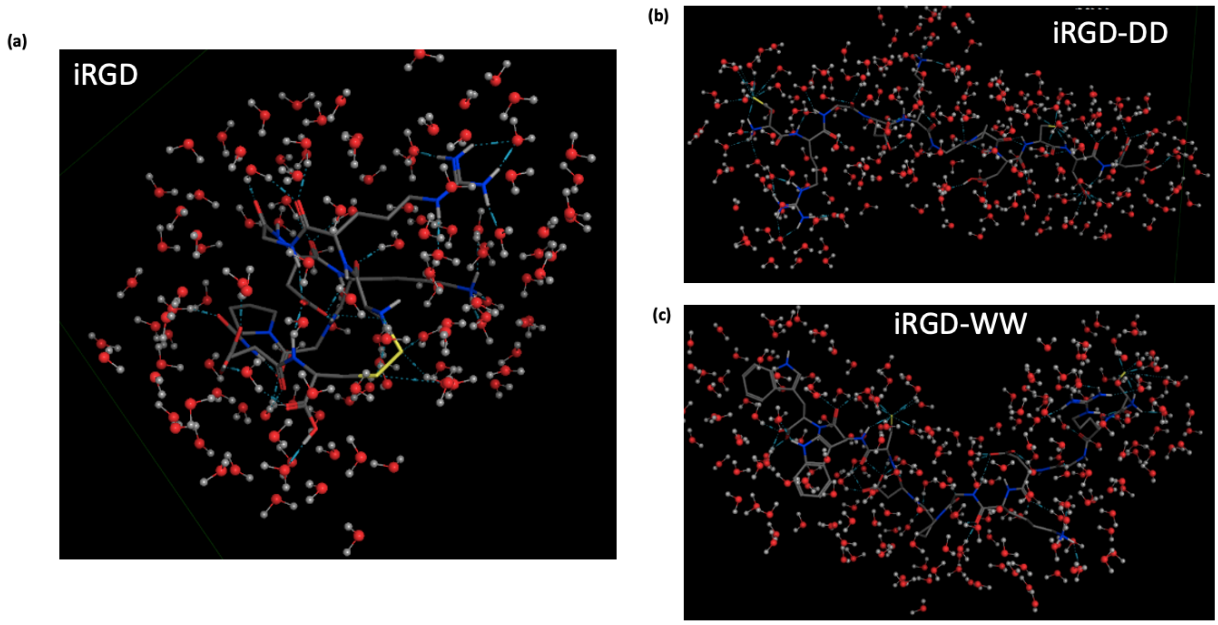

Figure 5. 6 Simulations of the iRGD and designer iRGD peptide structures using Molecular Operating Environment (MOE)

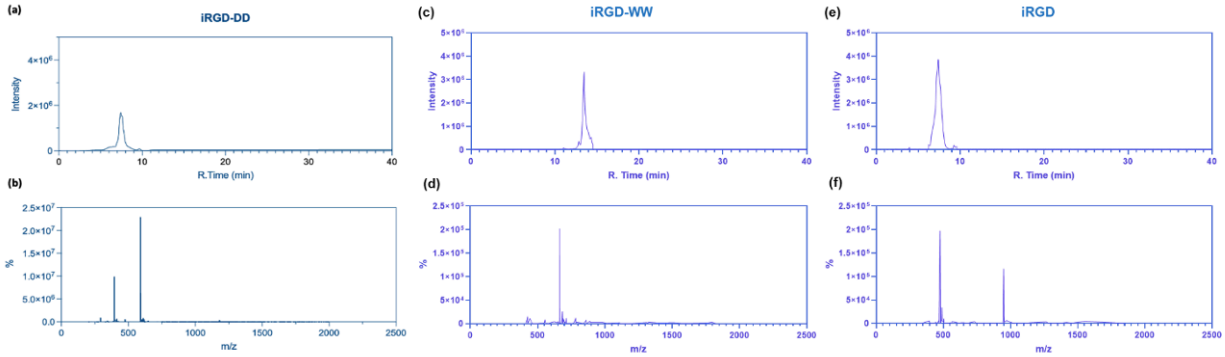

Figure 5. 7 Chromatograms and ESI-Mass spectra of the designer peptides.

(a) HPLC chromatogram of pure iRGD-DD peptide. (b) ESI-Mass spectra of the product. Expected m/z: 1180.43, 590.72, 394.15 for +1, +2, and +3 charges. Found: 1180.74, 590.25, 394.16. (c) HPLC chromatogram of pure iRGD-WW peptide. (d) ESI-Mass spectra of the product. Expected m/z: 660.76 +2 charges. Found: 661.21. (e) HPLC chromatogram of pure iRGD peptide. (f) ESI-Mass spectra of the product. Expected m/z: 949.37, 474.68 for +1 and +2 charges. Found: 949.86 and 475.59.

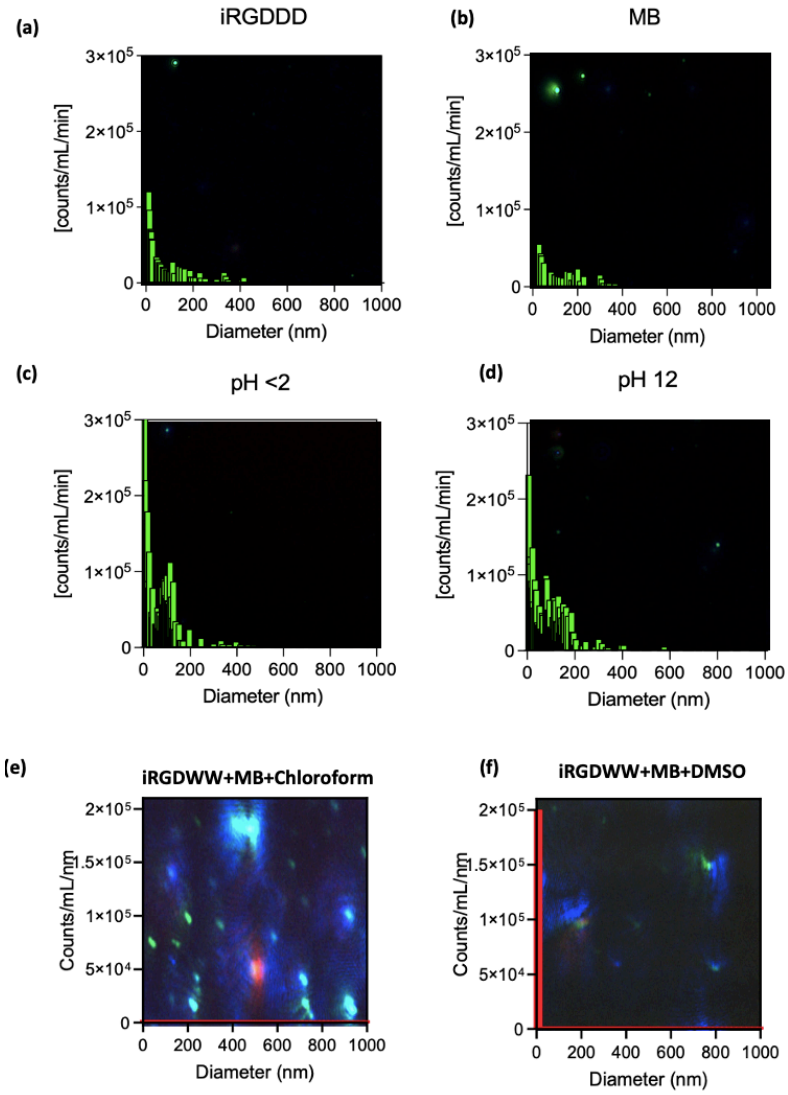

Figure 5. 8 Supplementary MANTA Results

(a) (b) designer iRGD-DD peptide and methylene blue dye show no distinct nanoparticle sizes relative to the formations from the assemblies in Figure 1 of the main manuscript. (c) and (d) challenge isoelectric points of the iRGD-DD peptide and methylene blue respectively to neutralize the component, showing no assembled particles.

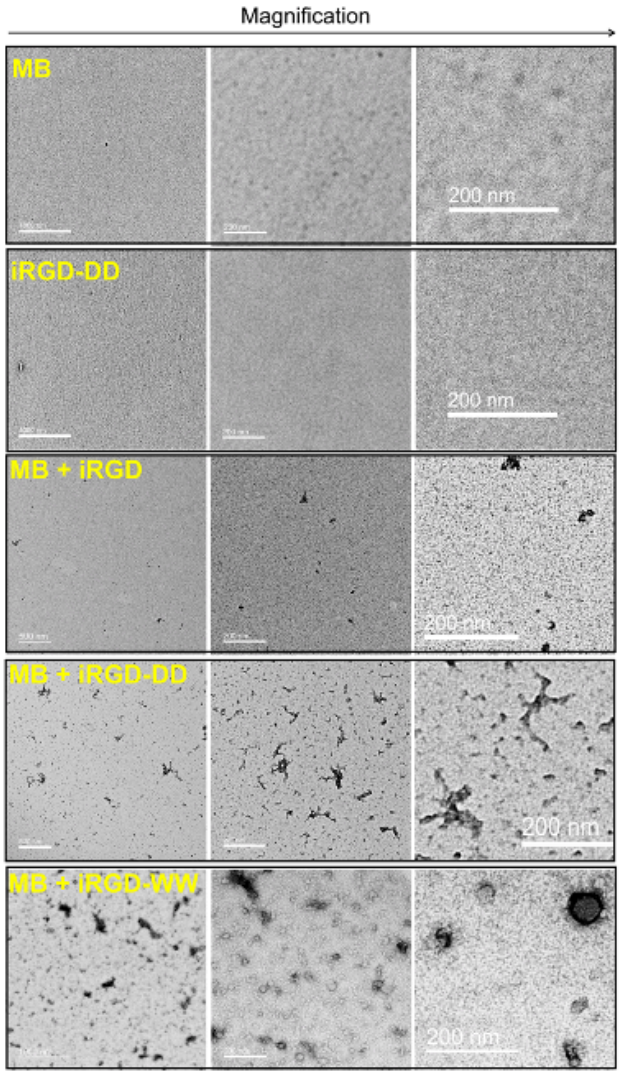

Figure 5. 9 TEM Micrographs of the assemblies with increasing magnification.

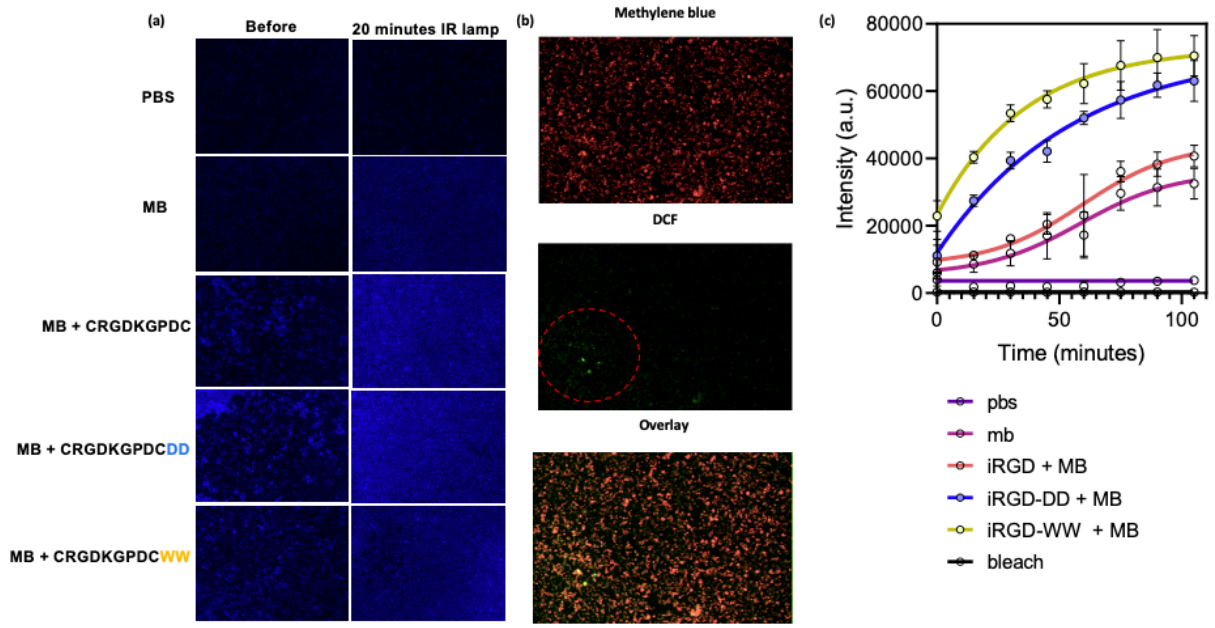

Figure 5. 10 Supplementary live cell data on targeted ROS production
(a) NucBlue stain shows increasing apoptosis activity after light irradiation when cells are incubated with the iRGD-NF and iRGD-NS assemblies. (b) shows area specific heightened ROS production, where DCF fluorescence is heightened at the area where the flask was exposed to the red laser (denoted by the red circle in the DCF fluorescence micrograph). (c) Time-dependent ROS generation shows the heightened ROS fluorescence from cells incubated with the fibers and spheres (yellow and blue respectively) after light irradiation starts at a faster rate iRGD+MB and MB alone (orange and red respectively) and then stabilizes after about 2 hours.

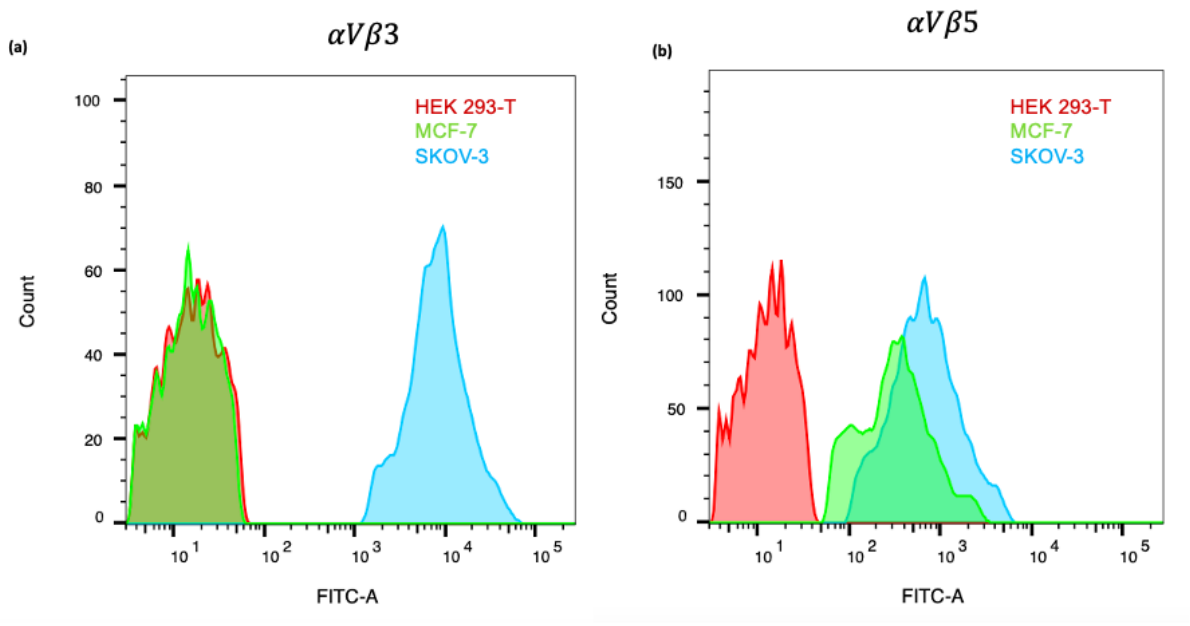

Figure 5. 11 Integrin expression validation of the tested cell lines using Alexa Fluor 488 tagged antibodies.

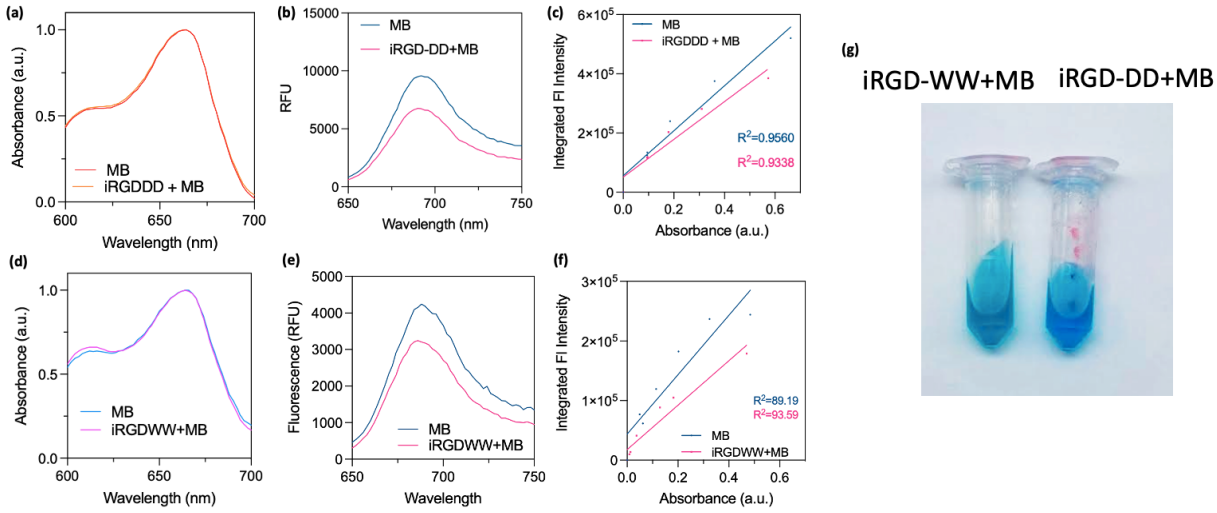

Figure 5. 12 Optical absorbance measurements.

(a-c) show no 614 nm optical shoulder growth between the iRGD-DD mediated assemblies, but increased fluorescent quenching at the same concentration, with a resultantly lower quantum yield relative to methylene blue. (d-f) show no 614 nm optical shoulder growth between the iRGD-WW mediated assemblies, but increased fluorescent quenching at the same concentration, with a resultantly lower quantum yield relative to methylene blue. (g) photograph of the designer peptide assemblies with methylene blue shows a green tint with the iRGD-WW mediated formation.

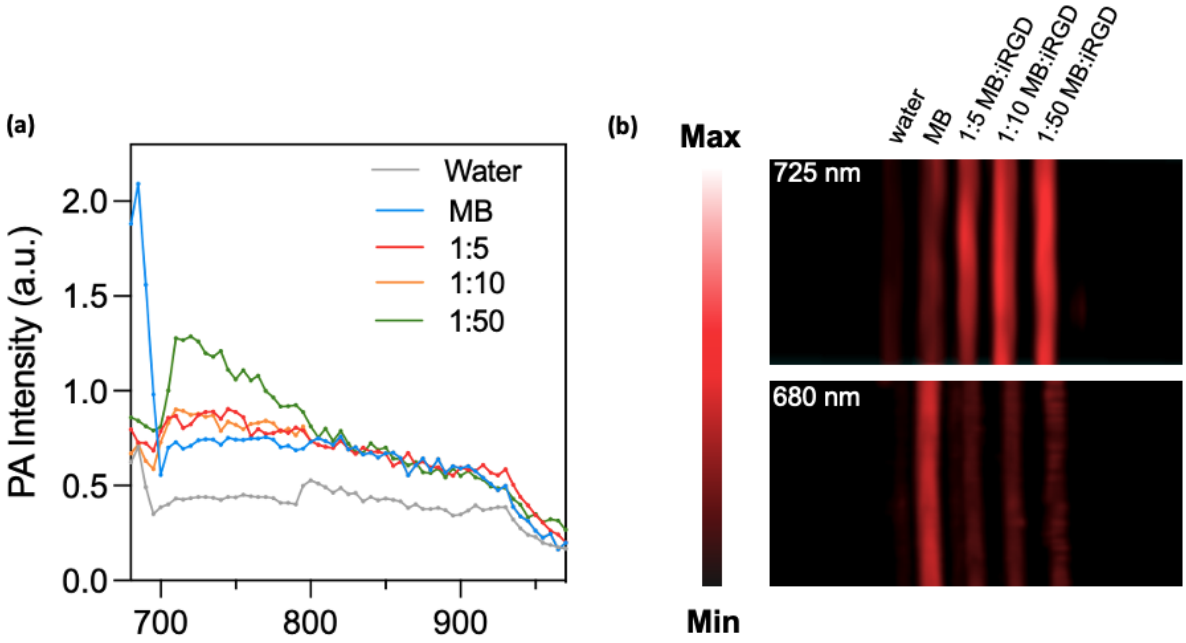

Figure 5. 13 Electrostatic nanofiber formulation's sustained 720 nm contrast

(a) corresponding spectra to in vitro photoacoustic image in (b) shows that despite the change in peptide to dye ratio, the nanofibers maintain photoacoustic contrast beyond methylene blue's signature 680 nm contrast peak.

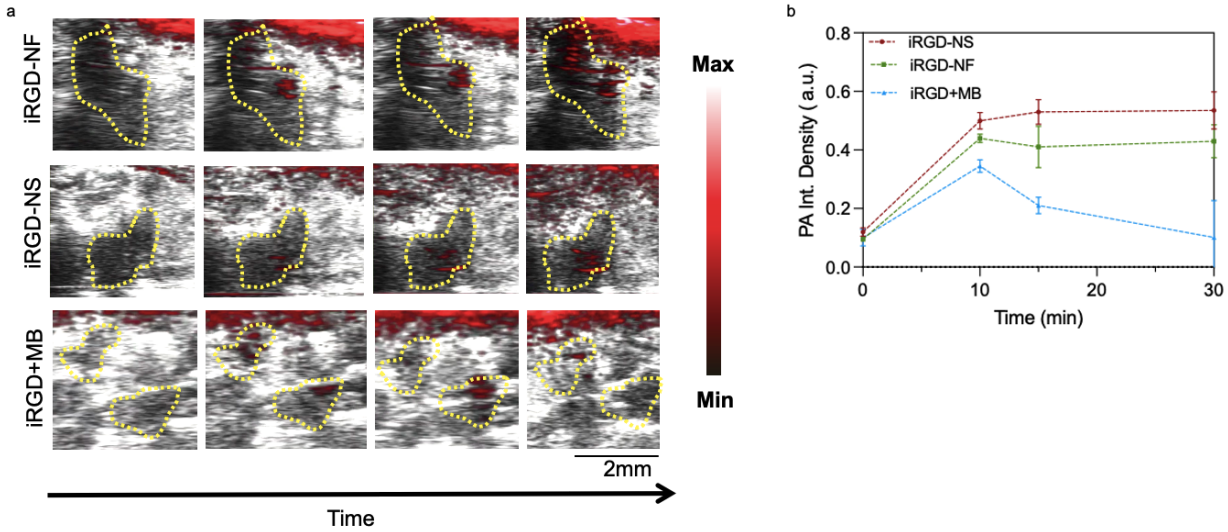

Figure 5. 14 . PA contrast sustainability
(a) overlaid PA and B-Mode images show tumor specific contrast (solid tumor ROI in yellow) for both the nanofiber, nanosphere, and coinjected formulations, but the PA contrast sustained over thirty minutes for the nanoparticulate assembly formulations while the PA contrast barely lasted over twenty minutes for the subject imaged with the co-injection of iRGD and MB. (b) quantitative PA analysis of the three different cases.

REFERENCES

(1) Oliver, S. L.; Yang, E.; Arvin, A. M. Varicella-Zoster Virus Glycoproteins: Entry, Replication, and Pathogenesis. *Curr Clin Microbiol Rep* **2016**, *3*, 204–215.

(2) Garg, H.; Joshi, A.; Freed, E. O.; Blumenthal, R. Site-Specific Mutations in HIV-1 Gp41 Reveal a Correlation between HIV-1-Mediated Bystander Apoptosis and Fusion/Hemifusion. *J Biol Chem* **2007**, *282*, 16899–16906.

(3) Plemper, R. K.; Hammond, A. L.; Gerlier, D.; Fielding, A. K.; Cattaneo, R. Strength of Envelope Protein Interaction Modulates Cytopathicity of Measles Virus. *J Virol* **2002**, *76*, 5051–5061.

(4) Spear, P. G.; Longnecker, R. Herpesvirus Entry: An Update. *J Virol* **2003**, *77*, 10179–10185.

(5) Hatziioannou, T.; Cowan, S.; Schwedler, U. K. V.; Sundquist, W. I.; Bieniasz, P. D. Species-Specific Tropism Determinants in the Human Immunodeficiency Virus Type 1 Capsid. *J Virol* **2004**, *78*, 6005–6012.

(6) Pelaz, B.; Alexiou, C.; Alvarez-Puebla, R. A.; Alves, F.; Andrews, A. M.; Ashraf, S.; Balogh, L. P.; Ballerini, L.; Bestetti, A.; Brendel, C. Diverse Applications of Nanomedicine. *ACS Nano* **2017**, *11*, 2313–2381.

(7) Vahey, M. D.; Fletcher, D. A. Influenza A Virus Surface Proteins Are Organized to Help Penetrate Host Mucus. *eLife* **2019**, *8*, 43764.

(8) Towers, G. J. Control of Viral Infectivity by Tripartite Motif Proteins. *Hum Gene Ther* **2005**, *16*, 1125–1132.

(9) Kummer, S.; Flöttmann, M.; Schwanhäusser, B.; Sieben, C.; Veit, M.; Selbach, M.; Klipp, E.; Herrmann, A. Alteration of Protein Levels during Influenza Virus H1N1 Infection in Host Cells: A Proteomic Survey of Host and Virus Reveals Differential Dynamics. *PLoS ONE* **2014**, *9*, 94257.

(10) Law, G. L.; Korth, M. J.; Benecke, A. G.; Katze, M. G. Systems Virology: Host-Directed Approaches to Viral Pathogenesis and Drug Targeting. *Nat Rev Microbiol* **2013**, *11*, 455–466.

(11) Kaufman, H. L.; Kohlhapp, F. J.; Zloza, A. Erratum: Oncolytic Viruses: A New Class of Immunotherapy Drugs. *Nat Rev Drug Discov* **2016**, *15*, 660.

(12) Andtbacka, R. H.; Kaufman, H. L.; Collichio, F.; Amatruda, T.; Senzer, N.; Chesney, J.; Delman, K. A.; Spitler, L. E.; Puzanov, I.; Agarwala, S. S. Talimogene Laherparepvec Improves Durable Response Rate in Patients with Advanced Melanoma. *J Clin Oncol* **2015**, *33*, 2780–2788.

(13) Ferguson, M. S.; Lemoine, N. R.; Wang, Y. Systemic Delivery of Oncolytic Viruses: Hopes and Hurdles. *Adv Virol* **2012**, *2012*, 1–14.

(14) Kuryk, L.; Vassilev, L.; Ranki, T.; Hemminki, A.; Karioja-Kallio, A.; Levälampi, O.; Vuolanto, A.; Cerullo, V.; Pesonen, S. Toxicological and Bio-Distribution Profile of a GM-CSF-Expressing, Double-Targeted, Chimeric Oncolytic Adenovirus ONCOS-102—Support for Clinical Studies on Advanced Cancer Treatment. *PLoS ONE* **2017**, *12*, 0182715.

(15) Kaufman, H. L.; Bommareddy, P. K. Two Roads for Oncolytic Immunotherapy Development. *J Immunother. Cancer* **2019**, *7*, 26.

(16) Liu, Y.; Luo, J.; Chen, X.; Liu, W.; Chen, T. Cell Membrane Coating Technology: A Promising Strategy for Biomedical Applications. *Nano-Micro Lett* **2019**, *11*, 100.

(17) Jin, J.; Bhujwalla, Z. M. Biomimetic Nanoparticles Camouflaged in Cancer Cell Membranes and Their Applications in Cancer Theranostics. *Front Oncol* **2020**, 9,.
(18) Chen, L.; Liu, J.; Zhang, Y.; Zhang, G.; Kang, Y.; Chen, A.; Feng, X.; Shao, L. The Toxicity of Silica Nanoparticles to the Immune System. *Nanomed.* **2018**, *13*, 1939–1962.
(19) Garay, R. P.; El-Gewely, R.; Armstrong, J. K.; Garratty, G.; Richette, P. Antibodies against Polyethylene Glycol in Healthy Subjects and in Patients Treated with PEG-Conjugated Agents. *Expert Opin Drug Deliv* **2012**, *9*, 1319–1323.
(20) Shen, C.; Li, J.; Zhang, Y.; Li, Y.; Shen, G.; Zhu, J.; Tao, J. Polyethylenimine-Based Micro/Nanoparticles as Vaccine Adjuvants [Corrigendum. *Int J Nanomed* **2017**, *12*, 7239–7240.
(21) Seeman, N. C. Structural DNA Nanotechnology: An overview. *Methods Mol Biol* **2015**, *303*, 143–166.
(22) Anderson, J.; Moss, M.; Nguyen, N.; Hughes, N.; Gee, A.; Ali, M. Optimization of Nucleic Acid Scaffold Design Using Fluorescence Measurements. *MRS Adv* **2019**, *4*, 1349–1354.
(23) Rothemund, P. W. K. Folding DNA to Create Nanoscale Shapes and Patterns. *Nature* **2006**, *440*, 297–302.
(24) Harris, C.; Saks, B. R.; Jayawickramarajah, J. Protein-Binding Molecular Switches via Host-Guest Stabilized DNA Hairpins. *J Am Chem Soc* **2011**, *133*, 7676–7679.
(25) Wang, P.; Meyer, T. A.; Pan, V.; Dutta, P. K.; Ke, Y. The Beauty and Utility of DNA Origami. *Chem* **2017**, *2*, 359–382.
(26) Seeman, N. C.; Sleiman, H. F. DNA Nanotechnology. *Nat Rev Mater* **2017**, *3*, 17068.
(27) Lee, H.; Lytton-Jean, A. K. R.; Chen, Y.; Love, K. T.; Park, A. I.; Karagiannis, E. D.; Sehgal, A.; Querbes, W.; Zurenko, C. S.; Jayaraman, M. Molecularly Self-Assembled Nucleic Acid Nanoparticles for Targeted in Vivo SiRNA Delivery. *Nat Nanotechnol* **2012**, *7*, 389–393.
(28) Angell, C.; Xie, S.; Zhang, L.; Chen, Y. DNA Nanotechnology for Precise Control over Drug Delivery and Gene Therapy. *Small* **2016**, *12*, 1117–1132.
(29) Mikkilä, J.; Eskelinen, A.-P.; Niemelä, E. H.; Linko, V.; Frilander, M. J.; Törmä, P.; Kostiainen, M. A. Virus-Encapsulated DNA Origami Nanostructures for Cellular Delivery. *Nano Lett* **2014**, *14*, 2196–2200.
(30) Kwon, P. S.; Ren, S.; Kwon, S.-J.; Kizer, M. E.; Kuo, L.; Xie, M.; Zhu, D.; Zhou, F.; Zhang, F.; Kim, D. Designer DNA Architecture Offers Precise and Multivalent Spatial Pattern-Recognition for Viral Sensing and Inhibition. *Nat Chem* **2019**, *12*, 26–35.
(31) Sigl, C.; Willner, E. M.; Engelen, W.; Kretzmann, J. A.; Sachenbacher, K.; Liedl, A.; Kolbe, F.; Wilsch, F.; Aghvami, S. A.; Protzer, U. Programmable Icosahedral Shell System for Virus Trapping. *Nat Mater* **2021**, *20*, 1281–1289.
(32) Liu, Y.-T.; Jih, J.; Dai, X.; Bi, G.-Q.; Zhou, Z. H. Cryo-EM Structures of Herpes Simplex Virus Type 1 Portal Vertex and Packaged Genome. *Nature* **2019**, *570*, 257–261.
(33) Kolhatkar, R.; Lote, A.; Khambhati, H. Active Tumor Targeting of Nanomaterials Using Folic Acid, Transferrin and Integrin Receptors. *Curr Drug Discov Technol* **2011**, *8*, 197–206.
(34) Low, P. S.; Henne, W. A.; Doorneweerd, D. D. ChemInform Abstract: Discovery and Development of Folic-Acid-Based Receptor Targeting for Imaging and Therapy of Cancer and Inflammatory Diseases. *Acc Chem Res* **2008**, *41*, 120–129.

(35) Weng, J.; Wang, Y.; Zhang, Y.; Ye, D. An Activatable Near-Infrared Fluorescence Probe for in Vivo Imaging of Acute Kidney Injury by Targeting Phosphatidylserine and Caspase-3. *J Am Chem Soc* **2021**, *143*, 18294–18304.
(36) Chen, C.; Ni, X.; Jia, S.; Liang, Y.; Wu, X.; Kong, D.; Ding, D. Massively Evoking Immunogenic Cell Death by Focused Mitochondrial Oxidative Stress Using an AIE Luminogen with a Twisted Molecular Structure. *Adv Mater* **2019**, *31*, 1902914.
(37) Baer, A.; Kehn-Hall, K. Viral Concentration Determination Through Plaque Assays: Using Traditional and Novel Overlay Systems. *J Vis Exp* **2014**, *93*, 52065.
(38) Chen, C.; Ke, J.; Zhou, X. E.; Yi, W.; Brunzelle, J. S.; Li, J.; Yong, E.-L.; Xu, H. E.; Melcher, K. Structural Basis for Molecular Recognition of Folic Acid by Folate Receptors. *Nature* **2013**, *500*, 486–489.
(39) Dao, V. H.; Cameron, N. R.; Saito, K. Synthesis, Properties, and Performance of Organic Polymers Employed in Flocculation Applications. *Polym Chem* **2016**, *7*, 11–25.
(40) Czemierska, M.; Szczes, A.; Jarosz-Wilkolazka, A. Purification of Wastewater by Natural Flocculants. *Biotechnologia* **2015**, *4*, 272–278.
(41) Bailey, M. H. J.; Wilson, M. Self assembly of model polymers into biological random networks. *Comput Struct Biotechnol J* **2021**, *19*, 1253–1262.
(42) Schleper, C.; Kubo, K.; Zillig, W. The Particle SSV1 from the Extremely Thermophilic Archaeon Sulfolobus Is a Virus: Demonstration of Infectivity and of Transfection with Viral DNA. *Proc Natl Acad Sci USA* **1992**, *89*, 7645–7649.
(43) Lieber, D.; Bailer, S. M. Determination of HSV-1 Infectivity by Plaque Assay and a Luciferase Reporter Cell Line. *Methods Mol Biol Virus-Host Interact* **2013**, *1064*, 171–181.
(44) Monjo, A.; Pringle, E.; Thornbury, M.; Duguay, B.; Monro, S.; Hetu, M.; Knight, D.; Cameron, C.; Mcfarland, S.; Mccormick, C. Photodynamic Inactivation of Herpes Simplex Viruses. *Viruses* **2018**, *10*, 532.
(45) Siwowska, K.; Schmid, R.; Cohrs, S.; Schibli, R.; Müller, C. Folate Receptor-Positive Gynecological Cancer Cells: In Vitro and In Vivo Characterization. *Pharmaceuticals* **2017**, *10*, 72.
(46) Chen, B.; Le, W.; Wang, Y.; Li, Z.; Wang, D.; Lin, L.; Cui, S.; Hu, J. J.; Hu, Y.; Yang, P. Targeting Negative Surface Charges of Cancer Cells by Multifunctional Nanoprobes. *Theranostics* **2016**, *6*, 1887–1898.
(47) Doerfler, W.; Schubbert, R.; Heller, H.; Hertz, J.; Remus, R.; Schröer, J.; Kämmer, C.; Hilger-Eversheim, K.; Gerhardt, U.; Schmitz, B. Foreign DNA in Mammalian Systems. *Apmis* **1998**, *106*, 62–68.
(48) Lehmann, M. J.; Sczakiel, G. Spontaneous Uptake of Biologically Active Recombinant DNA by Mammalian Cells via a Selected DNA Segment. *Gene Ther* **2004**, *12*, 446–451.
(49) Schubbert, R.; Renz, D.; Schmitz, B.; Doerfler, W. Foreign (M13) DNA Ingested by Mice Reaches Peripheral Leukocytes, Spleen, and Liver via the Intestinal Wall Mucosa and Can Be Covalently Linked to Mouse DNA. *Proc Natl Acad Sci USA* **1997**, *94*, 961–966.
(50) Conner, J.; Rixon, F. J.; Brown, S. M. Herpes Simplex Virus Type 1 Strain HSV1716 Grown in Baby Hamster Kidney Cells Has Altered Tropism for Nonpermissive Chinese Hamster Ovary Cells Compared to HSV1716 Grown in Vero Cells. *J. Virol.* **2005**, *79*, 9970–9981.
(51) Chen, Y.; Tezcan, O.; Li, D.; Beztsinna, N.; Lou, B.; Etrych, T.; Ulbrich, K.; Metselaar, J. M.; Lammers, T.; Hennink, W. E. Overcoming Multidrug Resistance Using Folate

Receptor-Targeted and PH-Responsive Polymeric Nanogels Containing Covalently Entrapped Doxorubicin. *Nanoscale* **2017**, *9*, 10404–10419.
(52) Goh, K. C. M.; Tang, C. K.; Norton, D. C.; Gan, E. S.; Tan, H. C.; Sun, B.; Syenina, A.; Yousuf, A.; Ong, X. M.; Kamaraj, U. S. Molecular Determinants of Plaque Size as an Indicator of Dengue Virus Attenuation. *Sci Rep* **2016**, *6*, 26100.
(53) Hahn, J.; Wickham, S. F. J.; Shih, W. M.; Perrault, S. D. Addressing the Instability of DNA Nanostructures in Tissue Culture. *ACS Nano* **2014**, *8*, 8765–8775.
(54) Ramakrishnan, S.; Ijäs, H.; Linko, V.; Keller, A. Structural Stability of DNA Origami Nanostructures under Application-Specific Conditions. *Comput Struct Biotechnol J* **2018**, *16*, 342–349.
(55) Lucas, C. R.; Halley, P. D.; Chowdury, A. A.; Harrington, B. K.; Beaver, L.; Lapalombella, R.; Johnson, A. J.; Hertlein, E. K.; Phelps, M. A.; Byrd, J. C.; Castro, C. E. DNA Origami Nanostructures Elicit Dose-Dependent Immunogenicity and Are Nontoxic up to High Doses In Vivo. *Small* **2022**, *18* (26), 2108063. https://doi.org/10.1002/smll.202108063.
(56) Schwarzenbach, H.; Hoon, D. S. B.; Pantel, K. Cell-Free Nucleic Acids as Biomarkers in Cancer Patients. *Nat. Rev. Cancer* **2011**, *11* (6), 426–437. https://doi.org/10.1038/nrc3066.
(57) P, M.; P, M. Les acides nucléiques du plasma sanguin chez I'homme. *C R Acad Sci Paris* **1948**, *142*, 241–243.
(58) Stroun, M.; Anker, P.; Maurice, P.; Lyautey, J.; Lederrey, C.; Beljanski, M. Neoplastic Characteristics of the DNA Found in the Plasma of Cancer Patients. *Oncology* **1989**, *46* (5), 318–322. https://doi.org/10.1159/000226740.
(59) Vasioukhin, V.; Anker, P.; Maurice, P.; Lyautey, J.; Lederrey, C.; Stroun, M. Point Mutations of the N-Ras Gene in the Blood Plasma DNA of Patients with Myelodysplastic Syndrome or Acute Myelogenous Leukaemia. *Br. J. Haematol.* **1994**, *86* (4), 774–779. https://doi.org/10.1111/j.1365-2141.1994.tb04828.x.
(60) Raghavendra, P.; Pullaiah, T. RNA-Based Applications in Diagnostic and Therapeutics for Cancer. In *Advances in Cell and Molecular Diagnostics*; Elsevier, 2018; pp 33–55. https://doi.org/10.1016/B978-0-12-813679-9.00002-6.
(61) Thakur, B. K.; Zhang, H.; Becker, A.; Matei, I.; Huang, Y.; Costa-Silva, B.; Zheng, Y.; Hoshino, A.; Brazier, H.; Xiang, J.; Williams, C.; Rodriguez-Barrueco, R.; Silva, J. M.; Zhang, W.; Hearn, S.; Elemento, O.; Paknejad, N.; Manova-Todorova, K.; Welte, K.; Bromberg, J.; Peinado, H.; Lyden, D. Double-Stranded DNA in Exosomes: A Novel Biomarker in Cancer Detection. *Cell Res.* **2014**, *24* (6), 766–769. https://doi.org/10.1038/cr.2014.44.
(62) Wang, M.; Yu, F.; Ding, H.; Wang, Y.; Li, P.; Wang, K. Emerging Function and Clinical Values of Exosomal MicroRNAs in Cancer. *Mol. Ther. - Nucleic Acids* **2019**, *16*, 791–804. https://doi.org/10.1016/j.omtn.2019.04.027.
(63) Bronkhorst, A. J.; Ungerer, V.; Holdenrieder, S. The Emerging Role of Cell-Free DNA as a Molecular Marker for Cancer Management. *Biomol. Detect. Quantif.* **2019**, *17*, 100087. https://doi.org/10.1016/j.bdq.2019.100087.
(64) Mitchell, P. S.; Parkin, R. K.; Kroh, E. M.; Fritz, B. R.; Wyman, S. K.; Pogosova-Agadjanyan, E. L.; Peterson, A.; Noteboom, J.; O'Briant, K. C.; Allen, A.; Lin, D. W.; Urban, N.; Drescher, C. W.; Knudsen, B. S.; Stirewalt, D. L.; Gentleman, R.; Vessella, R. L.; Nelson, P. S.; Martin, D. B.; Tewari, M. Circulating MicroRNAs as Stable Blood-Based Markers for Cancer Detection. *Proc. Natl. Acad. Sci. U. S. A.* **2008**, *105* (30), 10513–10518. https://doi.org/10.1073/pnas.0804549105.

(65) Cocucci, E.; Racchetti, G.; Meldolesi, J. Shedding Microvesicles: Artefacts No More. *Trends Cell Biol.* **2009**, *19* (2), 43–51. https://doi.org/10.1016/j.tcb.2008.11.003.
(66) Hu, Z.; Chen, X.; Zhao, Y.; Tian, T.; Jin, G.; Shu, Y.; Chen, Y.; Xu, L.; Zen, K.; Zhang, C.; Shen, H. Serum MicroRNA Signatures Identified in a Genome-Wide Serum MicroRNA Expression Profiling Predict Survival of Non-Small-Cell Lung Cancer. *J. Clin. Oncol. Off. J. Am. Soc. Clin. Oncol.* **2010**, *28* (10), 1721–1726. https://doi.org/10.1200/JCO.2009.24.9342.
(67) Kamat, A. A.; Baldwin, M.; Urbauer, D.; Dang, D.; Han, L. Y.; Godwin, A.; Karlan, B. Y.; Simpson, J. L.; Gershenson, D. M.; Coleman, R. L.; Bischoff, F. Z.; Sood, A. K. Plasma Cell-Free DNA in Ovarian Cancer: An Independent Prognostic Biomarker. *Cancer* **2010**, *116* (8), 1918–1925. https://doi.org/10.1002/cncr.24997.
(68) Burnham, P.; Dadhania, D.; Heyang, M.; Chen, F.; Westblade, L. F.; Suthanthiran, M.; Lee, J. R.; De Vlaminck, I. Urinary Cell-Free DNA Is a Versatile Analyte for Monitoring Infections of the Urinary Tract. *Nat. Commun.* **2018**, *9* (1), 2412. https://doi.org/10.1038/s41467-018-04745-0.
(69) Liao, P.-H.; Chang, Y.-C.; Huang, M.-F.; K-W, T.; Chou, M.-Y. *Oral Oncol.* **2000**, *36*, 272–276.
(70) Hyun, K.-A.; Gwak, H.; Lee, J.; B, K.; H.-l, J. *Micromachines* **2018**, *9*, 340.
(71) Birkenkamp-Demtröder, K.; Nordentoft, I.; Christensen, E.; Høyer, S.; Reinert, T.; Vang, S.; Borre, M.; Agerbæk, M.; Jensen, J. B.; Ørntoft, T. F.; Dyrskjøt, L. Genomic Alterations in Liquid Biopsies from Patients with Bladder Cancer. *Eur. Urol.* **2016**, *70* (1), 75–82. https://doi.org/10.1016/j.eururo.2016.01.007.
(72) Huang, Y.; Tao, M.; Luo, S.; Zhang, Y.; Situ, B.; Ye, X.; Chen, P.; Jiang, X.; Q, W.; Zheng, L. *Anal. Chim. Acta* **2020**, *1107*, 40–47.
(73) Hulbert, A.; Jusue-Torres, I.; Stark, A.; Chen, C.; Rodgers, K.; Lee, B.; Griffin, C.; Yang, A.; Huang, P.; Wrangle, J.; Belinsky, S. A.; Wang, T.-H.; Yang, S. C.; Baylin, S. B.; Brock, M. V.; Herman, J. G. Early Detection of Lung Cancer Using DNA Promoter Hypermethylation in Plasma and Sputum. *Clin. Cancer Res. Off. J. Am. Assoc. Cancer Res.* **2017**, *23* (8), 1998–2005. https://doi.org/10.1158/1078-0432.CCR-16-1371.
(74) Cohen, L.; Hartman, M. R.; Amardey-Wellington, A.; Walt, D. R. Digital Direct Detection of MicroRNAs Using Single Molecule Arrays. *Nucleic Acids Res.* **2017**, *45* (14), e137–e137. https://doi.org/10.1093/nar/gkx542.
(75) Wark, A. W.; Lee, H. J.; Corn, R. M. Multiplexed Detection Methods for Profiling MicroRNA Expression in Biological Samples. *Angew. Chem. Int. Ed Engl.* **2008**, *47* (4), 644–652. https://doi.org/10.1002/anie.200702450.
(76) Bustin, S. A.; Nolan, T. Pitfalls of Quantitative Real-Time Reverse-Transcription Polymerase Chain Reaction. *J. Biomol. Tech. JBT* **2004**, *15* (3), 155–166.
(77) Shi, H.; Wang, Y.; Zheng, J.; Ning, L.; Huang, Y.; Sheng, A.; Chen, T.; Xiang, Y.; Zhu, X.; Li, G. Dual-Responsive DNA Nanodevice for the Available Imaging of an Apoptotic Signaling Pathway *in Situ*. *ACS Nano* **2019**, *13* (11), 12840–12850. https://doi.org/10.1021/acsnano.9b05082.
(78) A, S.; IL, M.; Nanoscale. 2016, *8*, 9037–9095.
(79) Proudnikov, D.; Mirzabekov, A. Chemical Methods of DNA and RNA Fluorescent Labeling. *Nucleic Acids Res.* **1996**, *24* (22), 4535–4542. https://doi.org/10.1093/nar/24.22.4535.

(80) Ge, J.; Zhang, L.-L.; Liu, S.-J.; Yu, R.-Q.; Chu, X. A Highly Sensitive Target-Primed Rolling Circle Amplification (TPRCA) Method for Fluorescent in Situ Hybridization Detection of MicroRNA in Tumor Cells. *Anal. Chem.* **2014**, *86* (3), 1808–1815. https://doi.org/10.1021/ac403741y.
(81) Dirks, R. M.; Pierce, N. A. Triggered Amplification by Hybridization Chain Reaction. *Proc. Natl. Acad. Sci. U. S. A.* **2004**, *101* (43), 15275–15278. https://doi.org/10.1073/pnas.0407024101.
(82) Yin, P.; Choi, H. M. T.; Calvert, C. R.; Pierce, N. A. Programming Biomolecular Self-Assembly Pathways. *Nature* **2008**, *451* (7176), 318–322. https://doi.org/10.1038/nature06451.
(83) Yurke, B.; Turberfield, A. J.; Mills, A. P.; Simmel, F. C.; Neumann, J. L. A DNA-Fuelled Molecular Machine Made of DNA. *Nature* **2000**, *406* (6796), 605–608. https://doi.org/10.1038/35020524.
(84) Green, S. J.; Lubrich, D.; Turberfield, A. J. DNA Hairpins: Fuel for Autonomous DNA Devices. *Biophys. J.* **2006**, *91* (8), 2966–2975. https://doi.org/10.1529/biophysj.106.084681.
(85) Zhu, Z.; Tang, Y.; Jiang, Y. S.; Bhadra, S.; Du, Y.; Ellington, A. D.; Li, B. Strand-Exchange Nucleic Acid Circuitry with Enhanced Thermo-and Structure- Buffering Abilities Turns Gene Diagnostics Ultra-Reliable and Environmental Compatible. *Sci. Rep.* **2016**, *6* (1), 36605. https://doi.org/10.1038/srep36605.
(86) Zhang, Z.; Fan, T. W.; Hsing, I.-M. Integrating DNA Strand Displacement Circuitry to the Nonlinear Hybridization Chain Reaction. *Nanoscale* **2017**, *9* (8), 2748–2754. https://doi.org/10.1039/C6NR06589A.
(87) Choi, H. M. T.; Chang, J. Y.; Trinh, L. A.; Padilla, J. E.; Fraser, S. E.; Pierce, N. A. Programmable in Situ Amplification for Multiplexed Imaging of MRNA Expression. *Nat. Biotechnol.* **2010**, *28* (11), 1208–1212. https://doi.org/10.1038/nbt.1692.
(88) Dai, W.; Zhang, J.; Meng, X.; He, J.; Zhang, K.; Cao, Y.; Wang, D.; Dong, H.; Zhang, X. Catalytic Hairpin Assembly Gel Assay for Multiple and Sensitive MicroRNA Detection. *Theranostics* **2018**, *8* (10), 2646–2656. https://doi.org/10.7150/thno.24480.
(89) Peng, H.; Newbigging, A. M.; Reid, M. S.; Uppal, J. S.; Xu, J.; H, Z.; Le, X. C. *Anal Chem* **2020**, *92*, 292–308.
(90) Choi, H. M. T.; VA, B.; Pierce, N. A. *ACS Nano* **2014**, *8*, 4284–4294.
(91) Choi, H. M. T.; Schwarzkopf, M.; Fornace, M. E.; Acharya, A.; Artavanis, G.; Stegmaier, J.; Cunha, A.; Pierce, N. A. Third-Generation in Situ Hybridization Chain Reaction: Multiplexed, Quantitative, Sensitive, Versatile, Robust. *Dev. Camb. Engl.* **2018**, *145* (12), dev165753. https://doi.org/10.1242/dev.165753.
(92) Wu, Z.; Liu, G.-Q.; Yang, X.-L.; Jiang, J.-H. Electrostatic Nucleic Acid Nanoassembly Enables Hybridization Chain Reaction in Living Cells for Ultrasensitive MRNA Imaging. *J. Am. Chem. Soc.* **2015**, *137* (21), 6829–6836. https://doi.org/10.1021/jacs.5b01778.
(93) Zhou, H.; Liu, J.; Xu, J.-J.; Zhang, S.-S.; Chen, H.-Y. Optical Nano-Biosensing Interface *via* Nucleic Acid Amplification Strategy: Construction and Application. *Chem. Soc. Rev.* **2018**, *47* (6), 1996–2019. https://doi.org/10.1039/C7CS00573C.
(94) Li, S.; Li, P.; Ge, M.; Wang, H.; Cheng, Y.; Li, G.; Huang, Q.; He, H.; Cao, C.; Lin, D.; Yang, L. Elucidation of Leak-Resistance DNA Hybridization Chain Reaction with Universality and Extensibility. *Nucleic Acids Res.* **2020**, *48* (5), 2220–2231. https://doi.org/10.1093/nar/gkaa016.

(95) Wang, J.; Wang, D.-X.; Ma, J.-Y.; Wang, Y.-X.; Kong, D.-M. Three-Dimensional DNA Nanostructures to Improve the Hyperbranched Hybridization Chain Reaction. *Chem. Sci.* **2019**, *10* (42), 9758–9767. https://doi.org/10.1039/C9SC02281C.
(96) Huang, D.-J.; Cao, T.; Huang, Z.-M.; Wu, Z.; Tang, L.-J.; Jiang, J.-H. Crosslinking Catalytic Hairpin Assembly for High-Contrast Imaging of Multiple MRNAs in Living Cells. *Chem. Commun. Camb. Engl.* **2019**, *55* (27), 3899–3902. https://doi.org/10.1039/c9cc01033e.
(97) Choi, H. M. T.; Beck, V. A.; Pierce, N. A. Next-Generation in Situ Hybridization Chain Reaction: Higher Gain, Lower Cost, Greater Durability. *ACS Nano* **2014**, *8* (5), 4284–4294. https://doi.org/10.1021/nn405717p.
(98) Qing, Z.; Hu, J.; Xu, J.; Zou, Z.; Lei, Y.; Qing, T.; Yang, R. An Intramolecular Catalytic Hairpin Assembly on a DNA Tetrahedron for MRNA Imaging in Living Cells: Improving Reaction Kinetics and Signal Stability. *Chem. Sci.* **2020**, *11* (7), 1985–1990. https://doi.org/10.1039/C9SC04916A.
(99) Wen, X.; Yuan, B.; Zhang, J.; Meng, X.; Guo, Q.; Li, L.; Li, Z.; Jiang, H.; Wang, K. Enhanced Visualization of Cell Surface Glycans via a Hybridization Chain Reaction. *Chem. Commun. Camb. Engl.* **2019**, *55* (43), 6114–6117. https://doi.org/10.1039/c9cc02069a.
(100) Kimoto, M.; Shermane Lim, Y. W.; Hirao, I. Molecular Affinity Rulers: Systematic Evaluation of DNA Aptamers for Their Applicabilities in ELISA. *Nucleic Acids Res.* **2019**, *47* (16), 8362–8374. https://doi.org/10.1093/nar/gkz688.
(101) Lakhin, A. V.; Tarantul, V. Z.; Gening, L. V. Aptamers: Problems, Solutions and Prospects. *Acta Naturae* **2013**, *5* (4), 34–43.
(102) Qin, Y.; Li, D.; Yuan, R.; Xiang, Y. Netlike Hybridization Chain Reaction Assembly of DNA Nanostructures Enables Exceptional Signal Amplification for Sensing Trace Cytokines. *Nanoscale* **2019**, *11* (35), 16362–16367. https://doi.org/10.1039/c9nr04988f.
(103) Chang, X.; Zhang, C.; Lv, C.; Sun, Y.; Zhang, M.; Zhao, Y.; Yang, L.; Han, D.; Tan, W. Construction of a Multiple-Aptamer-Based DNA Logic Device on Live Cell Membranes via Associative Toehold Activation for Accurate Cancer Cell Identification. *J. Am. Chem. Soc.* **2019**, *141* (32), 12738–12743. https://doi.org/10.1021/jacs.9b05470.
(104) Xiong, Y.; Chen, Y.; Ding, L.; Liu, X.; Ju, H. Fluorescent Visual Quantitation of Cell-Secreted Sialoglycoconjugates by Chemoselective Recognition and Hybridization Chain Reaction. *The Analyst* **2019**, *144* (15), 4545–4551. https://doi.org/10.1039/c9an00572b.
(105) Li, Z.; Yuan, B.; Lin, X.; Meng, X.; Wen, X.; Guo, Q.; Li, L.; Jiang, H.; Wang, K. Intramolecular Trigger Remodeling-Induced HCR for Amplified Detection of Protein-Specific Glycosylation. *Talanta* **2020**, *215*, 120889. https://doi.org/10.1016/j.talanta.2020.120889.
(106) Hahn, J.; Wickham, S. F. J.; Shih, W. M.; Perrault, S. D. Addressing the Instability of DNA Nanostructures in Tissue Culture. *ACS Nano* **2014**, *8* (9), 8765–8775. https://doi.org/10.1021/nn503513p.
(107) Chu, H.; Zhao, J.; Mi, Y.; Zhao, Y.; Li, L. Near-Infrared Light-Initiated Hybridization Chain Reaction for Spatially and Temporally Resolved Signal Amplification. *Angew. Chem. Int. Ed Engl.* **2019**, *58* (42), 14877–14881. https://doi.org/10.1002/anie.201906224.
(108) Li, G.-L.; Xia, Y.-H.; Li, Q. Biodegradable MnO2 Nanosheet-Mediated Catalytic Hairpin Assembly for Two-Color Imaging of MRNAs in Living Cells. *Microchem. J.* **2020**, *153*, 104367. https://doi.org/10.1016/j.microc.2019.104367.

(109) Liu, G.; Chai, H.; Tang, Y.; Miao, P. Bright Carbon Nanodots for MiRNA Diagnostics Coupled with Concatenated Hybridization Chain Reaction. *Chem. Commun.* **2020**, *56* (8), 1175–1178. https://doi.org/10.1039/C9CC08753B.
(110) Yang, K.; Zeng, M.; Fu, X.; Li, J.; Ma, N.; Tao, L. Establishing Biodegradable Single-Layer MnO $_2$ Nanosheets as a Platform for Live Cell MicroRNA Sensing. *RSC Adv.* **2015**, *5* (126), 104245–104249. https://doi.org/10.1039/C5RA21467J.
(111) Li, G.; Li, J.; Li, Q. Biodegradable MnO2 Nanosheet Mediated Hybridization Chain Reaction for Imaging of Human Apurinic/Apyrimidinic Endonuclease 1 Activity in Living Cells. *Nanoscale* **2019**, *11* (43), 20456–20460. https://doi.org/10.1039/c9nr06436b.
(112) Chen, J.; Yang, H.-H.; Yin, W.; Zhang, Y.; Ma, Y.; Chen, D.; Xu, Y.; Liu, S.-Y.; Zhang, L.; Dai, Z.; Zou, X. Metastable Dumbbell Probe-Based Hybridization Chain Reaction for Sensitive and Accurate Imaging of Intracellular-Specific MicroRNAs In Situ in Living Cells. *Anal. Chem.* **2019**, *91* (7), 4625–4631. https://doi.org/10.1021/acs.analchem.8b05920.
(113) Ma, W.; Chen, B.; Zou, S.; Jia, R.; Cheng, H.; Huang, J.; Wang, H.; He, X.; Wang, K. I-Motif-Based in Situ Bipedal Hybridization Chain Reaction for Specific Activatable Imaging and Enhanced Delivery of Antisense Oligonucleotides. *Anal. Chem.* **2019**, *91* (19), 12538–12545. https://doi.org/10.1021/acs.analchem.9b03420.
(114) Zhong, Y.-Q.; Wei, J.; Fu, Y.-R.; Shao, J.; Liang, Y.-W.; Lin, Y.-H.; Liu, J.; Zhu, Z.-H. [Toxicity of cationic liposome Lipofectamine 2000 in human pancreatic cancer Capan-2 cells]. *Nan Fang Yi Ke Da Xue Xue Bao* **2008**, *28* (11), 1981–1984.
(115) Rust, A.; Hassan, H. H. A.; Sedelnikova, S.; Niranjan, D.; Hautbergue, G.; Abbas, S. A.; Partridge, L.; Rice, D.; Binz, T.; Davletov, B. Two Complementary Approaches for Intracellular Delivery of Exogenous Enzymes. *Sci. Rep.* **2015**, *5*, 12444. https://doi.org/10.1038/srep12444.
(116) Goers, L.; Freemont, P.; Polizzi, K. M. Co-Culture Systems and Technologies: Taking Synthetic Biology to the next Level. *J. R. Soc. Interface* **2014**, *11* (96), 20140065. https://doi.org/10.1098/rsif.2014.0065.
(117) Swaminathan, S.; Cranston, A. N.; Clyne, A. M. A Three-Dimensional In Vitro Coculture Model to Quantify Breast Epithelial Cell Adhesion to Endothelial Cells. *Tissue Eng. Part C Methods* **2019**, *25* (10), 609–618. https://doi.org/10.1089/ten.TEC.2019.0122.
(118) Raffort, J.; Hinault, C.; Dumortier, O.; Van Obberghen, E. Circulating MicroRNAs and Diabetes: Potential Applications in Medical Practice. *Diabetologia* **2015**, *58* (9), 1978–1992. https://doi.org/10.1007/s00125-015-3680-y.
(119) Wang, J.; Yi, X.; Tang, H.; Han, H.; Wu, M.; Zhou, F. Direct Quantification of MicroRNA at Low Picomolar Level in Sera of Glioma Patients Using a Competitive Hybridization Followed by Amplified Voltammetric Detection. *Anal. Chem.* **2012**, *84* (15), 6400–6406. https://doi.org/10.1021/ac203368h.
(120) Drummond, T. G.; Hill, M. G.; Barton, J. K. Electrochemical DNA Sensors. *Nat. Biotechnol.* **2003**, *21* (10), 1192–1199. https://doi.org/10.1038/nbt873.
(121) Palecek, E.; Fojta, M.; Jelen, F. New Approaches in the Development of DNA Sensors: Hybridization and Electrochemical Detection of DNA and RNA at Two Different Surfaces. *Bioelectrochemistry Amst. Neth.* **2002**, *56* (1–2), 85–90. https://doi.org/10.1016/s1567-5394(02)00025-7.

(122) Rasheed, P. A.; Sandhyarani, N. A Highly Sensitive DNA Sensor for Attomolar Detection of the BRCA1 Gene: Signal Amplification with Gold Nanoparticle Clusters. *The Analyst* **2015**, *140* (8), 2713–2718. https://doi.org/10.1039/c5an00004a.
(123) De Rache, A.; Doneux, T.; Kejnovská, I.; Buess-Herman, C. On the Interaction between [Ru(NH3)6]3+ and the G-Quadruplex Forming Thrombin Binding Aptamer Sequence. *J. Inorg. Biochem.* **2013**, *126*, 84–90. https://doi.org/10.1016/j.jinorgbio.2013.05.014.
(124) Guo, Q.; Yu, Y.; Zhang, H.; Cai, C.; Shen, Q. Electrochemical Sensing of Exosomal MicroRNA Based on Hybridization Chain Reaction Signal Amplification with Reduced False-Positive Signals. *Anal. Chem.* **2020**, *92* (7), 5302–5310. https://doi.org/10.1021/acs.analchem.9b05849.
(125) Lv, M.-M.; Fan, S.-F.; Wang, Q.-L.; Lv, Q.-Y.; Song, X.; Cui, H.-F. An Enzyme-Free Electrochemical Sandwich DNA Assay Based on the Use of Hybridization Chain Reaction and Gold Nanoparticles: Application to the Determination of the DNA of Helicobacter Pylori. *Microchim. Acta* **2020**, *187* (1), 73. https://doi.org/10.1007/s00604-019-3999-z.
(126) Chen, X.; Huang, J.; Zhang, S.; Mo, F.; Su, S.; Li, Y.; Fang, L.; Deng, J.; Huang, H.; Luo, Z.; Zheng, J. Electrochemical Biosensor for DNA Methylation Detection through Hybridization Chain-Amplified Reaction Coupled with a Tetrahedral DNA Nanostructure. *ACS Appl. Mater. Interfaces* **2019**, *11* (4), 3745–3752. https://doi.org/10.1021/acsami.8b20144.
(127) Zhou, L.; Wang, Y.; Yang, C.; Xu, H.; Luo, J.; Zhang, W.; Tang, X.; Yang, S.; Fu, W.; Chang, K.; Chen, M. A Label-Free Electrochemical Biosensor for MicroRNAs Detection Based on DNA Nanomaterial by Coupling with Y-Shaped DNA Structure and Non-Linear Hybridization Chain Reaction. *Biosens. Bioelectron.* **2019**, *126*, 657–663. https://doi.org/10.1016/j.bios.2018.11.028.
(128) Richter, M. M. Electrochemiluminescence (ECL). *Chem. Rev.* **2004**, *104* (6), 3003–3036. https://doi.org/10.1021/cr020373d.
(129) Zhang, X.; Li, W.; Zhou, Y.; Chai, Y.; Yuan, R. An Ultrasensitive Electrochemiluminescence Biosensor for MicroRNA Detection Based on Luminol-Functionalized Au NPs@ZnO Nanomaterials as Signal Probe and Dissolved O2 as Coreactant. *Biosens. Bioelectron.* **2019**, *135*, 8–13. https://doi.org/10.1016/j.bios.2019.04.004.
(130) Ge, J.; Li, C.; Zhao, Y.; Yu, X.; Jie, G. Versatile "on-off" Biosensing of Thrombin and MiRNA Based on Ag(i) Ion-Enhanced or Ag Nanocluster-Quenched Electrochemiluminescence Coupled with Hybridization Chain Reaction Amplification. *Chem. Commun. Camb. Engl.* **2019**, *55* (51), 7350–7353. https://doi.org/10.1039/c9cc03235e.
(131) Nam, J.-M.; Stoeva, S. I.; Mirkin, C. A. Bio-Bar-Code-Based DNA Detection with PCR-like Sensitivity. *J. Am. Chem. Soc.* **2004**, *126* (19), 5932–5933. https://doi.org/10.1021/ja049384+.
(132) Tang, S.; Gu, Y.; Lu, H.; Dong, H.; Zhang, K.; Dai, W.; Meng, X.; Yang, F.; Zhang, X. Highly-Sensitive MicroRNA Detection Based on Bio-Bar-Code Assay and Catalytic Hairpin Assembly Two-Stage Amplification. *Anal. Chim. Acta* **2018**, *1004*, 1–9. https://doi.org/10.1016/j.aca.2017.12.004.
(133) Luck, M. E.; Muljo, S. A.; Collins, C. B. Prospects for Therapeutic Targeting of MicroRNAs in Human Immunological Diseases. *J. Immunol. Baltim. Md 1950* **2015**, *194* (11), 5047–5052. https://doi.org/10.4049/jimmunol.1403146.

(134) Xu, G.; Lai, M.; Wilson, R.; Glidle, A.; Reboud, J.; Cooper, J. M. Branched Hybridization Chain Reaction-Using Highly Dimensional DNA Nanostructures for Label-Free, Reagent-Less, Multiplexed Molecular Diagnostics. *Microsyst. Nanoeng.* **2019**, *5*, 37. https://doi.org/10.1038/s41378-019-0076-z.
(135) Lv, M.-M.; Wu, Z.; Yu, R.-Q.; Jiang, J.-H. Three-Dimensional DNA Nanostructures for Dual-Color MicroRNA Imaging in Living Cells via Hybridization Chain Reaction. *Chem. Commun. Camb. Engl.* **2020**, *56* (49), 6668–6671. https://doi.org/10.1039/d0cc01626h.
(136) Xia, C.; Babcock, H. P.; Moffitt, J. R.; Zhuang, X. Multiplexed Detection of RNA Using MERFISH and Branched DNA Amplification. *Sci. Rep.* **2019**, *9* (1), 7721. https://doi.org/10.1038/s41598-019-43943-8.
(137) Lv, M.-M.; Wu, Z.; Yu, R.-Q.; Jiang, J.-H. Three-Dimensional DNA Nanostructures for Dual-Color MicroRNA Imaging in Living Cells *via* Hybridization Chain Reaction. *Chem. Commun.* **2020**, *56* (49), 6668–6671. https://doi.org/10.1039/D0CC01626H.
(138) Zhang, D.; Bian, F.; Cai, L.; Wang, T.; Kong, T.; Zhao, Y. Bioinspired Photonic Barcodes for Multiplexed Target Cycling and Hybridization Chain Reaction. *Biosens. Bioelectron.* **2019**, *143*, 111629. https://doi.org/10.1016/j.bios.2019.111629.
(139) Chen, K. H.; Boettiger, A. N.; Moffitt, J. R.; Wang, S.; Zhuang, X. RNA Imaging. Spatially Resolved, Highly Multiplexed RNA Profiling in Single Cells. *Science* **2015**, *348* (6233), aaa6090. https://doi.org/10.1126/science.aaa6090.
(140) Guo, J.; Mingoes, C.; Qiu, X.; Hildebrandt, N. Simple, Amplified, and Multiplexed Detection of MicroRNAs Using Time-Gated FRET and Hybridization Chain Reaction. *Anal. Chem.* **2019**, *91* (4), 3101–3109. https://doi.org/10.1021/acs.analchem.8b05600.
(141) Wang, Y.; Shang, L.; Bian, F.; Zhang, X.; Wang, S.; Zhou, M.; Zhao, Y. Hollow Colloid Assembled Photonic Crystal Clusters as Suspension Barcodes for Multiplex Bioassays. *Small* **2019**, *15* (13), 1900056. https://doi.org/10.1002/smll.201900056.
(142) Wang, J.; Sun, Y.; Lau, C.; Lu, J. Target-Fueled Catalytic Hairpin Assembly for Sensitive and Multiplex MicroRNA Detection. *Anal. Bioanal. Chem.* **2020**, *412* (13), 3019–3027. https://doi.org/10.1007/s00216-020-02531-w.
(143) Wu, H.; Chen, T.-T.; Wang, X.-N.; Ke, Y.; Jiang, J.-H. RNA Imaging in Living Mice Enabled by an in Vivo Hybridization Chain Reaction Circuit with a Tripartite DNA Probe. *Chem. Sci.* **2020**, *11* (1), 62–69. https://doi.org/10.1039/c9sc03469b.
(144) Zwicke, G. L.; Mansoori, G. A.; Jeffery, C. J. Utilizing the Folate Receptor for Active Targeting of Cancer Nanotherapeutics. *Nano Rev.* **2012**, *3*. https://doi.org/10.3402/nano.v3i0.18496.
(145) Fernández, M.; Javaid, F.; Chudasama, V. Advances in Targeting the Folate Receptor in the Treatment/Imaging of Cancers. *Chem. Sci.* **2018**, *9* (4), 790–810. https://doi.org/10.1039/c7sc04004k.
(146) Wu, H.; Chen, T.-T.; Wang, X.-N.; Ke, Y.; Jiang, J.-H. RNA Imaging in Living Mice Enabled by an *in Vivo* Hybridization Chain Reaction Circuit with a Tripartite DNA Probe. *Chem. Sci.* **2020**, *11* (1), 62–69. https://doi.org/10.1039/C9SC03469B.
(147) Wei, J.; Wang, H.; Wu, Q.; Gong, X.; Ma, K.; Liu, X.; Wang, F. A Smart, Autocatalytic, DNAzyme Biocircuit for in Vivo, Amplified, MicroRNA Imaging. *Angew. Chem.* **2020**, *132* (15), 6021–6027. https://doi.org/10.1002/ange.201911712.
(148) Feng, Q.; Wang, M.; Han, X.; Chen, Q.; Dou, B.; Wang, P. Construction of an Electrochemical Biosensing Platform Based on Hierarchical Mesoporous NiO@N-Doped C

Microspheres Coupled with Catalytic Hairpin Assembly. *ACS Appl. Bio Mater.* **2020**, *3* (2), 1276–1282. https://doi.org/10.1021/acsabm.9b01145.
(149) Wei, X.; Bian, F.; Cai, X.; Wang, Y.; Cai, L.; Yang, J.; Zhu, Y.; Zhao, Y. Multiplexed Detection Strategy for Bladder Cancer MicroRNAs Based on Photonic Crystal Barcodes. *Anal. Chem.* **2020**, *92* (8), 6121–6127. https://doi.org/10.1021/acs.analchem.0c00630.
(150) Jirakova, L.; Hrstka, R.; Campuzano, S.; Pingarrón, J. M.; Bartosik, M. Multiplexed Immunosensing Platform Coupled to Hybridization Chain Reaction for Electrochemical Determination of MicroRNAs in Clinical Samples. *Electroanalysis* **2019**, *31* (2), 293–302. https://doi.org/10.1002/elan.201800573.
(151) Huang, Y.; Tao, M.; Luo, S.; Zhang, Y.; Situ, B.; Ye, X.; Chen, P.; Jiang, X.; Wang, Q.; Zheng, L. A Novel Nest Hybridization Chain Reaction Based Electrochemical Assay for Sensitive Detection of Circulating Tumor DNA. *Anal. Chim. Acta* **2020**, *1107*, 40–47. https://doi.org/10.1016/j.aca.2020.02.006.
(152) Li, T.; Zou, L.; Zhang, J.; Li, G.; Ling, L. Non-Invasive Diagnosis of Bladder Cancer by Detecting Telomerase Activity in Human Urine Using Hybridization Chain Reaction and Dynamic Light Scattering. *Anal. Chim. Acta* **2019**, *1065*, 90–97. https://doi.org/10.1016/j.aca.2019.03.039.
(153) Herdy, B.; Mayer, C.; Varshney, D.; Marsico, G.; Murat, P.; Taylor, C.; D'Santos, C.; Tannahill, D.; Balasubramanian, S. Analysis of NRAS RNA G-Quadruplex Binding Proteins Reveals DDX3X as a Novel Interactor of Cellular G-Quadruplex Containing Transcripts. *Nucleic Acids Res.* **2018**, *46* (21), 11592–11604. https://doi.org/10.1093/nar/gky861.
(154) González, V.; Guo, K.; Hurley, L.; Sun, D. Identification and Characterization of Nucleolin as a C-Myc G-Quadruplex-Binding Protein. *J. Biol. Chem.* **2009**, *284* (35), 23622–23635. https://doi.org/10.1074/jbc.M109.018028.
(155) Jia, L.-P.; Wang, L.-J.; Ma, R.-N.; Shang, L.; Zhang, W.; Xue, Q.-W.; Wang, H.-S. An Electrochemical Aptasensor for the Highly Sensitive Detection of 8-Hydroxy-2'-Deoxyguanosine Based on the Hybridization Chain Reaction. *Talanta* **2018**, *179*, 414–419. https://doi.org/10.1016/j.talanta.2017.11.036.
(156) He, M.; He, M.; Zhang, J.; Liu, C.; Pan, Q.; Yi, J.; Chen, T. A Spatial-Confinement Hairpin Cascade Reaction-Based DNA Tetrahedral Amplifier for MRNA Imaging in Live Cells. *Talanta* **2020**, *207*, 120287. https://doi.org/10.1016/j.talanta.2019.120287.
(157) He, L.; Lu, D.; Liang, H.; Xie, S.; Zhang, X.; Liu, Q.; Yuan, Q.; Tan, W. MRNA-Initiated, Three-Dimensional DNA Amplifier Able to Function inside Living Cells. *J. Am. Chem. Soc.* **2018**, *140* (1), 258–263. https://doi.org/10.1021/jacs.7b09789.
(158) Jung, C.; Ellington, A. D. Diagnostic Applications of Nucleic Acid Circuits. *Acc. Chem. Res.* **2014**, *47* (6), 1825–1835. https://doi.org/10.1021/ar500059c.
(159) Arter, W. E.; Yusim, Y.; Peter, Q.; Taylor, C. G.; Klenerman, D.; Keyser, U. F.; Knowles, T. P. J. Digital Sensing and Molecular Computation by an Enzyme-Free DNA Circuit. *ACS Nano* **2020**, *14* (5), 5763–5771. https://doi.org/10.1021/acsnano.0c00628.
(160) Shi, H.; Dai, J.; Wang, F.; Xia, Y.; Xiao, D.; Zhou, C. Rapid and Colorimetric Detection of Nucleic Acids Based on Entropy-Driven Circuit and DNAzyme-Mediated Autocatalytic Reactions. *Anal. Methods* **2020**, *12* (21), 2779–2784. https://doi.org/10.1039/D0AY00341G.

(161) Zhang, K.; Wang, K.; Zhu, X.; Xie, M. Entropy-Driven Reactions in Living Cells for Assay Let-7a MicroRNA. *Anal. Chim. Acta* **2017**, *949*, 53–58. https://doi.org/10.1016/j.aca.2016.10.034.
(162) Meng, H.-M.; Shi, X.; Chen, J.; Gao, Y.; Qu, L.; Zhang, K.; Zhang, X.-B.; Li, Z. DNA Amplifier-Functionalized Metal–Organic Frameworks for Multiplexed Detection and Imaging of Intracellular MRNA. *ACS Sens.* **2020**, *5* (1), 103–109. https://doi.org/10.1021/acssensors.9b01759.
(163) Zhang, N.; Shi, X.-M.; Guo, H.-Q.; Zhao, X.-Z.; Zhao, W.-W.; Xu, J.-J.; Chen, H.-Y. Gold Nanoparticle Couples with Entropy-Driven Toehold-Mediated DNA Strand Displacement Reaction on Magnetic Beads: Toward Ultrasensitive Energy-Transfer-Based Photoelectrochemical Detection of MiRNA-141 in Real Blood Sample. *Anal. Chem.* **2018**, *90* (20), 11892–11898. https://doi.org/10.1021/acs.analchem.8b01966.
(164) Zhou, M.; Feng, C.; Mao, D.; Yang, S.; Ren, L.; Chen, G.; Zhu, X. An Electrochemical Biosensor Integrating Immunoassay and Enzyme Activity Analysis for Accurate Detection of Active Human Apurinic/Apyrimidinic Endonuclease 1. *Biosens. Bioelectron.* **2019**, *142*, 111558. https://doi.org/10.1016/j.bios.2019.111558.
(165) Zhao, R.-N.; Feng, Z.; Zhao, Y.-N.; Jia, L.-P.; Ma, R.-N.; Zhang, W.; Shang, L.; Xue, Q.-W.; Wang, H.-S. A Sensitive Electrochemical Aptasensor for Mucin 1 Detection Based on Catalytic Hairpin Assembly Coupled with PtPdNPs Peroxidase-like Activity. *Talanta* **2019**, *200*, 503–510. https://doi.org/10.1016/j.talanta.2019.03.012.
(166) Budman, L. I.; Kassouf, W.; Steinberg, J. R. Biomarkers for Detection and Surveillance of Bladder Cancer. *Can. Urol. Assoc. J.* **2013**, *2* (3), 212. https://doi.org/10.5489/cuaj.600.
(167) Diamandis, E. P. The Failure of Protein Cancer Biomarkers to Reach the Clinic: Why, and What Can Be Done to Address the Problem? *BMC Med.* **2012**, *10* (1), 87. https://doi.org/10.1186/1741-7015-10-87.
(168) Kilgour, E.; Rothwell, D. G.; Brady, G.; Dive, C. Liquid Biopsy-Based Biomarkers of Treatment Response and Resistance. *Cancer Cell* **2020**, *37* (4), 485–495. https://doi.org/10.1016/j.ccell.2020.03.012.
(169) Ronald, J. A.; Katzenberg, R.; Nielsen, C. H.; Jae, H. J.; Hofmann, L. V.; Gambhir, S. S. MicroRNA-Regulated Non-Viral Vectors with Improved Tumor Specificity in an Orthotopic Rat Model of Hepatocellular Carcinoma. *Gene Ther.* **2013**, *20* (10), 1006–1013. https://doi.org/10.1038/gt.2013.24.
(170) Jayanthi, V. S. P. K. S. A.; Das, A. B.; Saxena, U. Recent Advances in Biosensor Development for the Detection of Cancer Biomarkers. *Biosens. Bioelectron.* **2017**, *91*, 15–23. https://doi.org/10.1016/j.bios.2016.12.014.
(171) Dong, H.; Lei, J.; Ding, L.; Wen, Y.; Ju, H.; Zhang, X. MicroRNA: Function, Detection, and Bioanalysis. *Chem. Rev.* **2013**, *113* (8), 6207–6233. https://doi.org/10.1021/cr300362f.
(172) Chen, X.; Ba, Y.; Ma, L.; Cai, X.; Yin, Y.; Wang, K.; Guo, J.; Zhang, Y.; Chen, J.; Guo, X.; Li, Q.; Li, X.; Wang, W.; Zhang, Y.; Wang, J.; Jiang, X.; Xiang, Y.; Xu, C.; Zheng, P.; Zhang, J.; Li, R.; Zhang, H.; Shang, X.; Gong, T.; Ning, G.; Wang, J.; Zen, K.; Zhang, J.; Zhang, C.-Y. Characterization of MicroRNAs in Serum: A Novel Class of Biomarkers for Diagnosis of Cancer and Other Diseases. *Cell Res.* **2008**, *18* (10), 997–1006. https://doi.org/10.1038/cr.2008.282.
(173) Costinean, S.; Zanesi, N.; Pekarsky, Y.; Tili, E.; Volinia, S.; Heerema, N.; Croce, C. M. Pre-B Cell Proliferation and Lymphoblastic Leukemia/High-Grade Lymphoma in E -

MiR155 Transgenic Mice. *Proc. Natl. Acad. Sci.* **2006**, *103* (18), 7024–7029. https://doi.org/10.1073/pnas.0602266103.
(174) Igder, S.; Mohammadiasl, J.; Mokarram, P. Altered MiR-21, MiRNA-148a Expression in Relation to KRAS Mutation Status as Indicator of Adenoma-Carcinoma Transitional Pattern in Colorectal Adenoma and Carcinoma Lesions. *Biochem. Genet.* **2019**, *57* (6), 767–780. https://doi.org/10.1007/s10528-019-09918-0.
(175) Cammarata, G.; Augugliaro, L.; Salemi, D.; Agueli, C.; Rosa, M. L.; Dagnino, L.; Civiletto, G.; Messana, F.; Marfia, A.; Bica, M. G.; Cascio, L.; Floridia, P. M.; Mineo, A. M.; Russo, M.; Fabbiano, F.; Santoro, A. Differential Expression of Specific MicroRNA and Their Targets in Acute Myeloid Leukemia. *Am. J. Hematol.* **2010**, NA-NA. https://doi.org/10.1002/ajh.21667.
(176) Peng, Y.; Dai, Y.; Hitchcock, C.; Yang, X.; Kassis, E. S.; Liu, L.; Luo, Z.; Sun, H.-L.; Cui, R.; Wei, H.; Kim, T.; Lee, T. J.; Jeon, Y.-J.; Nuovo, G. J.; Volinia, S.; He, Q.; Yu, J.; Nana-Sinkam, P.; Croce, C. M. Insulin Growth Factor Signaling Is Regulated by MicroRNA-486, an Underexpressed MicroRNA in Lung Cancer. *Proc. Natl. Acad. Sci.* **2013**, *110* (37), 15043–15048. https://doi.org/10.1073/pnas.1307107110.
(177) Zhang, C.-Z.; Zhang, J.-X.; Zhang, A.-L.; Shi, Z.-D.; Han, L.; Jia, Z.-F.; Yang, W.-D.; Wang, G.-X.; Jiang, T.; You, Y.-P.; Pu, P.-Y.; Cheng, J.-Q.; Kang, C.-S. MiR-221 and MiR-222 Target PUMA to Induce Cell Survival in Glioblastoma. *Mol. Cancer* **2010**, *9* (1), 229. https://doi.org/10.1186/1476-4598-9-229.
(178) Udugama, B.; Kadhiresan, P.; Kozlowski, H. N.; Malekjahani, A.; Osborne, M.; Li, V. Y. C.; Chen, H.; Mubareka, S.; Gubbay, J. B.; Chan, W. C. W. Diagnosing COVID-19: The Disease and Tools for Detection. *ACS Nano* **2020**, *14* (4), 3822–3835. https://doi.org/10.1021/acsnano.0c02624.
(179) Chan, S. K.; Du, P.; Ignacio, C.; Mehta, S.; Newton, I. G.; Steinmetz, N. F. Biomimetic Virus-Like Particles as Severe Acute Respiratory Syndrome Coronavirus 2 Diagnostic Tools. *ACS Nano* **2021**, *15* (1), 1259–1272. https://doi.org/10.1021/acsnano.0c08430.
(180) Tang, Y.; Qiao, G.; Xu, E.; Xuan, Y.; Liao, M.; Yin, G. Biomarkers for Early Diagnosis, Prognosis, Prediction, and Recurrence Monitoring of Non-Small Cell Lung Cancer. *OncoTargets Ther.* **2017**, *Volume 10*, 4527–4534. https://doi.org/10.2147/OTT.S142149.
(181) Di Gioia, D.; Stieber, P.; Schmidt, G. P.; Nagel, D.; Heinemann, V.; Baur-Melnyk, A. Early Detection of Metastatic Disease in Asymptomatic Breast Cancer Patients with Whole-Body Imaging and Defined Tumour Marker Increase. *Br. J. Cancer* **2015**, *112* (5), 809–818. https://doi.org/10.1038/bjc.2015.8.
(182) O'Connor, J. P. B.; Aboagye, E. O.; Adams, J. E.; Aerts, H. J. W. L.; Barrington, S. F.; Beer, A. J.; Boellaard, R.; Bohndiek, S. E.; Brady, M.; Brown, G.; Buckley, D. L.; Chenevert, T. L.; Clarke, L. P.; Collette, S.; Cook, G. J.; deSouza, N. M.; Dickson, J. C.; Dive, C.; Evelhoch, J. L.; Faivre-Finn, C.; Gallagher, F. A.; Gilbert, F. J.; Gillies, R. J.; Goh, V.; Griffiths, J. R.; Groves, A. M.; Halligan, S.; Harris, A. L.; Hawkes, D. J.; Hoekstra, O. S.; Huang, E. P.; Hutton, B. F.; Jackson, E. F.; Jayson, G. C.; Jones, A.; Koh, D.-M.; Lacombe, D.; Lambin, P.; Lassau, N.; Leach, M. O.; Lee, T.-Y.; Leen, E. L.; Lewis, J. S.; Liu, Y.; Lythgoe, M. F.; Manoharan, P.; Maxwell, R. J.; Miles, K. A.; Morgan, B.; Morris, S.; Ng, T.; Padhani, A. R.; Parker, G. J. M.; Partridge, M.; Pathak, A. P.; Peet, A. C.; Punwani, S.; Reynolds, A. R.; Robinson, S. P.; Shankar, L. K.; Sharma, R. A.; Soloviev, D.; Stroobants, S.; Sullivan, D. C.; Taylor, S. A.; Tofts, P. S.; Tozer, G. M.; van Herk, M.; Walker-Samuel, S.; Wason, J.; Williams, K. J.; Workman, P.; Yankeelov, T. E.; Brindle, K.

M.; McShane, L. M.; Jackson, A.; Waterton, J. C. Imaging Biomarker Roadmap for Cancer Studies. *Nat. Rev. Clin. Oncol.* **2017**, *14* (3), 169–186. https://doi.org/10.1038/nrclinonc.2016.162.

(183) Borum, R. M.; Jokerst, J. V. Hybridizing Clinical Translatability with Enzyme-Free DNA Signal Amplifiers: Recent Advances in Nucleic Acid Detection and Imaging. *Biomater. Sci.* **2020**, 10.1039.D0BM00931H. https://doi.org/10.1039/D0BM00931H.

(184) Karunanayake Mudiyanselage, A. P. K. K.; Yu, Q.; Leon-Duque, M. A.; Zhao, B.; Wu, R.; You, M. Genetically Encoded Catalytic Hairpin Assembly for Sensitive RNA Imaging in Live Cells. *J. Am. Chem. Soc.* **2018**, *140* (28), 8739–8745. https://doi.org/10.1021/jacs.8b03956.

(185) Weber, J.; Beard, P. C.; Bohndiek, S. E. Contrast Agents for Molecular Photoacoustic Imaging. *Nat. Methods* **2016**, *13* (8), 639–650. https://doi.org/10.1038/nmeth.3929.

(186) Moore, C.; Jokerst, J. V. Strategies for Image-Guided Therapy, Surgery, and Drug Delivery Using Photoacoustic Imaging. *Theranostics* **2019**, *9* (6), 1550–1571. https://doi.org/10.7150/thno.32362.

(187) Cheng, P.; Chen, W.; Li, S.; He, S.; Miao, Q.; Pu, K. Fluoro-Photoacoustic Polymeric Renal Reporter for Real-Time Dual Imaging of Acute Kidney Injury. *Adv. Mater.* **2020**, *32* (17), 1908530. https://doi.org/10.1002/adma.201908530.

(188) Cao, W.; Gao, W.; Liu, Z.; Hao, W.; Li, X.; Sun, Y.; Tong, L.; Tang, B. Visualizing MiR-155 To Monitor Breast Tumorigenesis and Response to Chemotherapeutic Drugs by a Self-Assembled Photoacoustic Nanoprobe. *Anal. Chem.* **2018**, *90* (15), 9125–9131. https://doi.org/10.1021/acs.analchem.8b01537.

(189) Moore, T. L.; Rodriguez-Lorenzo, L.; Hirsch, V.; Balog, S.; Urban, D.; Jud, C.; Rothen-Rutishauser, B.; Lattuada, M.; Petri-Fink, A. Nanoparticle Colloidal Stability in Cell Culture Media and Impact on Cellular Interactions. *Chem. Soc. Rev.* **2015**, *44* (17), 6287–6305. https://doi.org/10.1039/C4CS00487F.

(190) H., A.; H., K.; T., L.; W., N.; M. An in Vivo Study on the Reaction of Hydroxyapatite-Sol Injected into Blood. *J Mater Sci Mater Med* **2000**, *11* (2), 67-72,. https://doi.org/10.1023/A:1008993814033.

(191) Pathak, P.; Yao, W.; Hook, K. D.; Vik, R.; Winnerdy, F. R.; Brown, J. Q.; Gibb, B. C.; Pursell, Z. F.; Phan, A. T.; Jayawickramarajah, J. Bright G-Quadruplex Nanostructures Functionalized with Porphyrin Lanterns. *J. Am. Chem. Soc.* **2019**, *141* (32), 12582–12591. https://doi.org/10.1021/jacs.9b03250.

(192) Miao, Q.; Pu, K. Emerging Designs of Activatable Photoacoustic Probes for Molecular Imaging. *Bioconjug. Chem.* **2016**, *27* (12), 2808–2823. https://doi.org/10.1021/acs.bioconjchem.6b00641.

(193) Joseph, J.; Baumann, K. N.; Koehler, P.; Zuehlsdorff, T. J.; Cole, D. J.; Weber, J.; Bohndiek, S. E.; Hernández-Ainsa, S. Distance Dependent Photoacoustics Revealed through DNA Nanostructures. *Nanoscale* **2017**, *9* (42), 16193–16199. https://doi.org/10.1039/C7NR05353C.

(194) Zhang, K.; Meng, X.; Yang, Z.; Cao, Y.; Cheng, Y.; Wang, D.; Lu, H.; Shi, Z.; Dong, H.; Zhang, X. Cancer Cell Membrane Camouflaged Nanoprobe for Catalytic Ratiometric Photoacoustic Imaging of MicroRNA in Living Mice. *Adv. Mater.* **2019**, *31* (12), 1807888. https://doi.org/10.1002/adma.201807888.

(195) Yang, L.; Li, J.; Pan, W.; Wang, H.; Li, N.; Tang, B. Fluorescence and Photoacoustic Dual-Mode Imaging of Tumor-Related MRNA with a Covalent Linkage-Based DNA

Nanoprobe. *Chem. Commun.* **2018**, *54* (29), 3656–3659. https://doi.org/10.1039/C8CC01335G.
(196) Feng, Y.-H.; Tsao, C.-J. Emerging Role of MicroRNA-21 in Cancer. *Biomed. Rep.* **2016**, *5* (4), 395–402. https://doi.org/10.3892/br.2016.747.
(197) Ou, M.; Huang, J.; Yang, X.; He, X.; Quan, K.; Yang, Y.; Xie, N.; Li, J.; Wang, K. Live-Cell MicroRNA Imaging through MnO_2 Nanosheet-Mediated DD-A Hybridization Chain Reaction. *ChemBioChem* **2018**, *19* (2), 147–152. https://doi.org/10.1002/cbic.201700573.
(198) Fuenzalida Werner, J. P.; Huang, Y.; Mishra, K.; Janowski, R.; Vetschera, P.; Heichler, C.; Chmyrov, A.; Neufert, C.; Niessing, D.; Ntziachristos, V.; Stiel, A. C. Challenging a Preconception: Optoacoustic Spectrum Differs from the Optical Absorption Spectrum of Proteins and Dyes for Molecular Imaging. *Anal. Chem.* **2020**, *92* (15), 10717–10724. https://doi.org/10.1021/acs.analchem.0c01902.
(199) Zafar, M.; Xu, Q.; Manwar, R. Importance of Signal and Image Processing in Photoacoustic Imaging. *ArXiv201207955 Phys.* **2020**.
(200) Yao, J.; Wang, L. V. Sensitivity of Photoacoustic Microscopy. *Photoacoustics* **2014**, *2* (2), 87–101. https://doi.org/10.1016/j.pacs.2014.04.002.
(201) Ferrand, A.; Schleicher, K. D.; Ehrenfeuchter, N.; Heusermann, W.; Biehlmaier, O. Using the NoiSee Workflow to Measure Signal-to-Noise Ratios of Confocal Microscopes. *Sci. Rep.* **2019**, *9* (1), 1165. https://doi.org/10.1038/s41598-018-37781-3.
(202) Armbruster, D. A.; Pry, T. Limit of Blank, Limit of Detection and Limit of Quantitation. *Clin. Biochem. Rev.* **2008**, *29 Suppl 1*, S49-52.
(203) Jet, T.; Gines, G.; Rondelez, Y.; Taly, V. Advances in Multiplexed Techniques for the Detection and Quantification of MicroRNAs. *Chem. Soc. Rev.* **2021**, *50* (6), 4141–4161. https://doi.org/10.1039/D0CS00609B.
(204) Zhang, J.; Smaga, L. P.; Satyavolu, N. S. R.; Chan, J.; Lu, Y. DNA Aptamer-Based Activatable Probes for Photoacoustic Imaging in Living Mice. *J. Am. Chem. Soc.* **2017**, *139* (48), 17225–17228. https://doi.org/10.1021/jacs.7b07913.
(205) Morales, J.; Pawle, R. H.; Akkilic, N.; Luo, Y.; Xavierselvan, M.; Albokhari, R.; Calderon, I. A. C.; Selfridge, S.; Minns, R.; Takiff, L.; Mallidi, S.; Clark, H. A. DNA-Based Photoacoustic Nanosensor for Interferon Gamma Detection. *ACS Sens.* **2019**, *4* (5), 1313–1322. https://doi.org/10.1021/acssensors.9b00209.
(206) Liu, H.-Y.; Zhang, Y.-Y.; Zhu, B.-L.; Feng, F.-Z.; Yan, H.; Zhang, H.-Y.; Zhou, B. MiR-21 Regulates the Proliferation and Apoptosis of Ovarian Cancer Cells through PTEN/PI3K/AKT. *Eur. Rev. Med. Pharmacol. Sci.* **2019**, *23* (10), 4149–4155. https://doi.org/10.26355/eurrev_201905_17917.
(207) Chak, K.; Roy-Chaudhuri, B.; Kim, H. K.; Kemp, K. C.; Porter, B. E.; Kay, M. A. Increased Precursor MicroRNA-21 Following Status Epilepticus Can Compete with Mature MicroRNA-21 to Alter Translation. *Exp. Neurol.* **2016**, *286*, 137–146. https://doi.org/10.1016/j.expneurol.2016.10.003.
(208) Strohm, E. M.; Moore, M. J.; Kolios, M. C. Single Cell Photoacoustic Microscopy: A Review. *IEEE J. Sel. Top. Quantum Electron.* **2016**, *22* (3), 137–151. https://doi.org/10.1109/JSTQE.2015.2497323.
(209) Hariri, A.; Palma-Chavez, J.; Wear, K. A.; Pfefer, T. J.; Jokerst, J. V.; Vogt, W. C. Polyacrylamide Hydrogel Phantoms for Performance Evaluation of Multispectral Photoacoustic Imaging Systems. *Photoacoustics* **2021**, *22*, 100245. https://doi.org/10.1016/j.pacs.2021.100245.

(210) Pogue, B. W.; Patterson, M. S. Review of Tissue Simulating Phantoms for Optical Spectroscopy, Imaging and Dosimetry. *J. Biomed. Opt.* **2006**, *11* (4), 041102. https://doi.org/10.1117/1.2335429.
(211) Mozaffarzadeh, M.; Moore, C.; Golmoghani, E. B.; Mantri, Y.; Hariri, A.; Jorns, A.; Fu, L.; Verweij, M. D.; Orooji, M.; de Jong, N.; Jokerst, J. V. Motion-Compensated Noninvasive Periodontal Health Monitoring Using Handheld and Motor-Based Photoacoustic-Ultrasound Imaging Systems. *Biomed. Opt. Express* **2021**, *12* (3), 1543. https://doi.org/10.1364/BOE.417345.
(212) Kobayashi, H.; Ogawa, M.; Alford, R.; Choyke, P. L.; Urano, Y. New Strategies for Fluorescent Probe Design in Medical Diagnostic Imaging. *Chem. Rev.* **2010**, *110* (5), 2620–2640. https://doi.org/10.1021/cr900263j.
(213) Huang, Y.; Chen, W.; Chung, J.; Yin, J.; Yoon, J. Recent Progress in Fluorescent Probes for Bacteria. *Chem. Soc. Rev.* **2021**, *50* (13), 7725–7744. https://doi.org/10.1039/D0CS01340D.
(214) Borg, R. E.; Rochford, J. Molecular Photoacoustic Contrast Agents: Design Principles & Applications. *Photochem. Photobiol.* **2018**, *94* (6), 1175–1209. https://doi.org/10.1111/php.12967.
(215) Wu, X.; Zhu, W. Stability Enhancement of Fluorophores for Lighting up Practical Application in Bioimaging. *Chem. Soc. Rev.* **2015**, *44* (13), 4179–4184. https://doi.org/10.1039/C4CS00152D.
(216) Ye, D.; Shuhendler, A. J.; Cui, L.; Tong, L.; Tee, S. S.; Tikhomirov, G.; Felsher, D. W.; Rao, J. Bioorthogonal Cyclization-Mediated in Situ Self-Assembly of Small-Molecule Probes for Imaging Caspase Activity in Vivo. *Nat. Chem.* **2014**, *6* (6), 519–526. https://doi.org/10.1038/nchem.1920.
(217) Lam, P.; Steinmetz, N. F. Plant Viral and Bacteriophage Delivery of Nucleic Acid Therapeutics. *WIREs Nanomedicine Nanobiotechnology* **2018**, *10* (1). https://doi.org/10.1002/wnan.1487.
(218) Zhu, G.; Zheng, J.; Song, E.; Donovan, M.; Zhang, K.; Liu, C.; Tan, W. Self-Assembled, Aptamer-Tethered DNA Nanotrains for Targeted Transport of Molecular Drugs in Cancer Theranostics. *Proc. Natl. Acad. Sci.* **2013**, *110* (20), 7998–8003. https://doi.org/10.1073/pnas.1220817110.
(219) Choi, V.; Rajora, M. A.; Zheng, G. Activating Drugs with Sound: Mechanisms Behind Sonodynamic Therapy and the Role of Nanomedicine. *Bioconjug. Chem.* **2020**, *31* (4), 967–989. https://doi.org/10.1021/acs.bioconjchem.0c00029.
(220) Mehrotra, N.; Gupta, M.; Kovar, A.; Meibohm, B. The Role of Pharmacokinetics and Pharmacodynamics in Phosphodiesterase-5 Inhibitor Therapy. *Int. J. Impot. Res.* **2007**, *19* (3), 253–264. https://doi.org/10.1038/sj.ijir.3901522.
(221) Cash, K. J.; Li, C.; Xia, J.; Wang, L. V.; Clark, H. A. Optical Drug Monitoring: Photoacoustic Imaging of Nanosensors to Monitor Therapeutic Lithium *in Vivo*. *ACS Nano* **2015**, *9* (2), 1692–1698. https://doi.org/10.1021/nn5064858.
(222) Zhu, X.; Li, J.; Peng, P.; Hosseini Nassab, N.; Smith, B. R. Quantitative Drug Release Monitoring in Tumors of Living Subjects by Magnetic Particle Imaging Nanocomposite. *Nano Lett.* **2019**, *19* (10), 6725–6733. https://doi.org/10.1021/acs.nanolett.9b01202.
(223) Zhu, X.; Li, J.; Peng, P.; Hosseini Nassab, N.; Smith, B. R. Quantitative Drug Release Monitoring in Tumors of Living Subjects by Magnetic Particle Imaging Nanocomposite. *Nano Lett.* **2019**, *19* (10), 6725–6733. https://doi.org/10.1021/acs.nanolett.9b01202.

(224) Moore, C.; Chen, F.; Wang, J.; Jokerst, J. V. Listening for the Therapeutic Window: Advances in Drug Delivery Utilizing Photoacoustic Imaging. *Adv. Drug Deliv. Rev.* **2019**, *144*, 78–89. https://doi.org/10.1016/j.addr.2019.07.003.
(225) Park, B.; Park, S.; Kim, J.; Kim, C. Listening to Drug Delivery and Responses via Photoacoustic Imaging. *Adv. Drug Deliv. Rev.* **2022**, *184*, 114235. https://doi.org/10.1016/j.addr.2022.114235.
(226) Huang, J.; Pu, K. Activatable Molecular Probes for Second Near-Infrared Fluorescence, Chemiluminescence, and Photoacoustic Imaging. *Angew. Chem. Int. Ed.* **2020**, *59* (29), 11717–11731. https://doi.org/10.1002/anie.202001783.
(227) Bhutiani, N.; Samykutty, A.; McMasters, K. M.; Egilmez, N. K.; McNally, L. R. In Vivo Tracking of Orally-Administered Particles within the Gastrointestinal Tract of Murine Models Using Multispectral Optoacoustic Tomography. *Photoacoustics* **2019**, *13*, 46–52. https://doi.org/10.1016/j.pacs.2018.11.003.
(228) Duan, Z.; Gao, Y.-J.; Qiao, Z.-Y.; Fan, G.; Liu, Y.; Zhang, D.; Wang, H. A Photoacoustic Approach for Monitoring the Drug Release of PH-Sensitive Poly(β-Amino Ester)s. *J Mater Chem B* **2014**, *2* (37), 6271–6282. https://doi.org/10.1039/C4TB00319E.
(229) Sun, Y.; Ding, F.; Chen, Z.; Zhang, R.; Li, C.; Xu, Y.; Zhang, Y.; Ni, R.; Li, X.; Yang, G.; Sun, Y.; Stang, P. J. Melanin-Dot–Mediated Delivery of Metallacycle for NIR-II/Photoacoustic Dual-Modal Imaging-Guided Chemo-Photothermal Synergistic Therapy. *Proc. Natl. Acad. Sci.* **2019**, *116* (34), 16729–16735. https://doi.org/10.1073/pnas.1908761116.
(230) Jeevarathinam, A. S.; Lemaster, J. E.; Chen, F.; Zhao, E.; Jokerst, J. V. Photoacoustic Imaging Quantifies Drug Release from Nanocarriers via Redox Chemistry of Dye-Labeled Cargo. *Angew. Chem. Int. Ed.* **2020**, *59* (12), 4678–4683. https://doi.org/10.1002/anie.201914120.
(231) Morya, V.; Walia, S.; Mandal, B. B.; Ghoroi, C.; Bhatia, D. Functional DNA Based Hydrogels: Development, Properties and Biological Applications. *ACS Biomater. Sci. Eng.* **2020**, *6* (11), 6021–6035. https://doi.org/10.1021/acsbiomaterials.0c01125.
(232) Gottlieb, H. E.; Kotlyar, V.; Nudelman, A. NMR Chemical Shifts of Common Laboratory Solvents as Trace Impurities. *J. Org. Chem.* **1997**, *62* (21), 7512–7515. https://doi.org/10.1021/jo971176v.
(233) Nguyen, L. P.; Gerstein, N. S. Cardiovascular Pharmacology in Noncardiac Surgery. In *Essentials of Cardiac Anesthesia for Noncardiac Surgery*; Elsevier, 2019; pp 247–288. https://doi.org/10.1016/B978-0-323-56716-9.00011-4.
(234) Peter, C.; Hongwan, D.; Küpfer, A.; Lauterburg, B. H. Pharmacokinetics and Organ Distribution of Intravenous and Oral Methylene Blue. *Eur. J. Clin. Pharmacol.* **2000**, *56* (3), 247–250. https://doi.org/10.1007/s002280000124.
(235) Hossain, M.; Suresh Kumar, G. DNA Intercalation of Methylene Blue and Quinacrine: New Insights into Base and Sequence Specificity from Structural and Thermodynamic Studies with Polynucleotides. *Mol. Biosyst.* **2009**, *5* (11), 1311. https://doi.org/10.1039/b909563b.
(236) Anderson, R. J.; Babson, J. R. Reduction of Doxorubicin Toxicity by Methylene Blue in Cultured Rat Myocardial Cells. *Biochem. Pharmacol.* **1989**, *38* (15), 2568–2572. https://doi.org/10.1016/0006-2952(89)90104-4.
(237) Hrushesky, WilliamJ. M.; Wood, P.; Olshefski, R.; Meshnick, S.; Eaton, JohnW. MODIFYING INTRACELLULAR REDOX BALANCE: AN APPROACH TO

IMPROVING THERAPEUTIC INDEX. *The Lancet* **1985**, *325* (8428), 565–567. https://doi.org/10.1016/S0140-6736(85)91218-8.
(238) Wang, J.; Lin, C.-Y.; Moore, C.; Jhunjhunwala, A.; Jokerst, J. V. Switchable Photoacoustic Intensity of Methylene Blue via Sodium Dodecyl Sulfate Micellization. *Langmuir* **2018**, *34* (1), 359–365. https://doi.org/10.1021/acs.langmuir.7b03718.
(239) Ebo, J. S.; Saunders, J. C.; Devine, P. W. A.; Gordon, A. M.; Warwick, A. S.; Schiffrin, B.; Chin, S. E.; England, E.; Button, J. D.; Lloyd, C.; Bond, N. J.; Ashcroft, A. E.; Radford, S. E.; Lowe, D. C.; Brockwell, D. J. An in Vivo Platform to Select and Evolve Aggregation-Resistant Proteins. *Nat. Commun.* **2020**, *11* (1), 1816. https://doi.org/10.1038/s41467-020-15667-1.
(240) Zheng, G.; Chen, J.; Stefflova, K.; Jarvi, M.; Li, H.; Wilson, B. C. Photodynamic Molecular Beacon as an Activatable Photosensitizer Based on Protease-Controlled Singlet Oxygen Quenching and Activation. *Proc. Natl. Acad. Sci.* **2007**, *104* (21), 8989–8994. https://doi.org/10.1073/pnas.0611142104.
(241) Maeda, H.; Khatami, M. Analyses of Repeated Failures in Cancer Therapy for Solid Tumors: Poor Tumor-selective Drug Delivery, Low Therapeutic Efficacy and Unsustainable Costs. *Clin. Transl. Med.* **2018**, *7* (1). https://doi.org/10.1186/s40169-018-0185-6.
(242) Prabhakar, U.; Maeda, H.; Jain, R. K.; Sevick-Muraca, E. M.; Zamboni, W.; Farokhzad, O. C.; Barry, S. T.; Gabizon, A.; Grodzinski, P.; Blakey, D. C. Challenges and Key Considerations of the Enhanced Permeability and Retention Effect for Nanomedicine Drug Delivery in Oncology. *Cancer Res.* **2013**, *73* (8), 2412–2417. https://doi.org/10.1158/0008-5472.CAN-12-4561.
(243) Li, J.; Mooney, D. J. Designing Hydrogels for Controlled Drug Delivery. *Nat. Rev. Mater.* **2016**, *1* (12), 16071. https://doi.org/10.1038/natrevmats.2016.71.
(244) Senapati, S.; Mahanta, A. K.; Kumar, S.; Maiti, P. Controlled Drug Delivery Vehicles for Cancer Treatment and Their Performance. *Signal Transduct. Target. Ther.* **2018**, *3*, 7. https://doi.org/10.1038/s41392-017-0004-3.
(245) Naskar, J.; Palui, G.; Banerjee, A. Tetrapeptide-Based Hydrogels: For Encapsulation and Slow Release of an Anticancer Drug at Physiological PH. *J. Phys. Chem. B* **2009**, *113* (35), 11787–11792. https://doi.org/10.1021/jp904251j.
(246) Miao, Q.; Pu, K. Organic Semiconducting Agents for Deep-Tissue Molecular Imaging: Second Near-Infrared Fluorescence, Self-Luminescence, and Photoacoustics. *Adv. Mater.* **2018**, *30* (49), 1801778. https://doi.org/10.1002/adma.201801778.
(247) Almaqwashi, A. A.; Paramanathan, T.; Rouzina, I.; Williams, M. C. Mechanisms of Small Molecule–DNA Interactions Probed by Single-Molecule Force Spectroscopy. *Nucleic Acids Res.* **2016**, *44* (9), 3971–3988. https://doi.org/10.1093/nar/gkw237.
(248) Mizuno, Y.; Naoi, T.; Nishikawa, M.; Rattanakiat, S.; Hamaguchi, N.; Hashida, M.; Takakura, Y. Simultaneous Delivery of Doxorubicin and Immunostimulatory CpG Motif to Tumors Using a Plasmid DNA/Doxorubicin Complex in Mice. *J. Controlled Release* **2010**, *141* (2), 252–259. https://doi.org/10.1016/j.jconrel.2009.09.014.
(249) Nishikawa, M.; Mizuno, Y.; Mohri, K.; Matsuoka, N.; Rattanakiat, S.; Takahashi, Y.; Funabashi, H.; Luo, D.; Takakura, Y. Biodegradable CpG DNA Hydrogels for Sustained Delivery of Doxorubicin and Immunostimulatory Signals in Tumor-Bearing Mice. *Biomaterials* **2011**, *32* (2), 488–494. https://doi.org/10.1016/j.biomaterials.2010.09.013.

(250) Trouet, A.; Campeneere, D. D.-D.; De Duve, C. Chemotherapy through Lysosomes with a DNA-Daunorubicin Complex. *Nature. New Biol.* **1972**, *239* (91), 110–112. https://doi.org/10.1038/newbio239110a0.
(251) Joseph, J.; Baumann, K. N.; Postigo, A.; Bollepalli, L.; Bohndiek, S. E.; Hernández-Ainsa, S. DNA-Based Nanocarriers to Enhance the Optoacoustic Contrast of Tumors In Vivo. *Adv. Healthc. Mater.* **2021**, *10* (2), 2001739. https://doi.org/10.1002/adhm.202001739.
(252) Borum, R. M.; Moore, C.; Chan, S. K.; Steinmetz, N. F.; Jokerst, J. V. A Photoacoustic Contrast Agent for MiR-21 via NIR Fluorescent Hybridization Chain Reaction. *Bioconjug. Chem.* **2021**, acs.bioconjchem.1c00375. https://doi.org/10.1021/acs.bioconjchem.1c00375.
(253) Jiang, Y.; Cui, D.; Fang, Y.; Zhen, X.; Upputuri, P. K.; Pramanik, M.; Ding, D.; Pu, K. Amphiphilic Semiconducting Polymer as Multifunctional Nanocarrier for Fluorescence/Photoacoustic Imaging Guided Chemo-Photothermal Therapy. *Biomaterials* **2017**, *145*, 168–177. https://doi.org/10.1016/j.biomaterials.2017.08.037.
(254) Wang, J.; Chao, J.; Liu, H.; Su, S.; Wang, L.; Huang, W.; Willner, I.; Fan, C. Clamped Hybridization Chain Reactions for the Self-Assembly of Patterned DNA Hydrogels. *Angew. Chem. Int. Ed.* **2017**, *56* (8), 2171–2175. https://doi.org/10.1002/anie.201610125.
(255) Liu, Y.; Yang, G.; Jin, S.; Xu, L.; Zhao, C. Development of High-Drug-Loading Nanoparticles. *ChemPlusChem* **2020**, *85* (9), 2143–2157. https://doi.org/10.1002/cplu.202000496.
(256) Wang, J.; Jeevarathinam, A. S.; Humphries, K.; Jhunjhunwala, A.; Chen, F.; Hariri, A.; Miller, B. R.; Jokerst, J. V. A Mechanistic Investigation of Methylene Blue and Heparin Interactions and Their Photoacoustic Enhancement. *Bioconjug. Chem.* **2018**, *29* (11), 3768–3775. https://doi.org/10.1021/acs.bioconjchem.8b00639.
(257) Biaggne, A.; Spear, L.; Barcenas, G.; Ketteridge, M.; Kim, Y. C.; Melinger, J. S.; Knowlton, W. B.; Yurke, B.; Li, L. Data-Driven and Multiscale Modeling of DNA-Templated Dye Aggregates. *Molecules* **2022**, *27* (11), 3456. https://doi.org/10.3390/molecules27113456.
(258) Liu, R.; Tang, J.; Xu, Y.; Zhou, Y.; Dai, Z. Nano-Sized Indocyanine Green J-Aggregate as a One-Component Theranostic Agent. *Nanotheranostics* **2017**, *1* (4), 430–439. https://doi.org/10.7150/ntno.19935.
(259) Moore, C.; Borum, R. M.; Mantri, Y.; Xu, M.; Fajtová, P.; O'Donoghue, A. J.; Jokerst, J. V. Activatable Carbocyanine Dimers for Photoacoustic and Fluorescent Detection of Protease Activity. *ACS Sens.* **2021**, *6* (6), 2356–2365. https://doi.org/10.1021/acssensors.1c00518.
(260) Zeng, W.; Wu, L.; Sun, Y.; Wang, Y.; Wang, J.; Ye, D. Ratiometric Imaging of MMP-2 Activity Facilitates Tumor Detection Using Activatable Near-Infrared Fluorescent Semiconducting Polymer Nanoparticles. *Small* **2021**, *17* (36), 2101924. https://doi.org/10.1002/smll.202101924.
(261) McMullen, J. R. W.; Selleck, M.; Wall, N. R.; Senthil, M. Peritoneal Carcinomatosis: Limits of Diagnosis and the Case for Liquid Biopsy. *Oncotarget* **2017**, *8* (26), 43481–43490. https://doi.org/10.18632/oncotarget.16480.
(262) Lu, Z.; Wang, J.; Wientjes, M. G.; Au, J. L.-S. Intraperitoneal Therapy for Peritoneal Cancer. *Future Oncol.* **2010**, *6* (10), 1625–1641. https://doi.org/10.2217/fon.10.100.

(263) Cui, D.; Li, P.; Zhen, X.; Li, J.; Jiang, Y.; Yu, A.; Hu, X.; Pu, K. Thermoresponsive Semiconducting Polymer Nanoparticles for Contrast-Enhanced Photoacoustic Imaging. *Adv. Funct. Mater.* **2019**, *29* (38), 1903461. https://doi.org/10.1002/adfm.201903461.
(264) Silverman, R. B. Prodrugs and Drug Delivery Systems. In *The Organic Chemistry of Drug Design and Drug Action*; Elsevier, 2004; pp 497–557. https://doi.org/10.1016/B978-0-08-051337-9.50013-4.
(265) Ashley, G. W.; Henise, J.; Reid, R.; Santi, D. V. Hydrogel Drug Delivery System with Predictable and Tunable Drug Release and Degradation Rates. *Proc. Natl. Acad. Sci.* **2013**, *110* (6), 2318–2323. https://doi.org/10.1073/pnas.1215498110.
(266) Aderibigbe, B. A.; Mukaya, H. E. Polymer Therapeutics: Design, Application, and Pharmacokinetics. In *Nano- and Microscale Drug Delivery Systems*; Elsevier, 2017; pp 33–48. https://doi.org/10.1016/B978-0-323-52727-9.00003-0.
(267) Malonis, R. J.; Lai, J. R.; Vergnolle, O. Peptide-Based Vaccines: Current Progress and Future Challenges. *Chem. Rev.* **2020**, *120* (6), 3210–3229. https://doi.org/10.1021/acs.chemrev.9b00472.
(268) Aloisio, A.; Nisticò, N.; Mimmi, S.; Maisano, D.; Vecchio, E.; Fiume, G.; Iaccino, E.; Quinto, I. Phage-Displayed Peptides for Targeting Tyrosine Kinase Membrane Receptors in Cancer Therapy. *Viruses* **2021**, *13* (4), 649. https://doi.org/10.3390/v13040649.
(269) J. Boohaker, R.; W. Lee, M.; Vishnubhotla, P.; M. Perez, J. L.; R. Khaled, A. The Use of Therapeutic Peptides to Target and to Kill Cancer Cells. *CMC* **2012**, *19* (22), 3794–3804. https://doi.org/10.2174/092986712801661004.
(270) Wang, L.; Wang, N.; Zhang, W.; Cheng, X.; Yan, Z.; Shao, G.; Wang, X.; Wang, R.; Fu, C. Therapeutic Peptides: Current Applications and Future Directions. *Sig Transduct Target Ther* **2022**, *7* (1), 48. https://doi.org/10.1038/s41392-022-00904-4.
(271) Zegota, M. M.; Müller, M. A.; Lantzberg, B.; Kizilsavas, G.; Coelho, J. A. S.; Moscariello, P.; Martínez-Negro, M.; Morsbach, S.; Gois, P. M. P.; Wagner, M.; Ng, D. Y. W.; Kuan, S. L.; Weil, T. Dual Stimuli-Responsive Dynamic Covalent Peptide Tags: Toward Sequence-Controlled Release in Tumor-like Microenvironments. *J. Am. Chem. Soc.* **2021**, *143* (41), 17047–17058. https://doi.org/10.1021/jacs.1c06559.
(272) Fitzgerald, M. C.; West, G. M. Painting Proteins with Covalent Labels: What's in the Picture? *J. Am. Soc. Mass Spectrom.* **2009**, *20* (6), 1193–1206. https://doi.org/10.1016/j.jasms.2009.02.006.
(273) Doll, T. A. P. F.; Dey, R.; Burkhard, P. Design and Optimization of Peptide Nanoparticles. *J Nanobiotechnol* **2015**, *13* (1), 73. https://doi.org/10.1186/s12951-015-0119-z.
(274) Boisguérin, P.; Konate, K.; Josse, E.; Vivès, E.; Deshayes, S. Peptide-Based Nanoparticles for Therapeutic Nucleic Acid Delivery. *Biomedicines* **2021**, *9* (5), 583. https://doi.org/10.3390/biomedicines9050583.
(275) Sun, L.; Zheng, C.; Webster, T. Self-Assembled Peptide Nanomaterials for Biomedical Applications: Promises and Pitfalls. *IJN* **2016**, *Volume 12*, 73–86. https://doi.org/10.2147/IJN.S117501.
(276) Sugahara, K. N.; Braun, G. B.; de Mendoza, T. H.; Kotamraju, V. R.; French, R. P.; Lowy, A. M.; Teesalu, T.; Ruoslahti, E. Tumor-Penetrating IRGD Peptide Inhibits Metastasis. *Molecular Cancer Therapeutics* **2015**, *14* (1), 120–128. https://doi.org/10.1158/1535-7163.MCT-14-0366.

(277) Kang, S.; Lee, S.; Park, S. IRGD Peptide as a Tumor-Penetrating Enhancer for Tumor-Targeted Drug Delivery. *Polymers* **2020**, *12* (9), 1906. https://doi.org/10.3390/polym12091906.
(278) Sugahara, K. N.; Teesalu, T.; Karmali, P. P.; Kotamraju, V. R.; Agemy, L.; Greenwald, D. R.; Ruoslahti, E. Coadministration of a Tumor-Penetrating Peptide Enhances the Efficacy of Cancer Drugs. *Science* **2010**, *328* (5981), 1031–1035. https://doi.org/10.1126/science.1183057.
(279) Jeon, M.; Song, W.; Huynh, E.; Kim, J.; Kim, J.; Helfield, B. L.; Leung, B. Y. C.; Goertz, D. E.; Zheng, G.; Oh, J.; Lovell, J. F.; Kim, C. Methylene Blue Microbubbles as a Model Dual-Modality Contrast Agent for Ultrasound and Activatable Photoacoustic Imaging. *J. Biomed. Opt* **2014**, *19* (1), 016005. https://doi.org/10.1117/1.JBO.19.1.016005.
(280) Shen, X.; Dong, L.; He, X.; Zhao, C.; Zhang, W.; Li, X.; Lu, Y. Treatment of Infected Wounds with Methylene Blue Photodynamic Therapy: An Effective and Safe Treatment Method. *Photodiagnosis and Photodynamic Therapy* **2020**, *32*, 102051. https://doi.org/10.1016/j.pdpdt.2020.102051.
(281) Chen, B.; Liu, X.; Li, Y.; Shan, T.; Bai, L.; Li, C.; Wang, Y. IRGD Tumor-Penetrating Peptide-Modified Nano-Delivery System Based on a Marine Sulfated Polysaccharide for Enhanced Anti-Tumor Efficiency Against Breast Cancer. *IJN* **2022**, *Volume 17*, 617–633. https://doi.org/10.2147/IJN.S343902.
(282) Hausig-Punke, F.; Richter, F.; Hoernke, M.; Brendel, J. C.; Traeger, A. Tracking the Endosomal Escape: A Closer Look at Calcein and Related Reporters. *Macromolecular Bioscience* **2022**, *22* (10), 2270027. https://doi.org/10.1002/mabi.202270027.
(283) Salim, H.; Pei, D. Assessing the Cellular Uptake, Endosomal Escape, and Cytosolic Entry Efficiencies of Cyclic Peptides. In *Peptide Macrocycles*; Coppock, M. B., Winton, A. J., Eds.; Methods in Molecular Biology; Springer US: New York, NY, 2022; Vol. 2371, pp 301–316. https://doi.org/10.1007/978-1-0716-1689-5_16.
(284) Lee; Trinh; Yoo; Shin; Lee; Kim; Hwang; Lim; Ryou. Self-Assembling Peptides and Their Application in the Treatment of Diseases. *IJMS* **2019**, *20* (23), 5850. https://doi.org/10.3390/ijms20235850.
(285) Zhang, S.; Holmes, T.; Lockshin, C.; Rich, A. Spontaneous Assembly of a Self-Complementary Oligopeptide to Form a Stable Macroscopic Membrane. *Proc. Natl. Acad. Sci. U.S.A.* **1993**, *90* (8), 3334–3338. https://doi.org/10.1073/pnas.90.8.3334.
(286) Bellomo, E. G.; Wyrsta, M. D.; Pakstis, L.; Pochan, D. J.; Deming, T. J. Stimuli-Responsive Polypeptide Vesicles by Conformation-Specific Assembly. *Nature Mater* **2004**, *3* (4), 244–248. https://doi.org/10.1038/nmat1093.
(287) Lönn, P.; Kacsinta, A. D.; Cui, X.-S.; Hamil, A. S.; Kaulich, M.; Gogoi, K.; Dowdy, S. F. Enhancing Endosomal Escape for Intracellular Delivery of Macromolecular Biologic Therapeutics. *Sci Rep* **2016**, *6* (1), 32301. https://doi.org/10.1038/srep32301.
(288) Simón-Gracia, L.; Hunt, H.; Scodeller, P.; Gaitzsch, J.; Kotamraju, V. R.; Sugahara, K. N.; Tammik, O.; Ruoslahti, E.; Battaglia, G.; Teesalu, T. IRGD Peptide Conjugation Potentiates Intraperitoneal Tumor Delivery of Paclitaxel with Polymersomes. *Biomaterials* **2016**, *104*, 247–257. https://doi.org/10.1016/j.biomaterials.2016.07.023.
(289) Tsoi, K. M.; MacParland, S. A.; Ma, X.-Z.; Spetzler, V. N.; Echeverri, J.; Ouyang, B.; Fadel, S. M.; Sykes, E. A.; Goldaracena, N.; Kaths, J. M.; Conneely, J. B.; Alman, B. A.; Selzner, M.; Ostrowski, M. A.; Adeyi, O. A.; Zilman, A.; McGilvray, I. D.; Chan, W. C. W.

Mechanism of Hard-Nanomaterial Clearance by the Liver. *Nature Mater* **2016**, *15* (11), 1212–1221. https://doi.org/10.1038/nmat4718.
(290) Cao, G.; He, X.; Sun, Q.; Chen, S.; Wan, K.; Xu, X.; Feng, X.; Li, P.; Chen, B.; Xiong, M. The Oncolytic Virus in Cancer Diagnosis and Treatment. *Front. Oncol.* **2020**, *10*, 1786. https://doi.org/10.3389/fonc.2020.01786.
(291) Blanco, E.; Shen, H.; Ferrari, M. Principles of Nanoparticle Design for Overcoming Biological Barriers to Drug Delivery. *Nat Biotechnol* **2015**, *33* (9), 941–951. https://doi.org/10.1038/nbt.3330.
(292) He, S.; Li, J.; Cheng, P.; Zeng, Z.; Zhang, C.; Duan, H.; Pu, K. Charge-Reversal Polymer Nano-modulators for Photodynamic Immunotherapy of Cancer. *Angewandte Chemie Intl Edit* **2021**, *60* (35), 19355–19363. https://doi.org/10.1002/anie.202106392.
(293) Wang, J.; Chen, F.; Arconada-Alvarez, S. J.; Hartanto, J.; Yap, L.-P.; Park, R.; Wang, F.; Vorobyova, I.; Dagliyan, G.; Conti, P. S.; Jokerst, J. V. A Nanoscale Tool for Photoacoustic-Based Measurements of Clotting Time and Therapeutic Drug Monitoring of Heparin. *Nano Lett.* **2016**, *16* (10), 6265–6271. https://doi.org/10.1021/acs.nanolett.6b02557.
(294) Bai, L.; Hu, Z.; Han, T.; Wang, Y.; Xu, J.; Jiang, G.; Feng, X.; Sun, B.; Liu, X.; Tian, R.; Sun, H.; Zhang, S.; Chen, X.; Zhu, S. Super-Stable Cyanine@albumin Fluorophore for Enhanced NIR-II Bioimaging. *Theranostics* **2022**, *12* (10), 4536–4547. https://doi.org/10.7150/thno.71443.
(295) Hao, Y.; Song, K.; Tan, X.; Ren, L.; Guo, X.; Zhou, C.; Li, H.; Wen, J.; Meng, Y.; Lin, M.; Zhang, Y.; Huang, H.; Wang, L.; Zheng, W. Reactive Oxygen Species-Responsive Polypeptide Drug Delivery System Targeted Activated Hepatic Stellate Cells to Ameliorate Liver Fibrosis. *ACS Nano* **2022**, *16* (12), 20739–20757. https://doi.org/10.1021/acsnano.2c07796.
(296) Guidolin, K.; Zheng, G. Nanomedicines Lost in Translation. *ACS Nano* **2019**, *13* (12), 13620–13626. https://doi.org/10.1021/acsnano.9b08659.
(297) Li, Y.; Yue, S.; Qi, H.; Ding, C.; Song, W.; Bi, S. Target-Triggered Dynamic Hairpin Assembly for Signal Amplification of MicroRNA and Oncogenes and Its Application in Live-Cell Imaging. *Chem Commun (Camb)* **2019**, *55* (28), 4103–4106. https://doi.org/10.1039/c9cc00747d.
(298) Li, D.; Wu, Y.; Gan, C.; Yuan, R.; Xiang, Y. Bio-Cleavable Nanoprobes for Target-Triggered Catalytic Hairpin Assembly Amplification Detection of MicroRNAs in Live Cancer Cells. *Nanoscale* **2018**, *10* (37), 17623–17628. https://doi.org/10.1039/c8nr05229h.
(299) Tang, S.; Li, Y.; Zhu, A.; Yao, Y.; Sun, J.; Zheng, F.; Lin, Z.; Shen, W. A Triple-Amplification Strategy Based on the Formation of Peroxidase-like Two-Dimensional DNA/Fe_3O_4 Networks Initiated by the Hybridization Chain Reaction for Highly Sensitive Detection of MicroRNA. *Chem. Commun.* **2019**, *55* (58), 8386–8389. https://doi.org/10.1039/C9CC03194D.
(300) Yu, L.; He, P.; Xu, Y.; Kou, X.; Yu, Z.; Xie, X.; Miao, P. Manipulations of DNA Four-Way Junction Architecture and DNA Modified Fe3O4@Au Nanomaterials for the Detection of MiRNA. *Sensors and Actuators B: Chemical* **2020**, *313*, 128015. https://doi.org/10.1016/j.snb.2020.128015.
(301) Cheng, H.; Li, W.; Duan, S.; Peng, J.; Liu, J.; Ma, W.; Wang, H.; He, X.; Wang, K. Mesoporous Silica Containers and Programmed Catalytic Hairpin Assembly/Hybridization Chain Reaction Based Electrochemical Sensing Platform for MicroRNA Ultrasensitive

Detection with Low Background. *Anal Chem* **2019**, *91* (16), 10672–10678. https://doi.org/10.1021/acs.analchem.9b01947.
(302) Zhuang, W.; Li, Y.; Chen, J.; Liu, W.; Huang, H. Copper Nanocluster-Labeled Hybridization Chain Reaction for Potentiometric Immunoassay of Matrix Metalloproteinase-7 in Acute Kidney Injury and Renal Cancer. *Anal. Methods* **2019**, *11* (19), 2597–2604. https://doi.org/10.1039/C9AY00681H.